Supramolecular Ru^{II},Pt^{II} Complexes

Bridged by 2,3,5,6-tetrakis(2-pyridyl)pyrazine (tppz)

Shengliang Zhao

Dissertation submitted to the Faculty of the
Virginia Polytechnic Institute and State University
in partial fulfillment of the requirements for the degree of

Doctor of Philosophy
in
Chemistry

Karen J. Brewer, Chair
Harry C. Dorn
Brenda S. J. Winkel
Brian E. Hanson
Gary L. Long

January 12, 2010
Blacksburg, VA

Keywords: electron transfer, luminescence, redox, supramolecular, ruthenium, platinum, DNA, tppz, heteronuclear, crystal, catalyst,

Supramolecular of Ru^{II},Pt^{II} Complexes Bridged by 2,3,5,6-tetrakis(2-pyridyl)pyrazine (tppz)

Shengliang Zhao

ABSTRACT

The main theme of this dissertation is the study of two racemic compounds: a bimetallic complex, [(tpy)Ru(tppz)PtCl]$(PF_6)_3$, and a trimetallic complex, [ClPt(tppz)Ru(tppz)PtCl]$(PF_6)_4$, in solution and in the solid state, where tpy is 2,2':6',2''-terpyridine and tppz is 2,3,5,6-tetrakis(2-pyridyl)pyrazine. These two supramolecular assemblies display remarkably different stereochemistry, electrochemistry and photochemistry. The chapters in this document deal with a multidisciplinary project that is fundamental to the design and synthesis of similar entities with potential applications as antitumor agents.

Chapter 1 gives an overview on the metal polyazine supramolecules. More specifically, the section is focused on the tridentate ruthenium and platinum metallic supramolecular assemblies with emphasis on their functionality and the methods used to study such systems.

Chapter 2 describes the design and syntheses of the title complexes and their analogs using a building block strategy. The details of the experimental methods are included in this section.

Chapter 3 presents the identification of the title complexes in solution and in the solid state by means of single crystal crystallography, mass spectrometry including FAB-MS and ESI-MS, and multiple NMR techniques including 1D ^{1}H-NMR, ^{195}Pt-NMR and 2D COSY, NOESY and ^{195}Pt-^{1}H HMQC, as well as dynamic ^{1}H-NMR at variable temperatures. The bi- and tri-metallic complexes are crystallized in the chiral space group of C2/c and P21/c as racemic compounds. The interconversion of the three steroisomers, M-M, P-P and M-P of trimetallic complexes are detected in the NMR timescale. The assignments of the atypical NMR resonance of the bi- and tri-metallic complexes are supported with the help of multidimensional NMR techniques and NMR spectroscopy of known systems. The process of assigning the NMR spectra is accomplished step by step with complexities presented by ring current effects. The 1D-fiber,

2D-plate and 3D-flowerlike topography of the trimetallic complex of $[ClPt(tppz)Ru(tppz)PtCl](PF_6)_4$ was illustrated by SEM.

Chapter 4 demonstrates the electrochemical and photochemical differences between the title complexes and a comparison to known systems. Electrochemically, the Ru^{II},Pt^{II} bimetallic and trimetallic complexes display $Ru^{II/III}$ oxidations at 1.63 and 1.83 V and ligand-based reduction at -0.16 and -0.03 V versus Ag/AgCl, respectively. Spectroscopically, the Ru(dπ)→tppz(π*) MLCT transitions are red-shifted relative to the monometallic synthons ($[(tpy)Ru(tppz)](PF_6)_2$, λ_{max}^{abs} = 472 nm and $[Ru(tppz)_2](PF_6)_2$, λ_{max}^{abs} = 478 nm) occurring in the visible region, centered at 530 and 538 nm in CH_3CN for $[(tpy)Ru(tppz)PtCl](PF_6)_3$ and $[ClPt(tppz)Ru(tppz)PtCl](PF_6)_4$, respectively, consistent with the bridging coordination of the tppz ligand. $[ClPt(tppz)Ru(tppz)PtCl](PF_6)_4$ displays an intense emission ($\Phi^{em} = 5.4\times10^{-4}$) from the Ru(dπ)→tppz(π*) ^{3}MLCT state at RT with λ_{max}^{em} = 754 nm and lifetime of τ = 80 ns in CH_3CN solution. The trimetallic complex, $[ClPt(tppz)Ru(tppz)PtCl](PF_6)_4$, exhibits a strong emission property in the solid state with λ_{max}^{em} = 764 nm, which was also studied by confocal laser induced emission scanning microscopy. By contrast, a barely detectable emission was observed for the bimetallic complex, $[(tpy)Ru(tppz)PtCl](PF_6)_3$. The redox and luminescence differences between bi- and tri-metallic complexes is the consequence of the nature of these supramolecular assemblies. All together the data suggest strong Pt···Pt interactions in solution providing for assembly of these molecules into dimers or larger assemblies.

Chapter 5 reports the applications of these complexes as bioactive species interacting with DNA. The prelimary data show the title complexes bind to DNA producing larger changes in DNA migration during gel electrophoreses than does the well-established anticancer drug, cisplatin. Preliminary study indicates trimetallic complex $[ClPt(tppz)Ru(tppz)PtCl](PF_6)_4$ can photochemically condenses DNA. This data could provide a form for development of a new class of photodynamic therapy agents in cancer treatment.

Chapter 6 concludes with summaries of current research and perspective for further work.

Dedication

To my wife, Huihua (Lucy) Luo and my son, Robert L. Zhao

Acknowledgements

I would like to thank my advisor, Prof. Karen J Brewer, for giving me the opportunity to work in her amazing group at Virginia Tech. She provided full intellectual freedom, helpful critique, and constant encouragement in my research. I would also like to thank my committee members: Dr. Harry C. Dorn, Dr. Brenda S. J. Winkel, Dr. Brian E. Hanson, and Dr. Gary L. Long for all their time and support.

Special thanks are expressed to Prof Harry C. Dorn for his resourceful advice. His encouragement has not only strengthened my belief in the scientific pursuit, but also excited my passion for the professional research.

I would like to thank Dr. Carla Slebodnick for her patience on solving the crystal structures of my complexes. I thank Mr. Aaron J. Prussin II for his help to run the DNA gel electrophoresis using my complexes. I thank Prof. Webster L. Santos for his useful discussion on the research. I thank Mr. Stephen McCartney for carrying out the SEM on my samples using instruments in the Nanoscale Characterization and Fabrication Laboratory (NCFL) in Virginia Tech. I would like to thank all past and present lab members in Prof. Brewer's group for a nice time and for encouragement and help whenever and whatever needed. Special thanks are given to Dr. Shamindri M. Arachchige, Dr. Ran Miao, Dr. Guangbin Wang, Dr. Matthew T. Mongelli, Dr. David F. Zigler, Dr. Mark Elvinton, Dr. Avijita Jain, Dr. Krishnan Rangan, Dr. Baburam Sedai, Jared R. Brown, Samantha Hopkins, Jessica Knoll, Joan Zapiter, Travis White and Jing Wang who helped out things like references, figures and spellings on the writing as well as some interesting and useful discussion.

I deeply thank my family: my father, Zhongfeng Zhao, my mother, Xingzhi Chen, my wife, Huihua Luo, and my son, Robert L. Zhao, who have always believed in me and kept me going. Without their help, support and encouragement, I don’t know what I would have done.

Table of Contents

Abstract ii
Dedication iv
Acknowledgements v
Table of Contents vi
List of Figures x
List of Tables xvii
List of Abbreviations xix
Thesis Statement xxi
Chapter 1. Introduction 1
1.1 Summary 1
1.2 Molecular Orbital (MO) Theory 2
1.3 Photochemistry 4
1.3.1 Selection Rules 4
1.3.2 Electronic Excited State Decay 6
1.4 Electrochemistry 8
1.4 $[Ru^{II}(NN)_3]^{2+}$ Complexes 12
1.4.1 Limitation of Bidentate Systems 14
1.4.2 Tuning of Photophysical Properties of Tridentate Ru^{II} Complexes 14
1.4.3 Oligonuclear Tridentate Ru^{II} Complexes Using tppz BL 16
1.5 Pt^{II} Tridentate Complexes 21
1.6 Oligonuclear Ru^{II} Complexes 24
1.7 Ru^{II},Pt^{II} Mixed Metal Complexes 25
1.8 Stereochemistry 28
1.8.1 Homochirality and Symmetry Breaking 28
1.8.2 Symmetry and Time-scale 30
1.9 Nuclear Magnetic Resonance (NMR) 32
1.9.1 Chemical Shift (δ) 32

1.9.2 Electron Withdrawing Effect via Metal-ligand Bonding 33
1.9.3 Ring Current Effect 35
1.9.4 Fluxionality in Tridentate Pt^{II} Complex Characterized by NMR 38
1.10 The Varied Binding Modes of the Ligand tppz 39
1.10.1 Binding Modes of tppz 40
1.10.2 Chirality in Complexes of tppz 43
1.11 Applications: DNA-Metal Complex (MC) Interactions 45
1.11.1 Structure of DNA 45
1.11.2 Binding Modes 46
1.11.3 Binding to DNA 46
1.12 Statement of Problem 49
Chapter 2: Experiments: Materials, Syntheses and Measurements 50
2.1 Materials 50
2.2 Syntheses 50
2.2.1 Synthesis of $[(tpy)RuCl_3]$ 51
2.2.2 Synthesis of $[Ru(tpy)_2](PF_6)_2$ 51
2.2.3 Synthesis of $[(tpy)Ru(tppz)](PF_6)_2$ 51
2.2.4 Synthesis of $[Ru(tppz)_2](PF_6)_2$ 52
2.2.5 Synthesis of $[(tpy)Ru(tppz)Ru(tpy)](PF_6)_3$ 53
2.2.6 Synthesis of $[(tpy)Ru(tppz)Ru(tppz)Ru(tpy)](PF_6)_3$ 53
2.2.7 Synthesis of $[(tpy)Ru(tppz)PtCl](PF_6)_3$ 53
2.2.8 Synthesis of $[ClPt(tppz)Ru(tppz)PtCl](PF_6)_4$ 54
2.3 Measurements 55
2.3.1 Mass Spectrometry 55
2.3.2 Crystallography 56
2.3.2.1 X-Ray Diffraction of $[(tpy)Ru(tppz)PtCl](PF_6)_3$ 56
2.3.2.2 X-Ray Diffraction of $[ClPt(tppz)Ru(tppz)PtCl](PF_6)_4$ 57
2.3.3 NMR Spectroscopy 58
2.3.4 Electrochemistry 58
2.3.5 Photochemistry 58
2.3.5.1 Electronic Absorption Spectroscopy 58

2.3.5.2 Emission Spectroscopy 58
2.3.5.3 Lifetime Measurement 60
2.3.6 DNA Gel Electrophoresis 61
Chapter 3. Identification and Characterization 62
3.1 Syntheses 62
3.2 Characterizations 65
3.2.1 Mass Spectrometry 65
3.2.1.1 FAB Mass Spectrometry 65
3.2.1.2 ESI Mass Spectrometry 67
3.2.2 NMR 71
3.2.2.1 Ring Current and Geometry 77
3.2.2.2 ^{1}H-^{1}H NOESY 81
3.2.2.3 ^{1}H-NMR Assignment of [(tpy)Ru(tppz)](PF$_6$)$_2$ 81
3.2.2.4 ^{1}H-NMR Assignment of [(tpy)Ru(tppz)PtCl](PF$_6$)$_2$ 86
3.2.2.5 ^{1}H NMR Assignment of [ClPt(tppz)Ru(tppz)PtCl](PF$_6$)$_4$ 91
3.2.2.6 Summary 93
3.2.3 Crystallography 94
3.2.3.1 Crystal Structure Determination 94
3.2.4 Morphology of the Aggregation 103
3.2.5 ^{1}H-NMR Revisited 105
Chapter 4. Electrochemical, Spectroscopic and Photophysical Properties 108
4.2 Electrochemistry 108
4.2.1 Electrochemical Properties of Monometallic Precursors 112
4.2.2 Electrochemical Properties of Ru^{II},Pt^{II} Mixed-metal Complexes 112
4.2.3 Comparison of Electrochemical Properties of Ru^{II}Pt^{II} Complexes with their Monometallic Precursors 114
4.3 Electronic Absorption and Emission Spectroscopy 116
4.3.1 Electronic Absorption Spectroscopy 118
4.3.2 Luminescent Properties of [(tpy)Ru(tppz)PtCl](PF$_6$)$_3$ and [ClPt(tppz)Ru(tppz)PtCl](PF$_6$)$_4$ 119

4.3.3 Concentration Dependent Study of the Luminescent Property of [(tpy)Ru(tppz)PtCl](PF$_6$)$_3$ 120
4.3.4 Solid State Emission Property of [ClPt(tppz)Ru(tppz)PtCl](PF$_6$)$_4$ 122
Chapter 5. Applications: Metal Complex-DNA Interactions 123
5.1 Thermal Binding Study 123
5.2 Light Activated DNA Interactions 128
5.2.1 Emission Titration 128
5.2.2 Photoreactivity of [ClPt(tppz)Ru(tppz)PtCl]Cl$_4$ with DNA 130
Chapter 6. Conclusions and Future Work 134
6.1 Highlights of the Contributions 134
6.2 Conclusions in Detail 135
6.3 Future Work 142
Reference 146
Appendix 159

List of Figures

Figure 1.1. Illustration of the molecular orbital diagram for a d^6 octahedral metal complex with π-back-bonding ligands. Shaded blocks are filled orbitals and unshaded blocks are empty ones. IL = internal ligand transitions, MLCT = metal to ligand charge transfer transitions, LF = ligand field transitions..... 3

Figure 1.2. Frank-Condon principle energy diagram to illustrate the electronic and vibrational states, showing the spin and symmetry allowed $^1GS \rightarrow {}^1ES$ transition from v_0 to v_2', and relaxation v_0' to v_2. 5

Figure 1.3. Jablonski diagram illustrating relative energies of states and the processes of moving among the excited states. →: radiative process, ⇝: non-radiative process, k_f: rate of fluorescence, k_{ic}: rate of internal conversion, k_{isc}: rate of intersystem crossing, k_p: rate of phosphorescence, and k_{nr}: rate of nonradiative pathways, ES = excited states, GS = ground state, IL = internal ligand, MLCT = metal to ligand charge transfer excited states, Δ = thermal population. 7

Figure 1.4. A typical cyclic voltammetry (CV)..... 8

Figure 1.5. The structure of the Creutz-Taube complex 10

Figure 1.6. Representation of Robin-Day's model to classify the mixed-valent binuclear complexes as class I (no coupling), class II (weak coupling) and class III (strong coupling). 11

Figure 1.7. (A) Electronic absorption and emission spectra of tris(2,2'-bipyridine)ruthenium (II), $[Ru(bpy)_3]^{2+}$, in CH_3CN at RT. (B) Jablonski diagram for $[Ru(bpy)_3]^{2+}$. (bpy = 2,2′-bipyridine, ^1GS = singlet electronic ground state, ^1IL = singlet internal ligand excited state, ^3LF = triplet ligand field excited state, ^1MLCT = singlet metal to ligand charge transfer excited state, ^3MLCT = triplet metal to ligand charge transfer excited state) 12

Figure 1.8. Representations of the commonly used polyazine ligands (bpy = 2,2'-bipyridine, dpp = 2,3 bis-(2-pyridyl)pyrazine, dpq = 2,3 bis-(2-pyridyl)quinoxaline, and dpb = 2,3 bis-(2-pyridyl)benzoquinoxaline, Ph_2phen = 4,7-diphenyl1,10-phenanthroline, Me_2phen = 4,7-

dimethyl1,10-phenanthroline, tpy = 2,2':6',2"-terpyridine, tppz = 2,3,5,6-tetrakis(2-pyridyl)pyrazine)..... 13

Figure 1.9. Comparison of the Jablonski diagrams of $[Ru(bpy)_3]^{2+}$ (A) and $[Ru(tpy)_2]^{2+}$ (B), indicative of more accessible, thermally populated ^{3}LF of $[Ru(tpy)_2]^{2+}$ vs. $[Ru(bpy)_3]^{2+}$. The ligand field excited state ^{3}LF will undergo the nonradiative (nr) decay, resulting in shorter lived excited states of ^{3}MLCT in $[Ru(tpy)_2]^{2+}$. (bpy = 2,2'-bipyridine, tpy = 2,2′:6′,2″-terpyridine, ^{1}GS = singlet electronic ground state, ^{1}IL = singlet internal ligand excited state, ^{3}LF = triplet ligand field excited state, ^{1}MLCT = singlet metal to ligand charge transfer excited state, ^{3}MLCT = triplet metal to ligand charge transfer excited state). 15

Figure 1.10. Comparison of the state diagrams of $[Ru(tpy)_2]^{2+}$ (λ_{max}^{em} = 620 nm, τ = 0.25 ns), $[(tpy)Ru(tppz)]^{2+}$ (λ_{max}^{em} = 665 nm, τ = 30 ns) and $[(tpy)Ru(tppz)Ru(tppz)](PF_6)_4$ (λ_{max}^{em} = 830 nm, τ = 100 ns), indicative of the stabilization of the ^{3}MLCT state based on the values of λ_{max}^{em}. (The relative energy of ^{1}GS is estimated based on the oxidation potentials of $Ru^{II/III}$ corresponding to the HOMO of these molecules, the ΔE between ^{1}GS and ^{1}MLCT is based on the λ_{max}^{abs} values of these complexes, tpy = 2,2′:6′,2″-terpyridine, tppz = 2,3,5,6-tetrakis(2-pyridyl)pyrazine, ^{1}GS = singlet electronic ground state, ^{3}LF = triplet ligand field excited state, ^{1}MLCT = singlet metal to ligand charge transfer excited state, ^{3}MLCT = triplet metal to ligand charge transfer excited state) 17

Figure 1.11. Hypothetical one dimensional molecular wire by incorporating metal ions and bis(tridentate) tppz BL ligands..... 20

Figure 1.12. Representative structures of the Pt^{II} terpyridyl complexes, Form A: $[(tpy)PtL]^{n+}$ (L = monodentate ligand) , Form B: $[(tpy)Pt(BL)Pt(tpy)]^{n+}$, Form C: $[LPt(tpy)\text{-}(BL)\text{-}(tpy)PtL]^{n+}$ (BL = bridging ligand) 23

Figure 1.13. The scheme of mixed-metal supramolecules bridged by bidentate BL dpp (dpq = 2,3 bis-(2-pyridyl)quinoxaline) with the Form A: $[(bpy)_2M(\mu\text{-}BL)PtCl_2]^{2+}$, Form B: $[\{(bpy)_2M(\mu\text{-}BL)\}_2Ru(\mu\text{-}BL)PtCl_2]^{6+}$, and Form C: $[(R\text{-}tpy)MCl(\mu\text{-}BL)PtCl_2]^{+}$, where M = Ru or Os. 26

Figure 1.14. Illustration of the interversion of an achiral molecule (an amine bonded with three different groups) *via* an achiral intermediate transformation..... 31

Figure 1.15. Illustration of the symmetry breaking by introducing bulky groups to limit the interconversion in the achiral molecule of biphenyl, the chiral molecule of naphthalene and 1,1'-bi-2-naphthol (BINOL). 31
Figure 1.16. The scheme to denote the dynamics of chemical shifts. 33
Figure 1.17. ^{1}H-NMR of free ligand terpyridine (top), and $[tpyPtCl]^{+}$ (bottom) in d^{6}-DMSO. The arrows show the chemical shift due to the electron withdrawing effect upon coordination. 34
Figure 1.18. 500 MHz ^{1}H-NMR spectra of $(bpy)_2RuCl_2$, free ligand bpy, and $[Ru(bpy)_3]^{2+}$ and CD_3CN. Our data are comparable to literature reported values. 36
Figure 1.19. The crystal structure of $[Ru(bpy)_3]^{2+}$ (right)and $(bpy)_2RuCl_2$ (left) displaying the H^{6} protons are subject to the ring-current effect and electron withdrawing effect, respectively. Our assignments are compared comparable to the literature reported values.[161] 37
Figure 1.20. The fluxional mode to interpret the NMR spectrum of a tridentate Pt^{II} complex ... 38
Figure 1.21. The illustration of the two conformations observed in the crystal structures of free tppz ligand (A, B) and binuclear ruthenium complex, $[(L)ClRu(\mu\text{-}tppz)RuCl(L)]^{2+}$, (L = arylazopyridine), exhibiting saddle-like geometry (C), and chair-like geometry (D), L and Cl are omitted for clarity. 39
Figure 1.22. Scheme of the multiple binding modes for tppz as the bidentate and tridentate ligand 41
Figure 1.23. Example of the multiple binding modes for tppz as the bidentate and tridentate ligand in the complexes of $[(phen)_2Ru(tppz)]^{2+}$, $[(tppz)Pt_2(PEt_3)_2Cl_2]^{2+}$ $[(tppz)Re(CO)_9Cl_3]$ and $[ClPt(tppz)PtCl]^{2+}$ 42
Figure 1.24. The skew-line chirality descriptors with Δ/Λ for the mononuclear complex, and P/M for the charility arising from the molecular components in a polynuclear complex 44
Figure 1.25. Illustration of the P and M geometries of the screw chiarlity in square planar coordinated tppz 44
Figure 1.26. Watson–Crick base pairs of the DNA and their electroactive sites (A), and the helix of the double stranded DNA (B) 45
Figure 1.27. Representation of the intercalation of tridentate Pt complex, $[(tpy)PtCl]^{+}$ into DNA bases. 48
Figure 2.28. Correction files for the Hamamatsu 1527 red sensitive photomultiplier tube. 60

Figure 3.29. Synthetic scheme of preparing the [(tpy)Ru(tppz)PtCl]$(PF_6)_3$. (tpy = 2,2′:6′,2″-terpyridine, tppz = 2,3,5,6-tetrakis(2-pyridyl)pyrazine). 63

Figure 3.30. Synthetic scheme of preparing the [ClPt(tppz)Ru(tppz)PtCl]$(PF_6)_4$. (tpy = 2,2′:6′,2″-terpyridine, tppz = 2,3,5,6-tetrakis(2-pyridyl)pyrazine)..... 64

Figure 3.31. ESI-MS of [(tpy)Ru(tppz)PtCl]$(PF_6)_3$, showing the dimer (2M), trimer (3M) and tetramer (4M) observed from CH_3CN solution, M represent the monomer of the neutral complex of [(tpy)Ru(tppz)PtCl]$(PF_6)_3$ with the molecular weight (MW) as 1388. MW of PF_6^- is 145..... 67

Figure 3.32. (A) ESI mass spectrum of [(tpy)Ru(tppz)PtCl]$(PF_6)_3$ showing the isotopic distribution pattern of the trimer, $[C_{117}H_{81}Cl_3N_{27}Pt_3Ru_3P_7F_{42}]^{2+}$, (B) Calculated isotopic distribution of the dimer from ChemBio Draw Ultra 11.0 68

Figure 3.33. The numbering scheme used for labeling protons in [(tpy)Ru(tppz)]$(PF_6)_2$, [Ru(tppz)$_2$]$(PF_6)_2$, [(tpy)Ru(tppz)PtCl]$(PF_6)_3$, and [ClPt(tppz)Ru(tppz)PtCl]$(PF_6)_4$ (tpy = 2,2′:6′,2″-terpyridine, tppz = 2,3,5,6-tetrakis(2-pyridyl)pyrazine). 72

Figure 3.34. 500 MHz ^{1}H-NMR spectra of tpy (I), tppz (II), [Ru(tpy)$_2$]$(PF_6)_2$ (III), [(tpy)Ru(tppz)]$(PF_6)_2$ (IV), [Ru(tppz)$_2$]$(PF_6)_2$ (V), [(tpy)Ru(tppz)PtCl]$(PF_6)_3$ (VI) and [ClPt(tppz)Ru(tppz)PtCl]$(PF_6)_4$ (VII) in CD_3CN at 298 K..... 73

Figure 3.35. The structures of [Ru(tpy)$_2$]$(PF_6)_2$ and [Ru(tppz)$_2$]$(PF_6)_2$. The blue arrow pointed H^6B in [Ru(tpy)$_2$]$(PF_6)_2$ displays upfield shift relative to the free ligand of tpy, while the blue arrow pointed H^6C in [Ru(tppz)$_2$]$(PF_6)_2$ exhibits downfield shift compared to the free ligand of tppz. 77

Figure 3.36. 500 MHz ^{1}H-NMR spectra of tpy, tppz, [Ru(tpy)$_2$]$(PF_6)_2$ and [Ru(tppz)$_2$]$(PF_6)_2$, in CD_3CN at 298 K in CD_3CN, (tpy = 2,2′:6′,2″−terpyridine, tppz = 2,3,5,6-tetrakis(2-pyridyl)pyrazine)..... 78

Figure 3.37. 500 MHz ^{1}H-NMR spectra of [Ru(tpy)$_2$]$(PF_6)_2$, [(tpy)Ru(tppz)]$(PF_6)_2$ and [Ru(tppz)$_2$]$(PF_6)_2$, in CD_3CN at 298 K in CD_3CN, (tpy = 2,2′:6′,2″−terpyridine, tppz = 2,3,5,6-tetrakis(2-pyridyl)pyrazine)..... 83

Figure 3.38. 500 MHz ^{1}H NMR spectrum of [(tpy)Ru(tppz)]$(PF_6)_2$ and [Ru(tppz)$_2$]$(PF_6)_4$ (tpy = 2,2′:6′,2″-terpyridine, tppz = 2,3,5,6-tetrakis(2-pyridyl)pyrazine) in CD_3CN at 298 K 84

Figure 3.39. 400 MHz ^{1}H-^{1}H NOESY of [(tpy)Ru(tppz)](PF$_6$)$_2$ (A), [(tpy)Ru(tppz)PtCl](PF$_6$)$_3$ (B),, and [ClPt(tppz)Ru(tppz)PtCl](PF$_6$)$_4$ (C)..... 85

Figure 3.40. 500 MHz ^{1}H-NMR spectra of [(tpy)Ru(tppz)](PF$_6$)$_2$, [(tpy)Ru(tppz)PtCl](PF$_6$)$_3$ [ClPt(tppz)Ru(tppz)PtCl](PF$_6$)$_4$ and [Ru(tppz)$_2$](PF$_6$)$_2$in CD$_3$CN at 298 K in CD$_3$CN, (tpy = 2,2′:6′,2″−terpyridine, tppz = 2,3,5,6-tetrakis(2-pyridyl)pyrazine)..... 87

Figure 3.41. 600 MHz ^{195}Pt-NMR spectra of [(tpy)Ru(tppz)PtCl](PF$_6$)$_3$ (A), [ClPt(tppz)Ru(tppz)PtCl](PF$_6$)$_4$ (B) in CD$_3$CN and reference compound, K$_2$PtCl$_4$ in D$_2$O (C). 89

Figure 3.42. 600 MHz ^{195}Pt-^{1}H HMQC spectrum of [(tpy)Ru(tppz)PtCl](PF$_6$)$_3$ in CD$_3$CN 90

Figure 3.43. Selected region of the 400 MHz ^{1}H NMR spectrum of [ClPt(tppz)Ru(tppz)PtCl](PF$_6$)$_4$ in CD$_3$CN at -20, RT and 60 ºC showing slow exchange (A), coalescent (B) and rapid exchange (C) regimes. 92

Figure 3.44. The 50% thermal ellipsoid representations of the cations [(tpy)Ru(tppz)PtCl]$^{3+}$ (top) and [ClPt(tppz)Ru(tppz)PtCl]$^{4+}$ (bottom) (tpy = 2,2':6',2''-terpyridine, tppz = 2,3,5,6-tetrakis(2-pyridyl)pyrazine), the counterions, solvents and hydrogens are omitted for clarity. 95

Figure 3.45. Illustration of the pairwise assembly of [(tpy)Ru(tppz)PtCl]$^{3+}$ motif comprises racemic dimer (M···P). The intermolecular interaction via Pt···Pt and C-H···Cl to form two paired dimers via face-to-face and edge-to-face π···π stacking. 100

Figure 3.46. Representation of the crystal structure of [ClPt(tppz)Ru(tppz)PtCl]$^{4+}$. Racemic conformations of the trimetallic complex, M-M (A) and P-P (B) form the racemic dimer (C) via C-H···π interactions (D), and the extension of the 1D chain via C-H···Cl interactions (E). 101

Figure 3.47. SEM images showing the self-assembly of the trimetallic complex, [ClPt(tppz)Ru(tppz)PtCl][PF$_6$]$_4$, from 1D fiber to 3D flower-like arrays. 104

Figure 3.48. Representation of the energy profile of the M-M, M-P and P-P stereoisomers of the trimetallic complex, [ClPt(tppz)Ru(tppz)PtCl](PF$_6$)$_4$..... 106

Figure 4.49. Cyclic voltammetry of the monometallic complexes, [(tpy)Ru(tppz)](PF$_6$)$_2$ (A) and [Ru(tppz)$_2$](PF$_6$)$_2$, (B) in CH$_3$CN with 0.1 M Bu$_4$NPF$_6$, scan rate = 100 mV/s. Potentials

reported vs. Ag/AgCl (0.21 V vs. NHE), tpy = 2,2':6',2"-terpyridine, tppz = 2,3,5,6-tetrakis(2-pyridyl)pyrazine 110
Figure 4.50. Cyclic voltammetry (A and B, scan rate = 100 mV/s) and square wave voltammetry (C and D, Step potential E = 4 mV, S.W. Amplitude = 25 mV, Frequency = 15 Hz) of bimetallic complex, $[(tpy)Ru(tppz)PtCl](PF_6)_3$ (A, C), and trimetallic complex, $[ClPt(tppz)Ru(tppz)PtCl](PF_6)_4$ (B, D) in CH_3CN with 0.1 M Bu_4NPF_6, Potentials reported vs. Ag/AgCl (0.21 V vs. NHE), tpy = 2,2':6',2"-terpyridine, tppz = 2,3,5,6-tetrakis(2-pyridyl)pyrazine 111
Figure 4.51. Electronic absorption and emission spectra for the mixed-metal supramolecular complexes and monometallic synthons (A) $[(tpy)Ru(tppz)](PF_6)_2$ (-----)and $[(tpy)Ru(tppz)PtCl](PF_6)_3$ (—) and (B) $[Ru(tppz)_2](PF_6)_2$ (-----) and $[ClPt(tppz)Ru(tppz)PtCl](PF_6)_4$ (—) measured in CH_3CN at RT (tpy = 2,2′,6′,2″-terpyridine and tppz = 2,3,5,6-tetrakis(2-pyridyl)pyrazine). 117
Figure 4.52. The concentration dependent emission spectra of $[(tpy)Ru(tppz)PtCl](PF_6)_3$ 121
Figure 4.53. Confocal laser scanning microscopies of bimetallic powder of $[(tpy)Ru(tppz)PtCl](PF_6)_3$ (A), trimetallic powder of $[ClPt(tppz)Ru(tppz)PtCl](PF_6)_4$ (B). The samples were excited with the 543 nm laser line (helium-neon) and emission detected by using a long pass filter (>633 nm). 122
Figure 5.54. Binding study of cisplatin (A), $[(tpy)Ru(tppz)PtCl](PF_6)_3$ (B), and $[ClPt(tppz)Ru(tppz)PtCl](PF_6)_4$ (C) using circular plasmid pUC18 DNA with different BP:MC ratios at RT. Lanes 1, 2, 3, 5, 10, 20, 30 and 50 are the metal complex-DNA with the BP:MC ratios as 1:1, 2:1, 3:1, 5:1, 10:1, 20:1, 30:1, and 50:1 respectively. tpy = 2,2′:6′,2″-terpyridine and tppz = 2,3,5,6-tetrakis(2-pyridyl)pyrazine). 125
Figure 5.55. The impact of temperature on DNA binding to pUC18 DNA by metal complexes (A), cisplatin with 5:1 BP:MC (B), $[(tpy)Ru(tppz)PtCl](PF_6)_3$ with 5:1 BP:MC (C), and $[ClPt(tppz)Ru(tppz)PtCl](PF_6)_4$ with 10:1 BP:MC (D) at 4ºC, 25ºC, 37ºC and 50ºC. (tpy = 2,2′:6′,2″-terpyridine and tppz = 2,3,5,6-tetrakis(2-pyridyl)pyrazine). 126
Figure 5.56. Emission titration data for of 1.3×10^{-5} M $[ClPt(tppz)Ru(tppz)PtCl]Cl_4$ in 10 mM phosphate buffer (pH = 7) upon addition of guanosine 5'-monophosphoric acid disodium salt (Na_2GMP) with the 5, 10, 20 and 40 Na_2GMP:MC ratios. The solution was

deoxygenated by bubbling with Ar for 15 minutes before conducting the emission measurements..... 130
Figure 5.57. The morphology of the condensed pUC18 DNA with the trimetallic complex at a 20:1 BP:MC ratio irradiated at 455 nm for 1 hr using a 5 W LED light source..... 131
Figure 5.58. Electronic absorption spectra of [ClPt(tppz)Ru(tppz)PtCl]Cl_4 in the absence (—) and presence of pUC18 (—) and following photolysis (—) in 10 mM phosphate buffer (pH = 7). Sample was photolyzed with 455 nm light from a 5W LED for one hour..... 133
Figure 5.59. Agarose gel electrophoresis studies on the MC-DNA interactions of the complex [ClPt(tppz)Ru(tppz)PtCl]Cl_4 with BP:MC = 20. Lane λ is the Lambda DNA hindIII digest molecular weight marker with bands at 23.1, 9.4, 6.6, 4.4, 2.3 and 2.0 k base pairs, Lane C is pUC18 DNA control without added metal complex, Lane 1 is the metal complex with pUC18 DNA at a 20:1 BP:MC ratio without photolysis, and Lane 2 is the metal complex with pUC18 DNA at a 20:1 BP:MC ratio after 1 hr photolysis at 455 nm using a 5 W LED light source. SC = supercoiled pUC18 DNA, OC = open circular pUC18 DNA..... 133
Figure 6.60. Proposed modifications on the bimetallic complex of [(tpy)Ru(tppz)PtCl]$(PF_6)_3$ 142
Figure 6.61. Proposed molecular wires..... 143

List of Tables

Table 1.1. Spectroscopic, photophysical and redox properties of 2,3,5,6-tetrakis(2-pyridyl)pyrazine (tppz) complexes of Ru^{II}, Os^{II}, Ir^{III} and Rh^{III}. (bpy = 2,2'-bipyridine, tpy = 2,2′:6′,2″-terpyridine, BL = bridging ligand, TL = terminal ligand)..... 19

Table 1.2. Redox and spectroscopic properties of homogeneous Ru^{II} polyazine complexes and Ru^{II},Pt^{II} mixed-metal supramolecules by using bidentate BL, BL = bridging ligand, TL = terminal ligand. 27

Table 1.3. 65 chiral space groups in crystals, where space groups of the enantiomorphous pairs are highlighted in the brackets 29

Table 1.4. 500 MHz ^{1}H-NMR chemical shifts (δ) and coupling constants (^3J) of bidentate free ligand bpy, $(bpy)_2RuCl_2$ and $[Ru(bpy)_3](PF_6)_2$, which are comparable to the literature reported values. 37

Table 3.5. FAB-MS data for $[(tpy)Ru(tppz)](PF_6)_2$, $[Ru(tppz)_2](PF_6)_2$, $[(tpy)Ru(tppz)PtCl](PF_6)_3$ and $[ClPt(tppz)Ru(tppz)PtCl](PF_6)_4$. Observed fragmentation patterns typically involving sequential loss of counterions and are consistent with the compositions of the complexes (tpy = 2,2′:6′,2″-terpyridine, tppz = 2,3,5,6-tetrakis(2-pyridyl)pyrazine). 66

Table 3.6. 500 MHz ^{1}H-NMR chemical shifts of $[(tpy)Ru(tppz)](PF_6)_2$, $[Ru(tppz)_2](PF_6)_2$, $[(tpy)Ru(tppz)PtCl](PF_6)_3$ and $[ClPt(tppz)Ru(tppz)PtCl](PF_6)_4$ in CD_3CN at 298K (tpy = 2,2′:6′,2″-terpyridine, tppz = 2,3,5,6-tetrakis(2-pyridyl)pyrazine). 74

Table 3.7. Literature reported ^{1}H-NMR chemical shifts of tpy, $[Ru(tpy)_2]^{2+}$, tppz, and $[Ru(tppz)_2](PF_6)_2$ (tpy = 2,2′:6′,2″–terpyridine, tppz = 2,3,5,6-tetrakis(2-pyridyl)pyrazine). 75

Table 3.8. 500 MHz ^{1}H-NMR chemical shifts (δ) and coupling constants (^3J) of tridentate free ligand tpy, tppz and $[Ru(tpy)_2](PF_6)_2$, which are comparable to the literature reported values 76

Table 3.9. Crystallographic data collection and structure refinement parameters for $[(tpy)Ru(tppz)PtCl](PF_6)_3$ and $[ClPt(tppz)Ru(tppz)PtCl](PF_6)_4$ 96

Table 3.10. Selected bond length (Å) and angles (deg) for $[(tpy)Ru(tppz)PtCl](PF_6)_3$. 97

Table 3.11. Selected bond length (Å) and angles (deg) for [ClPt(tppz)Ru(tppz)PtCl]$(PF_6)_4$..... 98

Table 4.12. Electrochemical data for Ru^{II} and Pt^{II} of the tridentate complexes. Potentials reported vs. Ag/AgCl (0.21 V vs. NHE) in CH_3CN with 0.1 M Bu_4NPF_6 (tpy = 2,2':6',2''-terpyridine, tppz = 2,3,5,6-tetrakis(2-pyridyl)pyrazine)..... 109

Table 4.13. Summary of the spectroscopic data of [(tpy)Ru(tppz)PtCl]$(PF_6)_3$ and [ClPt(tppz)Ru(tppz)PtCl]$(PF_6)_4$ with their precursors, where tpy = 2,2':6',2''-terpyridine, tppz = 2,3,5,6-tetrakis(2-pyridyl)pyrazine.....116

List of Abbreviations

BINOL: 1,1'-bi-2-naphthol

BP: DNA base pair

CT: charge transfer

DI: deionized

DNA: deoxyribonucleic acid

dpp: 2,3-bis(2-pyridyl)pyrazine

dpp: 2,3-bis(2-pyridyl)quinoxaline

dpb: 2,3-bis(2-pyridyl)benzoquinoxaline

ES: excited state

ESI : electrospray Ionization

ET: electron transfer

FAB: fast-atom bombardment

FC: Franck-Condon

GS: ground state

HMQC: heteronuclear multiple quantum coherence

HOMO: highest occupied molecular orbital

ic: internal conversion

LF: ligand field

IL: intraligand

isc: intersystem crossing

IUPAC: international union of pure and applied chemistry

LF: ligand field

LUMO: lowest unoccupied molecular orbital

MC: metal complex

MO: molecular orbital

MS: mass spectrometry

NOE: nuclear overhauser effect

NOESY: nuclear overhauser effect spectroscopy

NMR: nuclear magnetic resonance

nr: nonradiative decay

phen: 1,10-phenanthroline

qpy: quinquepridine

SEM: scanning electronic microscopy

SWV: square wave voltammetry

r: radiative decay

RT: room temperature

tpy: 2,2':6',2''-terpyridine

tppz: 2,3,5,6-tetrakis(2-pyridyl)pyrazine

Thesis Statement

The objective of this research was to explore the properties of Ru^{II},Pt^{II} supramolecular complexes bridged by tridentate polyazine ligands and to understand their stereochemistry, photochemistry, electrochemistry and biochemistry.

Chapter 1. Introduction

1.1 Summary

The study of polymetallic ruthenium complexes has attracted much attention due to their rich excited-state photochemical and photophysical properties. Complicated multicomponent systems incorporating light absorber (LA) units, electron relays (ERs), and reactive metals (RMs) within the molecular architecture are desirable for efficient light activated processes. Within this perspective, polyazine bridging ligands (BLs) have been used to chemically bond the individual components into the same molecular framework, allowing the construction of complex polymetallic supramolecular species.[1] One of the most extensively studied polymetallic ruthenium complexes are the class of bidentate-bridged systems. In each bidentate monometallic complex, there are typically two steroisomers (Δ/Λ). Typical bidentate ligands are AB chelates which provide additional stereoisomers. Consequently, the tris-chelated coordination mode of bidentate system yields a number of steroisomers that are typically not separated. This is stereochemically unfavorable for the design of polymetallic supramolecules as they lack control of sub-unit orientation and distance.

The use of tridentate ligands in the construction of polymetallic systems provides efficient control of sub-unit distance and orientation. The application of tridentate complexes has been somewhat limited by the short metal-to-ligand charge-transfer (^{3}MLCT) excited state lifetime in the prototype of tridentate complex, $[Ru(tpy)_2]^{2+}$ (τ = 0.25 ns, $\Phi^{em} = 5.6\times10^{-6}$ in CH_3CN, tpy = 2,2':6',2''-terpyridine).[2-3]

The design of tridentate complexes of Ru^{II} with longer lived ^{3}MLCT excited states than $[Ru(tpy)_2]^{2+}$ is an area of challenge. Mixed-metal complexes containing the tridentate bridging ligand tppz (2,3,5,6-tetrakis(2-pyridyl)pyrazine) often have long lived emissive ^{3}MLCT excited states are not well studied despite the promise such complexes hold in many forums.[15] The coupling of Ru^{II} to Pt^{II} within the tridentate bridged architectures such as that provided by tppz has not been reported yet.

The preparation of structurally diverse supramolecular complexes and investigation of their stereochemistry, electrochemistry and photochemistry are important for the ever-expanding potential applications in fields such as solar energy conversion and antitumor bioactivity. The macroscopic properties, such as color, luminescence and redox chemistry, have their roots at the molecular levels, which in turn have an influence on the structures.

This chapter begins with a general introduction to molecular orbital (MO) theory to describe the metal-ligand binding at the molecular level, followed by the description of the fundamentals of photochemistry, electrochemistry and stereochemistry, as well as NMR techniques. The Ru^{II},Pt^{II} supramolecular assemblies are reviewed with an emphasis on the modulation of their luminescent properties and potential application as DNA binding agents.

1.2 Molecular Orbital (MO) Theory

In free metal ions, the d orbitals have identical energy despite their different spatial orientations. Upon complexation with ligands, the d orbitals split. The magnitude of splitting energy (Δ) depends on the relative energy of the ligand and metal orbitals, the degree of their interaction and the ligands spatial orientation. When the ligand field is progressively strengthened, the change from a high spin to low spin ground states occurs for metal complexes. As a general rule, metal ligand bond lengths of high spin complexes are substantially longer than those of low spin complex with the same metal center. Depicted in **Figure 1.1** is the MO diagram for an octahedral metal complex (ML_6) with π back-bonding ligands.[4] This molecular orbital diagram uses a localized approach to labeling molecular orbitals, labeling MOs as transition metal (M) or ligands (L) based indicative of the major contribution to each molecular orbital. The common electronic transitions associated with metal complexes in an octahedral geometry are illustrated. Electronic transitions in these octahedral metal complexes can be classified into three types:

Metal-localized d-d transitions are termed ligand field (LF). LF transitions are symmetry forbidden transitions with low intensity.

Ligand-localized ππ* transitions are termed internal ligand (IL). IL transitions due to the π→π* transitions in the ligand are generally both spin and symmetry allowed, with high extinction coefficients on the order of 10^5-10^6 $M^{-1}cm^{-1}$.

Metal to ligand or ligand to metal transitions are termed charge transfer (CT). There are two kinds of CT transitions, ligand to metal charge transfer, LMCT, and metal-to-ligand charge transfer, MLCT. These transitions are typically symmetry and spin allowed with the extinction coefficients on the scale of 10^4 $M^{-1}cm^{-1}$. Transitions assigned as ^{3}LMCT or ^{3}MLCT are spin-forbidden transitions which gain intensively by the spin-orbit coupling.

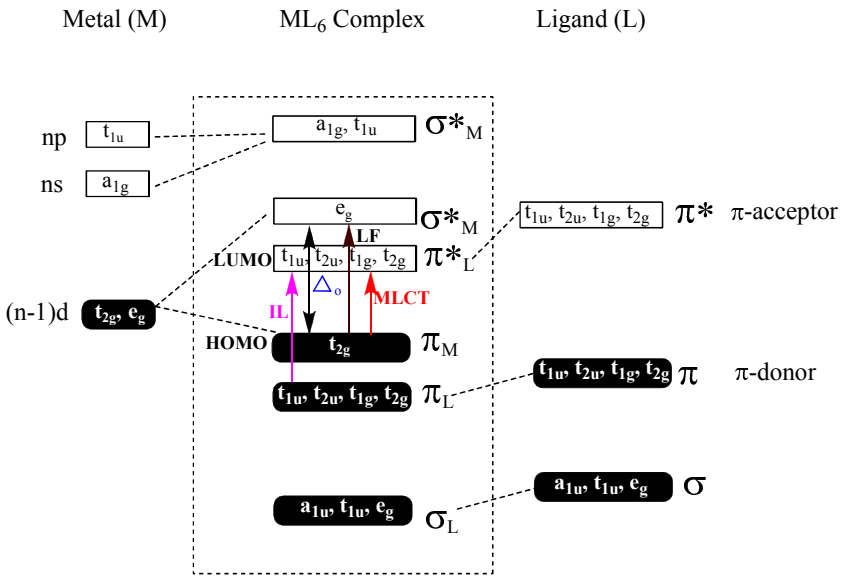

Figure 1.1. Illustration of the molecular orbital diagram for a d^6 octahedral metal complex with π-back-bonding ligands. Shaded blocks are filled orbitals and unshaded blocks are empty ones. IL = internal ligand transitions, MLCT = metal to ligand charge transfer transitions, LF = ligand field transitions.

1.3 Photochemistry

Electronic excited states and the electronic absorption spectroscopy describing their populations are the key to studying photochemistry. The probability and therefore intensity of the electronic transitions are governed by selection rules.

1.3.1 Selection Rules

Molecular orbitals involved in electronic transition must be coupled to allow electronic transitions. The intensity of an electronic transition is governed by the symmetry and spin selection rules. Selection rules determine which transitions are spectroscopically active.

The symmetry selection rule for an electronic transition is given by equation:[5]

$$f \propto \left| \int \psi_{GS} M \psi_{ES} \right|^2 = D$$

where f is the oscillator strength, which is proportional to the transition integrated intensity. Ψ_{GS} and Ψ_{ES} are the electronic wave functions of ground states (GS) and excited states (ES), and M is the electronic dipole moment operator. The symmetry allowed electronic transition can be observed when D is not equal to zero. Laporte selection rule is often applied to the electronic spectroscopy of transition metal complexes with inversion centers, in which the allowed transitions involve a change in parity. In a transition metal complex, fox example, the transition of $\pi \rightarrow \pi^*$ or $d \rightarrow \pi^*$ are often allowed.

Spin allowed transitions must involve the promotion of electrons without a change in their spin, i.e. $\Delta S = 0$ (S = total spin). For example, ^{1}GS to ^{3}MLCT transitions are spin-forbidden, while ^{1}GS to ^{1}MLCT or ^{1}IL transitions are spin allowed.

Relaxation of the selection rules can happen by means of spin-orbital coupling, vibronic coupling or Jahn-Teller effects. The intensity of a forbidden transition is much smaller than that of a fully allowed transition.

Vibrational levels are associated with each ground and excited electronic state. Electronic transitions are often accompanied by vibronic excitation. The transition between potential energy

surfaces of the GS and ES is depicted as in **Figure 1.2**, ΔE_{00} is the energy difference of the lowest vibrational level of the electronic GS and ES. According to the Franck-Condon principle, electronic transitions are vertical transitions without change in nuclear positions. This typically provides for electronic excitations to include substantial vibronic excitation due to the difference in the equilibrium intermolecular distance in the ground and excited electronic states. The Franck-Condon principle is applicable to both the absorption and emission processes. A molecule populates the excited states by absorbing a photon. The excited molecule is unstable and has to return to the ground state so that energy is emitted. Due to the vibronic relaxation (thermal), the emitted photon usually has less energy than the absorbed photon, the energy difference between the absorption and emission is termed a Stokes shift.

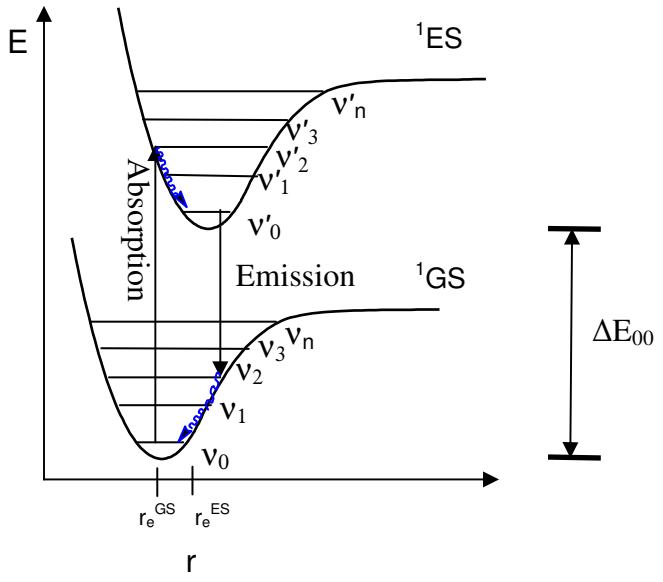

Figure 1.2. Frank-Condon principle energy diagram to illustrate the electronic and vibrational states, showing the spin and symmetry allowed $^1GS \rightarrow {}^1ES$ transition from v_0 to v_2', and relaxation v_0' to v_2.

1.3.2 Electronic Excited State Decay

Conversion between electronic states is generally illustrated by Jablonski (state) diagrams, **Figure 1.3**. Multiple pathways for the decay processes of electronically excited states involve the nonradiative processes (nr, wavy arrow) of internal conversion (ic) or intersystem crossing (isc) and radiative processes (r, straight arrow). Luminescence represents the radiative process that results in the emission of light when the electronically excited molecules relax to the GS. Fluorescence is a radiative process where spin multiplicities of the initial and final states are identical, while phosphorescence is used to describe an emission with change in spin state.

The quantum yield, Φ^{em}, and lifetime, τ, are two important parameters to describe the luminescent properties of the chromophores. The lifetime of an excited state is the reciprocal of the sum of the rate constants for deactivation of an excited state.

$$\tau = 1/(k_r + k_{nr})$$

The quantum yield of emission is the ratio of the emitted photons to the absorbed photons. For a directly populated state, the quantum yield of emission (Φ^{em}) corresponds to the ratio of the radiative rate constant over the sum of the rates that deactivate the emitting state. For an indirectly populated state, the Φ^{em} includes a term for the quantum yield for population of the emitting state. For most Ru^{II} polyazine complexes, the population of the ^{3}MLCT emitting state is unity and this term is typically omitted. Thus, the quantum yield can be written as:

$$\Phi^{em} = k_r/(k_r + k_{nr})$$

Two mechanisms of excited state energy transfer have been developed by Förster and Dexter. Förster's resonace energy transfer theory is based on dipole-dipole coupling between donor and acceptor. The rate of energy transfer is inversely proportional to intermolecular separation, and directly proportional to the density overlap between the interacting initial and final states. According to Förster's theory, the most intense energy transfer can be observed in a single noncentrosymmetric molecule if the two chromophores are identical. Dexter's energy transfer is

associated with the electron exchange between donor and acceptor molecules. Dexter introduces the spin wave functions of Hamiltonian to the exchange process, which is not considered by Förster. Dexter's electron transfer mechanism is important to triplet-triplet energy transfer.

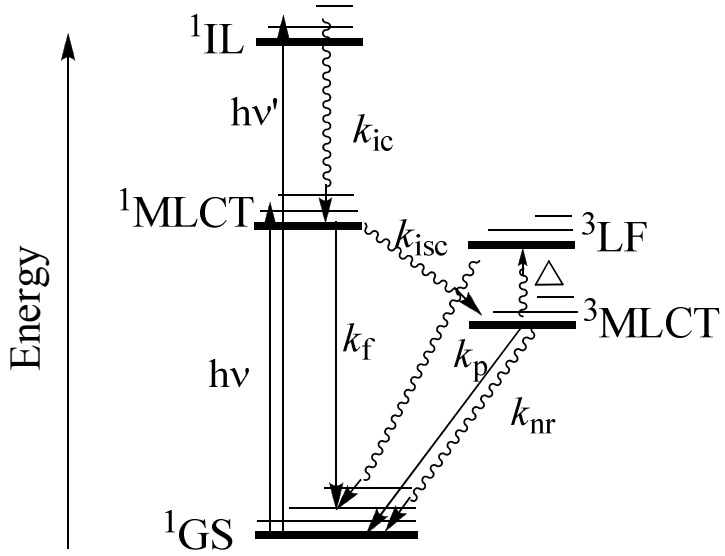

Figure 1.3. Jablonski diagram illustrating relative energies of states and the processes of moving among the excited states. →: radiative process, ⇝ : non-radiative process, k_f: rate of fluorescence, k_{ic}: rate of internal conversion, k_{isc}: rate of intersystem crossing, k_p: rate of phosphorescence, and k_{nr}: rate of nonradiative pathways, ES = excited states, GS = ground state, IL = internal ligand, MLCT = metal to ligand charge transfer excited states, Δ = thermal population.

1.4 Electrochemistry

Electrochemistry studies electron transfer between an electrode and a sample with an applied voltage. The redox potentials can be interpreted based on the relative orbital levels between the ligands and metal ions. Reversible electrochemical reactions typically show $i_p^c / i_p^a = 1$, and $\Delta E_p = E_p^c - E_p^a = 0.0591$ V/n at RT, where n is the number of the electrons involving in the reaction, i_p^c and i_p^a are the cathodic (c) and anodic (a) peak currents, and E_p^c and E_p^a are cathodic and anodic peak potential, respectively.

The thermodynamic redox potential obtained in this process is related to the Gibbs free energy of an electrochemical reaction:[6]

$$\Delta G = -nEF = -RT\ln K$$

Where ΔG is the Gibbs free energy change for the electrochemical reaction, E is the formal reduction potential, and K is the equilibrium constant of the redox reaction. n is the number of electrons in the reaction, F is Faraday constant, R is gas constant.

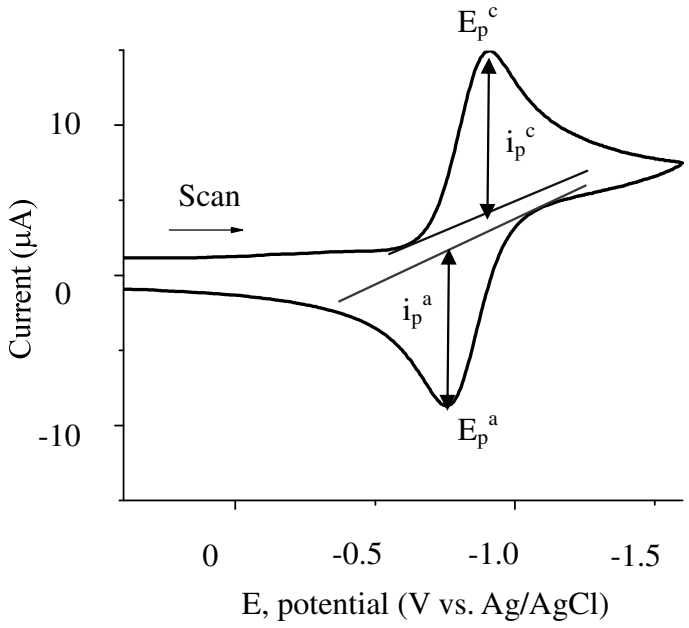

Figure 1.4. A typical cyclic voltammetry (CV)

Cyclic voltammetry (CV) is a commonly employed electroanalytical method. The current is monitored while linearly varying the applied potential at a working electrode in a cycle. The response of the cyclic voltammogram is plotted as the I (current) vs. V (Voltage) graph, **Figure 1.4**. The redox potentials of metal complexes can be tuned by varying the ligands. Polypyridine acting as π-accepting ligands will present a low lying π* orbital and stabilize the dπ orbital centered on the metal.

From the I-V graph as shown in **Figure 1.4**, the peak potential (E_p^c, E_p^a) and peak current (i_p^c, i_p^a) of the cathodic and anodic process can be obtained. These parameters can indicate the electrochemical properties of the sample. If the reaction is reversible (fast electron transfer process and no following chemical reactions), the ratio of $i_p^c/i_p^a = 1$. The peak current for a reversible couple is given by the Randles-Sevcik equation at 25°C:[6]

$$i_p = (2.69 \times 10^5)\, n^{1.5} A C D^{1/2} \nu^{1/2}$$

Where n is the number of electrons, A = the electrode area (in cm^2), C = concentration (in mol/cm^3), D = diffusion coefficient (in cm^2/s), and ν = scan rate (in V/s). Given a reversible electrochemical reaction, the ratio of i_p to the square root of scan rate (υ) is a constant, the plot of i_p vs square root of scan rate is a straight line.

At the half wave potential of a reversible reaction, the concentration of oxidized ([O]) molecules and the concentration of reduced ([R]) molecules are the same, according to the Nernst equation:[7]

$$E_{Red} = E^o_{Red} - \frac{nF}{RT} \ln \frac{[R]}{[O]}$$

F is Faraday constant, R is gas constant. The formal reduction potential E^o_{Red} for a reversible couple can be obtained from CV:

$$E^o_{Red} = E_{1/2} = (E^c_p + E^a_p)/2$$

The separation between the peaks is given by:

$$\Delta E_p = |(E_p^c - E_p^a)| = 2.303\ RT/nF$$

At at 25°C, $\Delta E_p = 59$ mV/n

The ΔE_p can be used to determine the number of electrons transferred in an electrochemical reaction. But care must be exercised in such evaluation as many other factors impact peak to peak splitting such as internal resistance and irreversible redox chemistry.

A reversible electrochemical process at an electrode surface can only be observed when both the oxidized and reduced form of the species are stable and the kinetics of the electron transfer process is controlled by mass transportation on the electrode surface, so that Nernstian equilibrium can be maintained at the small area of the electrode surface.

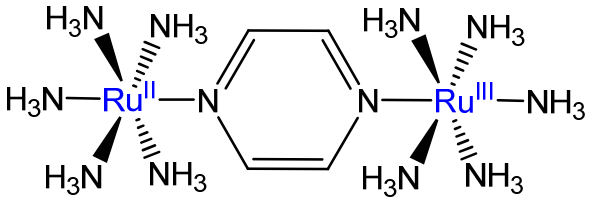

Figure 1.5. The structure of the Creutz-Taube complex

Symmetric bimetallic ruthenium complexes, such as Creutz-Taube ion, $[(NH_3)_5Ru(C_4H_4N_2)Ru(NH_3)_5]^{5+}$ (**Figure 1.5**), are widely studied to probe electronic coupling of the two Ru centers.[8-12] In the Creutz-Taube complex, the two rutheniums connected by a pyrazine BL display added stability of the mixed valenced state. The electronic communication between the two redox active Ru centers is related to the degree of delocalization of the charge via the BL. According to Robin-Day's classification, the degree of electronic coupling is

illustrated by a simple harmonic oscillator cartoon in **Figure 1.6**.[13] The more delocalized the charge, the stronger the electronic coupling. The longer the separation between electroactive ions, typically the weaker the coupling.

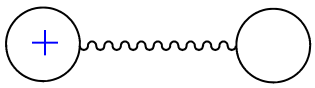

Class I: Localized: no coupling

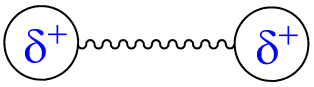

Class II: Slightly delocalized: weak coupling

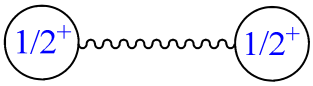

Class III: Completely delocalized: strong coupling

Figure 1.6. Representation of Robin-Day's model to classify the mixed-valent binuclear complexes as class I (no coupling), class II (weak coupling) and class III (strong coupling).

The electrochemistry of the polypyridyl complexes is discussed by using frontier molecular orbital theory. Electrochemically, oxidation is the abstraction of an electron from the highest occupied molecule orbital (HOMO) (dπ orbital centered on the metal). Reduction is the addition of an electron on the lowest unoccupied molecule orbital (LUMO) (π* orbital centered on the ligand). Ru^{II} complexes of polyazine ligands usually display reversible metal based oxidations for the $Ru^{II/III}$ processes and ligand based reductions.

1.4 $[Ru^{II}(NN)_3]^{2+}$ Complexes

The discovery of $[Ru(bpy)_3]^{2+}$ (bpy = 2,2'-bipyridine)[14] and its desirable excited state photochemical and photophysical properties has inspired much research towards exploiting this and related chromophores.[15-16] The electronic absorption and emission spectra of $[Ru(bpy)_3](PF_6)_2$, as well as its electronic state diagram are depicted in **Figure 1.7**. $[Ru(bpy)_3]^{2+}$ displays intense intraligand $\pi \rightarrow \pi^*$ (IL) transitions in the UV region and MLCT transitions in the visible region. The excited ^{1}MLCT state undergoes intersystem crossing (isc) to populate ^{3}MLCT with unit efficiency. $[Ru(bpy)_3]^{2+}$ possesses a lived lowest excited state (^{3}MLCT) with a quantum yield of emission, $\Phi^{em} = 0.1$, with an excited state long lifetime of $\tau = 1.1$ μs.[15] The long lifetime and efficient quantum yield for emission enable $[Ru(bpy)_3]^{2+}$ to undergo photoinduced electron transfer or energy transfer in the excited state that can be probed through emission studies.[17]

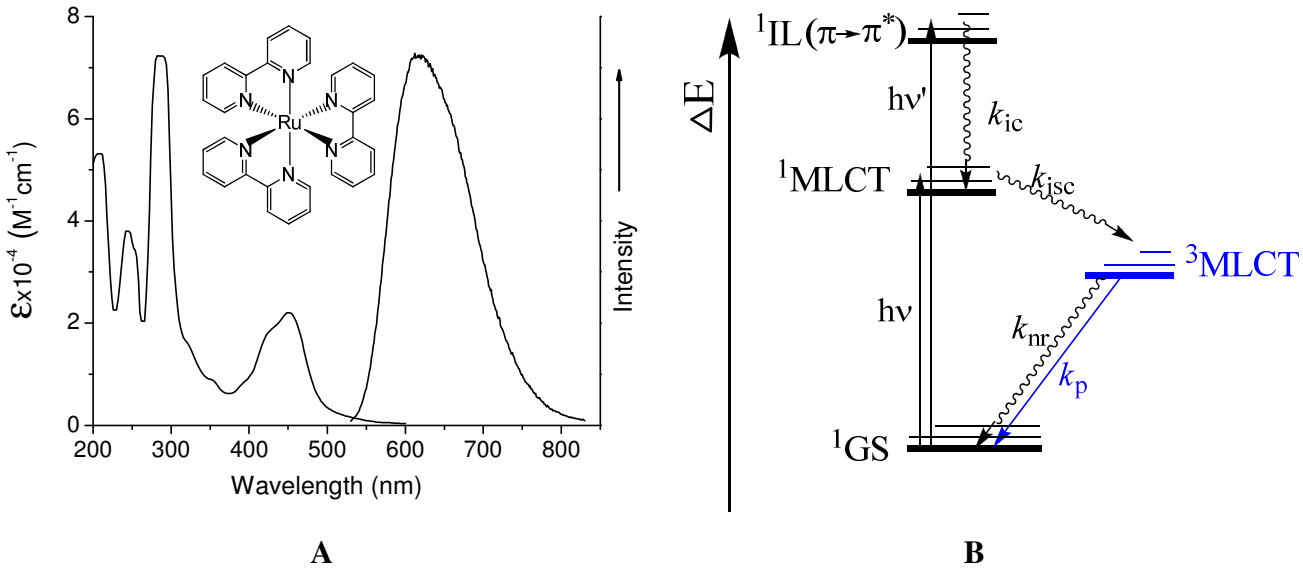

Figure 1.7. (A) Electronic absorption and emission spectra of tris(2,2'-bipyridine)ruthenium (II), $[Ru(bpy)_3]^{2+}$, in CH_3CN at RT. (B) Jablonski diagram for $[Ru(bpy)_3]^{2+}$. (bpy = 2,2′-bipyridine, ^{1}GS = singlet electronic ground state, ^{1}IL = singlet internal ligand excited state, ^{3}LF = triplet ligand field excited state, ^{1}MLCT = singlet metal to ligand charge transfer excited state, ^{3}MLCT = triplet metal to ligand charge transfer excited state)

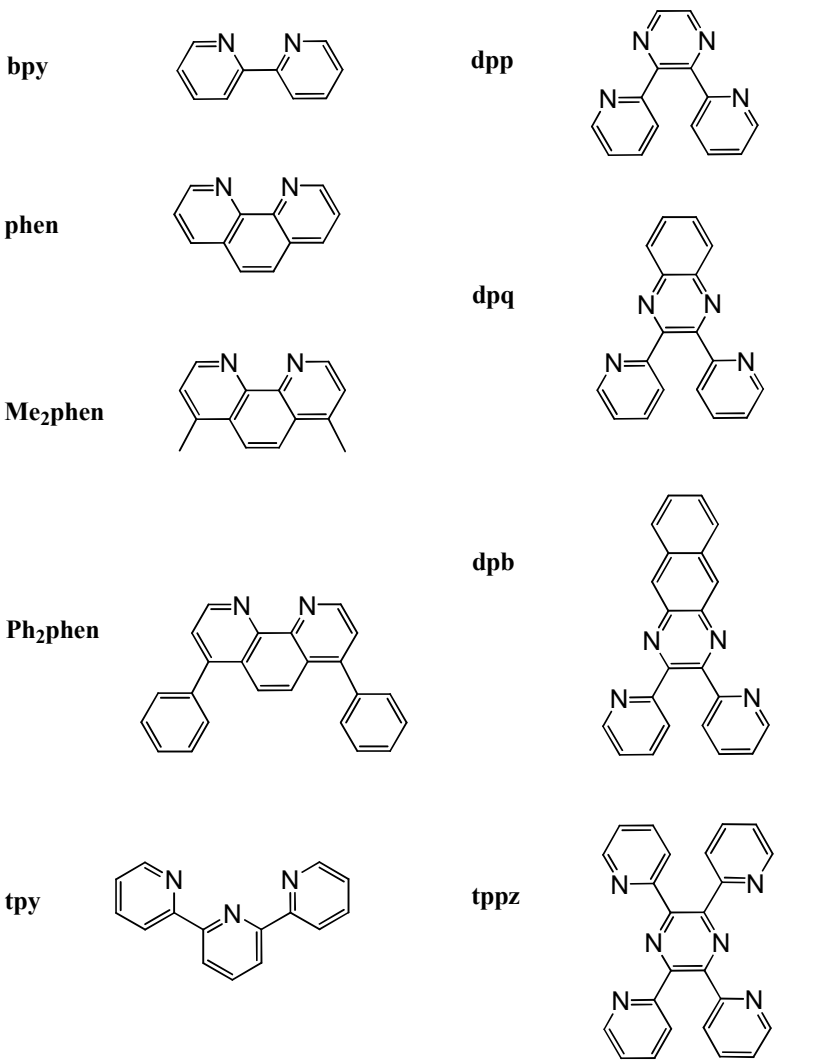

Figure 1.8. Representations of the commonly used polyazine ligands (bpy = 2,2'-bipyridine, dpp = 2,3 bis-(2-pyridyl)pyrazine, dpq = 2,3 bis-(2-pyridyl)quinoxaline, and dpb = 2,3 bis-(2-pyridyl)benzoquinoxaline, Ph_2phen = 4,7-diphenyl1,10-phenanthroline, Me_2phen = 4,7-dimethyl1,10-phenanthroline, tpy = 2,2':6',2''-terpyridine, tppz = 2,3,5,6-tetrakis(2-pyridyl)pyrazine).

Inspired by the luminescent and redox-active properties from $[Ru(bpy)_3]^{2+}$, a large number of polyazine ligands have been developed to construct a variety of polymetallic supramolecular species. **Figure 1.8** lists some of the widely used polypyridyl and polyazine ligands. The photochemical and redox properties of complexes can be tuned by modifications on the ligands.

1.4.1 Limitation of Bidentate Systems

Bidentate polyazine interactions with metal ions give access to a range of supramolecular systems of truly impressive architectures. In each bidentate monometallic complex, there are two stereoisomers (Δ/Λ). In addition, many bidentate BLs are AB chelates. As a result, this mode of coordination affords polymetallic complexes that are stereochemically ill defined. This limits the ability to control sub-unit orientation and distance within a supramolecular assembly. This is undesired for the rational design of assemblies capable of complex functions.[18]

1.4.2 Tuning of Photophysical Properties of Tridentate Ru^{II} Complexes

The use of tridentate ligand, such as 2,2':6',2''-terpyridine (tpy), in the construction of polymetallic systems leads to stereochemically defined systems that have efficient control of sub-unit distance and orientation. The arrangements of bis-tridentate units in $[M(tpy)_2]^{n+}$ in a linear fashion provide for stereochemical control. The applications of tridentate complexes in solar energy conversion schemes hasve been somewhat limited by the short excited state lifetime of $[Ru(tpy)_2]^{2+}$ (τ = 0.25 ns, $\Phi^{em} = 5.6\times10^{-6}$ in CH_3CN).[2-3] This short MLCT excited state lifetime resulting from the non-ideal bite angle of tpy providing low-lying ligand field states that are thermally accessible at room temperature, limits the application of the $[Ru(tpy)_2]^{2+}$.[2-3, 19-20] The low lying ^{3}LF state quenches the emission of the excited ^{3}MLCT of $[Ru(tpy)_2]^{2+}$ is illustrated in **Figure 1.9**. The thermally populated ^{3}LF state undergoes rapid non-radiative decay to the GS, resulting in the substantially shorter lifetime and lower quantum yield of emission of $[Ru(tpy)_2]^{2+}$ ($\Phi^{em} = 5.6\times10^{-6}$, τ = 0.25 ns) as compared to $[Ru(bpy)_3]^{2+}$ (Φ^{em} = 0.1, τ = 1.1 μs).

The design of tridentate complexes of Ru^{II} with longer lived ^{3}MLCT excited states than $[Ru(tpy)_2]^{2+}$ is an ongoing area of research.[21-23] Long excited states lifetime and high quantum yields of emission for tridentate complexes are required to ensure efficient energy and electron transfer processes and provide a probe to excited state dynamics. General strategies to increase

the excited state lifetime have proven somewhat successful either by enhancing the radiation process and/or by diminishing the radiationless decay.[24] A recent review by Hanan highlights a variety of approaches being employed with much focus on tuning the energetics of the ^{3}LF and ^{3}MLCT states by component modifications.[24-25]

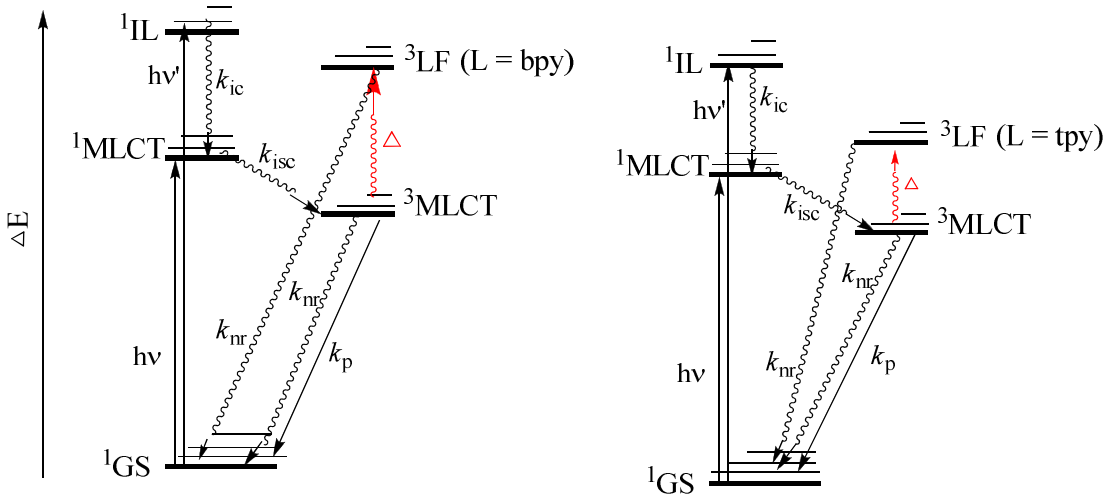

A: $[Ru(bpy)_3]^{2+}$ B: $[Ru(tpy)_2]^{2+}$

Figure 1.9. Comparison of the Jablonski diagrams of $[Ru(bpy)_3]^{2+}$ (A) and $[Ru(tpy)_2]^{2+}$ (B), indicative of more accessible, thermally populated ^{3}LF of $[Ru(tpy)_2]^{2+}$ vs. $[Ru(bpy)_3]^{2+}$. The ligand field excited state ^{3}LF will undergo the nonradiative (nr) decay, resulting in shorter lived excited states of ^{3}MLCT in $[Ru(tpy)_2]^{2+}$. (bpy = 2,2'-bipyridine, tpy = 2,2′:6′,2″-terpyridine, ^{1}GS = singlet electronic ground state, ^{1}IL = singlet internal ligand excited state, ^{3}LF = triplet ligand field excited state, ^{1}MLCT = singlet metal to ligand charge transfer excited state, ^{3}MLCT = triplet metal to ligand charge transfer excited state).

One approach to lengthen the excited state lifetime of $[Ru(tpy)_2]^{2+}$ type chromophores is to use electron donating or electron withdrawing substituts on the tpy ring system.[25] Attachment of electron withdrawing group to the 4′-position of tpy will stabilize the ^{3}MLCT excited states by a

greater stabilization of the ligand-based LUMO as compared to the metal-based HOMO.[24] The replacement of the 4′-H in tpy with electron withdrawing group of methyl-sulphonyl has prolonged the lifetime of the bis(tridentate) ruthenium complexes: $[Ru(MeSO_2\text{-}tpy)_2]$ with an excited sate lifetime of τ = 25 ns and $[(MeSO_2\text{-}tpy)Ru(tpy\text{-}OH)]$ with τ = 50 ns. Incorporating the electron donating group to the 4′-position of tpy will destabilize more effectively the metal-based HOMO than the ligand-based LUMO. The $[Ru(ttpy)(dpb')]^+$ (dpb′ = di-1,3-(2-pyridyl)benzene, ttpy = tolylterpyridine) gives an excited state lifetime of τ = 4.5 ns, eighteen times more than the excited lifetime of $[Ru(tpy)_2]^{2+}$ (τ = 0.25 ns).[24] Although the excited state lifetime of the ^{3}MLCT state has been extended successfully in these systems by limiting thermal population of the ^{3}LF state at room temperature, the optimization of the photophysical properties of tridentate Ru^{II} complexes is still a developing area to approach the relatively long lived excited lifetime of $[Ru(bpy)_3]^{2+}$ (τ = 1.1 μs).[26]

1.4.3 Oligonuclear Tridentate Ru^{II} Complexes Using tppz BL

Exploitation of the interesting photophysical and photochemical properties of Ru^{II} polyazine chromophores can be achieved by the construction of multimetallic complexes. These complexes typically possess bridging ligands with stabilized π* acceptor orbitals. The luminescent properties for these supramolecular assemblies are dependent on the extent of the electronic coupling associated with each of the individual components. The properties of the mononuclear components can be conveyed into the polynuclear systems important to developing light-harvesting devices on a large scale.[25]

The ligand of 2,3,5,6-tetrakis(2-pyridyl)pyrazine (tppz) can act as a tridentate bridging ligand in building polymetallic systems. Substitution of one tpy with one tppz in $[Ru(tpy)_2]^{2+}$, lowers the energy of the ^{3}MLCT state as a result of the stabilized tppz(π*) acceptor orbital. Coordination of a second Ru^{II} center to the tppz affords a further stabilized ^{3}MLCT state with a long lived excited state.[27] The syntheses of $[(tpy)Ru(tppz)](PF_6)_2$ and $[(tpy)Ru(tppz)Ru(tpy)](PF_6)_4$ were first reported by Petersen and Thummel et al.[28-29] The state diagram of $[Ru(tpy)_2]^{2+}$, $[(tpy)Ru(tppz)]^{2+}$ and $[(tpy)Ru(tppz)Ru(tpy)]^{4+}$ are given in **Figure 1.10**. These complexes display Ru(dπ)→tppz(π*) ^{3}MLCT emission. The complex $[(tpy)Ru(tppz)](PF_6)_2$ emits at 665 nm with a lifetime of τ = 30 ns in RT in CH_3CN solution,

while the bridged system, $[(tpy)Ru(tppz)Ru(tppz)](PF_6)_4$, emits at 830 nm with a lifetime of 100 ns under the same conditions.[30] This is unusual as the energy gap law predicts similar emitting states that are shifted to lower energy should be shorter lived. The change in thermal population of the ^{3}LF state is responsible for the trend in these systems. Incorporation of the tppz into $[Ru(tpy)_2]^{2+}$ stabilizes of the π^* orbital, leading to a stabilized ^{3}MLCT state. The stabilization of the ^{3}MLCT limits thermal population of the ^{3}LF state, contributing to the prolonged lifetime of τ = 0.25 ns, 30 ns and 100 ns for $[Ru(tpy)_2]^{2+}$, $[(tpy)Ru(tppz)]^{2+}$ and $[(tpy)Ru(tppz)Ru(tppz)](PF_6)_4$, respectively.

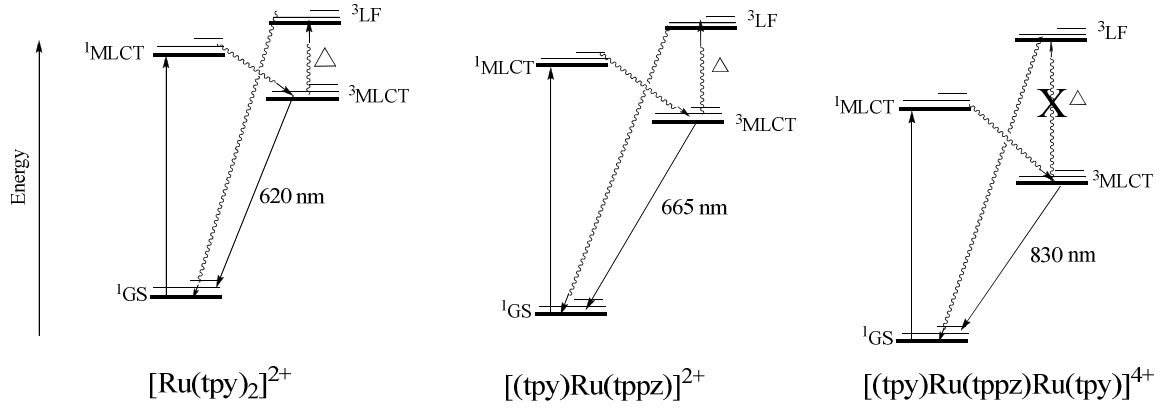

Figure 1.10. Comparison of the state diagrams of $[Ru(tpy)_2]^{2+}$ (λ_{max}^{em} = 620 nm, τ = 0.25 ns), $[(tpy)Ru(tppz)]^{2+}$ (λ_{max}^{em} = 665 nm, τ = 30 ns) and $[(tpy)Ru(tppz)Ru(tppz)](PF_6)_4$ (λ_{max}^{em} = 830 nm, τ = 100 ns), indicative of the stabilization of the ^{3}MLCT state based on the values of λ_{max}^{em}. (The relative energy of ^{1}GS is estimated based on the oxidation potentials of $Ru^{II/III}$ corresponding to the HOMO of these molecules, the ΔE between ^{1}GS and ^{1}MLCT is based on the λ_{max}^{abs} values of these complexes, tpy = 2,2′:6′,2″-terpyridine, tppz = 2,3,5,6-tetrakis(2-pyridyl)pyrazine, ^{1}GS = singlet electronic ground state, ^{3}LF = triplet ligand field excited state, ^{1}MLCT = singlet metal to ligand charge transfer excited state, ^{3}MLCT = triplet metal to ligand charge transfer excited state)

Metal-metal communication was investigated by using tppz as a BL in dirhodium complexes, $[Cl_3Rh(tppz)RhCl_3]$[31], as well as in diruthenium complexes, $[Cl_3Ru(tppz)RuCl_3]$[32], $[(ttpy)Ru(tppz)Ru(ttpy)]^{4+}$ [33-36] (ttpy = 4′-p-totyl-2,2′:6′,2″-terpyridine) $[Cl(dpk)Ru(tppz)Ru(dpk)Cl]^{2+}$ [37-38] (dpk = 2,2′-dipyridylketone), and $[Cl(Q)Ru(tppz)Ru(Q)Cl]^{2+}$ [11] (Q = 4,6-ditert-butyl-N-phenyl-o-iminobenzoquinone). These molecules were extensively analyzed in the mixed-valence state compared to the Creutz-Taube ion (Nobel Prize in Chemistry, 1983). It has been concluded that the strong electronic interactions between electroactive metal centers in these symmetric systems is mainly through the central pyrazine ring of the BL of tppz.

The coupling of reactive metals to Ru^{II} light absorbers is not well studied despite the promise such complexes hold in many forums including light-to-energy conversion schemes. Brewer et. al. have conducted research on the photophysical and electrochemical properties of the complexes of Ru^{II}, Os^{II}, Rh^{III} and Ir^{III} systems using tppz BL.[30, 39-41] The spectroscopic, photophysical and electrochemical properties of this series of complexes are summarized in **Table 1.1**. The electronic absorption spectroscopy for these complexes display M(dπ)→BL(π*) CT and M(dπ)→TL(π*) CT transitions in the visible region. The lowest lying excited states in all of these complexes is the characteristic of M(dπ)→BL(π*) CT state. Coupling a second metal to Ru^{II} via a BL (tppz) shifts the absorption maximum to lower energy, and the luminescence lifetime are prolonged in the bimetallic complexes compared to the monometallic system. For example, the complexes of $[(tpy)Ru(tppz)Ru(tpy)]^{4+}$ (λ_{max}^{abs} = 550 nm, τ = 100 ns) and $[(tpy)Ru(tppz)Ru(tppz)]^{4+}$ (λ_{max}^{abs} = 540 nm, τ = 100 ns) display red shift in the electronic absorption and longer lifetime than that of $[(tpy)Ru(tppz)]^{2+}$ (λ_{max}^{abs} = 474 nm, τ = 30 ns). Electrochemically, both the ligand based reduction and metal centered oxidation shift towards more positive potential compared to the monometallic synthons due to the electron withdrawing nature of the incorporated metal ions. Fox example, the potentials of the first reduction ($tppz^{0/-}$) and the first oxidation ($Ru^{II/III}$) shift to more positive potentials for $[(tpy)Ru(tppz)Ru(tppz)]^{4+}$ ($E_{1/2}^{ox}$ = 1.51 V, $E_{1/2}^{red}$ = -0.32 V) and $[(tpy)Ru(tppz)Ru(tpy)]^{4+}$ ($E_{1/2}^{ox}$ = 1.44 V, $E_{1/2}^{red}$ = -0.35V) compared to $[(tpy)Ru(tppz)]^{2+}$ ($E_{1/2}^{ox}$ = 1.40 V, $E_{1/2}^{red}$ = -0.97 V), consistent with the spectroscopic data. In the bimetallic complex, for example $[(tpy)Ru(tppz)Ru(tpy)]^{4+}$ ($E_{1/2}^{ox}$ = 1.44 V, $E_{1/2}^{ox}$ = 1.76 V), two oxidations of the $Ru^{II/III}$ were observed, indicating the electronic communication of the two ruthenium centers through the tppz BL.

Table 1.1. Spectroscopic, photophysical and redox properties of 2,3,5,6-tetrakis(2-pyridyl)pyrazine (tppz) complexes of Ru^{II}, Os^{II}, Ir^{III} and Rh^{III} . (bpy = 2,2'-bipyridine, tpy = 2,2′:6′,2″-terpyridine, BL = bridging ligand, TL = terminal ligand)

Complex	λ_{max}^{abs} (nm)[a]	λ_{max}^{em} (nm)[a]	τ (ns)[a]	$E_{1/2}^{ox}$ (V. vs Ag/AgCl)[b]	$E_{1/2}^{red}$ (V. vs Ag/AgCl)[b]		
					$BL^{0/-}$	$BL^{-/2-}$	$TL^{0/-}$
$[Ru(bpy)_3]^{2+}$ [c]	452	605	1100	1.32 ($Ru^{II/III}$)			-1.30
$[Ru(tpy)_2]^{2+}$ [d]	475	620	0.25	1.35 ($Ru^{II/III}$)			-1.28
$[Ru(tppz)_2]^{2+}$ [e]	480	648	50	1.57 ($Ru^{II/III}$)			-0.82
$[Os(tppz)_2]^{2+}$ [e]	468	750	300	1.26 ($Os^{II/III}$)			-0.80
$[(tpy)Ru(tppz)]^{2+}$ [e]	474	665	30	1.40 ($Ru^{II/III}$)	-0.97		-1.38
$[(tpy)Ru(tppz)Ru(tpy)]^{4+}$ [e]	550	826	100	1.44 ($Ru^{II/III}$) 1.76 ($Ru^{II/III}$)	-0.35	-0.84	
$[(tpy)Ru(tppz)Ru(tppz)]^{4+}$ [e]	548	833	100	1.51 ($Ru^{II/III}$) 1.86 ($Ru^{II/III}$)	-0.32		-0.82
$[(tpy)Os(tppz)]^{2+}$ [e]	468	775	260	1.06 ($Os^{II/III}$)	-0.97		-1.39
$[(tpy)Os(tppz)Ru(tppz)]^{4+}$ [e]	546	833	100	1.17 ($Os^{II/III}$) 1.81 ($Os^{II/III}$)	-0.36	-0.81	
$[(tpy)Ru(tppz)RuCl_3]^{2+}$ [e]	612	N/A[g]	N/A[g]	0.73 ($Ru^{II/III}$) 1.61 ($Ru^{II/III}$)	-0.60 -1.10	-1.50	
$[(tpy)Os(tppz)RuCl_3]^{2+}$ [e]	678	N/A[g]	N/A[g]	0.66 ($Ru^{II/III}$) 1.32 ($Os^{II/III}$)	-0.59 -1.10	-1.50	
$[(tpy)Ru(tppz)IrCl_3]^{2+}$ [e]	660	810	22	1.56 ($Ru^{II/III}$) 1.92 ($Ir^{III/IV}$) -1.42 ($Ir^{III/I}$)	-0.29 -0.83		
$[(tpy)Ru(tppz)RhCl_3]^{2+}$ [f]	516	830	22	1.60 ($Ru^{II/III}$) -0.23 ($Rh^{III/I}$)	-0.60 -0.98	-1.40	

[a] The λ_{max}^{abs} corresponds to the lowest energy ^{1}MLCT band, the λ_{max}^{em} is the emission upon excitation into that ^{1}MLCT band. The RT lifetime (τ) was measured in deoxygenated acetonitrile solution.

[b] Recorded in 0.1 M Bu_4NPF_6 CH_3CN with E in V vs. Ag/AgCl (0.29 V vs. NHE)

[c] Ref.[16]

[d] Ref.[42]

[e] Ref.[40]

[f] Ref.[41]

N/A[g] No detectable emission

A

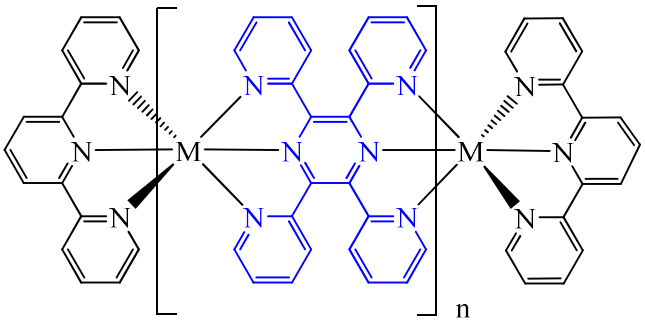

B

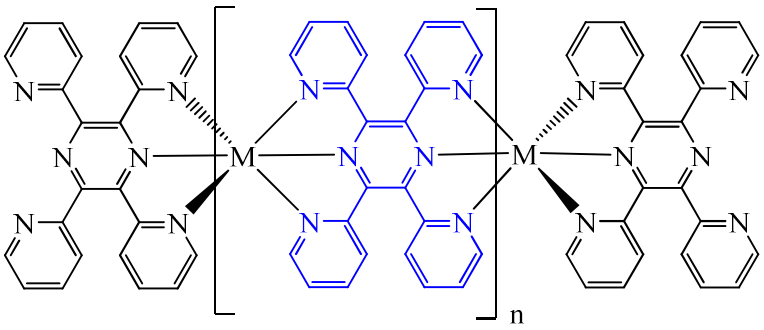

Figure 1.11. Hypothetical one dimensional molecular wire by incorporating metal ions and bis(tridentate) tppz BL ligands

Comparing the photophysical properties of the Ru^{II} and Os^{II} systems provide insight into the tppz BL. Os^{II} has a higher energy LF state, and thus the thermal population of ^{3}LF states is not observed. This provides a longer excited state lifetime. For example, $[(tpy)Ru(tppz)]^{2+}$ exhibits an emission at 665 nm with a lifetime of τ = 30 ns, while $[(tpy)Os(tppz)]^{2+}$ has an emission at 775 nm with a lifetime of τ = 260 ns, **Table 1.1**.

We previously reported mixed-metal heterobimetallic entities of Ru^{II}-Rh^{III} and Ru^{II}-Ir^{III} incorporating tppz.[27,30, 39-40, 43] The complex, $[(tpy)Ru(tppz)RhCl_3](PF_6)_2$, displays quenching of the ^{3}MLCT state proposed to occur via electron transfer to generate a lower lying Ru-to-Rh metal-to-metal charge transfer state.[41] The coupling of Ru^{II} to Pt^{II} within tridentate bridged architecture of tppz had not yet been reported prior to my work.

Recently, the design of molecular wire by exploiting the tppz to mediate the intermetallic coupling has been studied. Abruna's and Fantacci's group investigated a series of multimetallic Ru^{II}-tppz systems with both tpy-capped and tppz-capped oligomers of $[(tpy)_2Ru_n(tppz)_{n-1}]^{2n+}$ and $[Ru_n(tppz)_{n+1}]^{2n+}$, **Figure 1.11**.[27, 44-45] Investigation of the electrochemical and spectroscopic properties suggests high degrees of delocalization of these complexes, attributing to the metal interunit communication.[45-46] No emission properties were given in these complexes.

Coordination of two metals to tppz requires two pyridine rings, and the central pyrazine ring becomes nearly coplanar. Failure of the bis-tridentate conformation has been reported by the analyses of the crystal structures. A diversity of binding modes has been observed due to the steric repulsion and multiple binding modes of tppz.

1.5 Pt^{II} Tridentate Complexes

Pt^{II} complexes are d^8 and electronically prefer square planar geometry to accommodate the intermolecular interactions, and the steric straints arising from the coordinated ligands.[47-50] Pt^{II} complexes of polyazine ligands have been well studied. Square planar Pt^{II} complexes typically undergo aggregation forming linear chain structures through Pt···Pt interactions. Consequently, the properties of Pt^{II} complexes are very sensitive to the environments: such as temperature,[51] counterions[52-53] and solvents,[51, 54-56] which impact the extent of metal-metal and interligand interactions. Such robust and dynamic character has provided platinum complexes with a variety

of potential applications as sensors,[57] catalysts,[58-60] and one dimensional conductors, as well as bioactive probes,[61-68] with promise in the areas of non-linear optics and photovoltaics.[69-73]

$[(tpy)PtCl]^+$ and its analogs have been extensively studied with the focus on modulating their spectroscopic and luminescent behaviors. Complexes of Pt^{II} with tridentate ligands are typically not emissive or weakly emissive at RT in solution due to Pt···Pt intermolecular interactions and/or low lying LF states.[74-75] Recently, modified $[(tpy)PtL]^{n+}$ (L = monodentate ligand) analogs have been designed to display enhanced emission through the substitution of the tpy ligand[52, 76-79] or replacement with modified monodentate ligand, L.[80] The RT luminescence lifetimes of [(tpy)Pt(C≡C-C≡CH)](OTf) (τ = 200 ns, Φ^{em} = 0.011), [(tpy)Pt(C≡C-C_6H_5)](OTf) (τ = 500 ns, Φ^{em} = 0.012) and [(4′-CH_3O-tpy)Pt(C≡C-C_6H_5)](OTf) (τ = 500 ns, Φ^{em} = 0.025) (OTf = trifluoromethanesulfonate) have been tuned in CH_3CN solution by varying the tpy and L, preventing the aggregation.[52]

Pt^{II} complexes usually self-quench in fluid solution at RT via the formation of Pt···Pt interactoins.[81-82] Modification of the tpy with bulky groups R_1, R_2 and R_3 (like tetra-butyls), as well as the monodentate ligand (L) can afford high luminescent efficiency by decreasing the self-quenching Pt···Pt interactions.[51, 54, 57, 70, 74, 83-97] The emitting state in Pt^{II} polyazine complexes is typically ^{3}MLCT nature. Stabilization of the ^{3}IL by the extension of the conjugation of the ligand may afford an energetically accessible $^3\pi\pi^*$, in which the vibronically structured narrow-width emission is observed.[70, 98] **Figure 1.12 (A)** illustrates the ligand modification on the form of monometallic platinum, $[(tpy)PtL]^{n+}$. The emission of the substituted L with electron withdrawing or electron donating group is red-shifted or blue-shifted respectively, consistent with the MLCT assignment for the excited state. For example, replacement of the (-CH_2COMe) in $[(^tBu_3tpy)Pt(CH_2COMe)]^+$ [89] (λ^{em} = 595 nm) with electron donating group (-C≡C-C≡CH) has resulted the emission red-shift 32 nm for $[(^tBu_3tpy)Pt(C{\equiv}C\text{-}C{\equiv}CH)]^+$ [53] (λ^{em} = 627 nm), while no emission was observed for $[(^tBu_3tpy)PtCl]^+$ in solution.

A

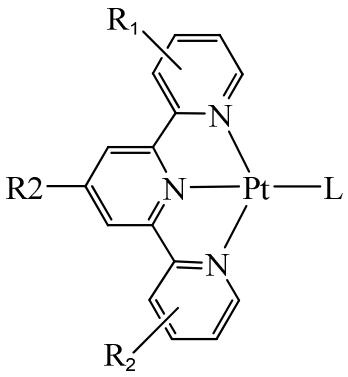

B

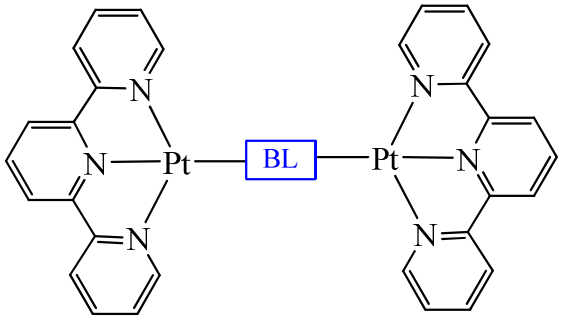

C

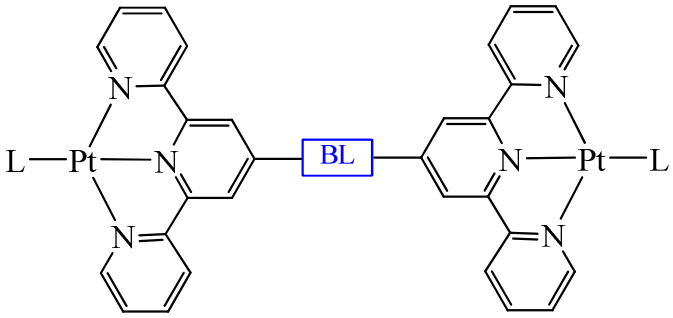

Figure 1.12. Representative structures of the Pt^{II} terpyridyl complexes, Form A: $[(tpy)PtL]^{n+}$ (L = monodentate ligand) , Form B: $[(tpy)Pt(BL)Pt(tpy)]^{n+}$, Form C: $[LPt(tpy)\text{-}(BL)\text{-}(tpy)PtL]^{n+}$ (BL = bridging ligand)

Similar strategies to modulate the photophysical properties of Ru^{II} complexes are applicable to Pt^{II} tridentate systems. The optical and electrochemical properties of platinum complex can be manipulated by extending the conjugated system using BL to stabilize MLCT excited states limiting thermal population of LF excited state. The type of platinum complexes, $[(tpy)Pt(BL)Pt(tpy)]^{n+}$ (**Figure 1.12 B**)[70, 83, 99-104] has been investigated, in which the electronic coupling of the Pt centers through the π-conjugated BL has been facilitated. An intense emission has been observed at 615 nm with a lifetime of 0.2 μs in $[(^tBu_3tpy)Pt\text{-}C\equiv C\text{-}Pt(^tBu_3tpy)]^{2+}$.[100] The type of platinum complexes with the form of $[LPt(tpy)\text{-}(BL)\text{-}(tpy)PtL]^{n+}$ (**Figure 1.12 C**) possesses the geometry with the reactive metal center orienting toward outside, which is more accessible to the targets than those of form B. Two parallel cofacially disposed terpyridyl-Pt-Cl in $[LPt(tpy)\text{-}(BL)\text{-}(tpy)PtL]^{n+}$ can stack on each other. This intermolecular association has been demonstrated by the crystallography.[103, 105] The configuration of Pt complexes with form C resembles our trimetallic complex, $[ClPt(tppz)Ru(tppz)PtCl](PF_6)_4$.

1.6 Oligonuclear Ru^{II} Complexes

The evolution of the supramolecular chemistry will proceed as new functionalities are introduced to these well-organized entities. Multicomponent supramolecular dendrimers based on Ru^{II} and/or Os^{II} polypyridine or polyazine building blocks are appealing due to their robust photoinitiated properties. The bidentate ligand dpp (2,3-bis(2-pyridyl)pyrazine) is widely used as the polyazine bridging ligand to build up the supramolecular entities.[1, 106-108]

The dpp ligand acts as an AB chelate and binds two metal centers through a pyridyl and a pyrazine nitrogen. Campagna's group reported a photoinduced energy transfer in a homogenous heptametallic ruthenium (II) system, $[Cl_2Ru\{(\mu\text{-}dpp)Ru[(\mu\text{-}dpp)Ru(bpy)_2]_2\}_2](PF_6)_{12}$.[109] This complex exhibits very intense absorption bands in the UV region ($\varepsilon = 10^5\text{-}10^6\ M^{-1}cm^{-1}$) and visible region ($\varepsilon = 10^4\text{-}10^5\ M^{-1}cm^{-1}$), which is attributed to the ligand-based $\pi\rightarrow\pi^*$ transition in UV region and $Ru(d\pi)\rightarrow bpy(\pi^*)$ and $Ru(d\pi)\rightarrow dpp(\pi^*)$ CT transitions in the visible region centered at 544 nm. The compound displays luminescent properties both at RT (λ_{max}^{em} = 895 nm) and 77 K (λ_{max}^{em} = 880 nm). The electrochemistry of this molecule reveals a series of reversible Ru-centered oxidation ($E_{1/2}^{ox}$ = 1.56, 0.86 V vs. SCE) and ligand-based reduction processes ($E_{1/2}^{ox}$ = -0.51, 0.62, -0.72, -1.16 V vs. SCE). The ultrafast spectroscopic study suggests energy

that transfer from the peripheral chromophores to the core is very fast (0.6 ps) with unit efficiency. The results indicate that such supramolecular assemblies can act as artificial light harvesting systems for photochemical conversion of light energy.

1.7 Ru^{II},Pt^{II} Mixed Metal Complexes

Coupling of ruthenium chromophores to a cis-$Pt^{II}Cl_2$ moiety has been exploited as luminescent compounds,[110-119] water splitting catalysts,[120] and antitumor agents[62, 117, 121-132].

Brewer's group has long been engaged in the design of Ru polyazine based chromophore coupled to a cis-$PtCl_2$ unit with the focus on their potential applications.[117, 121-122, 124, 129, 133-135] A series of supramolecular architectures have been constructed with the form $[(bpy)_2M(\mu\text{-}BL)PtCl_2]^{2+}$ (**Figure 1.13 A**), $[\{(bpy)_2M(\mu\text{-}BL)\}_2Ru(\mu\text{-}BL)PtCl_2]^{6+}$ (**Figure 1.13 B**), and $[(R\text{-}tpy)MCl(\mu\text{-}BL)PtCl_2]^{+}$ (**Figure 1.13 C**), where M = Ru or Os, and BL = dpp (2,3 bis-(2-pyridyl)pyrazine), dpq (2,3 bis-(2-pyridyl)quinoxaline), and dpb (2,3 bis-(2-pyridyl)benzoquinoxaline). The electrochemical and spectroscopic data of such mixed metal supramolecules are summarized in **Table 1.2**. Coupling of Pt^{II} to Ru^{II} in bidentate coordination environments to produce hetero-bimetallic complexes leads to systems that possess further stabilized ^{3}MLCT excited states relative to the monometallic analogs, which is displayed as a red shift in the electronic absorption data. This implies the spectroscopic properties of these kinds of complexes are associated with both the chromophoric Ru part and the Pt site. Fox example, $[(bpy)_2Ru(dpp)PtCl_2]^{2+}$ demonstrates $Ru(d\pi)\rightarrow dpp(\pi^*)$ CT transition at λ_{max}^{abs} = 509 nm with a red shift compared to the monometallic synthon $[(bpy)_2Ru(dpp)]^{2+}$ (λ_{max}^{abs} = 470). Coupling of electron withdrawing unit of cis-$PtCl_2$ to the monometallic precursor of $[(bpy)_2Ru(dpp)]^{2+}$ stabilizes the $dpp(\pi^*)$ orbital, resulting in a lower energy shift of the MLCT transition. Electrochemically, the heteronuclear complex of $[(bpy)_2Ru(dpp)PtCl_2]^{2+}$ ($E_{1/2}^{red}$ = -0.49 V) exhibits substantially more positive potential shift at the first reduction than its homogeneous synthons of $[(bpy)_2Ru(dpp)]^{2+}$ ($E_{1/2}^{red}$ = -1.30 V) upon the platinum coordination, consistent with the electronic absorption data. This positive potential shift as well as the red shift of spectroscopic data is indicative of the formation of the mixed-metal Ru^{II},Pt^{II} complex.

A

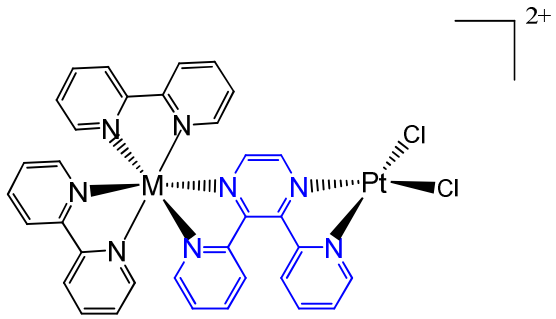

B

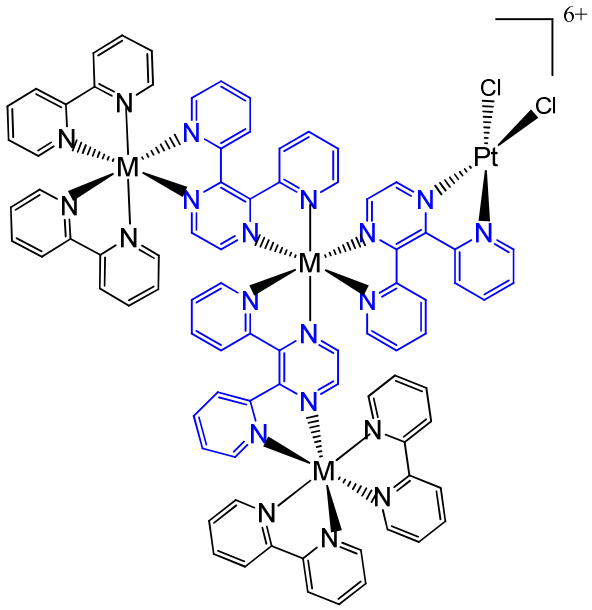

C

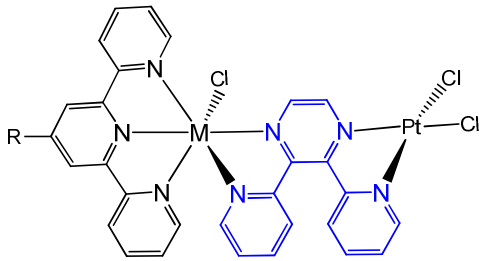

Figure 1.13. The scheme of mixed-metal supramolecules bridged by bidentate BL dpp (dpq = 2,3 bis-(2-pyridyl)quinoxaline) with the Form A: $[(bpy)_2M(\mu\text{-}BL)PtCl_2]^{2+}$, Form B: $[\{(bpy)_2M(\mu\text{-}BL)\}_2Ru(\mu\text{-}BL)PtCl_2]^{6+}$, and Form C: $[(R\text{-}tpy)MCl(\mu\text{-}BL)PtCl_2]^{+}$, where M = Ru or Os.

Table 1.2. Redox[a] and spectroscopic properties of homogeneous Ru^{II} polyazine complexes and Ru^{II},Pt^{II} mixed-metal supramolecules by using bidentate BL, BL = bridging ligand, TL = terminal ligand.

Complex	λ_{max}^{abs} (nm)	$E_{1/2}^{ox}$ (V vs. Ag/AgCl)	$E_{1/2}^{red}$ (V vs. Ag/AgCl)			
			$BL^{0/-}$	$BL^{-/2-}$	$TL^{0/-}$	$TL^{0/-}$
$[Ru(bpy)_3]^{2+}$ [c]	452	1.32			-1.30	-1.49
$[(bpy)_2Ru(dpp)]^{2+}$ [d]	470	1.38	-1.01		-1.46	-1.67
$[(bpy)_2Ru(dpp)PtCl_2]^{2+}$ [d]	509	1.62	-0.49	-1.06	-1.44	
$[(bpy)_2Ru(dpq)]^{2+}$ [e]	515	1.47	-0.72		-1.40	-1.62
$[(bpy)_2Ru(dpq)PtCl_2]^{2+}$ [e]	582	1.72	-0.28	-0.83		
$[(bpy)_2Ru(dpb)]^{2+}$ [e]	550	1.48	-0.62		-1.26	-1.60
$[(bpy)_2Ru(dpb)PtCl_2]^{2+}$ [e]	630	1.61	-0.11	-0.75		
$[(tpy)RuCl(dpp)]^{+}$ [f]	510	1.04	-1.07		-1.27	
$[(tpy)RuCl(dpp)PtCl_2]^{+}$ [f]	544	1.14	-0.50	-1.05	-1.43	
$[(tpy)RuCl(dpq)]^{+}$ [f]	570	1.06	-0.77		-1.27	
$[(tpy)RuCl(dpq)PtCl_2]^{+}$ [f]	632	1.10	-0.32	-0.91	-1.50	
$[(tpy)RuCl(dpb)]^{+}$ [f]	595	1.02	-0.61		-1.25	
$[(tpy)RuCl(dpb)PtCl_2]^{+}$ [f]	682	1.12	-0.20	-0.81	-1.51	
$[\{(bpy)_2Ru(dpp)\}_2Ru(dpp)]^{6+}$ [g]	747	1.58	-0.50	-0.64		
$[\{(bpy)_2Ru(dpp)\}_2Ru(dpp)PtCl_2]^{6+}$ [g]	750	1.58	-0.40	-0.60		

[a] Measured in CH_3CN, bpy = 2,2'-bipyridine, dpp = 2,3 bis-(2-pyridyl)pyrazine, dpq = 2,3 bis-(2-pyridyl)quinoxaline, and dpb = 2,3 bis-(2-pyridyl)benzoquinoxaline.

[b] Recorded in 0.1 M Bu_4NPF_6 CH_3CN with E in V vs. Ag/AgCl (0.29 V vs. NHE)

[c] Ref.[16]

[d] Ref.[117]

[e] Ref.[117]

[f] Ref.[121]

[g] Ref.[134]

1.8 Stereochemistry

1.8.1 Homochirality and Symmetry Breaking

In biochemistry, macromolecular chirality arises from the self-recognition of intrinsically homochiral molecules (D-sugars and L-amino acids). A good example of complete symmetry breaking in chirality is the fact that a series of natural products exsit only as one of the two enantiomers. Origins of chirality are still controversial,[136-139] and have long been argued. Thermodynamically, chiral compounds synthesized from achiral starting materials and reagents are racemic (with identical amount of the two enantiomers). The excess of either the left-handed or right-handed enantiomer can be achieved by making use of chiral auxiliaries or asymmetric catalyst. Chiral discrimination has been established by the formation of crystals (Pasteur, 1848) which requires a process whereby the molecules assemble at early stages to form structured aggregates.[139-141] It is believed that such amplification of chirality by crystallization or surface adsorption reduces the freedom of the motion of 3D molecules in fluid or gas state. Alternatively, nature's spontaneous enantioselectivity is also proposed as a result of the circularly polarized light radiation,[142-143] magnetic induction,[144-146] or electroweak interactions arising from the parity violation.[147-148] None of them, however, are conclusive.[137, 149]

A chiral molecule has to be in the point groups of C_n or D_n, I, O or T which do not possess improper rotation axes, S_n. The molecule and its non-superimposable mirror image are referred to as enantiomers or optical isomers. A mixture with the same amount of enantiomers is defined as a racemic mixture and is not optically active. The molecule with more than one chiral center superimposable to its mirror image is a meso molecule. A meso compound is a diastereomer of the enantiomers. The assembly of the asymmetric molecular units can only present in the 65 Sohncke space groups (chiral space group **as summarized in Table 1.3**) among the total 230 possible arrangements of symmetry elements in the solid state.[150] There are three possible arrangements of the enantiomers in the solid crystals.[150]

1) Racemate, in which two equal amount of the two enantimoers are distributed in the lattice with well-defined order. The racemic compound is the most common form of the crystalline enantiomers. There are 60-80% of racemic crystals in the $P2_1/c$, C_2/c and P1 groups.[151]

2) Conglomerate, in which each enantiomer condensates with itself to form a homochiral enantiopure crystal, such as sodium ammonium tartrate tetrahydrate (Pasteur's salt). Up to 90% of the conglomerates are found in $P2_12_12_1$, $P2_1$, C_2 and P1.

3) Racemic solid solution, in which there are 1:1 ratio of the two enantiomers with disorder arrangements in the solid state, are probably due to the strong similarity between the two enantiomers.[150-151]

Table 1.3. 65 chiral space groups in crystals, where space groups of the enantiomorphous pairs are highlighted in the brackets, Ref.[150]

Crystal	**Space groups**
Cubic	*P*23, *P*2$_1$3, *I*23, *I*2$_1$3, *F*23, *P*432, (***P*4$_1$32, *P*4$_3$32**), *P*4$_2$32, *I*432, *I*4$_1$32, *F*432, *F*4$_1$32
Tetragonal	*P*4, (***P*4$_1$, *P*4$_3$**), *P*4$_2$, *I*4, *I*4$_1$, *P*422, *P*42$_1$2, (***P*4$_1$22, *P*4$_3$22**), (***P*4$_1$2$_1$2, *P*4$_3$2$_1$2**), *P*4$_2$22, *P*4$_2$2$_1$2, *I*422, *I*4$_1$22
Monoclinic	*P*2, *P*2$_1$, *C*2
Orthorhombic	*P*222, *P*222$_1$, *P*2$_1$2$_1$2, *P*2$_1$2$_1$2$_1$, *C*222, *C*222$_1$, *I*222, *I*2$_1$2$_1$2$_1$, *F*222
Triclinic	*P*1
Trigonal	*P*3, (***P*3$_1$, *P*3$_2$**), *P*312, *P*321, (***P*3$_1$12, *P*3$_2$12**), (***P*3$_1$21, *P*3$_2$21**), *R*3, *R*32,
Hexagonal	*P*6, (***P*6$_1$, *P*6$_5$**), (***P*6$_2$, *P*6$_4$**), *P*63, *P*622, (***P*6$_1$22, *P*6$_5$22**), *P*6$_3$22, (***P*6$_2$22, *P*6$_4$22**)

1.8.2 Symmetry and Time-scale

Real molecules are always in motion with time. Even though the enantiomers are non-superimposable, the conformations of some enatiomers are interconvertable with low energy barrier. If the inversion is fast compared to the time scale by all the means of observations, the chirality argument makes no sense. Therefore, configurational stability is essential to maintain the chirality with the respective of measurements.[152]

A flexible molecule can achieve a sustainable conformation with a certain symmetry element. A typical example to address this issue is an amine with three different groups. In principle, the pyramidal form of such amine is a chiral molecule. In fact, the two conformations rapidly convert to each other through an achiral plane. The rapid inversion makes an effectively achiral system without isolable stereoisomers (**Figure 1.14**). On the other hand, such conformational isomers can be stable at RT owing to the high energy barriers for conversion between isomers. The type of these stereoisomers is depicted as atropisomers. Atropoisomers can convert to each other by passing through a substantial energy barrier with the increasing of the temperature.[152]

Stable conformations can be facilitated by incorporating steric bulk groups to prevent the racemization, or by coordinating to multiple metal ions.[153] As illustrated in **Figure 1.15**, the two benzene rings in biphenyl are not planar as a consequence of the steric crowding from the neighboring hydrogen. The resulting chiral conformation is racemized by the rapid rotation of the C-C single bond. Upon enlarging the benzene rings to naphthalene rings, the conglomerate of 1,1'-binaphthyl is resolved by the spontaneous process from the racemic melt.[141] Replacement of the two ortho-hydrogens in naphthalene rings with two –OH groups to form the 1,1'-bi-2-naphthol (BINOL) molecule, The enantiomers of BINOL and its derivatives have been resolved in the solution at RT and widely used as dissymmetric catalysts in chemistry.[154]

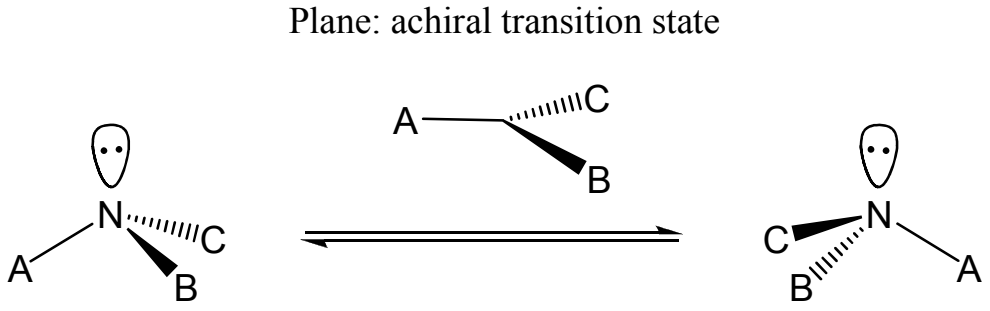

Figure 1.14. Illustration of the interversion of an achiral molecule (an amine bonded with three different groups) *via* an achiral intermediate transformation.

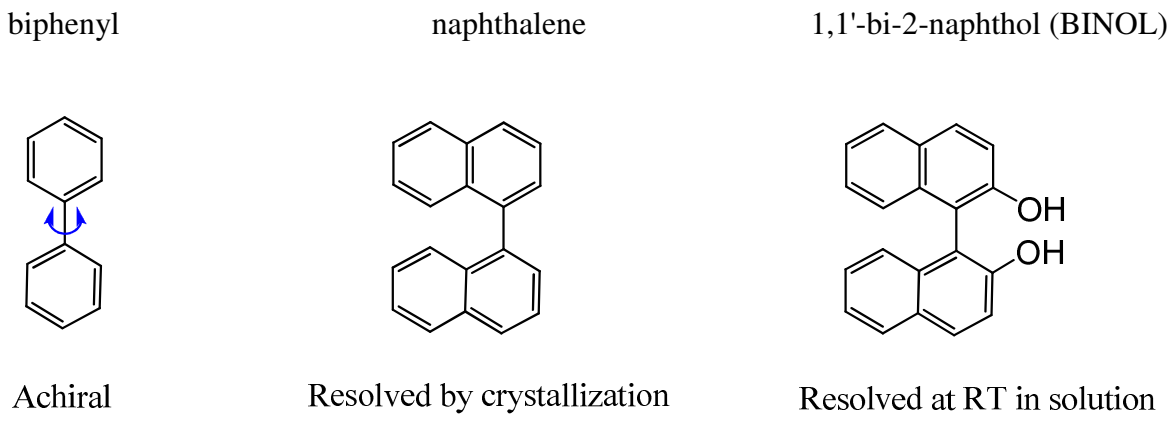

Figure 1.15. Illustration of the symmetry breaking by introducing bulky groups to limit the interconversion in the achiral molecule of biphenyl, the chiral molecule of naphthalene and 1,1'-bi-2-naphthol (BINOL).

1.9 Nuclear Magnetic Resonance (NMR)

NMR techniques can provide much information about molecules with NMR active nuclei such as ^{1}H, ^{13}C or ^{195}Pt.[155-158]

1.9.1 Chemical Shift (δ)

When a magnetic field is applied to an atom, the electrons of the atom circulate in the applied magnetic field. Thus, a small magnetic field is induced by the circulating electrons with an opposite direction to the applied magnetic field (Lenz's law). The effective field is less than the externally applied field. As a result, the nucleus is shielded. If the nucleus possesses an overall spin, the electronic environment of a nucleus can be investigated by (NMR) techniques. The more the applied field is, the greater the resonance frequency for the various nuclei. Therefore, the chemical shift was developed to avoid the difference of the NMR spectra taken on different spectrometers in different field strengths. Chemical shift, δ, is usually expressed in parts per million (ppm) by frequency:[159]

$$\delta = \frac{\text{frequency of signal - frequency of reference}}{\text{spectrometer frequency}} X 10^{6}$$

The frequency (in Hz) of the signal of ^{1}H, ^{13}C are usually referenced against tetramethylsilane (TMS, δ = 0). Chemical shift (δ) is a function of the nucleus and its chemical environment. δ is useful to distinguish the structure and conformation of the molecules, even their aggregation.

For the same nucleus like ^{1}H, the trend of chemical shift correlates to the degree of shielding or deshielding effect with the variation on the electron density. When the nucleus is exposed to the external magnetic field, electron donating and electron withdrawing group can shield and deshield the applied field, respectively. As a

consequence, the shielding and deshielding effect will cause the signal of the δ move towards upfield and downfield, respectively (**Figure 1.16**).[159]

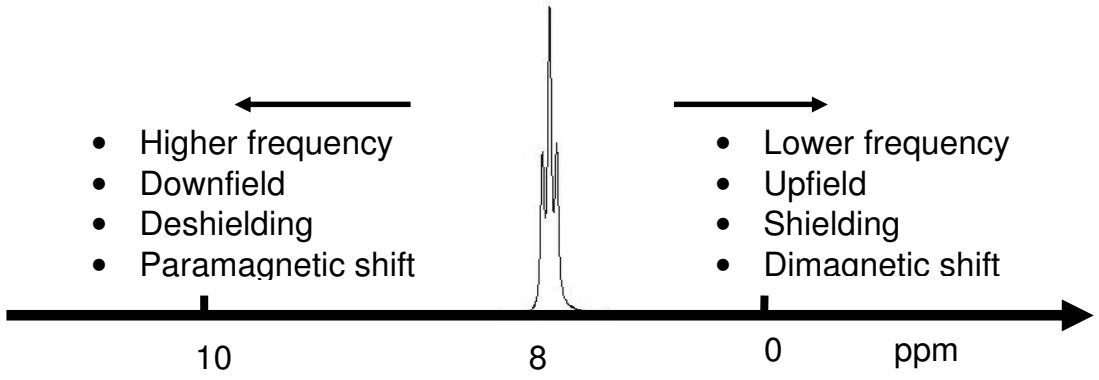

Figure 1.16. The scheme to denote the dynamics of chemical shifts.

1.9.2 Electron Withdrawing Effect via Metal-ligand Bonding

A change of the δ of a nucleus such as ^{1}H of free ligand can be observed after coordinating to metal center. The cause of this behavior is based on the chemical (electronic) environment variations, which can arise from not only the metal-ligand bond, but also the configuration change within the complex. For example, downfield shift is observed in $[(tpy)PtCl]^{+}$ vs. tpy arising from the electron withdrawing effect of positive charged Pt^{II} on the tpy. The ^{1}H-NMR spectra of tpy ligand and its platinated complex show a characteristic shift for the electron withdrawing effect, **Figure 1.17**. It is important to note free ligands have free rotation of C-C bond between pyridyl rings. The energetically favored conformation of uncomplexed and unprotonated terpyridine adopt the trans configuration, which results from electrostatic repulsion of the lone pair electrons on nitrogen atoms and steric repulsion of the ortho-hydrogen atoms in Ring A and B. The free ligand of tpy in solution presents trans/trans orientation with the rotation of the σ–bonds. After coordinating to Pt^{II}, the three N atoms must be nearly coplanar with the Pt^{II} and Cl in $[(tpy)PtCl]^{+}$, in which the three pyridine rings are almost coplanar with the coordination plane with a slightly torsion angle 2.0º between the two peripheral pyridine rings. Such conformations of the free tpy and $[(tpy)PtCl]^{+}$ complex are

consistent with the NMR data, as depicted in **Figure 1.17**. The ^{1}H-NMR spectrum of tpy displays six nonequivalent proton resonances with expected splitting patterns. Upon complexation, the protons in $[(tpy)PtCl]^{+}$ undergo dramatic downfield shifts due to the coordination of the electron withdrawing Pt^{II} cation. The resonances at δ 8.53, 7.97, 8.93 undergo significant downfield shifts for the proton H^{4B} (Δδ = 0.51 ppm), the H^{5B} (Δδ = o.46 ppm), and the H^{6B} (Δδ = 0.20 ppm), respectively.[160] The multiplet at 8.65 ppm corresponds to the protons of H^{3A}, H^{4A} and H^{3B}.

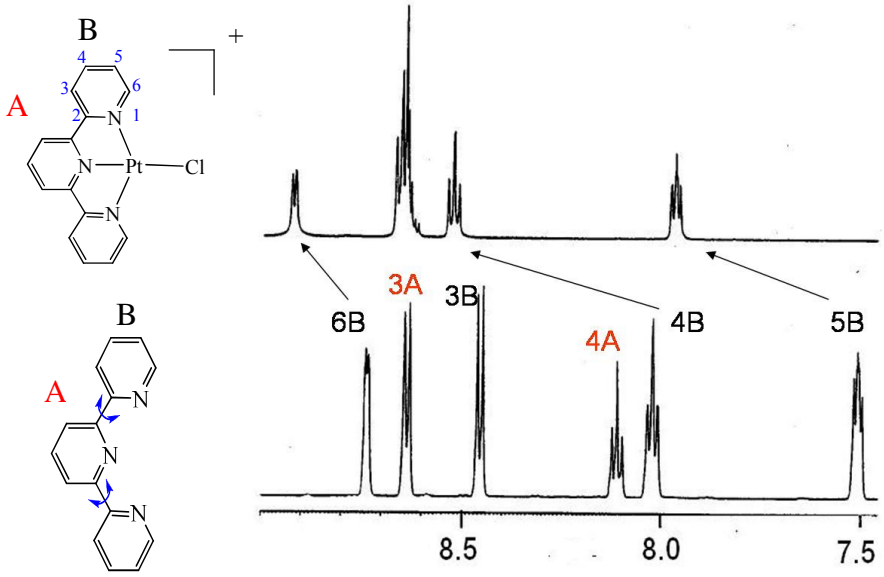

Figure 1.17. ^{1}H-NMR of free ligand terpyridine (top), and $[tpyPtCl]^{+}$ (bottom) in d^{6}-DMSO. The arrows show the chemical shift due to the electron withdrawing effect upon coordination. Adapted from Ref.[160]

1.9.3 Ring Current Effect

Chemical shifts are influenced by delocalized π-electrons in the rings of aromatic molecule which induce a ring current in the presence of an external magntic field as stipulated by Ampere's law. This can lead to somewhat unexpected chemical shifts for aromatic systems.

Geometry of the compounds is an important factor in determining the δ values of protons. Three factors including steric repulsion from ortho-hydrogen, electrostatic repulsion from the lone pair electrons on nitrogens and the free rotation of the σ-bond make pyridyl or pyrazine free ligands exhibit the expected trans-conformations in their solid states and have characteristic ^{1}H-NMR spectra in the solution. The ^{1}H-NMR spectrum of bpy was shown in **Figure 1.18**. Analyzing the spectrum from left to right, the δ of H^{6} protons are assigned to the lowest field with its representative resonance pattern (doublet) and characteristic coupling constant, *J* (5.0-7.0 Hz). This is attributed to the inductive effects from the nitrogen (electron withdrawing effect). Upon the identification of H^{6}, the assignments of the rest of the protons were accomplished by using ^{1}H-^{1}H COSY. The observed chemical shifts and splitting pattern for the free ligands, tpy and tppz hereinafter are consistent with the literature reported data.[29, 161]

The δ differences between free and coordinated ligands provide information on the metal complexes. With metal-ligand complexation, the metal ion is the electron acceptor resembling the electron withdrawing group, and ligand is the electron donor acting as the electron donating group. Usually, the σ-bond (L→M) reduces the electron density on the ligand, thus a deshielding effect is observed on the δ of ligands in the complexation, although the π back-bonding (M→L) or π-bonding should also be taken into account. The effect of the long distance coupling can influence δ through bonds or through space. The through-space impact on δ is stronger in larger conjugated systems. Ring current arises from the polycyclic aromatic moieties with the delocalized electrons in an external magnetic field, which can shield and deshield the nucleus located over or outside of the rings. For example, in the $[Ru(bpy)_3](PF_6)_2$, **Figure, 1.19 (left)** [162] three bpy ligands coordinate to Ru and display an octahedral configuration. Such conformation will cause large ring current effect for the protons located over the aromatic rings, undergoing

upfield shifts. The shield effect was observed on H^6, shifting the signal to the upper field up to 2.23 ppm comparing to free ligand, **Figure 1.18**.[161] By contrast, a deshielding effect is observed for H^3A and H^3B, shifting their signals to the lowest field by 0.44 ppm in relation to the free ligand.

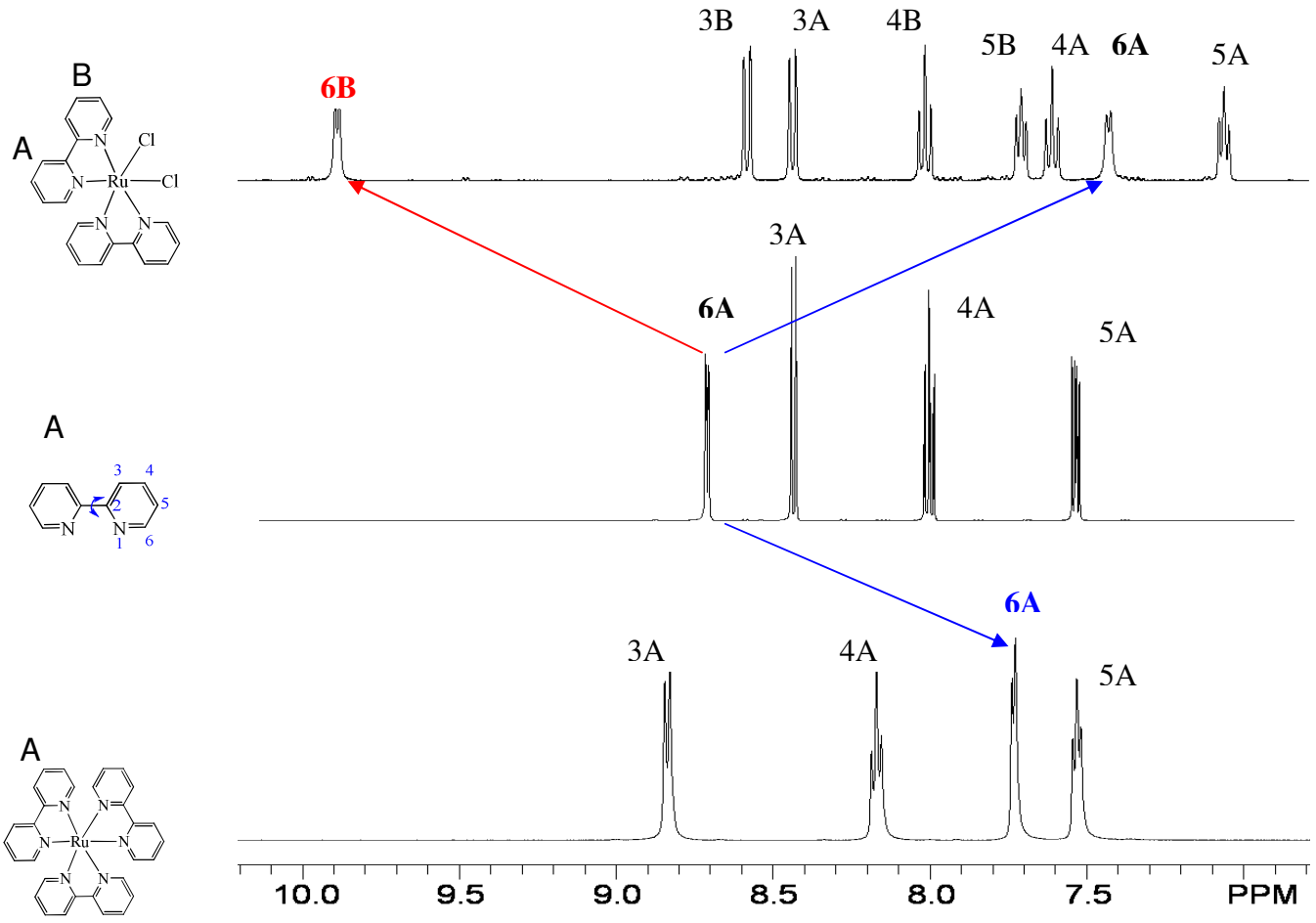

Figure 1.18. 500 MHz ^{1}H-NMR spectra of $(bpy)_2RuCl_2$, free ligand bpy, and $[Ru(bpy)_3]^{2+}$ and CD_3CN. Our data are comparable to literature reported values.[161]

Table 1.4. 500 MHz ^{1}H-NMR chemical shifts (δ) and coupling constants (^3J) of bidentate free ligand bpy, $(bpy)_2RuCl_2$ and $[Ru(bpy)_3](PF_6)_2$, which are comparable to the literature reported values.[161]

Ring	H position on the Ring	bpy δ(ppm) (^3J in Hz)	$(bpy)_2RuCl_2$ δ(ppm) (^3J in Hz)	$[Ru(bpy)_3](PF_6)_2$ δ(ppm) (^3J in Hz)
A	3	8.40 (8.0)	8.44 (10)	8.84 (8.0)
	4	7.94 (7.5)	7.61 (9.5)	8.17 (8.0)
	5	7.44 (5.5)	7.06 (7.5)	7.53 (6.5)
	6	8.69 (5.0)	7.43 (7.0)	7.73 (6.0)
B	3		8.58 (10)	
	4		8.02 (10)	
	5		7.71 (7.5)	
	6		9.90 (7.0)	

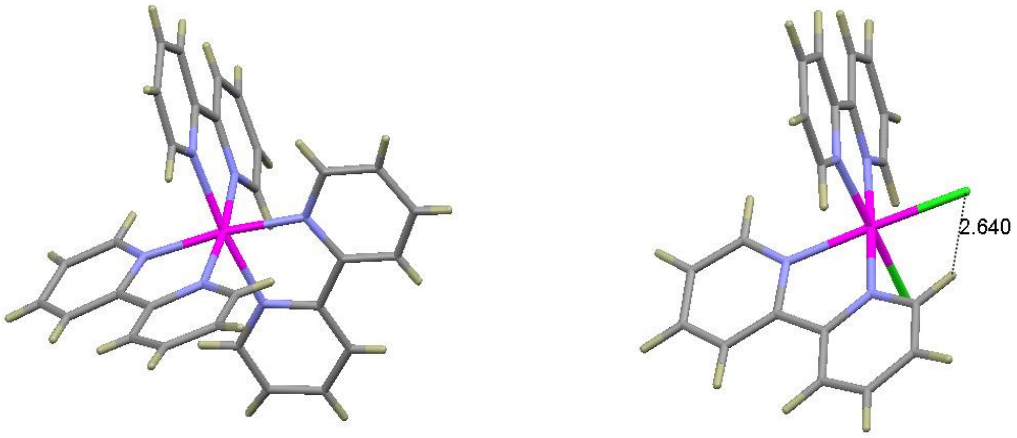

Figure 1.19. The crystal structure of $[Ru(bpy)_3]^{2+}$ (right)and $(bpy)_2RuCl_2$ (left) displaying the H^6 protons are subject to the ring-current effect and electron withdrawing effect, respectively. Our assignments are compared comparable to the literature reported values.[161]

A combination of both the ring current effect and the electron withdrawing effect are presented in $[(bpy)_2RuCl_2]$ moiety, in which the protons in the two pyridyl rings of bpy are split into eight non-equivalent signals. Remarkably, the H^6 on ring B is located just above the Cl^- ion as shown in the crystal structure of bpy_2RuCl_2 in **Figure 1.19 (right)**,[163] and is shifted downfield by 2.17 ppm in relation to the same proton in $[Ru(bpy)_3]^{2+}$. Such inductive effects have been observed in many bis(bipyridine)ruthenium chloride complexes.[164-167] On the other hand, the H^6 on ring A buried over ring B is shifted to upfield by 1.26 ppm comparing to the same proton in bpy, which happened to $[Ru(bpy)_3]^{2+}$ in the same way due to ring current effect.

1.9.4 Fluxionality in Tridentate Pt^{II} Complex Characterized by NMR

The conformations of the metal complexes with flexible ligands bearing diverse binding modes (like tppz) can lead to unexpected properties. Factors such as solvent (polarity or H-bond) and inter-, intra-molecular interactions can cause the changing modes of binding and varied intermolecular interactions. A fluxional binding mode has been suggested for the substituted terpyridine (tpy) ligands.[168-171] It seems that NMR data provides reasonable evidence on the fluxional process associated with Pt^{II} complex. As shown in **Figure 1.20**, the ^1H NMR spectrum exhibited two different isomers with a 2:1 integration ratio at RT. The energy difference of the two isomers resulted from the unsymmetrical ligand.[168]

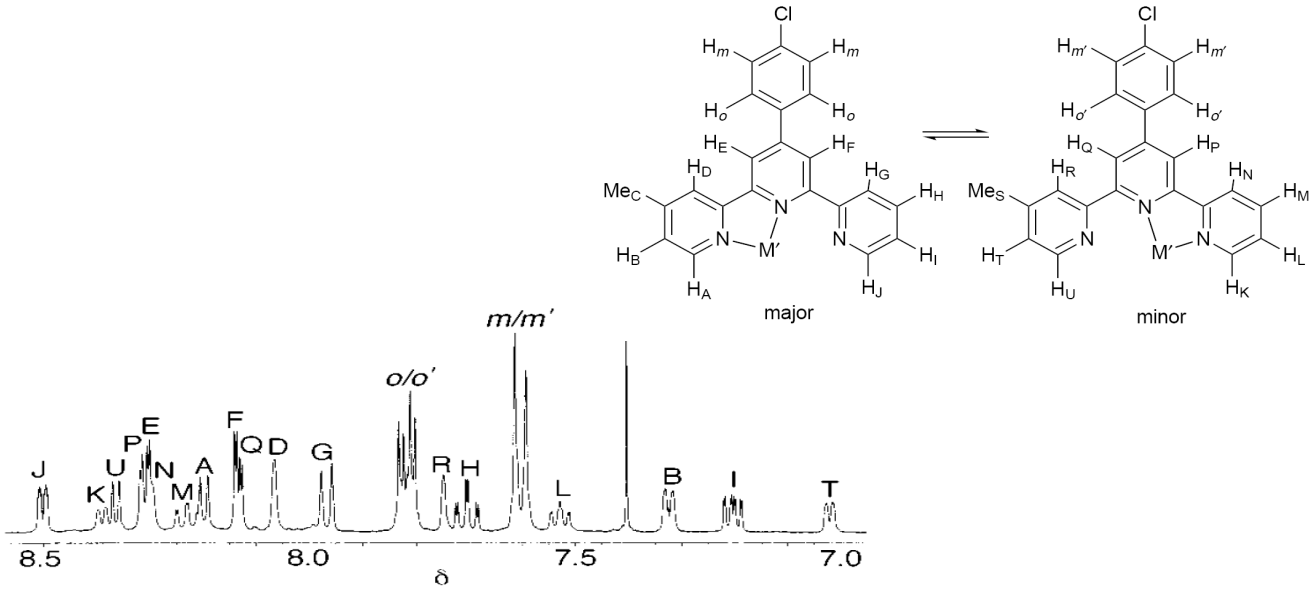

Figure 1.20. The fluxional mode to interpret the NMR spectrum of a tridentate Pt^{II} complex, adapted from Ref.[168]

1.10 The Varied Binding Modes of the Ligand tppz

The ligand of tppz was first reported by Goodwin in 1959.[172] It consists of four pyridine rings bonded to a pyrazine ring with four σ C-C axes. There are two reported solid state conformations on neutral tppz (**Figure 1.21 I & II**), in which neighboring pyridine rings are twisted out of the pyrazine ring plane either in the same direction or in the opposite orientation to relieve H^3-H^3 steric repulsion if all the pyridine rings are coplanar. Both of these two forms of tppz possess C(i) symmetry, and have planar pyrazine rings.[173-174]

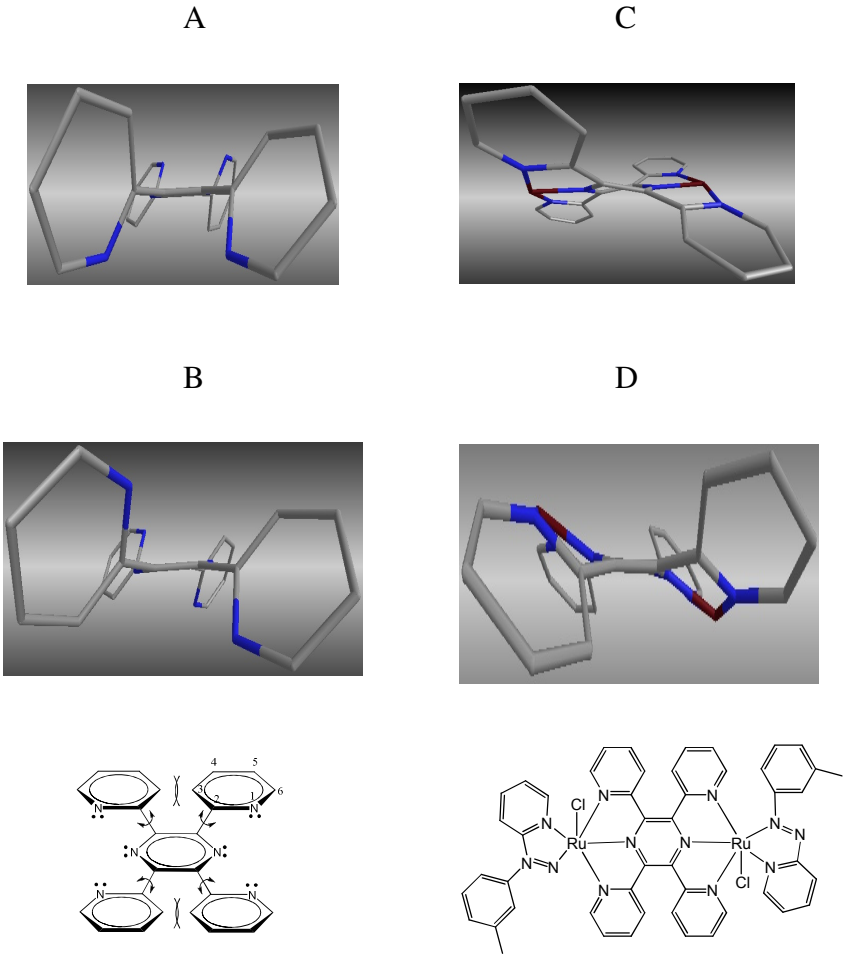

Figure 1.21. The illustration of the two conformations observed in the crystal structures of free tppz ligand (A, B) and binuclear ruthenium complex, $[(L)ClRu(\mu\text{-tppz})RuCl(L)]^{2+}$, (L = arylazopyridine), exhibiting saddle-like geometry (C), and chair-like geometry (D), L and Cl are omitted for clarity.

1.10.1 Binding Modes of tppz

Since the discovery of the tppz ligand, the observed properties have stimulated extensive research on the utilization of tppz as proton sponge[173] fluorescence sensors,[190-191] molecular wire,[45, 192-193] ferroelectrics,[194] magnetics,[177] charge separators,[32] and BL on supramolecular assemblies.[1]

Upon complexation, the deformations of the pyrazine ring play an important role in reducing steric crowding between neighboring H^3 atoms on the pyridine rings.[175-177] Due to the flexible orientation of the four pyridine rings and multiple binding sites, the tppz ligand is shown to coordinate to metals in a variety of unusual coordination environments, highlighted in a review by Pennington.[176]

For chelating purpose, the nitrogens of the rings participating in the coordination have to adopt a cis-conformation via rotation of the C-C single bonds connecting the ring systems. The steric hindrances arising from the formed rotation of the pyridine rings to allow simultaneous complexation to multiple N atoms leads to the tppz distortion from planarity to relieve steric crowding. A diversity of binding modes of the tppz has been identified and characterized.

Many conformations of the tppz metal complexes have been confirmed by X-ray crystallography. In the tridentate binding mode, there are three basic binding coordinations observed, M(tppz), $M(tppz)_2$, and $M_2(\mu\text{-tppz})$ (**Figure 1.22**). The forms of M(tppz) and $M(tppz)_2$ exhibit similar structures as $M_2(\mu\text{-tppz})$, in which tppz adopts two conformations: the saddle-like and chair-like geometries (**Figure 1.21 C & D**). Interestingly, these two conformations can exist in one unit cell of a binuclear ruthenium complex, $[(L)ClRu(\mu\text{-tppz})RuCl(L)]^{2+}$, where L is an arylazopyridine ligand.[178] In the saddle-like configuration, the mutually trans pair of pyridyl rings are twisted in the same sense towards one side of the pyrazine ring.[179-180] By contrast, in chair-like symmetry, the pyridine rings bow out of the pyrazine ring plane, like the free ligand's conformation II.[181-184] In both of these structures of $[(L)ClRu(\mu\text{-tppz})RuCl(L)]^{2+}$, the distortions from the four pyridine rings are offset to make the pyrazine closer to planarity (minimal distortion from planarity).

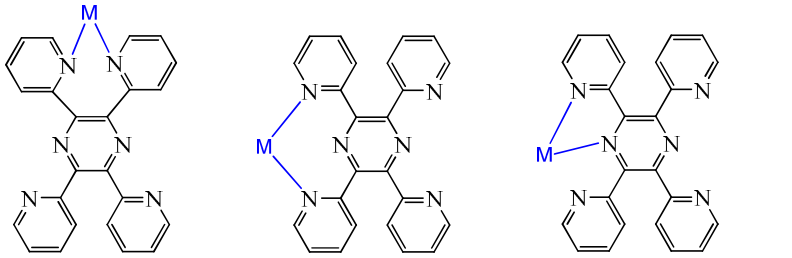

α β γ

η^2 – binding modes:

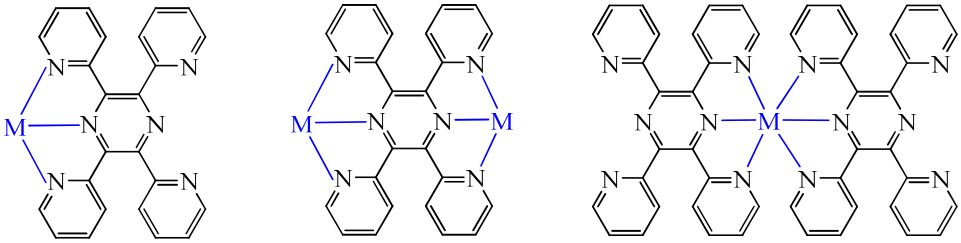

M(tppz) $M(tppz)_2$ $M_2(\mu\text{-tppz})$

Tridentate modes

Figure 1.22. Scheme of the multiple binding modes for tppz as the bidentate and tridentate ligand, Ref.[175]

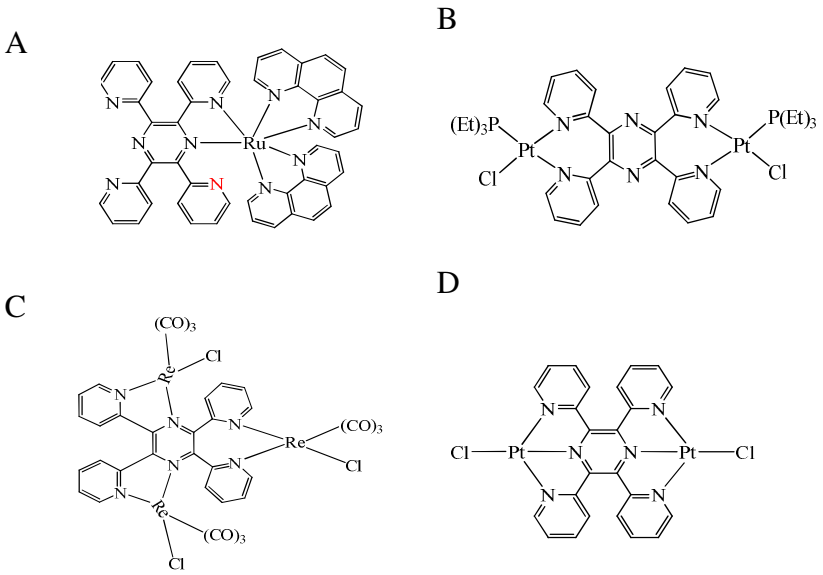

Figure 1.23. Example of the multiple binding modes for tppz as the bidentate and tridentate ligand in the complexes of $[(phen)_2Ru(tppz)]^{2+}$, $[(tppz)Pt_2(PEt_3)_2Cl_2]^{2+}$ $[(tppz)Re(CO)_9Cl_3]$ and $[ClPt(tppz)PtCl]^{2+}$, Ref.[185-187, 189]

The ligand tppz can have three possible bidentate binding modes: α,[185-187] β,[188] and γ[186] as shown in **Figure 1.22**, or a mixture of them to have bis-, and tris-bidentate coordination configurations. These biding modes have been observed in the complexes of $[(phen)_2Ru(tppz)]^{2+}$ $[(tppz)Pt_2(PEt_3)_2Cl_2]^{2+}$ and $[(tppz)Re(CO)_9Cl_3]$ as illustrated in **Figure 1.23 (A), (B) and (C)**, respectively.

The ligand tppz also can adopt various binding modes on the same metal centers, which have been structurally confirmed for some metal complex in the solid state. For the square planar coordination Pt, the ligand tppz in $[Cl(PEt_3)Pt(\mu\text{-}tppz)(PEt_3)Cl]^{2+}$[185] (**Figure 1.23 B**) and $[ClPt(\mu\text{-}tppz)PtCl]^{2+}$,[189] (**Figure 1.23 D**) exhibited bis(bidentate) and bis(tridentate) in a μ fashion, respectively. The variety of binding modes of tppz make it critical that assumptions are not made concerning binding modes in metal complexes but rather carefully probed as unexpected coordination is often encountered.

1.10.2 Chirality in Complexes of tppz

Chirality arising from structure variations of tppz has been mentioned but not yet characterized.[172, 176] Molecules with a helical structure can be described as right-handed (P) if it resembles a screw that rotates clockwise away from the viewer or as left-handed (M) if the rotation is counterclockwise (**Figure 1.24**). Helical chirality can also be present in the metal complex containing two or more bidentate ligands. The assignment of this chirality of complexes uses Δ as the right handed configuration, and Λ as the left-handed configuration. The universal chiarlity descriptors were summarized by Brown as two systems: 1) Steering-wheel system, and 2) Skew-line system.[195-196] The skew-line convention is recommended by IUPAC as the chirality namenclature if the CIP (Cahn-Ingold-Prelog) priority rules cannot apply.[197-198] In metal complexes, two skew lines are the projections of the two planar chelating rings or non-planar chelating rings. The Δ/Λ descriptors of the chirality are for the two or three bidentate ligands bound to a metal, and the P/M descriptor can feature the helical chirlaity resulting from the different components in one molecule.[199] The skew-line descriptor of the chiral complex is illustrated in **Figure 1.24**.[200]

The restriction of rotation of pyridine rings by complexation could render stable stereoisomer for tppz metal complexes. As Goodwin mentioned, in the mono-tridentate tppz binding mode, the two uncomplexed pyridine rings could be on the same side or opposite side of the pyrazine plane when tppz attached to a four-covalent metal atoms (like Pt^{II}). The former conformation (chair-like) has a plane of symmetry. While the latter (saddle-like) have a diad axis of symmetry, resulting in two enantiomorphous configurations (**Figure 1.25 A & B**).[172] It is worthwhile to point out the complexes with the $[M_1(tppz)M_2]$ entities would also possess possible stereoisomers no matter whether the two metal ions are same or not. Although such arrangements of tppz have been structurally observed in solid single crystals, little discussion this chiarlity has been presented. Our work will uncover chiral tppz metal complexes with significant barriers to interconversion in fluid solution.

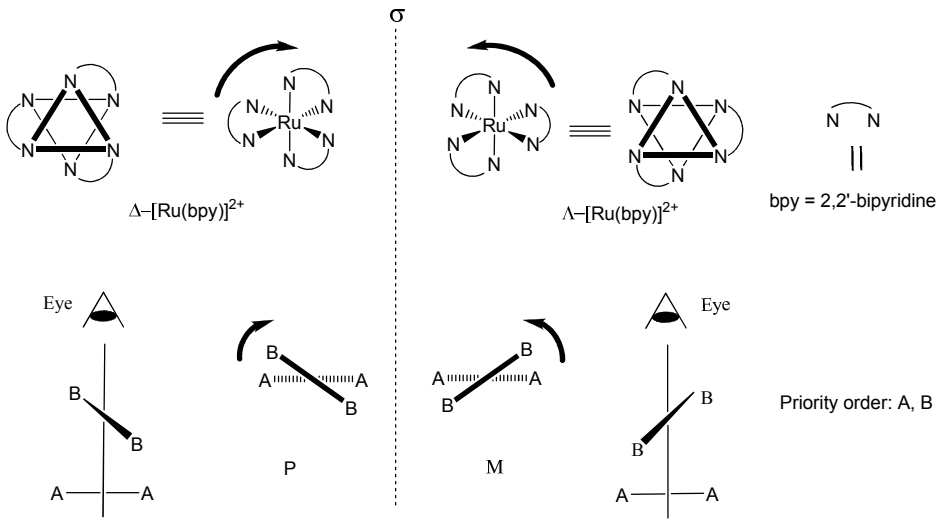

Figure 1.24. The skew-line chirality descriptors with Δ/ Λ for the mononuclear complex, and P/M for the charility arising from the molecular components in a polynuclear complex. Ref.[200]

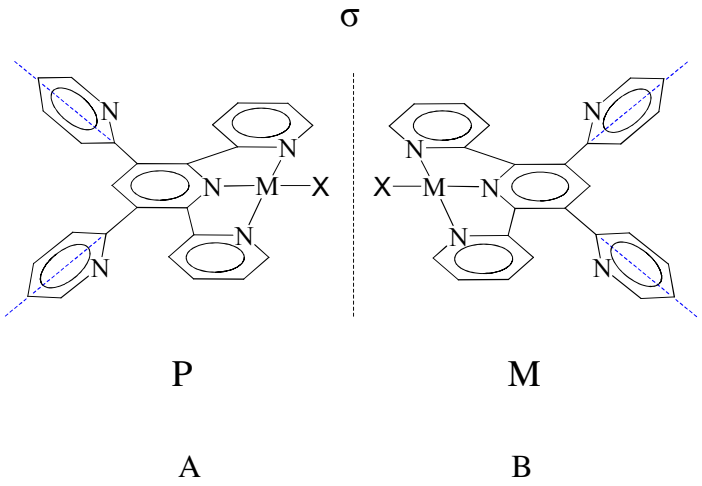

Figure 1.25. Illustration of the P and M geometries of the screw chiarlity in square planar coordinated tppz. Ref.[172]

1.11 Applications: DNA-Metal Complex (MC) Interactions

1.11.1 Structure of DNA

DNA, or deoxyribonucleic acid, is a biological macromolecule made of four different monomers. Each monomer unit, called a nucleotide, consists of a phosphate group, a 2'-deoxyribose (a 5-carbon sugar), and one of four bases: thymine (T), cytosine (C), adenine (A), 0r guanine (G). Within the monomer, the 5' and 3' carbons are attached to the phosphate group on either side. The phosphate on the 5' carbon of deoxyribose is linked to the 3' carbon of the next deoxyribose. This lends a 5' and 3' directionality to the DNA strand. The joining of two complementary single strands of DNA through hydrogen bonding to form a double-stranded DNA is called hybridization. The two strands of a DNA double helix are arranged in opposite or anti-parallel directions, so that one strand is 5'-3' and the complementary strand is 3'-5', as illustrated in **Figure 1.26**. The bases form a π-stack thought to enable electron transfer through DNA.[201] The DNA helical structure is an example of the many chiral systems in biology.

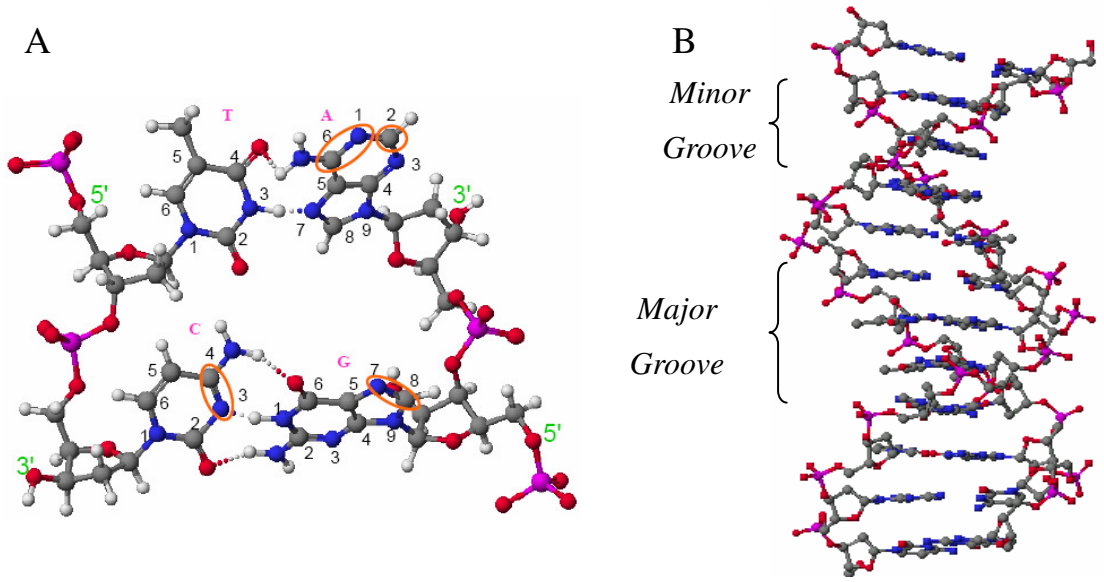

Figure 1.26. Watson–Crick base pairs of the DNA and their electroactive sites (A), and the helix of the double stranded DNA (B)

1.11.2 Binding Modes

The properties mentioned above enable DNA to interact with metal complexes. The interactions between metal complexes and DNA are generally distinguished as four modes: external or ionic binding, groove binding, intercalation and covalent binding. The external or ionic binding involves electrostatic interaction between the positively charged metal complex and the negatively charged phosphate sugar backbone of the DNA molecule. The luminescence enhancement of the complex of $[Ru(bpy)_3]^{2+}$ (bpy = 2, 2´-bipyridine) upon binding to DNA via an electrostatic mode is strongly dependent on the ionic strength. Cations like Mg^{2+} electrostatically bind DNA in this way. Groove binding is the approach of a metal complex within van der Waals contact and in the DNA grooves, Geometric and steric factors of the complex play an important role during groove binding to DNA. Intercalation is insertion of a complex with a planar ligand between the DNA base pairs and is thus less sensitive to ionic strength relative to the two other binding modes. The process of the intercalation is favored by the presence of an extended fused aromatic ligand in the complex, e. g $[Ru(phen)_2(PHEHAT)]^{2+}$ (phen = 1, 10-phenanthroline, PHEHAT = 1, 10-phenanthrolino[5, 6-b]1, 4, 5, 8, 9, 12-hexaazatriphenylene).[202] Covalent binding of the metal complex to DNA enables the best control of orientation and selectivity. Most of the antitumor platinum complexes such as cisplatin (cis-$[(NH_3)_2PtCl_2]$) bind to DNA in this way.

1.11.3 Binding to DNA

The anti-tumor activity of cisplatin was discovered serendipitously by Rosenberg in 1965.[203-204] Cisplatin was clinically approved for cancer treatment in 1978. Cisplatin coordinates with DNA mainly through the N-7 atom of guanine and adenine, illustrated via X-ray crystallography.[205-208] Interaction of cisplatin with DNA occurs in two steps through the positive charged aquated intermediate. The first step involves the replacement of one chloride atom by water to form the mono aqua species with one positive charge, which can bind to either a single adenine or guanine bases of DNA. Monofunctional binding is followed by hydrolysis of the second chloride and binding to a nearby purine base to form an intrastrand cross-link or to a purine base to form an

interstrand cross-link on its complementary DNA strand. The dominant intrastrand crosslink is believed to be responsible for cisplatin's antitumor actions. During this process, the square planar Pt^{II} covalently binds to DNA.[209] The success of cisplatin as an anti-cancer agent has given rise to a new field of analog research aimed at overcoming the limitations of drug resistance and toxic side effects. The general strategy has been to develop cisplatin analogs that have a better therapeutic index than cisplatin by reducing side effects and/or increasing potency.[211-212] New metal complexes with multiple bioactive sites have also been exploited as potential antitumor agents, as reviewed by Zaleski et al.[213]

The mechanism of cisplatin-DNA interaction provides guidelines for the rational design of other metallic anti-tumor agents.[210] Brewer's group has conduct extensive research to develop a new class of cisplatin antitumor agents coupled with Ru^{II} chromophore.[117, 121-124] A series of metal complexes with cis-$PtCl_2$ moiety have been investigated with the form $[(bpy)_2Ru(BL)PtCl_2]^{2+}$ or $[(tpy)RuCl(BL)PtCl_2]^{+}$ (BL = bidentate bridging ligand). Complexes of the formula, $[(bpy)_2Ru(BL)PtCl_2]^{2+}$, bind to DNA through the cis-$PtCl_2$ or intercalate into DNA through the BL.[117] The labile Cl ligands enable the covalent binding of these complexes to DNA. The positive charges imparted by the Ru^{II} lead a greater binding of these complexes to DNA compared to cisplatin. Complexes of the formula, $[(tpy)RuCl(BL)PtCl_2]^{+}$, exhibit avidly bind with DNA.[121, 124] Brewer et al have reported a tetrametallic $Ru^{II}Pt^{II}$ complex which photocleaves DNA via $^1O_2$ mediated pathway.[123]

Although many bidentate Pt^{II} complexes have been synthesized for DNA binding study, the search continues for tumor specific agents with higher efficiency and lower side effects relative to the cisplatin.

Planar tridentate Pt complexes can bind to DNA either by covalent attachment, ionic interactions, or intercalation. The tridentate Pt^{II} complex, $[(tpy)Pt^{II}Cl]$, has been reported to intercalate between the DNA base pairs through π-π stacking. The crystallographic unit contains two molecule of $[(tpy)PtCl]^{+}$ and a hydrogen-bonded (adenosine-5'-monophosphate) AMP base pairs. The two $[(tpy)PtCl]^{+}$ cations are intercalated between the base pair, which in turn are stacked on one another in the crystal lattice (**Figure 1.27**).[214] Another metallointercalator, $[(tpy)Pt(HET)]Cl$[215] (HET = 2-

hydroxyethanethiolate) can unwind the deoxycytidyyl-(3',5')-deoxyguanosine (deoxy CpG) antiparallel double helix. The interaction between deoxy CpG. and a mixed metallic complex, $[(tpy)Ru(dtdeg)PtCl]Cl_3$[216] (dtdeg = bis[4-(2,2′:6,2″-terpyridyl)]diethylenglycol), are reported covalently binds to DNA by Pt due to labilization of the Cl group.

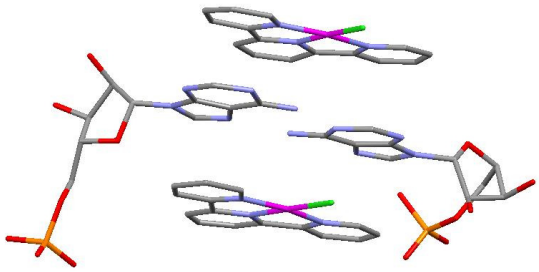

Figure 1.27. Representation of the intercalation of tridentate Pt complex, $[(tpy)PtCl]^+$ into DNA bases.

Incorporating of the Ru^{II} photosensitizer to a bioactive Pt site allows for the development of supramolecules as the antibacterial compounds with multiple binding modes. This design provides a means to deliver the Ru^{II} chromophore to the DNA target. The spectroscopic and redox properties of the designed complexes play an important role to understand the mechanism during the DNA binding or DNA photocleavage.

1.12 Statement of Problem

The primary goal of this research is to investigate the redox and optical properties of mixed-metal Ru^{II},Pt^{II} supramolecules bridged by a tridentate polypyridyl ligand, tppz (tppz = 2,3,5,6-tetrakis(2-pyridyl)pyrazine). This involves the development of methods to synthesize, identify and characterize such complexes as well as the study of their electrochemical, photophysical, photochemical properties and potential biological activities.

Chapter 2: Experiments: Materials, Syntheses and Measurements

2.1 Materials

$RuCl_3 \cdot xH_2O$ (Alfar Aesar), K_2PtCl_4 (Alfar Aesar), 2,2′:6′,2″-terpyridine (tpy) (Aldrich), 2,3,5,6-tetrakis(2-pyridyl)pyrazine (tppz) (Aldrich), (NH_4PF_6) (Alfar Aesar), tetrabutylammonium hexafluorophosphate (Bu_4NPF_6) (Fluka), spectral and ACS grade acetonitrile, and toluene NH_4PF_6, K_2PtCl_4 (Alfar Aesar), 2,2′:6′,2″-terpyridine (tpy, Aldrich), Ethidium bromide, bromophenol blue, xylene cyanol, 2,3,5,6-tetrakis(2-pyridyl)pyrazine (tppz, Aldrich), Bu_4NPF_6 (Fluka), spectral grade acetonitrile (Burdick and Jackson) were all used without further purification.

Electrophoresis grade boric acid, agarose, molecular biology grade tris(hydroxymethyl)aminomethane, and glycerol were all obtained from Fisher Scientific (Pittsburgh, PA). Plasmid (pUC18) DNA was purchased from Bayou Biolabs (Harahan, LA). Lambda DNA/Hind III molecular marker was obtained from Promega (Madison, WI).

2.2 Syntheses

$[Ru(tppz)_2](PF_6)_2$,[27] $[(tpy)Ru(tppz)](PF_6)_2$[30] and $[PtCl_2(DMSO)_2]$[217] were prepared as the precursors to obtain the two new complexes. The other complexes: $[(bpy)_2RuCl_2]$,[218] $[Ru(tpy)Cl_3]$,[219] $[Ru(tpy)_2](PF_6)_2$,[220] $[(tpy)Ru(tppz)Ru(tpy)](PF_6)_3$ $[(tpy)Ru(tppz)Ru(tppz)Ru(tpy)](PF_6)_6$ were prepared by modification of the published methods, and served as control complexes to more clearly understand the results of studies of the title $[(tpy)Ru(tppz)PtCl](PF_6)_3$ and $[ClPt(tppz)Ru(tppz)PtCl](PF_6)_4$ complexes.

2.2.1 Synthesis of [(tpy)$RuCl_3$]

The [(tpy)$RuCl_3$] was made by reacting $RuCl_3 \cdot 3H_2O$ (10 mmol, 2.6 g) with tpy (10 mmol, 2.2 g) with stoichiometry ratio, stirring at reflux in 200 mL absolute ethanol under argon for 4 hrs as previously reported.[219] The solid was separated by vacuum filtration washed with ethanol (3 X 30 mL), deionized (DI) water (3 X 30 mL) and dried under vacuum with a typical yield of 89%. The product served as starting material to prepare $[Ru(tpy)_2](PF_6)_2$, $[(tpy)Ru(tppz)](PF_6)_3$, $[(tpy)Ru(tppz)Ru(tpy)](PF_6)_3$, $[(tpy)Ru(tppz)Ru(tppz)Ru(tpy)](PF_6)_3$ and $[(tpy)Ru(tppz)PtCl](PF_6)_3$.

2.2.2 Synthesis of $[Ru(tpy)_2](PF_6)_2$

$[Ru(tpy)_2](PF_6)_2$ was prepared by a modification of the published method.[220] The mixture of $RuCl_3 \cdot 3H_2O$ (1.0 mmol, 0.26 g) and tpy (2.5 mmol, 0.55 g) with 1:2.5 equivalent was heated at reflux under Ar in 1:1 (v/v) ethanol/water for 12 hrs. The resulting yellow solution was allowed to cool using ice-water and filtered to remove the unreacted tpy. Upon addition of 30 mL 4.0 M aqueous ammonium hexafluorophosphate, the yellow precipitate that formed was collected by vacuum filtration, rinsed with water (4 X 20 mL) and dried under vacuum. ^{1}H-NMR (500 MHz in CD_3CN, δ in ppm (J in Hz), J in Hz): 8.74 (J = 7.5 4H), 8.41 (J = 8.0, 2H), 8.49 (J = 8.0, 4H), 7.91 (J = 8.0, 4H), 7.16 (J = 6.0, 4H), 7.34 (J = 5.0, 4H).

2.2.3 Synthesis of $[(tpy)Ru(tppz)](PF_6)_2$

The building block approach was utilized to synthesize $[(tpy)Ru(tppz)](PF_6)_2$. For our work a modification of the published procedure was performed.[43, 221] To a solution of [(tpy)$RuCl_3$] (0.31 g, 0.67 mmol) in 50 mL 95% ethanol was added tppz (1.10 g, 2.84 mmol) in the presence of 3.0 mL triethylamine. The mixture was heated at reflux for 6 hrs under argon atmosphere. The resulting solution was cooled and filtered. The crude product was then precipitated with 4.0 M aqueous ammonium hexafluorophosphate, vacuum filtered, washed with water (3 X 20 mL), and dried by washing with diethyl ether (3 X 20 mL). The solid was purified via column chromatography (40 mm X 15 cm) on

neutral alumina with 1:1 (v/v) toluene/acetonitrile as the eluant. The orange band was collected and concentrated by rotary evaporation, followed by the purple band, which is the product of $[(tpy)Ru(tppz)Ru(tpy)](PF_6)_4$. The resulting products were then dissolved in a minimum amount of acetonitrile and flash precipitated by addition to stirring diethyl ether. The final product was obtained by vacuum filtration and vacuum drying. The typical yield is 55% (0.37 g, 0.37 mmol). ^{1}H-NMR (500 MHz in CD_3CN at RT) of $[(tpy)Ru(tppz)](PF_6)_2$: δ in ppm (*J* in Hz), 8.80 (*J* = 8.5, 2H), 8.50 (*J* = 8.3, 1H), 8.53 (*J* = 8.0, 2H), 7.97 (*J* = 8.0, 6.8, 1.2, 2H), 7.24 (*J* = 7.5, 6.0, 1.0, 2H), 7.59 (*J* = 6.0, 1.0, 2H), 8.36 (*J* = 7.5, 1.8, 2H), 8.24 (*J* = 8.0, 6.5, 1.7, 2H), 7.74 (*J* = 7.8, 6.8, 1.7, 2H), 8.73 (*J* = 5.0, 2.0, 2H), 7.51 (*J* = 8.0, 1.0, 2H), 7.60 (*J* = 8.0, 6.0, 1.8, 2H), 7.13 (*J* = 7.8, 6.3, 1.5, 2H), 7.40 (*J* = 5.5, 1.5, 2H), FAB-MS [m/z]:calculated $(M\text{-}PF_6)^+$: 868. This compound is used to make the new mixed Ru^{II},Pt^{II} bimetallic complex, $[(tpy)Ru(tppz)PtCl](PF_6)_3$.

2.2.4 Synthesis of $[Ru(tppz)_2](PF_6)_2$

$[Ru(tppz)_2](PF_6)_2$ was prepared by a modification of the previously published procedure.[27] A mixture of tppz (190 mg, 0.50 mmol) and $RuCl_3$ (410 mg, 0.20 mmol) in 60 mL 95% ethonol was heated at reflux under argon overnight. The compound was precipitated by 4.0 M aqueous ammonium hexafluorophosphate and separated by vacuum filtration. The product was chromatographed on adsorption alumina using 3:2 (v/v) toluene/actonitrile as the eluent. The desired product was eluted as an orange band, followed by the purple band, which is likely the product of $[Ru_2(tppz)_3](PF_6)_4$. The orange band compound was recovered and concentrated by rotary evaporation, dissolved in a minimum amount of acetontrile and flash precipitated by addition to a vigorous stirring solution of diethyl ether. Final product was separated by filtration and dried under vacuum. The yield for this complex is 35% (0.081 g. 0.071 mmol). ^{1}H-NMR (500 MHz in CD_3CN) of $[Ru(tppz)_2](PF_6)_2$: δ in ppm (*J* in Hz), 8.38 (*J* = 8.0, 4H), 8.27 (*J* = 8.4, 6.9, 1.4, 4H), 7.78 (*J* = 7.8, 2.0, 4H), 8.76 (*J* = 5.0, 4H), 7.63 (*J* = 7.5, 4H), 7.66 (*J* = 8.0, 4H), 7.22 (*J* = 6.0, 4H), 7.67 (*J* = 5.0, 4H). FAB-MS [m/z]: calculated $(M\text{-}PF_6)^+$: 1023.

2.2.5 Synthesis of $[(tpy)Ru(tppz)Ru(tpy)](PF_6)_3$

The synthesis of $[(tpy)Ru(tppz)Ru(tpy)](PF_6)_3$ was achieved by a building block method via a modification of the published procedure.[27] The precursor $[(tpy)Ru(tppz)](PF_6)_2$ (0.10 g, 0.10 mmol) and the $[(tpy)RuCl_3]$ (0.18 g, 0.40 mmol) were mixed into 60 mL ethylene glycol and heated at reflux for 48 hrs under an argon atmosphere in the presence of triethylamine (0.11 mL, 0.80 mmol). The initial orange black solution gradually changes to purple. The solution was then removed from the heat and 4.0 M aqueous ammonium hexafluorophosphate (100 mL) was added to induce precipitation. The solid product thus obtained was filtered and wash thoroughly by ethanol, diethyl ether and ice-cold water. The sample is obtained by recrystallization via CH_3CN/Et_2O by slow diffusion. Yield: 87% (0.14 g, 0.091 mmol).

2.2.6 Synthesis of $[(tpy)Ru(tppz)Ru(tppz)Ru(tpy)](PF_6)_3$

$[(tpy)Ru(tppz)Ru(tppz)Ru(tpy)](PF_6)_3$ has been prepared previously by Abruna's group following a different synthetic procedure.[27] A similar procedure was applied to the synthesis of $[(tpy)Ru(tppz)Ru(tpy)](PF_6)_3$. Specifically, $[Ru(tppz)_2](PF_6)_2$ (0.12 g, 0.10 mmol), $[(tpy)RuCl_3]$ (0.37 g, 0.80 mmol), triethylamine (0.22 mL, 1.60 mmol) were added into 60 mL ethylene glycol and refluxed for three days under argon atmosphere. The reaction solution goes from a black to a reddish color. To this was added a 4.0 M aqueous ammonium hexafluorophosphate (100 mL) with stirring to form precipitate as the PF_6^- salt. The precipitate was collected by vacuum filtration, followed by rinsing with ice-cold water and diethyl ether. The solid sample is recrystallized from CH_3CN/Et_2O. Yield: 73% (0.18 g, 0.071 mmol).

2.2.7 Synthesis of $[(tpy)Ru(tppz)PtCl](PF_6)_3$

The complex $[(tpy)Ru(tppz)PtCl](PF_6)_3$ was prepared by dropwise addition of $[(tpy)Ru(tppz)](PF_6)_2$ (51 mg, 0.050 mmol) in CH_3CN (*ca*. 10 mL) to a solution of $[Pt(DMSO)_2Cl_2]$ (84 mg, 0.40 mmol) in CH_3CN (*ca*. 10 mL) under an Ar atmosphere.[221] The reaction mixture was heated at reflux for *ca*. 4 h under Ar, cooled to RT, vacuum filtered, and added dropwise to an aqueous solution of 4.0 M NH_4PF_6 (*ca*. 50 mL). The

violet product which precipitates upon addition to aqueous NH_4PF_6 was collected by vacuum filtration and washed with EtOH (*ca*. 20 mL), distilled H_2O (*ca*. 10 mL at 0 °C), and diethyl ether (50 mL). The product yield is 76% (0.05 g, 0.04 mmol). ^{1}H NMR (500 MHz in CD_3CN): δ in ppm (*J* in Hz), 9.45 (*J* = 5.5, 1.5 Hz, 2H), 8.87 (*J* = 8.5 Hz, 2H), 8.86 (*J* = 8.5, 1.0 Hz, 2H), 8.74 (*J* = 8.0, 1.0 Hz, 2H), 8.63 (*J* = 7.8 Hz, 1H), 8.56 (*J* = 7.5 Hz, 2H), 8.43 (*J* = 8.0, 6.3, 1.7 Hz, 2H), 8.11 (*J* = 7.8, 5.0, 1.3 Hz, 2H), 8.01 (*J* = 8.5, 7.0, 1.3 Hz, 2H), 7.99 (*J* = 7.8, 6.3, 1.5 Hz, 2H), 7.66 (*J* = 6.3, 1.0 Hz, 2H), 7.48 (*J* = 6.2, 1.0 Hz, 2H), 7.44 (*J* = 7.8, 6.8, 1.5 Hz, 2H), 7.17 (*J* = 7.8, 6.3, 1.5 Hz, 2H); ^{195}H-NMR, δ_{Pt} = -2579 ppm at 600 MHz in CD_3CN vs. K2PtCl4 δ_{Pt} = -1613 ppm at 600 MHz in D_2O; FAB-MS [m/z]:calculated $(M\text{-}PF_6)^+$: 1243. FAB-MS spectrum is attached in **Appendix, Figure A.1**. The structure of this complex was confirmed by X-ray crystallography analysis.

2.2.8 Synthesis of $[ClPt(tppz)Ru(tppz)PtCl](PF_6)_4$

Using a similar approach to the synthesis of $[(tpy)Ru(tppz)PtCl](PF_6)_3$, the complex $[ClPt(tppz)Ru(tppz)PtCl](PF_6)_4$ was prepared by dropwise addition of $[Ru(tppz)_2](PF_6)_2$ (72 mg, 0.062 mmol) in CH_3CN (*ca*. 10 mL) to a refluxing solution of $[Pt(DMSO)_2Cl_2]$ (210 mg, 0.50 mmol) in CH_3CN (*ca*. 10 mL).[221] The reaction mixture was heated at reflux for 4 h under an Ar atmosphere, cooled to RT, filtered, and added dropwise to an aqueous solution of 4.0 M NH_4PF_6 (*ca*. 50 mL). The violet product which forms upon addition to aqueous NH_4PF_6 is collected by vacuum filtration and washed with EtOH (*ca*. 20 mL), distilled H_2O (*ca*. 10 mL at 0 °C), and diethyl ether (50 mL). The product yield is 82% (0.097 g, 0.051 mmol). ^{1}H NMR (500 MHz in CD_3CN): δ in ppm (*J* in Hz), 9.50 (*J*= 5.5 Hz, 4H), 8.90 (*J* = 8.5 Hz, 4H), 8.77 (*J* = 8.0 Hz, 4H), 8.48 (*J* = 7.8 Hz, 4H), 8.18 (*J* = 6.5 Hz, 4H), 8.06 (*J* = 8.5 Hz, 4H), 7.85 (br, 4H), 7.50 (br, 4H); ^{195}H-NMR, δ_{Pt} = -2500 ppm at 600 MHz in CD_3CN vs. K2PtCl4 δ_{Pt} = -1613 ppm at 600 MHz in D_2O; FAB-MS [m/z]:calculated $(M\text{-}PF_6^+)$: 1772. FAB-MS spectrum is attached in **Appendix, Figure A.2**. This complex was crystallized from toluene/nitromethane and analyzed by single crystal X-ray crystallographic analysis.

2.3 Measurements

2.3.1 Mass Spectrometry

Mass spectrometry is a powerful technique to characterize the composition of the molecule with high specificity and resolution. Fast atom bombardment mass spectrometry (FAB-MS) and electrospray ionization mass spectrometry (ESI-MS) are applied to study the synthesized molecules.

FAB-MS was performed by M-Scan Incorporated, West Chester, Pennsylvania, on a VG Analytical ZAB 2-SE high field mass spectrometer using *m*-nitrobenzyl alcohol as a matrix. The sample was prepared in CH_3CN and infused into a capillary with a 5 mL/min flow rate.

ESI-MS was carried out on a Micromass VG Platform. The mass spectrometer was equipped with a thermal pneumatic nebulizer and single quadrupole analyzer. The mass spectrometer was operated in the ESI positive ion mode with a source temperature at 110 °C. The nebulizer gas flow is 20 L/hr and the dry gas flow is 400 L/hr. In order to obtain good sensitivity, the cone voltage can be tuned along the standard value of 30 V. ESI-MS provides the profile of multiply charged gas-phase ions by using a soft-ionization technique, in which noncovalent features of the molecules can be maintained. Therefore, a series of multiple charged states can be observed in ESI-MS for molecules with non-covalent bonds, e.g. hydrogen bond, electrostatic attraction, or π···π stacking.[222-225] Taking into account the phase transferring effects of the analytes from solvent to gas state upon ionization, ESI-MS data can still monitor the thermodynamic equilibrium of non-covalent molecular interactions in solution.[226] ESI-MS has been utilized to investigate the self-assembling of supramolecules through metal-ligand bonds,[95c] dimerization of protein via hydrogen bond,[227] and self-association of individual molecules driven by electrostatic forces [228] in organic and aqueous solutions.

2.3.2 Crystallography

[(tpy)Ru(tppz)PtCl](PF$_6$)$_3$ and [ClPt(tppz)Ru(tppz)PtCl][PF$_6$]$_4$ were crystallized by vapor diffusion. A solution of the sample was prepared using a good solvent in a small vial. This small vial was then placed in a sealed big vial with a poor solvent. The sample is more soluble in the good solvent than in the poor solvent. Thus the crystal may form when the good solvent slowly diffuse into the big vial.

X-ray crystallography was performed by Prof. Carla Slebodnick at the Chemistry Department of Virginia Tech. Shengliang Zhao acknowledges her hard work to screen multiple crystals to allow us to report the first two mixed-metal Ru^{II},Pt^{II} complexes of [(tpy)Ru(tppz)PtCl](PF$_6$)$_3$ and [ClPt(tppz)Ru(tppz)PtCl][PF$_6$]$_4$ bridged by tppz BL.[221]

2.3.2.1 X-Ray Diffraction of [(tpy)Ru(tppz)PtCl](PF$_6$)$_3$

Black parallelepipeds of [(tpy)Ru(tppz)PtCl][PF$_6$]$_3$ were crystallized from toluene/CH_3NO_2. The chosen crystal (0.09 x 0.15 x 0.25 mm^3) was centered on the goniometer of an Oxford Diffraction Gemini diffractometer equipped with a Sapphire 3 CCD detector and operating with MoKα radiation. The data collection routine, unit cell refinement, and data processing were carried out with the program CrysAlisPro.[229] The Laue symmetry and systematic absences were consistent with the monoclinic space group *Cc* and *C*2/*c*. The centric space group *C*2/*c* was chosen. The structure was solved by direct methods and refined using SHELXTL NT.[230] The asymmetric unit of the structure comprises one crystallographically independent [(tpy)Ru(tppz)PtCl][PF$_6$]$_3$ salt. After locating the [(tpy)Ru(tppz)PtCl][PF$_6$]$_3$, residual electron density in remaining void spaces suggested the presence of disordered solvent. Various attempts were made to model or correct for this disorder, including multi-position solvent disorder and running the PLATON routine SQUEEZE[231] to subtract out the solvent electron density. With most models used, the goodness-of-fit suggested we were overfitting the data, yet the refinement model did not improve substantially. In the final refinement, the solvent was modeled as a toluene disordered over 2 positions with relative occupancies of 74(2)% and 26(2)%. The phenyl ring of the toluene molecule was restrained to fit a hexagon. The

toluene atoms were refined isotropically; all remaining non-hydrogen atoms were refined anisotropically and a riding model was used for all hydrogen atoms.

2.3.2.2 X-Ray Diffraction of $[ClPt(tppz)Ru(tppz)PtCl](PF_6)_4$

Black plates of $[ClPt(tppz)Ru(tppz)PtCl][PF_6]_4$ were crystallized from CH_3CN/Et_2O. The chosen crystal (0.01 x 0.11 x 0.29 mm^3) was centered on the goniometer of an Oxford Diffraction Gemini diffractometer equipped with a Sapphire 3 CCD detector and operating with MoKα radiation. The data collection routine, unit cell refinement, and data processing were carried out with the program CrysAlisPro.[229] The Laue symmetry and systematic absences were consistent with the monoclinic space group $P2_1/c$. The structure was solved by direct methods and refined using SHELXTL NT.[230] The asymmetric unit of the structure comprises one crystallographically independent $[ClPt(tppz)Ru(tppz)PtCl][PF_6]_4$ salt. After locating the $[ClPt(tppz)Ru(tppz)PtCl][PF_6]_4$, residual electron density in remaining void spaces suggested the presence of disordered solvent. Various attempts were made to model or correct for this disorder, including a variety of multi-position disorder models for the ether molecule and PF_6 anions, as well as running the PLATON routine SQUEEZE[231] to subtract out the ether electron density. Regardless of the model used, the R-values tended to improve, but the anisotropic displacement parameters remained unsatisfactory. Presumably the small crystal size and potential dynamic motion in the solvents and PF_6^- limit the data quality. In the final refinement the solvent was modeled as two CH_3CN molecules and one Et_2O molecule without disorder. The Et_2O atoms were refined isotropically; all remaining non-hydrogen atoms were refined anisotropically and a riding model was used for all hydrogen atoms.

2.3.3 NMR Spectroscopy

All standard ^{1}H NMR spectra were record on JOEL 500 MHz NMR spectrometer at 298 K. All the 2D spectroscopies were performed on a Varian INOVA 400 MHz NMR spectrometer at 298 K. The samples (~5 mg) were dissolved in the CD_3CN and syringe filtered prior to placing in NMR tubes for data collection. Chemical shifts are referenced to TMS in CD_3CN.

2.3.4 Electrochemistry

Electrochemical analysis experiments are performed on the platform of Bioanalytical Systems (BAS) 100B workstation. A one-compartment, three-electrode cell was used on the measurement. The three electrodes are working electrode (Pt or glassy carbon), reference electrode (Ag/AgCl electrode) and auxiliary electrode (Pt wire). The potential of the reference electrode is 0.21 V vs. NHE , which was calibrated against the $FeCp_2/FeCp_2^+$ redox couple (0.67 V vs. NHE).[232] And the supporting electrolyte was 0.1 M Bu_4NPF_6.

2.3.5 Photochemistry

2.3.5.1 Electronic Absorption Spectroscopy

Electronic absorption spectra were generated at RT in a 1 cm quartz cuvette using a Hewlett- Packard 8452 diode array spectrometer with a 2 nm resolution and a spectral range of 190 to 820 nm. Extinction coefficients were collected in triplicate from separate solutions prepared gravimetrically and averaged.

2.3.5.2 Emission Spectroscopy

Emission spectra were recorded at RT in deoxygenated acetonitrile solutions using a modified QuantaMaster Model QM-200-45E fluorimeter from Photon Technology Inc.

The system was modified to use a 150 W water cooled xenon lamp excitation source collected at a right angle by a thermoelectrically cooled Hamamatsu 1527 photomultiplier tube operating in photon counting mode with 0.25 nm resolution.

The quantum efficiency, Φ^{em}, was determined vs. $[Os(bpy)_3](PF_6)_2$ (λ_{max}^{em} = 746 nm, Φ^{em} = 0.00462)[233] or $[Ru(bpy)_3](PF_6)_2$ (λ_{max}^{em} = 605 nm, Φ^{em} = 0.062) in absorbance matched deoxygenated solutions by choosing the closest λ_{max}^{em} and the same excitation wavelength ensure the equal amounts of photons are absorbed by the sample and reference.

Since the photomultiplier response was not equal for the whole detection region, a correction file (**Figure 2.28**) was used to obtain an accurate signal. All reported spectra are corrected for photomultipler tube (PMT) response. The emission spectra are normalized for PMT response before the quantum yield calculation. The quantum yields of the complexes reported herein were corrected for PMT response and the quantum efficiency, Φ^{em}, determined vs. $[Os(bpy)_3](PF_6)_2$ (Φ^{em} = 0.00462)[233] or $[Ru(bpy)_3](PF_6)_2$ (Φ^{em} = 0.062) in absorbance matched deoxygenated solutions.[234] The quantum yield can be calculated from the peak area ratio by the equation:

$$\Phi = \Phi_0 \times \frac{A}{A_0} \times \frac{Abs_0}{Abs}$$

Where Φ and Φ_0 is the quantum yield of the sample and the reference respectively, A and A_0 is the area under the emission peak of the sample and reference respectively, Abs and Abs_0 are the absorbance of the sample and reference respectively.

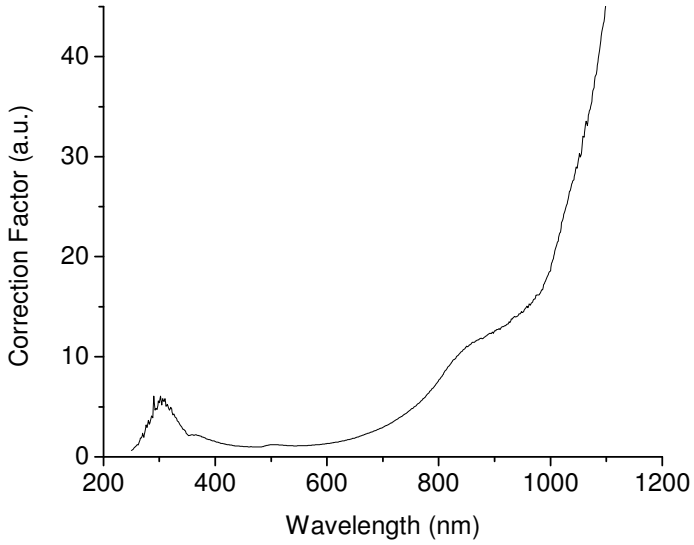

Figure 2.28. Correction files for the Hamamatsu 1527 red sensitive photomultiplier tube.

2.3.5.3 Lifetime Measurement

Laser-induced emission lifetime measurements were obtained on a system that utilizes a Photon Technology Inc. PL-2300 nitrogen laser equipped with a PL-201 continuously tunable dye laser (360-900 nm) excitation source (Coumarin 500, 490-540 nm). The emission was passed through a monochromator and detected at a right angle to the excitation by a Hamamatsu R928 photomultiplier tube operating in direct analog mode. The signal was recorded on a LeCroy 9361 oscilloscope (2.5 GSa/s) and the data transferred to a computer for analysis. The sample was dissolved in the deoxygenated solvent of CH_3CN. The raw data from the PMT response, which is an average of 200 traces, was fit to a single exponential function of the form $Y = A + B(\exp(-X/c))$, where $c = \tau = 1/k$ (in s), after discarding the initial segment of the data containing the laser pulse. All emission data fit well to a single exponential decay.

2.3.6 DNA Gel Electrophoresis

The interactions of the metal complexes with DNA were analyzed using pUC18 circular plasmid DNA employing agarose gel electrophoresis. Using *Lambda* DNA/*Hind* III as the molecular weight marker, the circular pUC18 with or without metal complex was loaded to the 0.8% agarose gel and run at 104V for 90 minutes, followed by staining with ethidium bromide for 45 minutes and destaining in ddH_2O for 30 minutes. The gels were then illuminated with a Fisher Scientific FBTI-88 transilluminator and photographed using an Olympus SP-320 digital camera equipped with an ethidium bromide filter purchased from Peca Scientific (Beloit, WI).

Concentrations of the metal complexes solutions were determined by spectroscopy using the extinction coefficients for $[(tpy)Ru(tppz)PtCl](PF_6)_3$ ($\varepsilon = 2.8 \times 10^4\ M^{-1}cm^{-1}$ at $\lambda_{max}^{abs} = 530$ nm) and $[ClPt(tppz)Ru(tppz)PtCl](PF_6)_4$ ($\varepsilon = 3.0 \times 10^4\ M^{-1}cm^{-1}$ at $\lambda_{max}^{abs} = 538$ nm).

The concentration of DNA was calculated using the absorbance reading at 260 nm by equation:[235]

$$\text{Concentration of DNA in } \mu g/mL = \text{Absorbance } @260 \cdot 50\mu g/mL \cdot (2250/15)$$

or

$$\text{Concentration of base pairs in } mol \cdot L^{-1} = \text{Absorbance}@260 \cdot 13200\ M^{-1} \cdot L\text{-}1 \cdot cm^{-1} \cdot (2250/15)$$

This equation utilizes the fact that one absorbance unit corresponds to a 50µg/mL concentration of DNA and the absorbance maximum is assumed to be 6600 $(mol \cdot L^{-1} \cdot base)^{-1} \cdot cm^{-1}$

Chapter 3. Identification and Characterization

3.1 Syntheses

The supramolecular complexes $[(tpy)Ru(tppz)PtCl](PF_6)_3$ and $[ClPt(tppz)Ru(tppz)PtCl](PF_6)_4$ have been prepared in good yield using a building block approach with coordination of the Pt center being the final step. The synthetic routes of $[(tpy)Ru(tppz)PtCl](PF_6)_3$ and $[ClPt(tppz)Ru(tppz)PtCl](PF_6)_4$ are illustrated in **Figures 3.29 and 3.30, respectively**.

The title bimetallic and trimetallic complexes, $[(tpy)Ru(tppz)PtCl](PF_6)_3$ and $[ClPt(tppz)Ru(tppz)PtCl](PF_6)_4$, were synthesized by reacting their precursors and excess $[Pt(DMSO)_2Cl_2]$ in acetonitrile under argon atmosphere. The unreacted $[Pt(DMSO)_2Cl_2]$ was removed by washing with ethanol and chloroform. The use of acetonitrile plays a critical role in the syntheses of these complexes, so that the reaction occurs in a homogenous solution. As a consequence, the overall yield of the reaction is improved significantly.

The complexes have been identified by mass spectrometry, X-ray crystallography, and ^1H NMR spectroscopy. The X-ray crystallographic analysis of these complexes confirm the structures of the $[(tpy)Ru(tppz)PtCl](PF_6)_3$ and $[ClPt(tppz)Ru(tppz)PtCl](PF_6)_4$ in the solid state. ^1H NMR spectroscopies of these complexes in solution exhibit the expected splitting pattern.

The bimetallic and trimetallic complexes are unusual in their coupling of Ru^{II} LA units to a Pt^{II} center, in which tppz coordinates to the metal centers in a μ-fashion as a bis(tridentate) BL. Such supramolecular assemblies provide a TL-LA-BL-RM (TL = terminal ligand, LA = light absorber, BL = bridging ligand, RM = reactive metal) architecture in the bimetallic complex, $[(tpy)Ru(tppz)PtCl](PF_6)_3$, and a RM-BL-LA-BL-RM architecture in the trimetallic complex, $[ClPt(tppz)Ru(tppz)PtCl](PF_6)_4$.

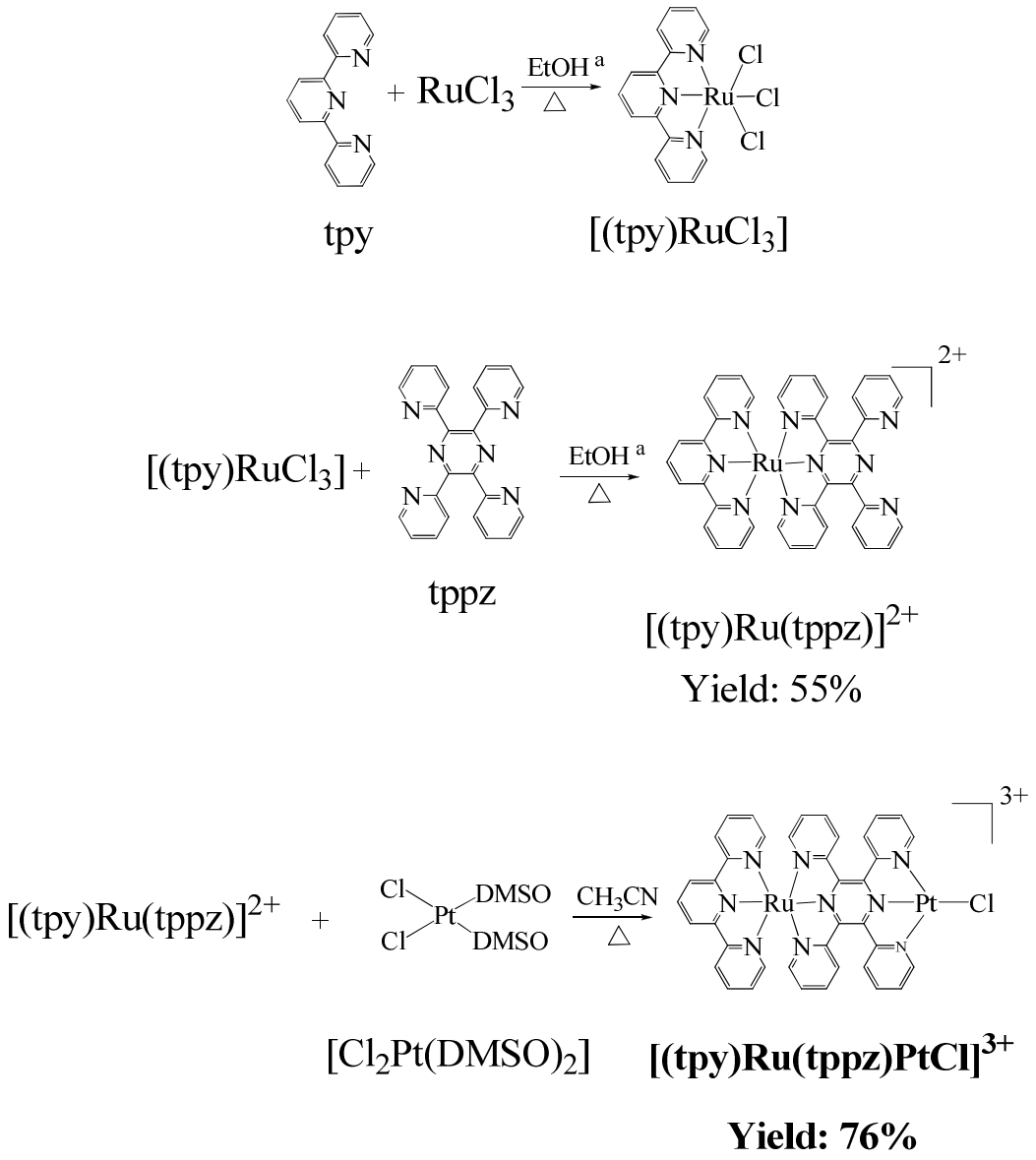

Figure 3.29. Synthetic scheme of preparing the $[(tpy)Ru(tppz)PtCl](PF_6)_3$. (tpy = 2,2′:6′,2″-terpyridine, tppz = 2,3,5,6-tetrakis(2-pyridyl)pyrazine).

[a] modified from Ref.[30]

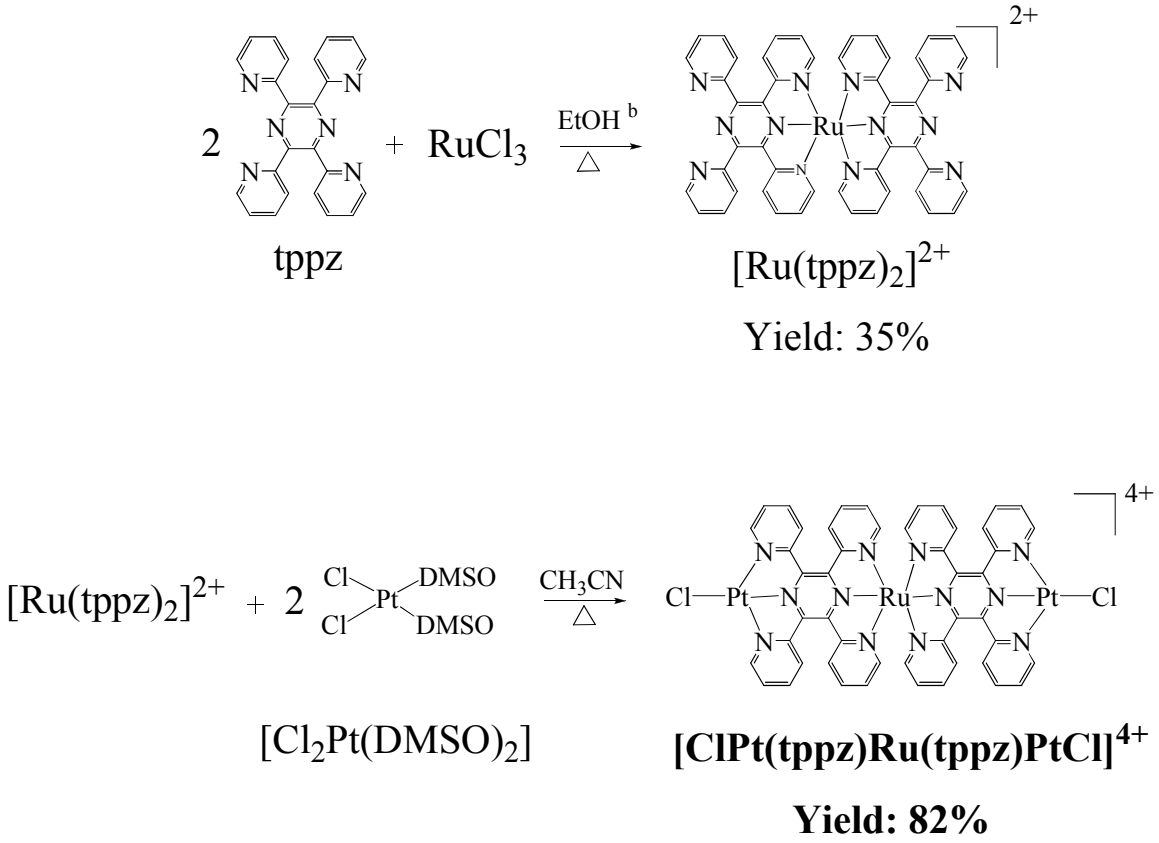

Figure 3.30. Synthetic scheme of preparing the $[ClPt(tppz)Ru(tppz)PtCl](PF_6)_4$. (tpy = 2,2′:6′,2″-terpyridine, tppz = 2,3,5,6-tetrakis(2-pyridyl)pyrazine).

[b] modified from Ref.[27]

3.2 Characterizations

3.2.1 Mass Spectrometry

The $[(tpy)Ru(tppz)PtCl](PF_6)_3$ and $[ClPt(tppz)Ru(tppz)PtCl](PF_6)_4$ systems and their precursors display mass spectra consistent with their formulation. The observed fragments in FAB for bimetallic and trimetallic complexes with their precursors were summarized in **Table 3.5**. The details of the mass spectra with the isotope distributions are given in **Appendix, Figures A.1-6**.

3.2.1.1 FAB Mass Spectrometry

FAB-MS is typically used to measure the mass (m) to charge (z) ratio of metal complexes. Neutral molecules usually display the $[M+H]^+$ or $[M-H]^-$ signals in FAB-MS, and ionic compounds have characteristic patterns with consecutive loss of counterions in FAB-MS.[236-237] Typically, complexes of this tpye display FAB mass spectra characteristic of the metal complex with loss of anions and often intact ligands. Observed fragmentation patterns include sequential loss of counterions and are consistent with the compositions of the complexes.

The FAB mass spectrum of $[(tpy)Ru(tppz)PtCl](PF_6)_3$ displayed the molecular ion minus PF_6 peak $[M-PF_6]^+$ at m/z = 1243. The successive loss of PF_6^- groups leads to the peak at 1098 and 953, corresponding to the $[M-2PF_6]^+$ and $[M-3PF_6]^+$, respectively. The peak at 619 is due to the loss of peripheral $(tpy)Ru^{II}$ to give the $(tppz)Pt^{II}Cl$ fragments.

Similar fragmentation of FAB mass spectrum was observed for the trimetallic complex, $[ClPt(tppz)Ru(tppz)PtCl](PF_6)_4$. The displayed m/z peak at 1773 corresponds to $[M-PF_6+H]^+$, a typical process of H addition for FAB-MS during the ionization process. The successive loss of PF_6^- groups gives the peak at 1669, 1484 and 1339, corresponding to the $[M-2PF_6]^+$, $[M-3PF_6]^+$ and $[M-4PF_6]^+$, respectively. The same fragments $(tppz)Pt^{II}Cl$ at 619 was also observed in $[ClPt(tppz)Ru(tppz)PtCl](PF_6)_4$ as in $[(tpy)Ru(tppz)PtCl](PF_6)_3$. $[(tpy)Ru(tppz)PtCl](PF_6)_3$ and $[ClPt(tppz)Ru(tppz)PtCl](PF_6)_4$ display the similar FAB-MS fragmentations. The characteristic fragmentation patterns of FAB-MS identify the presence of the proposed complexes.

Table 3.5. FAB-MS data for $[(tpy)Ru(tppz)](PF_6)_2$, $[Ru(tppz)_2](PF_6)_2$, $[(tpy)Ru(tppz)PtCl](PF_6)_3$ and $[ClPt(tppz)Ru(tppz)PtCl](PF_6)_4$. Observed fragmentation patterns typically involving sequential loss of counterions and are consistent with the compositions of the complexes (tpy = 2,2′:6′,2″-terpyridine, tppz = 2,3,5,6-tetrakis(2-pyridyl)pyrazine).

Complex	m/z	Assignment	Relative Abundance (%)
$[(tpy)Ru(tppz)](PF_6)_2$	868	$[M\text{-}PF_6]^+$	44
	723	$[M\text{-}2PF_6]^+$	100
$[(tpy)Ru(tppz)PtCl](PF_6)_3$	1243	$[M\text{-}PF_6]^+$	35
	1098	$[M\text{-}2PF_6]^+$	100
	953	$[M\text{-}3PF_6]^+$	71
	619	$[(tppz)PtCl]^+$	49
$[Ru(tppz)_2](PF_6)_2$	1023	$[M\text{-}PF_6]^+$	55
	878	$[M\text{-}2PF_6]^+$	100
$[ClPt(tppz)Ru(tppz)PtCl](PF_6)_4$	1773	$[M\text{-}PF_6+H]^+$	13
	1629	$[M\text{-}2PF_6]^+$	39
	1484	$[M\text{-}3PF_6]^+$	29
	1339	$[M\text{-}4PF_6]^+$	12
	619	$[(tppz)PtCl]^+$	100

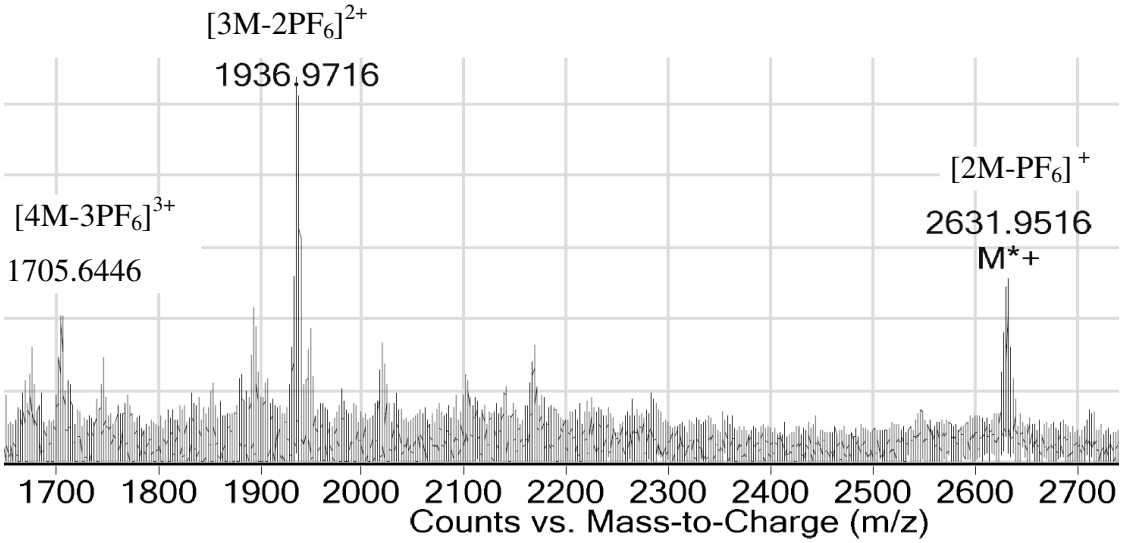

Figure 3.31. ESI-MS of 1×10^{-2} M $[(tpy)Ru(tppz)PtCl](PF_6)_3$, showing the dimer (2M), trimer (3M) and tetramer (4M) observed from CH_3CN solution, M represent the monomer of the neutral complex of $[(tpy)Ru(tppz)PtCl](PF_6)_3$ with the molecular weight (MW) as 1388. MW of PF_6^- is 145. No monomer $[M\text{-}PF_6]^+$ fragementation was observed at the concentration of 1×10^{-2} M.

3.2.1.2 ESI Mass Spectrometry

ESI-MS of $[(tpy)Ru(tppz)PtCl](PF_6)_3$ and $[ClPt(tppz)Ru(tppz)PtCl](PF_6)_4$ complexes were conducted to give a better understanding on the intermolecular interactions of these supramolecular entities in solution, motivated by emission studies described below that suggested Pt···Pt interactions via intermolecular interactions were occurring in solution. The ESI-MS spectrum of $[(tpy)Ru(tppz)PtCl](PF_6)_3$ obtained from a CH_3CN solution is given in **Figure 3.31**. The ESI-MS spectrum exhibits peaks for the aggregation of $[(tpy)Ru(tppz)PtCl](PF_6)_3$ to form dimers, trimers and tetramers. As depicted in **Figure 3.32**, A singly charged dimer, doubly charged trimer and triply charged tetramer with significant intensity are detected at m/z 2632, 1937 and 1706, respectively. The peak at

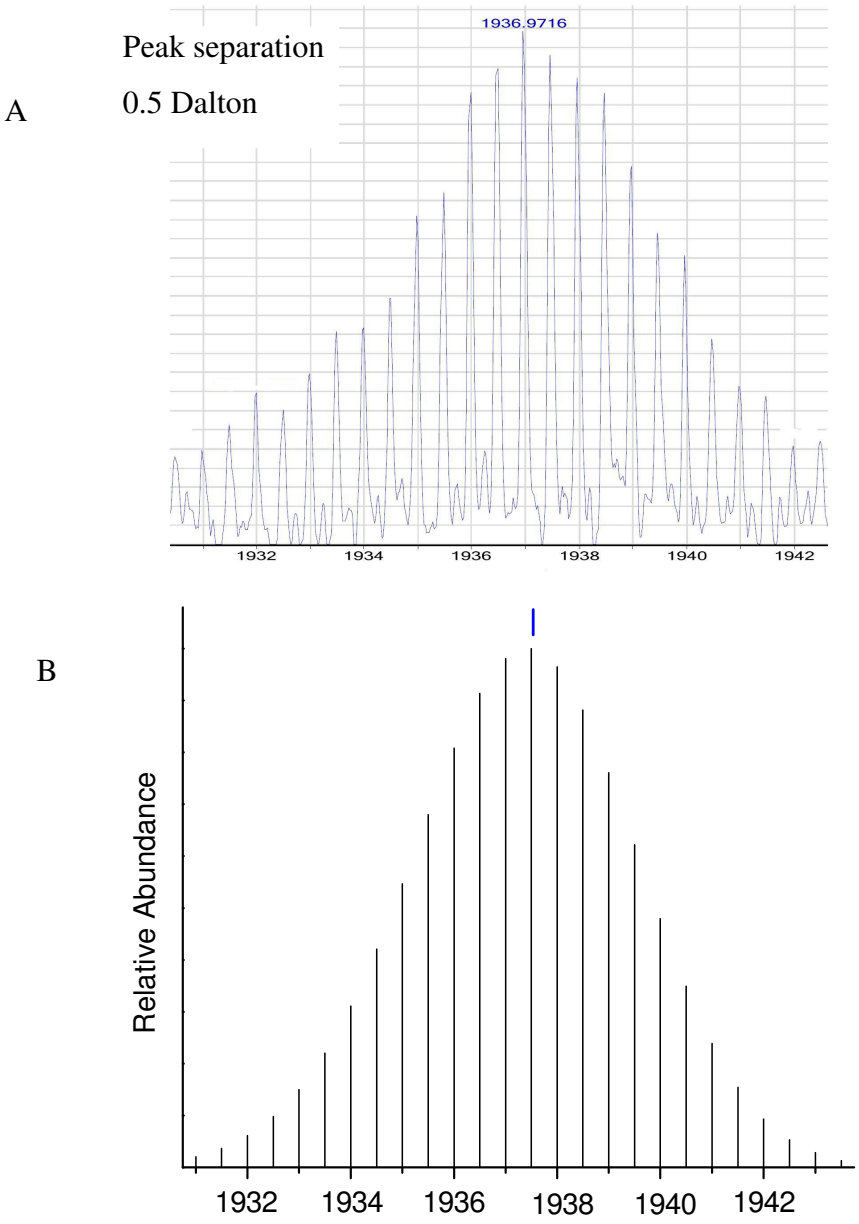

Figure 3.32. (A) ESI mass spectrum of [(tpy)Ru(tppz)PtCl](PF$_6$)$_3$ showing the isotopic distribution pattern of the trimer, $[C_{117}H_{81}Cl_3N_{27}Pt_3Ru_3P_7F_{42}]^{2+}$, (B) Calculated isotopic distribution of the dimer from ChemBio Draw Ultra 11.0

2632 is the dimer with the loss of one PF_6^- group. The distance between the isotope peaks is one dalton, so we know it is a 1+ charge. The peak at 1937 corresponds to the trimer with 0.5 dalton peak distance between the isotope peaks, which is from the $[3M-2PF_6]^{2+}$ ion of the 4164 trimer. The 1705 peak is attributed to the tetramer with a plus three charge $[3M-3PF]^{3+}$ by losing three PF_6^- groups with 0.33 dalton peak distance between the isotope peaks. The expansions of these three peaks are included in the **Appendix, Figure A.3-5**. This data suggests the assembly of this complex in solution likely via Pt···Pt interaction typical of planar Pt^{II} polyazine complexes.

The ESI mass spectra demonstrate the stabilities of the aggregation of $[(tpy)Ru(tppz)PtCl](PF_6)_3$ molecules in solutions. A number of forces such as C-H···Cl hydrogen bonds, π···π stacking and Pt···Pt interactions can be important to the self-association behaviors of the $[(tpy)Ru(tppz)PtCl](PF_6)_3$ molecules in solution. The formation of such assemblies is concentration dependent. At the concentration of 1×10^{-2} M, no monomer ions $[M-PF_6]^+$ was observed on the ESI mass spectrum. At 2×10^{-3} M, 4×10^{-4} M and 4×10^{-5} M, the monomer $[M-PF_6]^+$ was observed in the diluted solutions. The intensity of these monomer signals are qualitatively variable with the decreasing of concentration of bimetallic complex, **Appendix, Figure A.7**. This concentration dependent assembly of bimetallic complex was further supported by the emission properties of this complex discussed on **Section 4.3.3**.

It is notable that the association of the molecules are disfavored by coulombic repulsion and favored by non-covalent interactions. The self-assembly of supramolecules in organic solvent typically require the cooperation of the multiple non-covalent forces. This led us to measure the ESI-MS of $[(tpy)Ru(tppz)PtCl](PF_6)_3$ in different solvents. Similar mass spectral fragmentation patterns of $[(tpy)Ru(tppz)PtCl](PF_6)_3$ were also observed in the organic solvents of acetone, DMSO and DMF. Their ESI mass spectra are provided in **Appendix, Figure A.6**. This implies that the intermolecular interactions are maintained in these organic solvents. However, when the sample of $[(tpy)Ru(tppz)PtCl]Cl_3$ is analyzed in DI H_2O under the same condition, no signal was detected to show the molecular association in the ESI-MS. This might result from the reduction of the intermolecular hydrogen bonding in the presence of water, or the association of H_2O with the Pt sites preventing the Pt···Pt interactions.

Presumably, both $[(tpy)Ru(tppz)PtCl](PF_6)_3$ and $[ClPt(tppz)Ru(tppz)PtCl](PF_6)_4$ should give rise to the similar intermolecular associations in solution because the same $ClPt^{II}(tppz)Ru^{II}$ unit appears in each of these molecules. Surprisingly, the similar character of ESI-MS is not observed for $[ClPt(tppz)Ru(tppz)PtCl](PF_6)_4$ although several trials are attempted to acquire the ESI spectra by optimizing the experimental conditions. There are two possible reasons resulting in the different ESI-MS for bimetallic and trimetallic complexes. Firstly, it becomes challenging when ESI method is applied to the larger supramolecular assemblies. The higher charge and higher mass of trimetallic complex relative to bimetallic complex makes the larger trimetallic complex assemblies less likely to survive in the plume. Secondly, the trimetallic complex may not assemble as the same way as bimetallic complex. Further examinations of these two complexes also demonstrate different behaviors in the packing mode in the solid state by comparing their single crystal structures as will be discussed in detail later.

3.2.2 NMR

^{1}H-NMR spectroscopy is a commonly employed method to analyze metal complexes in solution. The chemical shifts of the protons in title complexes are impacted by the electron withdrawing effects imposed by the ligand and coordinated metal, and ring-current effects.[220, 238] The entry points to assign the NMR spectra are protons that have distinctive features (chemical shift, integrations, coupling pattern or coupling constants). Referring the spectra of the known compounds is helpful to resolve the complicated systems.

In comparison to the known systems, $[Ru(bpy)_3](PF_6)_2$, $[(bpy)_2RuCl_2]$, $[Ru(tpy)_2](PF_6)_2$, $[Ru(tppz)_2](PF_6)_2$, bpy, tpy, and tppz, the assignments of $[(tpy)Ru(tppz)](PF_6)_2$, $[(tpy)Ru(tppz)PtCl](PF_6)_3$, $[ClPt(tppz)Ru(tppz)PtCl](PF_6)_4$ were confirmed based on the coupling constants, ^{1}H-^{1}H correlation spectroscopy (^{1}H-^{1}H COSY), nuclear overhauser effect spectroscopy (NOESY), and ^{195}Pt-^{1}H heteronuclear multiple bond coherence (HMQC) spectroscopy. All of the chemical shifts and their coupling constants are summarized in **Table 3.6, 3.8**, some of the reported values in literature are provided in the **Table 3.7**. The numbering scheme used for the assignments of the protons is given in **Figure 3.33**. The NMR spectra of these complexes as well as the free ligands of tpy and tppz are given in **Figure 3.34**. The 2D COSY spectra of $[Ru(tppz)_2](PF_6)_2$, $[(tpy)Ru(tppz)](PF_6)_2$, $[(tpy)Ru(tppz)PtCl](PF_6)_3$ and $[ClPt(tppz)Ru(tppz)PtCl](PF_6)_4$ were attached in the **Appendix, Figures A.8-11**.

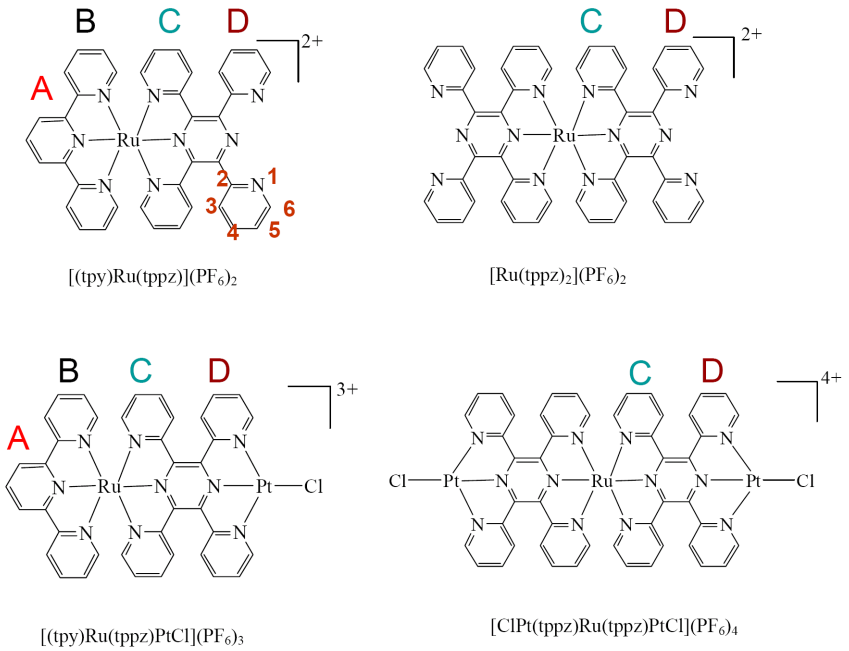

Figure 3.33. The numbering scheme used for labeling protons in $[(tpy)Ru(tppz)](PF_6)_2$, $[Ru(tppz)_2](PF_6)_2$, $[(tpy)Ru(tppz)PtCl](PF_6)_3$, and $[ClPt(tppz)Ru(tppz)PtCl](PF_6)_4$ (tpy = 2,2′:6′,2″-terpyridine, tppz = 2,3,5,6-tetrakis(2-pyridyl)pyrazine).

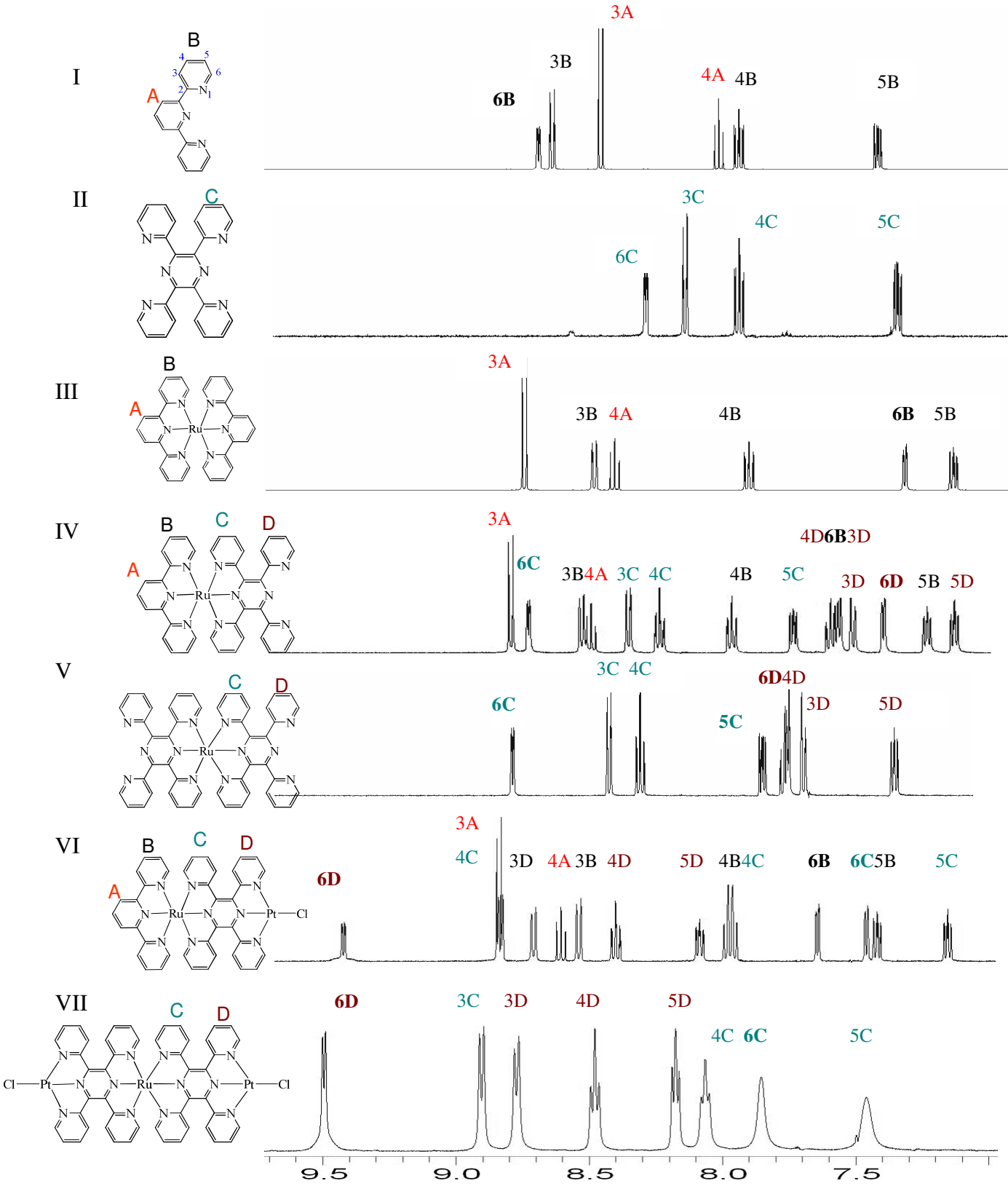

Figure 3.34. 500 MHz ^{1}H-NMR spectra of tpy (I), tppz (II), $[Ru(tpy)_2](PF_6)_2$ (III), $[(tpy)Ru(tppz)](PF_6)_2$ (IV), $[Ru(tppz)_2](PF_6)_2$ (V), $[(tpy)Ru(tppz)PtCl](PF_6)_3$ (VI) and $[ClPt(tppz)Ru(tppz)PtCl](PF_6)_4$ (VII) in CD_3CN at 298 K

Table 3.6. 500 MHz ^{1}H-NMR chemical shifts of [(tpy)Ru(tppz)]$(PF_6)_2$, [Ru(tppz)$_2$]$(PF_6)_2$, [(tpy)Ru(tppz)PtCl]$(PF_6)_3$ and [ClPt(tppz)Ru(tppz)PtCl]$(PF_6)_4$ in CD_3CN at 298K (tpy = 2,2′:6′,2″-terpyridine, tppz = 2,3,5,6-tetrakis(2-pyridyl)pyrazine).

Ring	H position on the ring	[(tpy)Ru(tppz)]$^{2+}$ δ(ppm) (*J* in Hz)	[Ru(tppz)$_2$]$^{2+}$ δ(ppm) (*J* in Hz)	[(tpy)Ru(tppz)PtCl]$^{3+}$ δ(ppm) (*J* in Hz)	[ClPt(tppz)Ru(tppz)PtCl$_2$]$^{4+}$ δ(ppm) (*J* in Hz)
A	**3**	8.80 (8.5)		8.87 (8.5)	
	4	8.50 (8.3)		8.63 (7.8)	
B	**3**	8.53 (8.0)		8.56 (7.5)	
	4	7.97 (8.0, 6.8, 1.2)		7.99 (7.8, 6.3, 1.5)	
	5	7.24 (7.5, 6.0, 1.0)		7.44 (7.8, 6.8, 1.5)	
	6	7.59 (6.0, 1.0)		7.66 (6.3, 1.0)	
C	**3**	8.36 (7.5, 1.8)	8.38 (8.0)	8.86 (8.5)	8.90 (8.5)
	4	8.24 (8.0, 6.5, 1.7)	8.27 (8.4, 6.9, 1.4)	8.01 (8.5, 7.0, 1.3)	8.06 (8.5)
	5	7.74 (7.8, 6.8, 1.7)	7.78 (7.8, 2.0)	7.17 (7.8, 6.3, 1.5)	7.50 (*br*^{1})
	6	8.73 (5.0, 2.0)	8.76 (5.0)	7.48 (6.2, 1.0)	7.85 (*br*^{2})
D	**3**	7.51 (8.0, 1.0)	7.63 (7.5)	8.74 (8.0, 1.0)	8.77 (8.0)
	4	7.60 (8.0, 6.0, 1.8)	7.66 (8.0)	8.43 (8.0, 6.3, 1.7)	8.48 (7.8)
	5	7.13 (7.8, 6.3, 1.5)	7.22 (6.0)	8.11 (7.8, 5.0, 1.3)	8.18 (6.5)
	6	7.40 (5.5, 1.5)	7.67 (5.0)	9.45 (5.5, 1.5)	9.50 (5.5)

br^1: broad at RT, *J*=6.6 Hz at 60 °C in 400 MHz.

br^2: broad at RT, *J*=5.6 Hz at 60 °C in 400 MHz.

Table 3.7. Literature reported ^{1}H-NMR chemical shifts of tpy, $[Ru(tpy)_2]^{2+}$, tppz, and $[Ru(tppz)_2](PF_6)_2$ (tpy = 2,2′:6′,2″–terpyridine, tppz = 2,3,5,6-tetrakis(2-pyridyl)pyrazine).

Ring	H position on the ring	tpy δ(ppm) [a,b]	$[Ru(tpy)_2]^{2+}$ δ(ppm) [a,b]	tppz δ(ppm) [b]	$[Ru(tppz)_2]^{2+}$ δ(ppm) [c]
A	**3**	8.46	8.76		
	4	7.96	8.42		
B	**3**	8.62	8.50		
	4	7.86	7.42		
	5	7.33	7.17		
	6	8.70	7.34		
C	**3**				8.58
	4				8.35
	5				7.83
	6				8.81
D	**3**			8.05	7.89
	4			7.80	7.88
	5			7.23	7.41
	6			8.38	8.12

[a] In $CDCl_3$, Ref.[239]

[b] In CD_3CN, Ref.[29]

[c] In d_6-acetone, Ref.[45]

Table 3.8. 500 MHz ^{1}H-NMR chemical shifts (δ) and coupling constants (^{3}J) of tridentate free ligand tpy, tppz and $[Ru(tpy)_2](PF_6)_2$, which are comparable to the literature reported values[29]

Ring	H position on the ring	tpy δ(ppm)	tppz δ(ppm)	$[Ru(tpy)_2]^{2+}$ δ(ppm)
A	**3**	8.45 (8.0)		8.74 (7.5)
	4	8.00 (8.0)		8.41 (8.0)
B	**3**	8.63 (8.0)	8.01 (8.0)	8.49 (8.0)
	4	7.93 (8.0)	7.93 (8.0)	7.91 (8.0)
	5	7.40 (5.0)	7.32 (5.0)	7.16 (6.0)
	6	8.68 (5.0)	8.26 (5.0)	7.34 (5.0)

3.2.2.1 Ring Current and Geometry

The ring current effects on protons within an assembly arising from polycyclic aromatic systems are highly dependent on molecular geometry.[240-241] In this sub-section, we discuss the ring current effect in relation to the molecular geometry by comparing the ^{1}H-NMR spectra between $[Ru(tpy)_2](PF_6)_2$ and $[Ru(tppz)_2](PF_6)_2$. The structures of these complexes are illustrated in **Figure 3.35**, and ^{1}H-NMR spectra of these complexes as well as the free ligands tpy and tppz are provided in **Figure 3.36**. δ of H^6B in $[Ru(tpy)_2](PF_6)_2$ exhibited upfield shift upon complexation, which is attributed to ring current effect. However, the ring current effect is not appreciated in the ^{1}H-NMR spectrum of $[Ru(tppz)_2](PF_6)_2$ for the H^6C protons which are also located over the pyrazine ring.

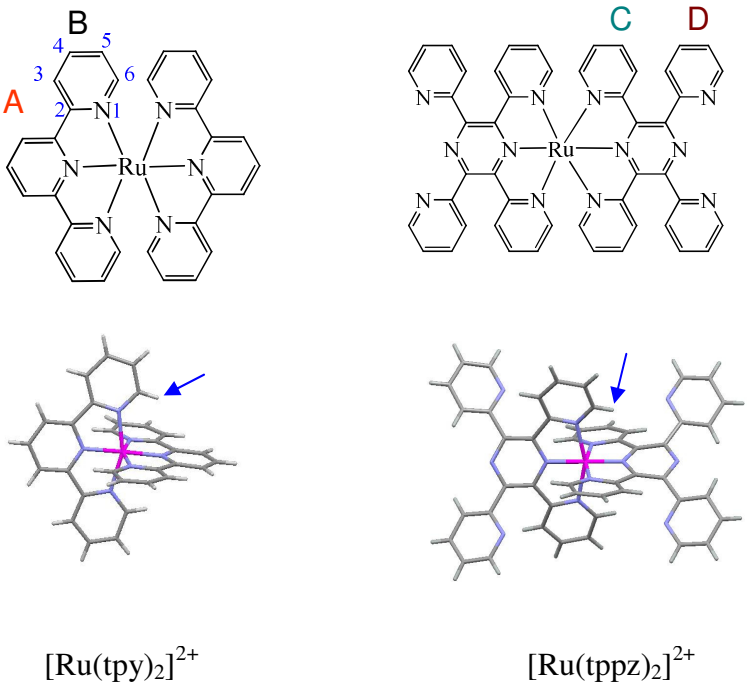

$[Ru(tpy)_2]^{2+}$ $[Ru(tppz)_2]^{2+}$

Figure 3.35. The structures of $[Ru(tpy)_2](PF_6)_2$ and $[Ru(tppz)_2](PF_6)_2$. The blue arrow pointed H^6B in $[Ru(tpy)_2](PF_6)_2$ displays upfield shift relative to the free ligand of tpy, while the blue arrow pointed H^6C in $[Ru(tppz)_2](PF_6)_2$ exhibits downfield shift compared to the free ligand of tppz.

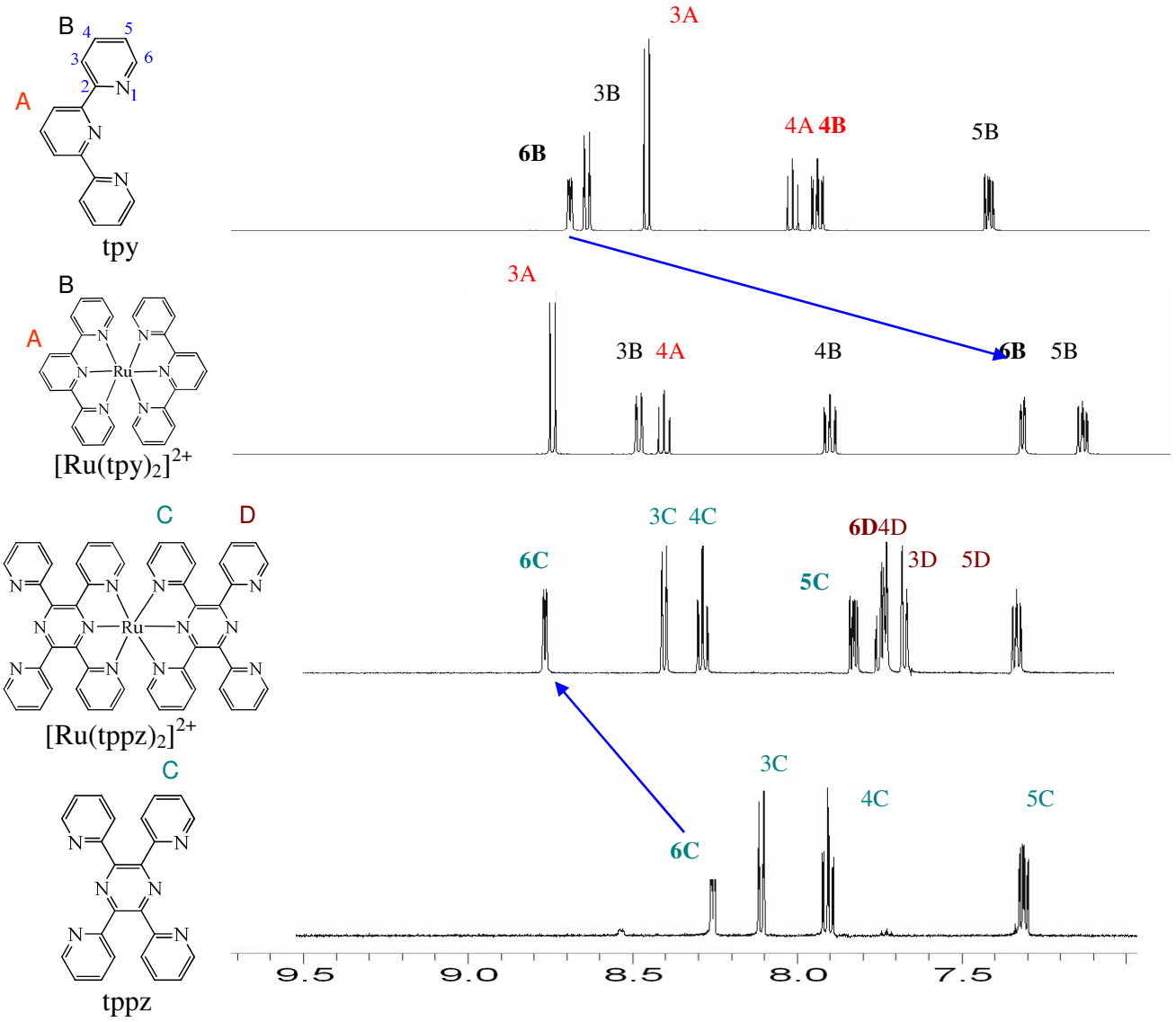

Figure 3.36. 500 MHz ^{1}H-NMR spectra of tpy, tppz, $[Ru(tpy)_2](PF_6)_2$ and $[Ru(tppz)_2](PF_6)_2$, in CD_3CN at 298 K in CD_3CN, (tpy = 2,2′:6′,2″–terpyridine, tppz = 2,3,5,6-tetrakis(2-pyridyl)pyrazine).

The identification of the H^6 protons in the complexes of $[Ru(tpy)_2](PF_6)_2$ and $[Ru(tppz)_2](PF_6)_2$ can be accomplished by examining the distinct coupling constants on the H^3, H^4, H^5 and H^6 positions.

Coupling constant, *J*, is the frequency difference in Hz between the components peaks. *J* value is proportional to the intensity of the coupling and independent of the external field. As we know, spins of protons are coupled through the intervening bonding electrons in the molecule. Spin coupling will cause the splitting of the NMR spectrum. The multiplicity of the spectrum follow the general formula 2nI +1 in the first order multiplet system (n being the neighboring nuclei number, I being the quantum spin number, for proton, I=1/2). Therefore, given the information of the *J* and δ, the different nuclei can be identified in the molecule. In addition, the enhancement of peak intensity from the coupled nuclei can further facilitate the assignments.

Our assignments of the ^{1}H-NMR spectrum on $[Ru(tpy)_2](PF_6)_2$, **Figure 3.36**, are consistent with the literature reported data.[220, 238, 242] Firstly, The H^4A lying on the mirror plane of the complexes can be assigned without ambiguity as its integral is half of the other aromatic protons. Then the H^3A can be easily tracked from the ^{1}H-^{1}H COSY spectrum. Secondly, with the help of the characteristic coupling constants, the sequence of the protons on each rings can be accomplished for Ring B. H^3B & H^4B, and H^5B & H^6B in $[Ru(tpy)_2](PF_6)_2$ demonstrate the characteristic splitting coupling with the distinct ^3J as 8.0 and 6.0 Hz respectively, **Table 3.8**. The chemical shifts of such assignments reflect the nature of the configuration of the complex. The two terpyridines in $[Ru(tpy)_2](PF_6)_2$ are perpendicular to each other, the sixth proton (blue arrow pointed proton, **Figure 3.35**) in the peripheral pyridyl rings resides above the aromatic ring of the adjacent ligand, resulting in the upfield shift due to the ring current effect. The change of the chemical shift of H^6B between tpy and $[Ru(tpy)_2](PF_6)_2$ is opposite to the change of chemical shift between tpy and $[(tpy)PtCl](PF_6)$ (**Figure 1.17**).

In the same way, the full assignments of the ^{1}H-NMR of $[Ru(tppz)_2](PF_6)_2$, **Figure 3.36**, can be achieved by ^{1}H-^{1}H COSY spectrum and the typical coupling constants for each protons. Briefly, protons belonging to the complexed and uncomplexed pyridyl rings are grouped into two sets by using ^{1}H-^{1}H COSY (**Appendix, A.8**). The sequence of the protons is assigned by analyzing their distinctive coupling constants, *J*. The doublet at

8.76 (^3J = 5.0 Hz) represents the protons on the H^6C which is coupled to the H^5C. All of the protons of ring C present in the lower field than the protons of ring D in $[Ru(tppz)_2](PF_6)_2$ due to the influence of the metal-ligand bond (electron withdrawing effects). The H^6C of $[Ru(tppz)_2](PF_6)_2$ displays downfield shift relative to the tppz ligand. The assignments on $[Ru(tppz)_2](PF_6)_2$ in CD_3CN is comparable to the literature reported values.[45]

In a comparison of the spectra between $[Ru(tpy)_2](PF_6)_2$ and $[Ru(tppz)_2](PF_6)_2$, the H^6C in $[Ru(tppz)_2](PF_6)_2$ (blue arrow pointed hydrogen, **Figure 3.35**) is also exposed to the aromatic pyrazine ring, the δ of H^6C doesn't exhibit the upfield shifts as observed in $[Ru(tpy)_2](PF_6)_2$ owing to the ring current. Presumably, it is due to the deshielding effect from the uncomplexed Ring D, chelation effect upon complexation to Ru, and electron withdrawing effect from the uncoordinated lone pair N in pyrazine ring. These combinational effects outweigh the ring current effect.

If the H^6 protons display different chemical shifts in $[Ru(tpy)_2](PF_6)_2$ and $[Ru(tppz)_2](PF_6)_2$, it will be a dilemma to assign the ^{1}H-NMR spectrum of $[(tpy)Ru(tppz)](PF_6)_2$, which contain the $(tpy)Ru^{II}$ component and $(tppz)Ru^{II}$ component from half of $[Ru(tpy)_2](PF_6)_2$ and half of $[Ru(tppz)_2](PF_6)_2$. The issue is how to distinguish Ring B and Ring C in $[(tpy)Ru(tppz)](PF_6)_2$.

3.2.2.2 ^{1}H-^{1}H NOESY

Nuclear Overhauser Effect Spectroscopy (NOESY) is a very useful tool to study the conformation of molecules. The Nuclear Overhauser Effect (NOE) is used to study the dipolar coupling interactions throughout space. The intensity of the NOE decreases as the inverse of the sixth power of the distance between the nuclei (like protons). A signal can be detected by NOESY if the two protons' distance is less than 5Å through space. Here NOESY can be used to distinguish the Ring B and C in $[(tpy)Ru(tppz)](PF_6)_2$ molecule.

The synthesis and study of $[(tpy)Ru(tppz)](PF_6)_2$ has been reported by Abruna,[27] Thummel[29] and Brewer's[30] group. The characterization and study of $[(tpy)Ru(tppz)](PF_6)_2$ are based on the MS, electrochemical and photophysical properties. To date, there is no direct evidence to confirm the structure of $[(tpy)Ru(tppz)](PF_6)_2$ with respect to the variable binding modes of tppz.[176]

3.2.2.3 ^{1}H-NMR Assignment of $[(tpy)Ru(tppz)](PF_6)_2$

The well resolved ^{1}H-NMR spectrum of $[(tpy)Ru(tppz)](PF_6)_2$ reveals fourteen non-equivalent proton resonances in accord with the molecular formula $[(tpy)Ru(tppz)](PF_6)_2$ as shown in **Figure 3.37**, the enlarged spectrum is given in **Figure 3.38**. With the background to assign $[Ru(tpy)_2](PF_6)_2$ and $[Ru(tppz)_2](PF_6)_2$, the 14 non-equivalent protons in $[(tpy)Ru(tppz)](PF_6)_2$ can be separated as four groups by using ^{1}H-^{1}H COSY (**Appendix, A.9**). The H^4A is unique and can be assigned as it is half the number of protons as the other aromatic protons. Then the H^3A can be easily tracked from the ^{1}H-^{1}H COSY spectrum. The sequence of the protons on each ring can be accomplished for the other three unidentified Ring B, C and D by examining their characteristic coupling constants. The signals of the uncoordinated Ring D are expected to be upfield with the similar resonance pattern as in $[Ru(tppz)_2](PF_6)_2$. Finally, the distinction between Ring B and Ring C was carried out by the NOESY experiments. The ^{1}H-^{1}H NOESY spectrum of $[(tpy)Ru(tppz)](PF_6)_2$ is given in **Figure 3.39**. As expected, the NOESY spectrum displays two crossing peaks from H^{3A} and H^{3B}. Since Ring A has been assigned, proceeding H^3B by using ^{1}H-^{1}H COSY again, the protons on Ring B can be fully assigned based on their correlations.

Examining the assigned spectrum on $[(tpy)Ru(tppz)](PF_6)_2$, **Figure 3.37**, it is notable that the δ values of the $[(tpy)Ru^{II}]$ moiety in $[(tpy)Ru(tppz)](PF_6)_2$ follow the same pattern observed for the $[Ru(tpy)_2]^{2+}$, such resonance coupling is in agreement with other similar systems in literature.[220, 243] As one can see, however, the signals of H^6C in the $(tppz)Ru^{II}$ component present to much lower field compared to H^6B; this dramatic difference might be due to the deshielding effect from the rotational Ring D on H^6C as we observed in $[Ru(tppz)_2](PF_6)_2$.[221]

In comparison of the δ of H^6B in $[Ru(tpy)_2]^{2+}$ (δ_{H6B} = 7.34) and $[(tpy)Ru(tppz)](PF_6)_2$ (δ_{H6B} = 7.50), Substitution of tpy with tppz in $[Ru(tpy)_2]^{2+}$ makes the δ of H^6B undergo downfield shift due to the electron withdrawing effect from the component of $(tppz)Ru^{II}$ over the part of $(tpy)Ru^{II}$. On the other hand, the signal of H^6C in $[(tpy)Ru(tppz)](PF_6)_2$ (δ_{H6B} = 7.73) slightly shifts to upfield in relative to the H^6C in $[Ru(tppz)_2]^{2+}$ (δ_{H6B} = 8.76). The cause of these behaviors is inherent in the configuration of the complex.

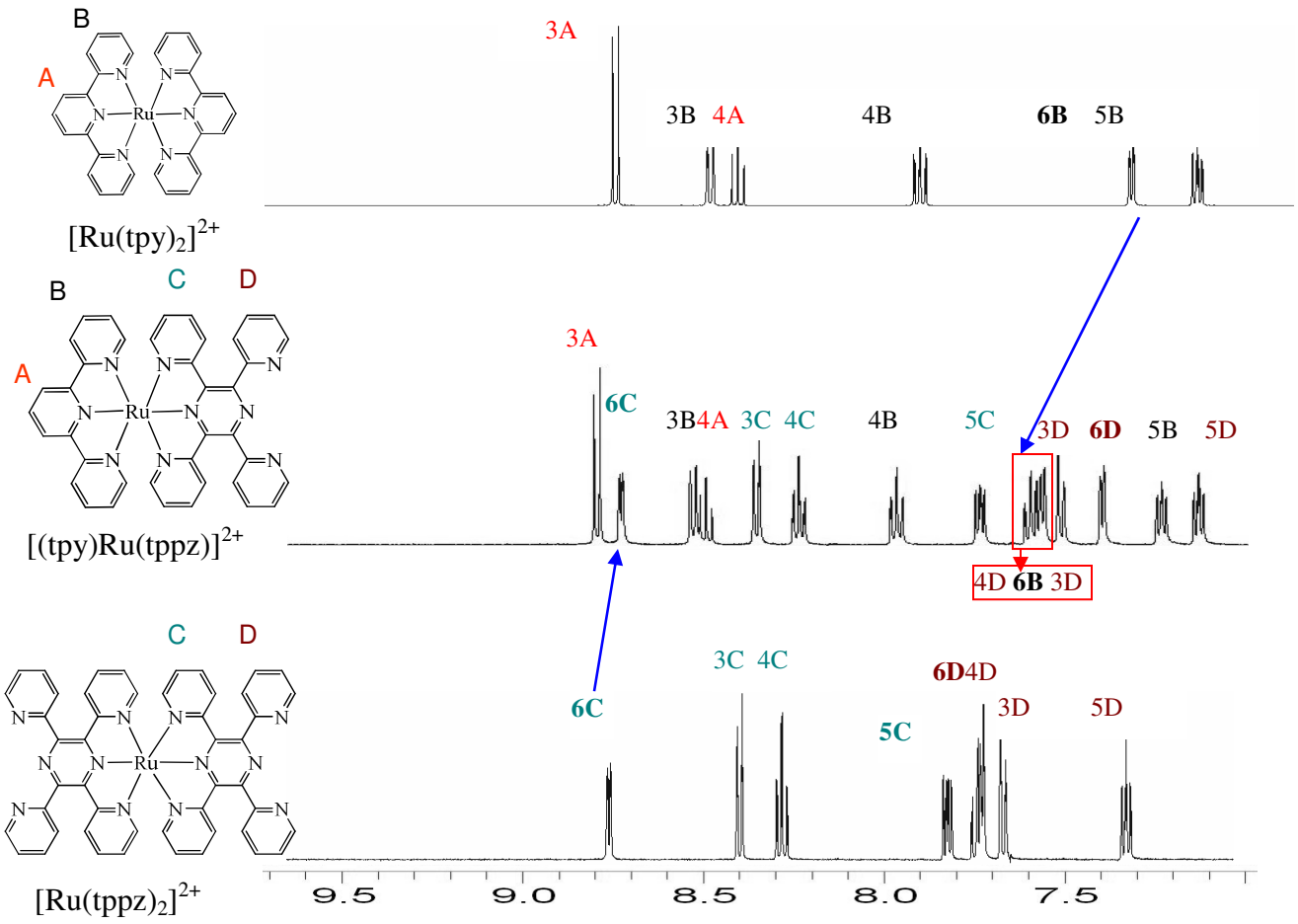

Figure 3.37. 500 MHz ^{1}H-NMR spectra of $[Ru(tpy)_2](PF_6)_2$, $[(tpy)Ru(tppz)](PF_6)_2$ and $[Ru(tppz)_2](PF_6)_2$, in CD_3CN at 298 K in CD_3CN, (tpy = 2,2′:6′,2″–terpyridine, tppz = 2,3,5,6-tetrakis(2-pyridyl)pyrazine).

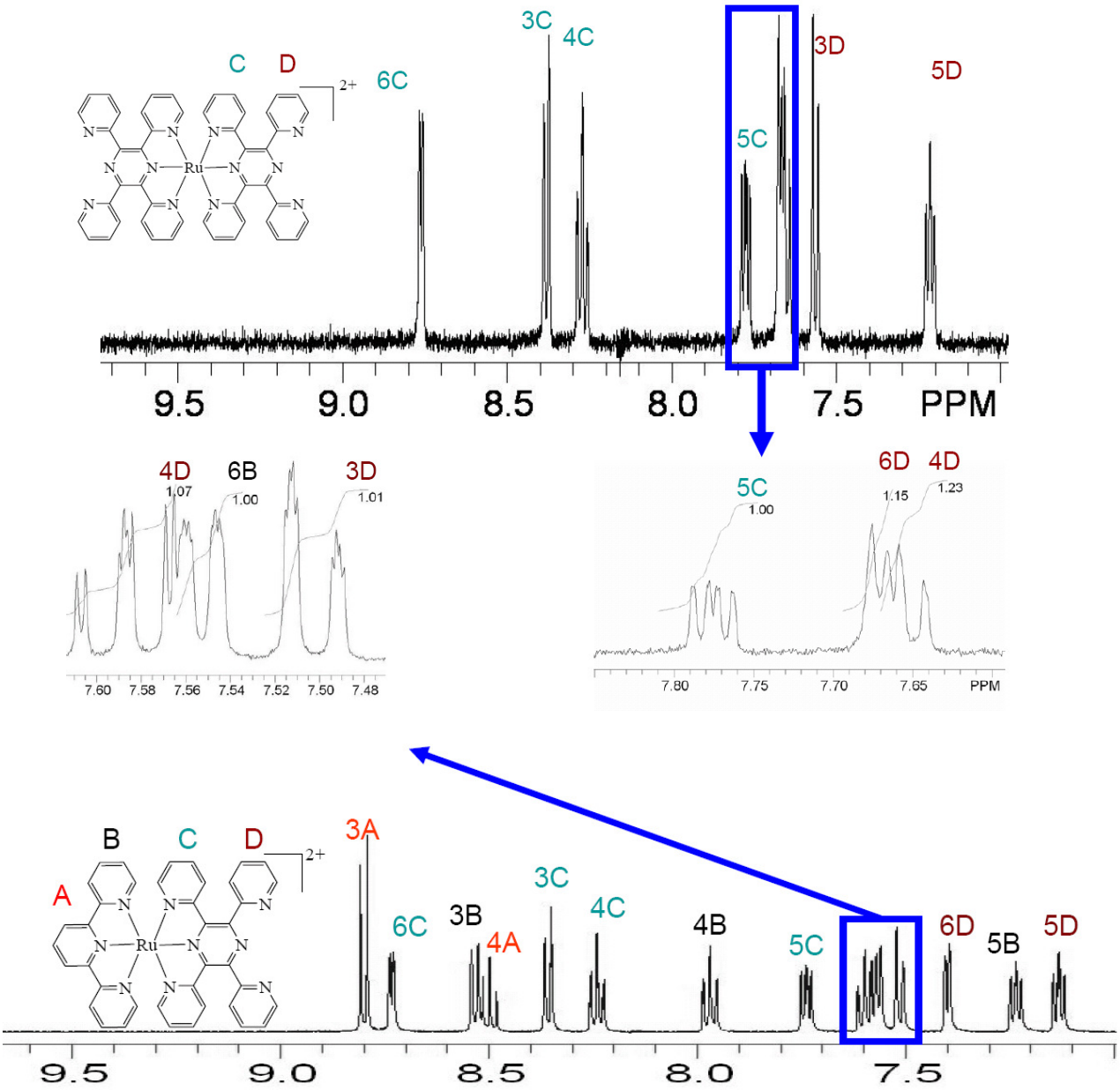

Figure 3.38. 500 MHz ^{1}H NMR spectrum of [(tpy)Ru(tppz)]$(PF_6)_2$ and [Ru(tppz)$_2$]$(PF_6)_4$ (tpy = 2,2′:6′,2″-terpyridine, tppz = 2,3,5,6-tetrakis(2-pyridyl)pyrazine) in CD_3CN at 298 K

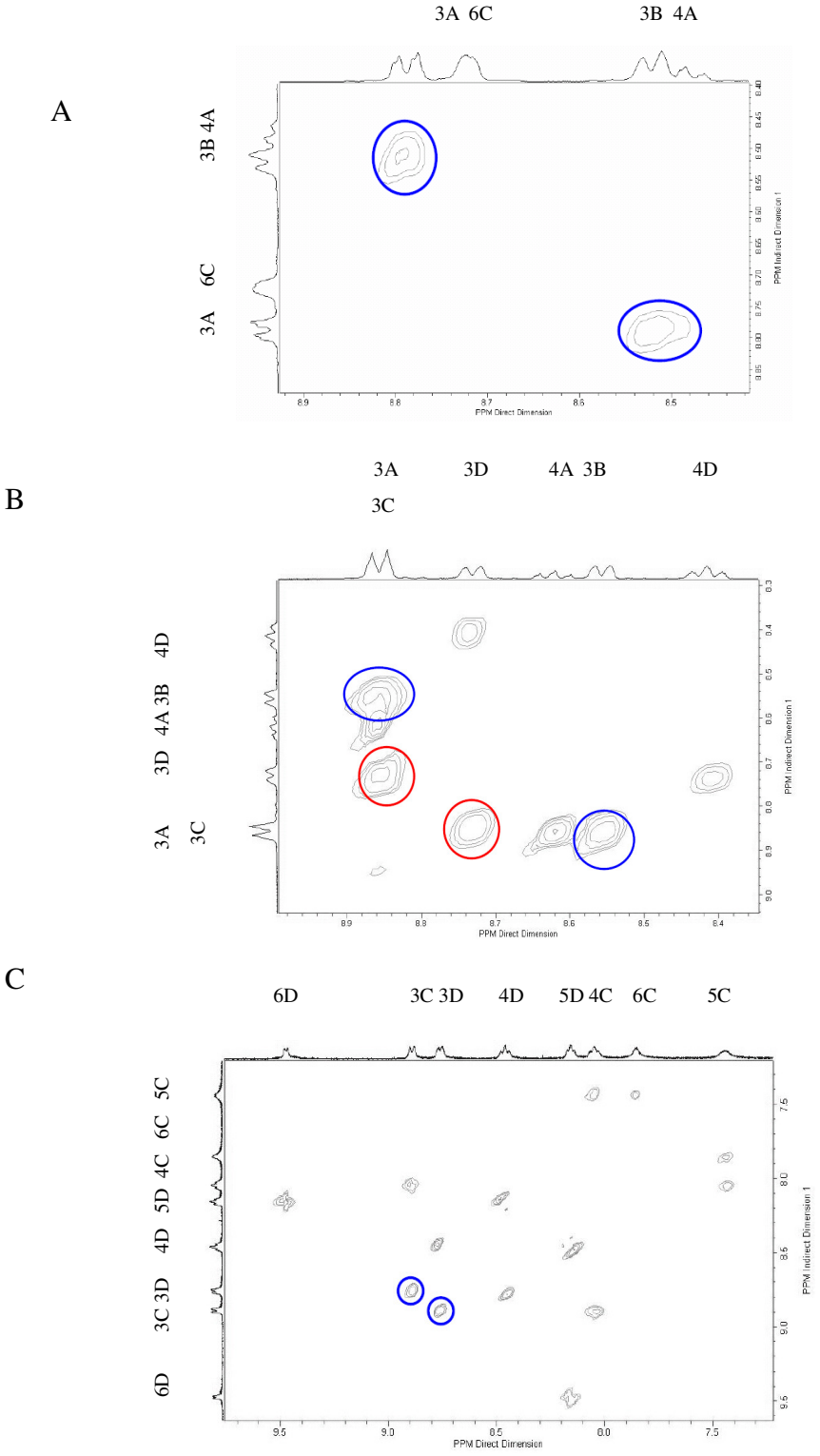

Figure 3.39. 400 MHz ^{1}H-^{1}H NOESY of $[(tpy)Ru(tppz)](PF_6)_2$ (A), $[(tpy)Ru(tppz)PtCl](PF_6)_3$ (B),, and $[ClPt(tppz)Ru(tppz)PtCl](PF_6)_4$ (C).

3.2.2.4 ^{1}H-NMR Assignment of [(tpy)Ru(tppz)PtCl](PF$_6$)$_2$

In presence of the free flipping of the uncomplexed pyridyl rings in [Ru(tppz)$_2$](PF$_6$)$_2$ and [(tpy)Ru(tppz)](PF$_6$)$_2$), ring current effect can't be applied to the assignment of the protons on the adjacent coordinated rings. Similar arguments can be induced to rationalize the assignments on the ^{1}H-NMR spectra of [(tpy)Ru(tppz)PtCl](PF$_6$)$_3$ and [ClPt(tppz)Ru(tppz)PtCl](PF$_6$)$_4$.

The ^{1}H NMR spectrum of [(tpy)Ru(tppz)PtCl](PF$_6$)$_3$ in CD$_3$CN at room temperature, **Figure 3.40**, agrees well with that predicted from its solid state structure and displays 14 non-equivalent proton resonances. Correlation of the structure of a complex with its spectrum is much easier than resolving and interpreting the spectra in such a complicated system.

The assignments of the ^{1}H NMR spectrum of [(tpy)Ru(tppz)PtCl](PF$_6$)$_3$ can be accomplished by the comparison to the assigned ^{1}H NMR spectrum of [(tpy)Ru(tppz)](PF$_6$)$_2$. The H^{4}A proton in [(tpy)Ru(tppz)PtCl](PF$_6$)$_3$ is distinct and appears as a virtual triplet at δ 8.63 with half the integral intensity of the other protons. Upon assignment of H^{4}A, the doublet at δ 8.87 can be easily assigned to H^{3}A using ^{1}H-^{1}H COSY (**Appendix, A.10**). The distinction between protons of rings B and C was achieved using NOESY, while the assignments of the sets of protons on each individual ring were achieved using ^{1}H-^{1}H COSY. For example, the NOESY spectrum of [(tpy)Ru(tppz)PtCl](PF$_6$)$_3$ indicated through space interactions between H^{3}A and the doublet at δ 8.56 attributed to H^{3}B, **Figure 3.39**. The rest of the protons of ring B were identified based on this interaction and ^{1}H-^{1}H COSY correlations. The resonances at δ 7.99, 7.44, and 7.66 display the expected splitting pattern for H^{4}B, H^{5}B, and H^{6}B, respectively. The individual assignments of the (tpy)Ru^{II} component of [(tpy)Ru(tppz)PtCl](PF$_6$)$_3$, are comparable with those of the (tpy)Ru^{II} component of [(tpy)Ru(tppz)](PF$_6$)$_2$ and [Ru(tpy)$_2$]$^{2+}$.[220] The H^6 protons of rings C and D in [(tpy)Ru(tppz)](PF$_6$)$_2$, appear as doublet of doublets, with H^{6}C shifted downfield (δ 8.73) relative to H^{6}D (δ 7.40), consistent with the electron withdrawing effect imposed by Ru on ring C. The significant downfield shift of H^{6}C (δ 8.73) relative to H^{6}B (δ 7.59) in [(tpy)Ru(tppz)](PF$_6$)$_2$, may be a combination effect of the coordination of ring C to Ru

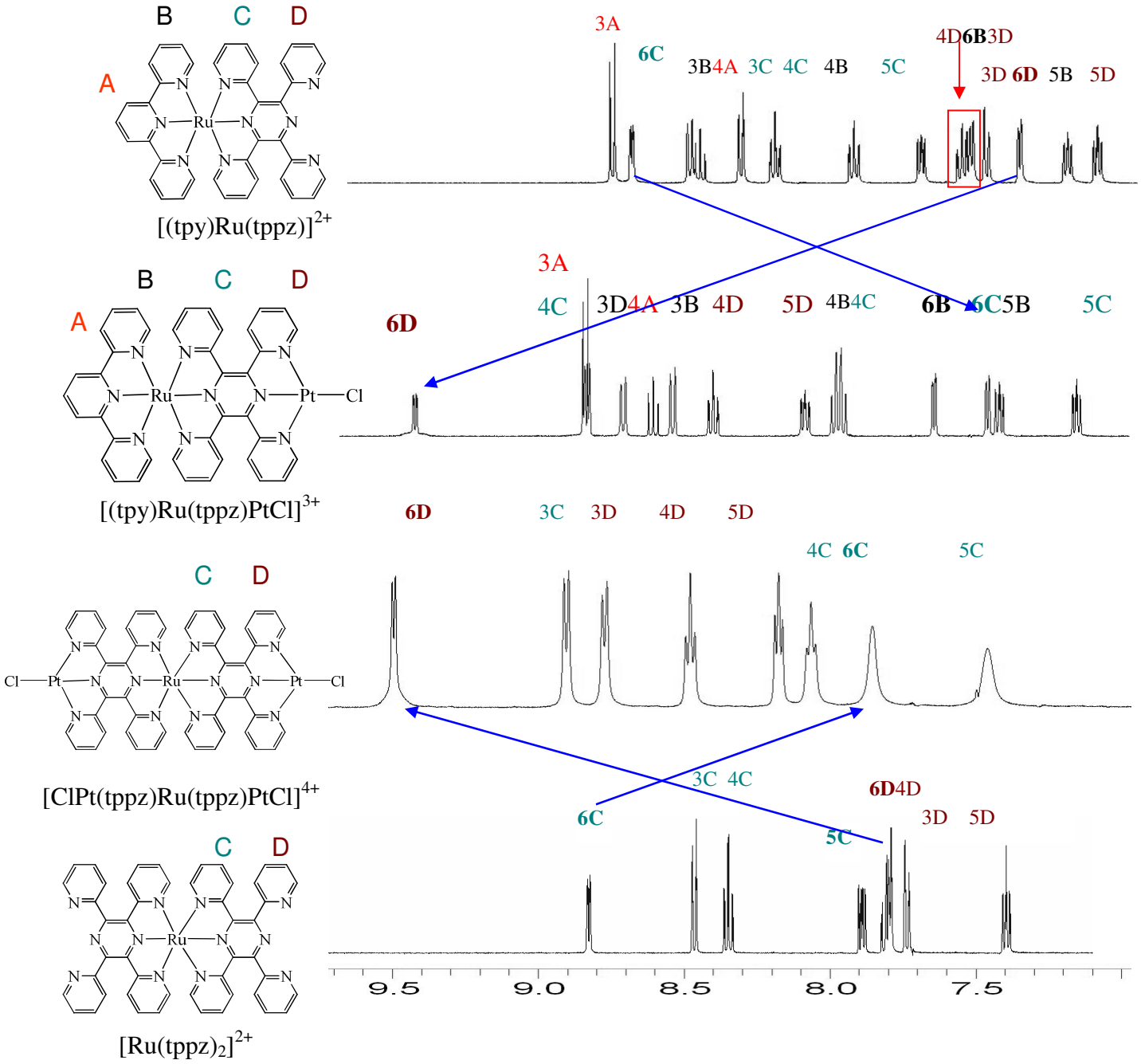

Figure 3.40. 500 MHz ^{1}H-NMR spectra of $[(tpy)Ru(tppz)](PF_6)_2$, $[(tpy)Ru(tppz)PtCl](PF_6)_3$ $[ClPt(tppz)Ru(tppz)PtCl](PF_6)_4$ and $[Ru(tppz)_2](PF_6)_2$in CD_3CN at 298 K in CD_3CN, (tpy = 2,2′:6′,2″–terpyridine, tppz = 2,3,5,6-tetrakis(2-pyridyl)pyrazine).

and its attachment to the pyrazine ring of tppz, shifting the H^6C resonance to low field. Coordination of a Pt center to ring D in $[(tpy)Ru(tppz)PtCl](PF_6)_3$, leads to a significant downfield shift in H^6D (δ 9.45). Using ^1H-^1H COSY, the resonances at δ 8.74, 8.43, and 8.11 were assigned to H^3D, H^4D, and H^5D, respectively, consistent with Pt coordination. H^3D, H^4D, and H^5D of $[(tpy)Ru(tppz)PtCl](PF_6)_3$ occur significantly downfield relative to the corresponding protons of $[(tpy)Ru(tppz)](PF_6)_2$. By contrast, the upfield shift of H^6C in $[(tpy)Ru(tppz)PtCl](PF_6)_3$ (δ 7.48) relative to $[(tpy)Ru(tppz)](PF_6)_2$ (δ 8.73) is due to pronounced shielding of H^6C when ring D is complexed to Pt in $[(tpy)Ru(tppz)PtCl](PF_6)_3$ relative to the free tppz of $[(tpy)Ru(tppz)](PF_6)_2$. This shielding is imposed by ring current effects as H^6C lies directly above the π cloud of ring A in $[(tpy)Ru(tppz)PtCl](PF_6)_3$. The remaining resonances at δ 8.86, 8.01, and 7.17 were assigned to H^3C, H^4C, and H^5C of $[(tpy)Ru(tppz)PtCl](PF_6)_3$ using ^1H-^1H COSY. The NOESY spectrum of $[(tpy)Ru(tppz)PtCl](PF_6)_3$ revealed the through space interactions between H^{3C} and H^{3D}, consistent with our assignments.

Comparison of the δ of H^6C on $[(tpy)Ru(tppz)](PF_6)_2$ (δ_{H^6C} = 8.73 ppm) and $[(tpy)Ru(tppz)PtCl](PF_6)_3$ (δ_{H^6C} = 7.48 ppm), in which the δ of H^6C appear in the downfield and upfield with a separation up to 1.25 ppm. Such unpredicted assignments must be established by compelling evidence. ^{195}Pt-^1H HMQC experiment was carried out to confirm our assignments at the suggestion of Prof. Harry C. Dorn.

Heteronuclear Multiple Quantum Coherence (HMQC) experiments established correlation between protons and other atoms with nuclear spin, such as ^{13}C, ^{15}N or ^{195}Pt. ^{195}Pt atom has ½ nuclear spin with 33.8% abundance in nature. The relative sensitivity of ^{195}Pt-NMR is 0.00994 vs. 1.0 for ^1H. Recently, a number of ^{195}Pt-NMR topics have been reviewed.[244-246] In our study, all the δ (Pt) values were referenced to potassium tetrachloroplatinate (II) (K_2PtCl_4) (δ (Pt) = -1613 ppm in D_2O at 600 MHz), as depicted on **Figure 3.41**.

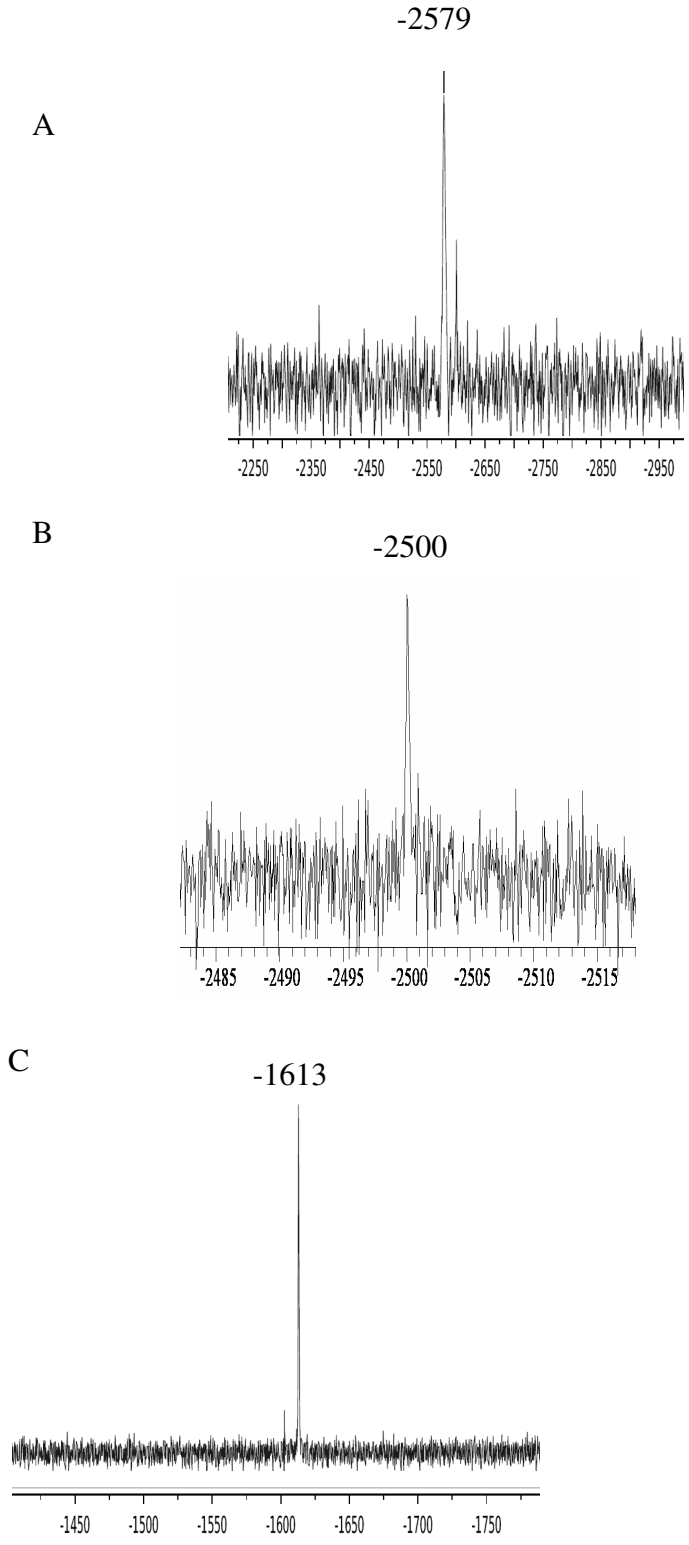

Figure 3.41. 600 MHz ^{195}Pt-NMR spectra of $[(tpy)Ru(tppz)PtCl](PF_6)_3$ (A), $[ClPt(tppz)Ru(tppz)PtCl](PF_6)_4$ (B) in CD_3CN and reference compound, K_2PtCl_4 in D_2O (C).

In **Figure 3.41 A**, ^{195}Pt resonance in [(tpy)Ru(tppz)PtCl](PF$_6$)$_3$ was observed at -2579 ppm, characteristic of N3 coordination sphere for Pt^{2+}.[246-247] When the tpy is replaced by ClPt^{II}(tppz) in [(tpy)Ru(tppz)PtCl](PF$_6$)$_3$ to give [ClPt(tppz)Ru(tppz)PtCl](PF$_6$)$_4$, ^{195}Pt resonance in [ClPt(tppz)Ru(tppz)PtCl](PF$_6$)$_4$ was observed at -2500 ppm (**Figure 3.41 B**), downfield shift 79 ppm compared to [(tpy)Ru(tppz)PtCl](PF$_6$)$_3$, characteristic of electron withdrawing effect from the Pt coordination. Similar ^{195}Pt resonances were observed in the Ru^{II},Pt^{II} bidentate system at around δ_{Pt} = -2200 ppm (600 MHz, CD$_3$CN, RT) for the complexes with the form [(TL)RuCl(dpp)PtCl$_2$](PF$_6$), where TL = 2,2′:6′2″-terpyridine, 4′-(4-methylphenyl)-2,2′:6′2″-terpyridine or 4,4′,4″-tri-tert-butyl-terpyridine and dpp = 2,3-bis(2-pyridyl)pyrazine.[248] Comparable ^{195}Pt resonances were also reported in the Ru^{II},Pt^{II} tridentate system at δ_{Pt} = -2701 ppm (300 MHz, MeOH, RT) for the terpyridyl-Pt^{II} complex: [(tpy)Ru(dtdeg)PtCl]$^{3+}$ (tpy=2,2′:6′,2″-terpyridine, dtdeg=bis[4′-(2,2′:6′,2″-terpyridyl)]-diethyleneglycol ether).[62]

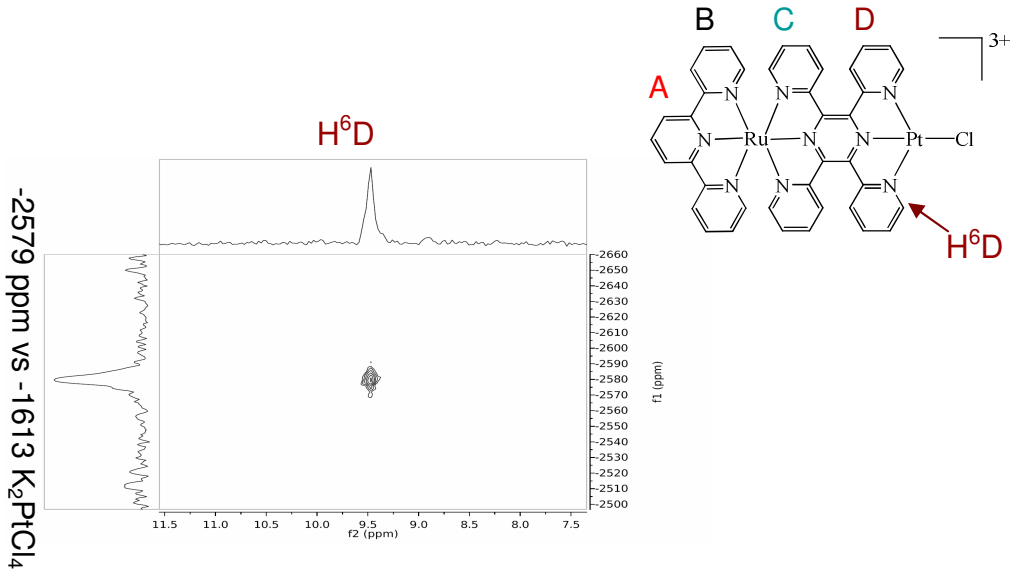

Figure 3.42. 600 MHz ^{195}Pt-^{1}H HMQC spectrum of [(tpy)Ru(tppz)PtCl](PF$_6$)$_3$ in CD$_3$CN

A cross signal was exhibited in the ^{195}Pt-^{1}H HMQC spectrum arising from the Pt and H^{6}D coupling (**Figure 3.42**). The Pt-H coupling results in slightly broadening of the signal of H^{6}C in ^{1}H-NMR, and the jagged edges are evidence of the Pt satellites owing to the long-range coupling. The δ of H^{6}C is observed at the lowest field (δ = 9.45 ppm) due

to the electron withdrawing effect of the coordinated chloride. With the confirmation on Ring D, the assignments of Ring C were straightforward with the help of the ^{1}H-^{1}H NOESY correlation and ^{1}H-^{1}H COSY.

In comparison to the ^{1}H-NMR spectra on $[Ru(tpy)_2](PF_6)_2$, $[(tpy)Ru(tppz)](PF_6)_2$ and $[(tpy)Ru(tppz)PtCl](PF_6)_3$, The δ of H^6B from $(tpy)Ru^{II}$ unit is always shown in the higher field than the δ of H^3B, attributing to the ring current effect on H^6B. While the ring current effect on the H^6C in $Ru^{II}(tppz)$ units is dependent on the coordination configurations. The δ of H^6C was influenced by the ring current effect in $[(tpy)Ru(tppz)PtCl](PF_6)_3$, but not in $[(tpy)Ru(tppz)](PF_6)_2$ and $[Ru(tppz)_2](PF_6)_2$ as the bridging mode of binding is needed to fix ring D in space.

3.2.2.5 ^{1}H NMR Assignment of $[ClPt(tppz)Ru(tppz)PtCl](PF_6)_4$

The ^{1}H NMR spectrum of $[ClPt(tppz)Ru(tppz)PtCl](PF_6)_4$ revealed eight resonances consistent with its structure. The NMR spectrum of $[ClPt(tppz)Ru(tppz)PtCl](PF_6)_4$ is simplified relative to $[(tpy)Ru(tppz)PtCl](PF_6)_3$ due to the presence of only tppz protons. Based on the identification of the H^3 protons by NOESY (**Figure 3. 39 (C)**), the sequence of the protons on ring C and D can be easily assigned. At room temperature in CD_3CN, the ^{1}H NMR spectrum of $[ClPt(tppz)Ru(tppz)PtCl](PF_6)_4$, reveals resonances due to protons of rings C and D that are quite comparable to $[(tpy)Ru(tppz)PtCl](PF_6)_3$. The H^6C are upfield shift arising from the ring current effect as expected. A unique feature in the ^{1}H NMR spectrum of $[ClPt(tppz)Ru(tppz)PtCl](PF_6)_4$ is the broadening of the resonances at δ 7.85 and 7.50 of protons H^{6C} and H^{5C}, respectively. As illustrated in **Figures 3.43**, variable temperature ^{1}H NMR spectroscopy in CD_3CN at -20 °C reveal two individual resonances for H^{6C} and H^{5C}, reflective of slow exchange at -20 °C. By contrast, the ^{1}H NMR spectrum of $[ClPt(tppz)Ru(tppz)PtCl](PF_6)_4$ at 60 °C show sharp resonances with the expected splitting pattern for H^{6C} and H^{5C} consistent with rapid exchange at this temperature. Surprisingly, the split peaks display a 2:1 integration ratio, which means that there are at least two conformations with different energy in the tri-metallic complex which are present in a 2:1 ratio.

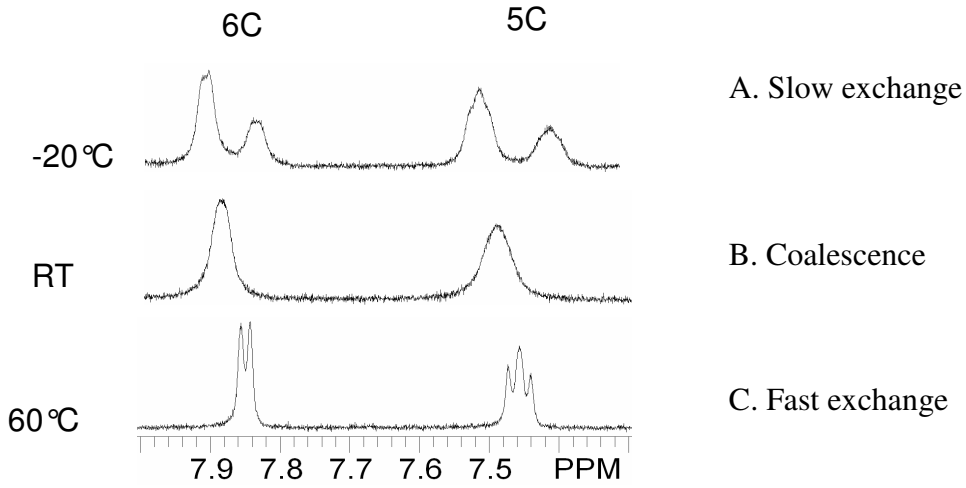

Figure 3.43. Selected region of the 400 MHz ^{1}H NMR spectrum of [ClPt(tppz)Ru(tppz)PtCl](PF$_6$)$_4$ in CD_3CN at -20, RT and 60 ºC showing slow exchange (A), coalescent (B) and rapid exchange (C) regimes.

For a situation in fast exchange, the observed chemical shift is the average of the individual species chemical shifts:[249]

$$\delta_{obs} = f_1\delta_1 + f_2\delta_2$$
$$f_1 + f_2 = 1$$

Where f_1 and f_2 are the mole fraction of each species, and δ_1 and δ_2 are the chemical shift of each species. From **Figure 3.43 (I)**, the 2:1 integration ratio corresponds to the population of the species in the two energy states. The calculated chemical shifts for H^{6}C and H^{5}C are 7.88 and 7.46 ppm, which are very close to the observed values, 7.85 and 7.47 ppm in **Figure 3.43 (III)**. The rationalization of the two separate forms of this complex as well as the 2:1 ratio of these will be discussed in **Section 3.2.5**.

3.2.2.6 Summary

A combination of NMR techniques is demonstrated to fully assign the spectra of the class of tpy and tppz Ru^{II},Pt^{II} mixed-metallic complexes. The assignments of the resonances on [(tpy)Ru(tppz)]$(PF_6)_2$, [(tpy)Ru(tppz)PtCl]$(PF_6)_3$, and [ClPt(tppz)Ru(tppz)PtCl]$(PF_6)_4$ were confirmed by the direct evidence from 1D ^{1}H-NMR and ^{195}Pt-NMR, 2D ^{1}H-^{1}H COSY, ^{1}H-^{1}H NOESY and ^{195}Pt-^{1}H HMQC, and variable temperature dynamic NMR techniques. Precautions must be taken in assigning ^{1}H resonances in systems with significant ring current effects on the NMR spectra despite the apparent simplicity of the ^{1}H-NMR spectra. The molecular conformation, chelation effect, electron withdrawing effect should also be taken into account when making assignments. The results and information gained here can be applied for the assignments of the ^{1}H NMR spectra of such tridentate complexes with substituted tpy/tppz ligands.

3.2.3 Crystallography

The use of tppz as a bridging ligand has been an intriguing synthetic approach to construct supramolecular building blocks due to tppz's structure versatility.

3.2.3.1 Crystal Structure Determination

After numerous trials, the single crystals of $[(tpy)Ru(tppz)PtCl](PF_6)_3$ and $[ClPt(tppz)Ru(tppz)PtCl][PF_6]_4$ suitable for X-ray crystallography were successfully obtained (Special thanks are given to our X-ray crystallographer: Dr. Carla Slebodnick, for her patient and professional assistance to help me solve the structures of the bimetallic and trimetallic complexes, $[(tpy)Ru(tppz)PtCl](PF_6)_3$ and $[ClPt(tppz)Ru(tppz)PtCl][PF_6]_4$). The experimental crystallographic data and selected bond lengths and angles for $[(tpy)Ru(tppz)PtCl](PF_6)_3$ and $[ClPt(tppz)Ru(tppz)PtCl][PF_6]_4$ are given in **Tables 3.9, 3.10 and 3.11**, and the perspective views are illustrated in **Figure 3.44**.

In each structure, Pt^{II} atoms displaying a distorted square planar geometry, and Ru^{II} centers display distorted octahedral geometry. The coordinated tppz adopted the saddle-like configurations to relieve the steric repulsion arising from the H^3 positions on neighboring rings. The four pyridine rings are in alternating trans positions from the pyrazine plane. Such binding mode causes a substantial distortion on the pyrazine rings with the torsion angle in the pyrazine ring ranging from -14.24º to 21.60º. The X-ray structures of these two complexes reveal some intermolecular interactions, such as C-H···Cl hydrogen bonds, C-H···π, π···π interactions and Pt···Pt interactions.

X-ray analyses reveal a racemic mixture of polymorphs with heterochiral packing fashion in the crystal lattice for both $[(tpy)Ru(tppz)PtCl](PF_6)_3$ and $[ClPt(tppz)Ru(tppz)PtCl][PF_6]_4$. The M (like the nomenclature of S or Λ) and P (like the nomenclature of Δ or R) descriptors are used to address the chirality of the skew-line convention arising from the translation and rotation in the molecules, **Figure 1. 25**.[200]

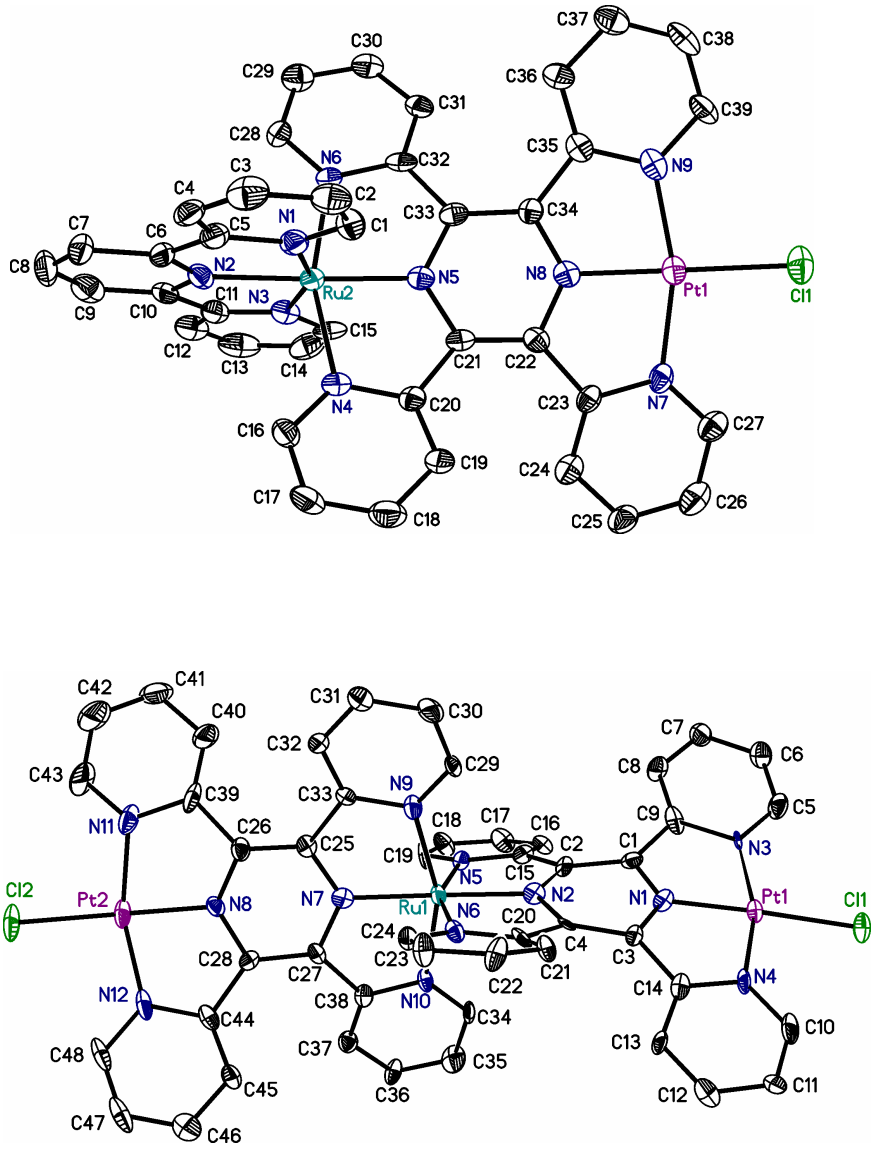

Figure 3.44. The 50% thermal ellipsoid representations of the cations $[(tpy)Ru(tppz)PtCl]^{3+}$ (top) and $[ClPt(tppz)Ru(tppz)PtCl]^{4+}$ (bottom) (tpy = 2,2':6',2''-terpyridine, tppz = 2,3,5,6-tetrakis(2-pyridyl)pyrazine), the counterions, solvents and hydrogens are omitted for clarity.

Table 3.9. Crystallographic data collection and structure refinement parameters for $[(tpy)Ru(tppz)PtCl](PF_6)_3$ and $[ClPt(tppz)Ru(tppz)PtCl](PF_6)_4$

Identification code	$[(tpy)Ru(tppz)PtCl](PF_6)_3$	$[ClPt(tppz)Ru(tppz)PtCl][PF_6]\cdot 2CH_3CN\cdot Et_2O$
Empirical formula	$[C_{39}H_{27}ClN_9PtRu][PF_6]_3\cdot C_7H_8$	$C_{56}H_{48}Cl_2F_{24}N_{14}OP_4Pt_2Ru$
Formula weight	1480.35	2075.11
Space group	C2/c	$P2_1/c$
a (Å)	16.4811(3)	12.4793(2)
b (Å)	31.2657(7)	24.3668(5)
c (Å)	19.9039(3)	22.5775(4)
α (°)	90	90
β (°)	94.364(2)	103.4360(10)
γ (°)	90	90
Volume ($Å^3$)	10226.6(3)	6677.5(2)
Z	8	4
Temperature (K)	100(2)	100(2)
Density (calcd., Mg/m^3)	1.923	2.064
Wavelength (Å)	0.71073	0.71073
Absorption coefficient (mm^{-1})	3.286	4.700
Final R indices	R1 = 0.0432, wR2 = 0.1282	R1 = 0.0605, wR2 = 0.1111
R indices (all data)	R1 = 0.0596, wR2 = 0.1384	R1 = 0.0955, wR2 = 0.1268

Table 3.10. Selected bond length (Å) and angles (deg) for [(tpy)Ru(tppz)PtCl]$(PF_6)_3$.

Pt(1)-N(7)	2.012(6)	N(2)-Ru(2)-N(1)	78.5(2)
Pt(1)-N(8)	1.947(6)	N(5)-Ru(2)-N(6)	80.3(2)
Pt(1)-N(9)	1.999(6)	N(8)-Pt(1)-N(9)	81.5(2)
Pt(1)-Cl(1)	2.2971(19)	N(8)-Pt(1)-Cl(1)	179.58(17)
Ru(2)-N(1)	2.066(6)	C(19)-C(20)-C(21)-C(22)	18.1(11)
Ru(2)-N(2)	1.989(6)	C(20)-C(21)-C(22)-C(23)	21.2(12)
Ru(2)-N(3)	2.084(6)	C(21)-C(22)-C(23)-C(24)	17.0(11)
Ru(2)-N(4)	2.066(5)	C(31)-C(32)-C(33)-C(34)	19.7(11)
Ru(2)-N(5)	1.951(6)	C(32)-C(33)-C(34)-C(35)	20.7(12)
Ru(2)-N(6)	2.050(5)	C(33)-C(34)-C(35)-C(36)	14.4(11)

Table 3.11. Selected bond length (Å) and angles (deg) for [ClPt(tppz)Ru(tppz)PtCl]$(PF_6)_4$.

Pt(1)-N(1)	1.923(8)	N(1)-Pt(1)-Cl(1)	177.4(2)
Pt(1)-N(3)	1.982(8)	N(1)-Pt(1)-N(3)	82.0(3)
Pt(1)-N(4)	1.999(9)	N(5)-Ru(1)-N(6)	157.2(3)
Pt(1)-Cl(1)	2.291(2)	N(8)-Pt(2)-N(12)	81.4(3)
Pt(2)-N(8)	1.928(7)	N(8)-Pt(2)-Cl(2)	179.7(3)
Pt(2)-N(12)	1.987(9)	N(9)-Ru(1)-N(10)	158.0(3)
Pt(2)-N(11)	2.006(10)	C(2)-C(1)-C(9)-C(8)	22.4(17)
Pt(2)-Cl(2)	2.294(2)	C(9)-C(1)-C(2)-C(15)	27.1(17)
Ru(1)-N(2)	1.982(8)	C(1)-C(2)-C(15)-C(16)	11.8(16)
Ru(1)-N(5)	2.072(8)	C(2)-C(15)-C(16)-C(17)	173.9(10)
Ru(1)-N(6)	2.086(8)	C(3)-C(4)-C(20)-C(21)	19.8(16)
Ru(1)-N(7)	1.986(8)	C(4)-C(3)-C(14)-C(13)	7.2(16)
Ru(1)-N(9)	2.070(8)	C(14)-C(3)-C(4)-C(20)	30.6(17)
Ru(1)-N(10)	2.083(7)	C(25)-C(26)-C(39)-C(40)	14.7(18)
N(2)-Ru(1)-N(7)	178.9(3)	C(26)-C(25)-C(33)-C(32)	11.5(17)
N(2)-Ru(1)-N(5)	78.9(3)	C(28)-C(44)-C(45)-C(46)	173.7(9)
N(7)-Ru(1)-N(9)	78.7(3)	C(28)-C(27)-C(38)-C(37)	16.2(16)
		C(33)-C(25)-C(26)-C(39)	23.9(17)

The bimetallic complex, $[(tpy)Ru(tppz)PtCl](PF_6)_3$, crystallizes in the chiral C_2/c space group. A discrete pair of enantiomers (**Figure 3.45, A & B**) is stacked in a head to tail fashion in the solid state structure, in which the two Pt centers of the two independent molecules in the unit cell have a Pt···Pt distance of 3.3218(5) Å, indicating a weak Pt···Pt interaction. As depicted in **Figure 3.45 D**, such packing pattern is stabilized by the two C-H···Cl interactions, which are separated by a typical distance of 2.670 Å, enhancing the π···π stacking from the pyrazine planes. These pairs of racemic motifs propagate into two dimensional grids via the offset face-to-face and edge-to-face π···π interactions (**Figure 3.45 E**). Such packing mode resembles the analogous $[M(tpy)_2]^{n+}$ complexes with orthogonal heteroaromatic ligand planes.[250]

The trimetallic complex, $[ClPt(tppz)Ru(tppz)PtCl](PF_6)_4$, crystallizes in a chiral $P2_1/c$ space group. Analysis of the crystal packing of $[ClPt(tppz)Ru(tppz)PtCl](PF_6)_4$ reveals that the molecules are arranged in different patterns compared to $[(tpy)Ru(tppz)PtCl](PF_6)_3$. In the solid structure of $[ClPt(tppz)Ru(tppz)PtCl](PF_6)_4$, **Figure 3.46 A & B**, the tppz skeletons clearly adopt the saddle-like conformations with the four pyridine units pointing up and down alternating with respect to the mean plane of the pyrazine ring. This results in a pair of enantiomers, denoted as M-M and P-P. The unit cell carries two pairs of enantiomers of M-M···P-P via C-H···π interactions (2.543 and 3.003 Å), **Figure 3.46 C & D**. These two species are arranged in an alternating manner in the supramolecular architecture. The short C-H···Cl interactions (2.744 Å and 2.771 Å) direct the self-assembly along a continuous one-dimensional chain, enhanced by π ···π interactions from the peripheral pyridine rings, **Figure 3.46 E**.

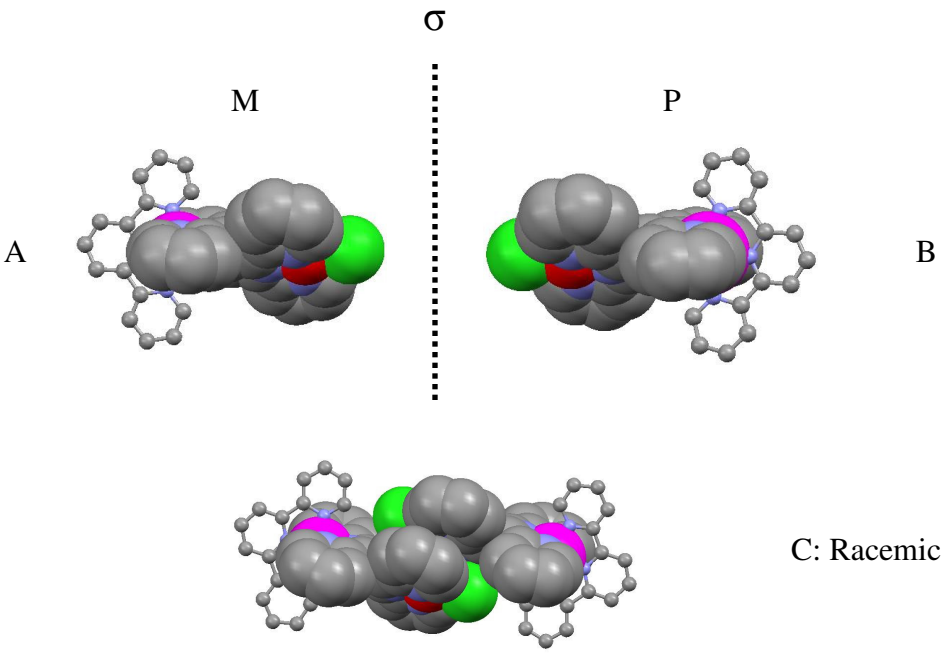

C: Racemic M···P dimer

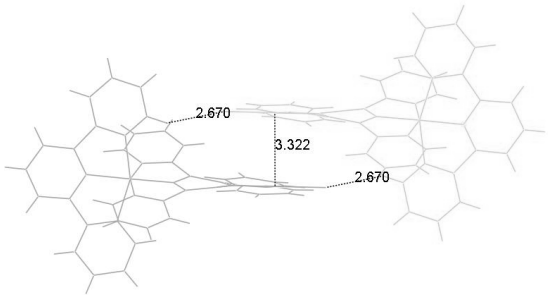

D: Intermolecular interactions in one pair of enantiomers via Pt···Pt interaction (3.322 Å) enhanced by the C-H···Cl hydrogen bonds (2.670 Å).

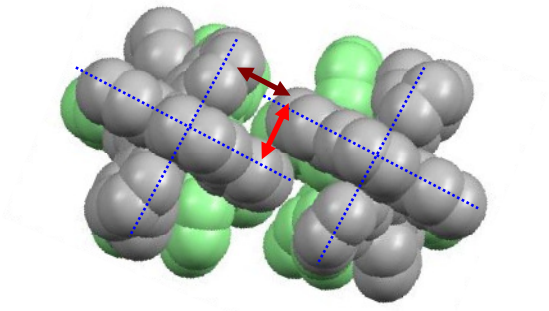

E: Stacking of the two pairs of enantiomers via face-to-face and edge-to-face π···π interactions.

Figure 3.45. Illustration of the pairwise assembly of $[(tpy)Ru(tppz)PtCl]^{3+}$ motif comprises racemic dimer (M···P). The intermolecular interaction via Pt···Pt and C-H···Cl to form two paired dimers via face-to-face and edge-to-face π···π stacking.

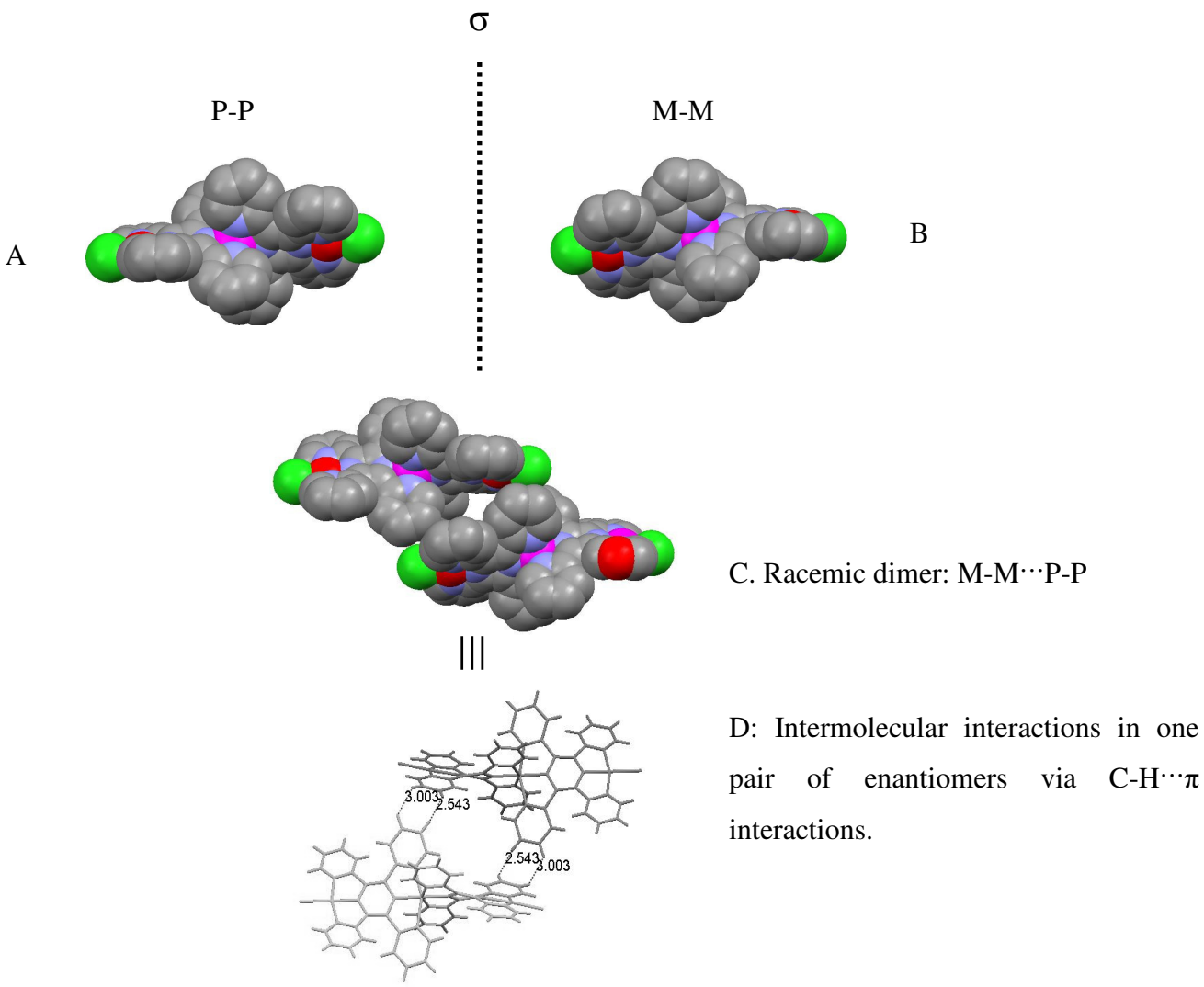

Figure 3.46. Representation of the crystal structure of $[ClPt(tppz)Ru(tppz)PtCl]^{4+}$. Racemic conformations of the trimetallic complex, M-M (A) and P-P (B) form the racemic dimer (C) via C-H···π interactions (D), and the extension of the 1D chain via C-H···Cl interactions (E).

In summary, X-ray crystallographic data of the two complexes confirm the identity of the metal complexes. In the tpy-capped bimetallic complex, $[(tpy)Ru(tppz)PtCl](PF_6)_3$, Pt···Pt interactions dominate the supramolecular assembling with a Pt···Pt distance of 3.3218(5) Å, enhanced by the C-H···Cl hydrogen bonds, **Figure 3.45 D**. In the open-ended trimetallic complex, $[ClPt(tppz)Ru(tppz)PtCl][PF_6]_4$, concerted interactions of the two enantiomers combo can be extended to 2D lamellar assemblies by utilizing the self-complementary molecular recognitions though C-H···Cl and π ··· π interactions, **Figure 3.46, D**.

3.2.4 Morphology of the Aggregation

The X-ray analysis demonstrates the self-assembly of the trimetallic complex via weak intermolecular interactions. With these results in mind, the self-assembly process was further investigated by electron microscopy.

A strategy to build up the 3D supramolecular architecture was systematically made from the 1D, 2D to 3D controlled assemblies. The two enantiomers were arranged in a well-defined pattern. The morphology of the self assembling racemic compound was further verified by scanning electronic microscopy (SEM) studies (SEM was carried out using instruments in the Nanoscale Characterization and Fabrication Laboratory, a Virginia Tech facility operated by the Institute for Critical Technology and Applied Science (ICTAS)). The sample was prepared by casting a drop of CH_3CN/Et_2O solution of the $[ClPt(tppz)Ru(tppz)PtCl](PF_6)_4$ on silica. The sample solution was the one in which the single crystal was grown and solved by X-ray crystallography. As shown in **Figure 3.46**, presumably, in the early stage, the molecular association and the growth of the fibrous structure can occur most advantageously in dilute solution. Then the aggregation should proceed to form a sheet-like structure at high concentration. The SEM image of this mixture established that the sheet-like structure was constructed. With the evaporation of the solvent, the lamellar structures are propagated to a 3D network leading to the formation of the flower-like structure. Such characteristic structure is due to the nature of the molecular geometry. This architecture opens the door for potential application of these solid structures of the trimetallic complex as a catalytic material with high surface area and channels containing reactive Pt sites.

The surface of the 3D flower-like image contains the fingerprints of the 1D fibrous structures and 2D plate-like structures. It is notable that cooperation and/or competition between the intermolecular interactions result in the formation of structures with different morphologies. The 3D flower network is possibly initiated from any of the direction of a, b or c axes.

A: 1D fibrous assembly

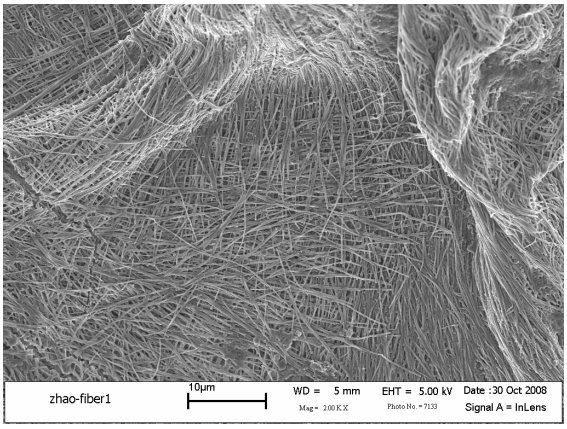

C: 3D flower-like assembly

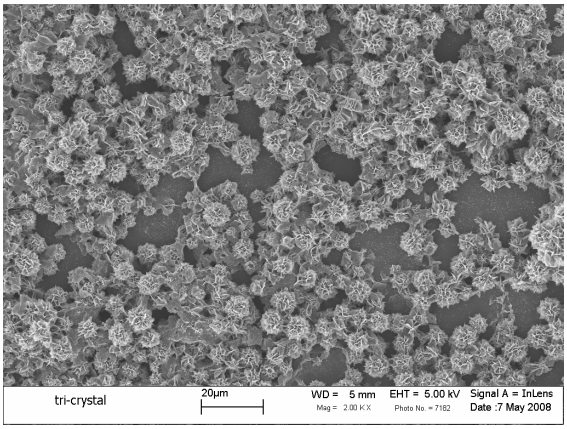

B: zoomed 1D fibrous assembly

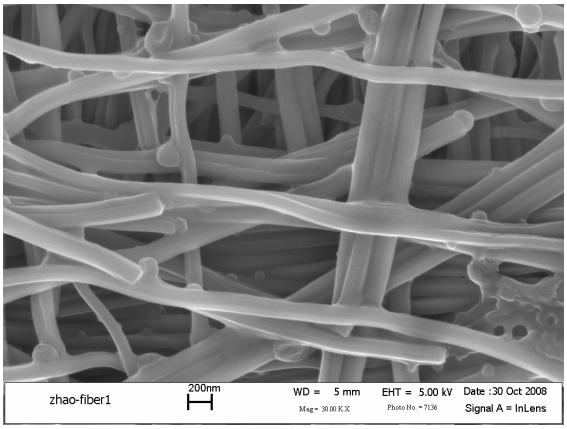

D: zoomed 3D flower-like assembly

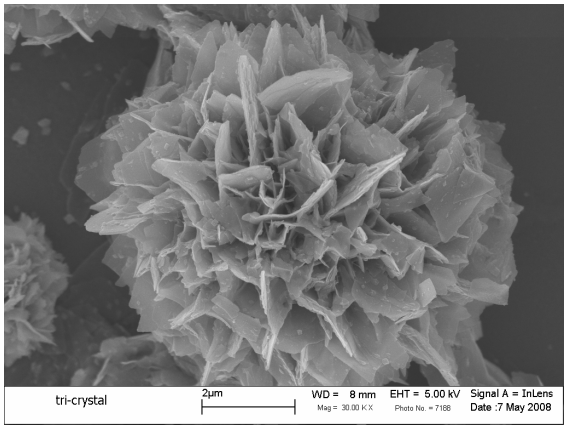

Figure 3.47. SEM images showing the self-assembly of the trimetallic complex, $[ClPt(tppz)Ru(tppz)PtCl][PF_6]_4$, from 1D fiber to 3D flower-like arrays.

3.2.5 ^{1}H-NMR Revisited

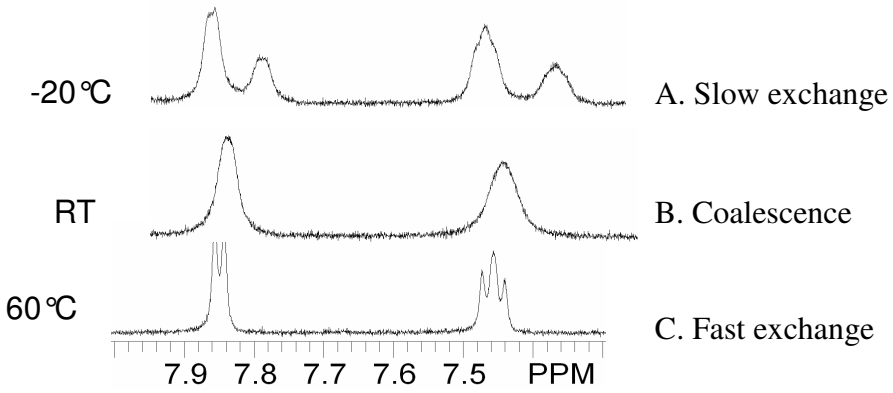

Figure 3.43. Selected region of the 400 MHz ^{1}H NMR spectrum of [ClPt(tppz)Ru(tppz)PtCl](PF$_6$)$_4$ in CD_3CN at -20, RT and 60 ºC showing slow exchange (A), coalescent (B) and rapid exchange (C) regimes.

The X-ray crystallography provides insight into the broadened ^{1}H-NMR spectrum of [ClPt(tppz)Ru(tppz)PtCl](PF$_6$)$_4$, specifically for H^{6}C and H^{5}C peaks, **Figure 3.43**. From the X-ray analysis, two stable conformations of the trimetallic complex, M-M and P-P are confirmed in the solid state. These two stereoisomers have the same energy state because of their symmetries and should give the same ^{1}H-NMR spectrum. The two conformations can convert to each other via an intermediate in solution. If there are two chiral centers in one molecule, another meso type isomer is possible, M-P or P-M. As a result, the exchange between M-M and P-P can take place at RT via the intermediate, M-P, with the possible energy profile being illustrated in **Figure 3.48**. The exchange process between the three stereoisomers can be studied by the variable temperature NMR experiments. By lowering the temperature to -20ºC, two individual resonances for H^{6}C and H^{5}C appears, reflective of slow exchange between the M-M, P-P and M-P, P-M isomers. The ^{1}H resonances for both sets of isomers can be observed during this dynamic process at lower temperature. The relative energy of these pair of isomers should be such that the population of M-P (or P-M) is half of the total population of the two enantiomers, M-M

and P-P although we can not rule out the reverse being true. Our data does not rule out the possibility that M-P (or P-M) isomers are twice the population of the M-M and P-P enantiomers. The M-P or P-M isomers are likely less stable conformations, because these configurations require an unusual unusual distortion of the octahedral geometry at the Ru center. The ^{1}H-NMR spectrum at -20ºC agrees with this interpretation with a 2:1 integration ratio from the two separated peaks. On the other hand, sharp resonances with the expected splitting pattern for $H^{6}C$ and $H^{5}C$ were observed at 60ºC, indicating the rapid exchange at this temperature.

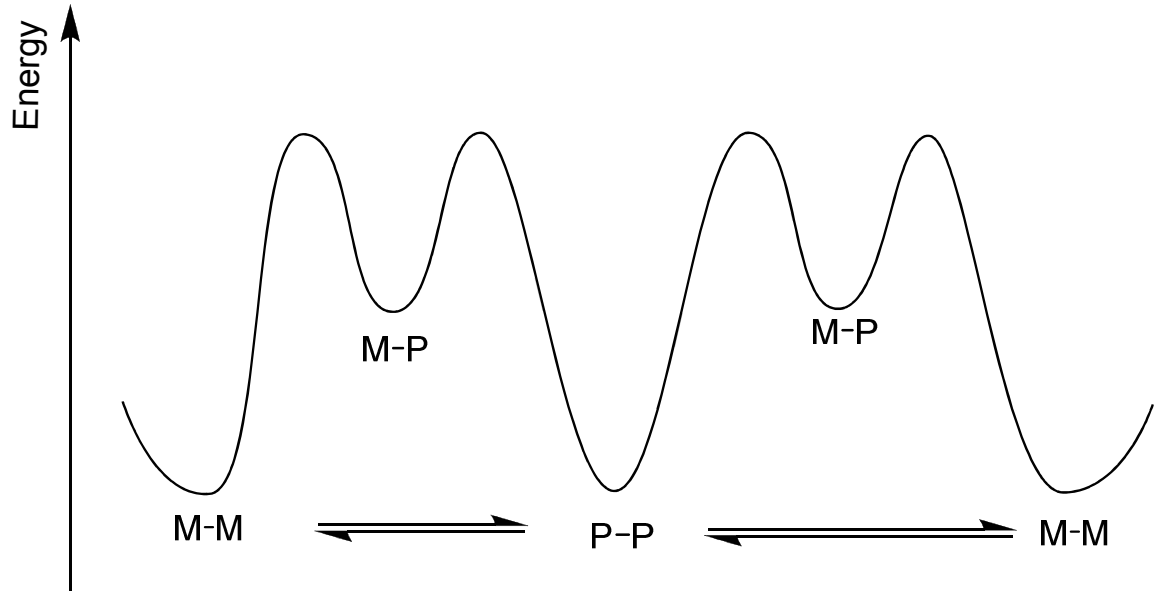

Figure 3.48. Representation of the energy profile of the M-M, M-P and P-P stereoisomers of the trimetallic complex, $[ClPt(tppz)Ru(tppz)PtCl](PF_6)_4$

The exchange rates (k) can be obtained from the NMR data by the following equations for the fast exchange, coalescent and slow exchange:[249]

$$k_{fast} = \frac{\pi \Delta \upsilon_0^2}{2(W_{1/2,E} - W_{1/2,O})}$$

$$k_{coalescence} = \frac{\pi \Delta \upsilon_0}{\sqrt{2}}$$

$$k_{slow} = \pi (W_{1/2,E} - W_{1/2,O})$$

where k is the exchange rate, $W_{1/2}$ is the peak width at half height, υ_0 is the peak frequency, W_E is the the peak width at half height at the limit of fast exchang, and W_O is the the peak width at half height at the limit of no exchange.

Since H^6C an H^5C are equally populated exchange sites with the identical ratio of 2:1, the activation energy ($\Delta^{\neq}G$) can be calculated from the exchange rate (k) by the following equation:[249]

$$\Delta G^{\neq} = RT[23.8 + \ln \frac{k}{T}]$$

where R is the gas constant, T is the temperature in kelvin.

The exchange rate and activation energy of $[ClPt(tppz)Ru(tppz)PtCl][PF_6]_4$ at RT can be estimated as 62~93 s^{-1} and 33~35 kJ/mol, respectively. Noteworthy, it is difficult to determine the accurate exchange rate from the NMR data if there are two different broadening positions, since this will cause two different $\Delta\upsilon_0$ values. Additional information such as the computational study could be carried out to support these calculated values from NMR data in the future.

No broadening in the ^{1}H-NMR spectrum for $[(tpy)Ru(tppz)PtCl](PF_6)_3$ is observed at RT. Low temperature NMR of $[(tpy)Ru(tppz)PtCl](PF_6)_3$ was carried out at -20ºC. No broadening and/or splitting of the peaks were observed. This supports the ^{1}H-NMR interpretation on the broadening of the trimetallic complexes. The bimetallic complex just has two enatiomers (M and P), which give the same ^{1}H-NMR spectrum. By contrast, the trimetallic complex has diastereomer (M-M, P-P, M-P), which give the proton resonance NMR spectrum with two distinctive peaks.

Chapter 4. Electrochemical, Spectroscopic and Photophysical Properties

In this chapter, we study the response of the metal complexes to changes in redox state and optical excitation. This provides insight into the ground and excited state reactivity of these complexes as well as providing information about orbital energetics.

4.2 Electrochemistry

The electrochemical data of the title complexes $[(tpy)Ru(tppz)PtCl](PF_6)_3$ and $[ClPt(tppz)Ru(tppz)PtCl](PF_6)_4$, along with related complexes and free ligands, are given in **Table 4.12**. The electrochemical properties are all measured in acetonitrile solution with 0.1 M Bu_4NPF_6 as the supporting electrolyte. All reported potentials ($E_{1/2}$) are calculated by averaging the E_p^a and E_p^c obtained by cyclic voltammetry (CV), the potential values are in V vs Ag/AgCl reference electrode (0.21 V vs. NHE) calibrated against Fc/Fc^+ couple (0.665 V vs. NHE).[251] The redox processes are assigned based on the electrochemistry of the free ligand tppz and tpy,[3, 20, 31, 42, 252] and the reported monometallic complexes of $[Ru(tppz)_2]^{2+}$ and $[(tpy)Ru(tppz)]^{2+}$ by Thummel,[29] Abruna[27] and our group[40]. The potentials presented in **Table 4.12** for these complexes are all based on our own synthesized complexes under our own conditions for comparison. The CVs of these complexes can be found in the **Appendix, Figures A.12-14**.

Table 4.12. Electrochemical data for Ru^{II} and Pt^{II} of the tridentate complexes. Potentials reported vs. Ag/AgCl (0.21 V vs. NHE) in CH_3CN with 0.1 M Bu_4NPF_6 (tpy = 2,2':6',2''-terpyridine, tppz = 2,3,5,6-tetrakis(2-pyridyl)pyrazine).

Compound	$E_{1/2}$ (V vs. Ag/AgCl)	Assignments
$[Ru(tppz)_2](PF_6)_2$	1.54	$Ru^{II/III}$
	-0.85	$tppz^{0/-}$
	-1.06	$tppz^{0/-}$
$[(tpy)Ru(tppz)](PF_6)_2$	1.42	$Ru^{II/III}$
	-0.95	$tppz^{0/-}$
	-1.39	$tpy^{0/-}$
$[(tpy)Ru(tppz)Ru(tppz)](PF_6)_4$	1.51	$Ru^{II/III}$
	1.86	$Ru^{II/III}$
	-0.30	$tppz^{0/-}$
	-0.82	$tppz^{0/-}$
$[(tpy)Ru(tppz)Ru(tpy)](PF_6)_4$	1.39	$Ru^{II/III}$
	1.72	$Ru^{II/III}$
	-0.45	$tppz^{0/-}$
	-0.94	$tppz^{-/2-}$
$[(tpy)Ru(tppz)PtCl](PF_6)_3$	1.63	$Ru^{II/III}$
	1.12	$Pt^{II/IV}$
	-0.16	$tppz^{0/-}$
	-0.70	$tppz^{-/2-}$
$[ClPt(tppz)Ru(tppz)PtCl](PF_6)_4$	1.83	$Ru^{II/III}$
	1.24	$Pt^{II/IV}$
	-0.03	$tppz^{0/-}$
	-0.17	$tppz^{0/-}$

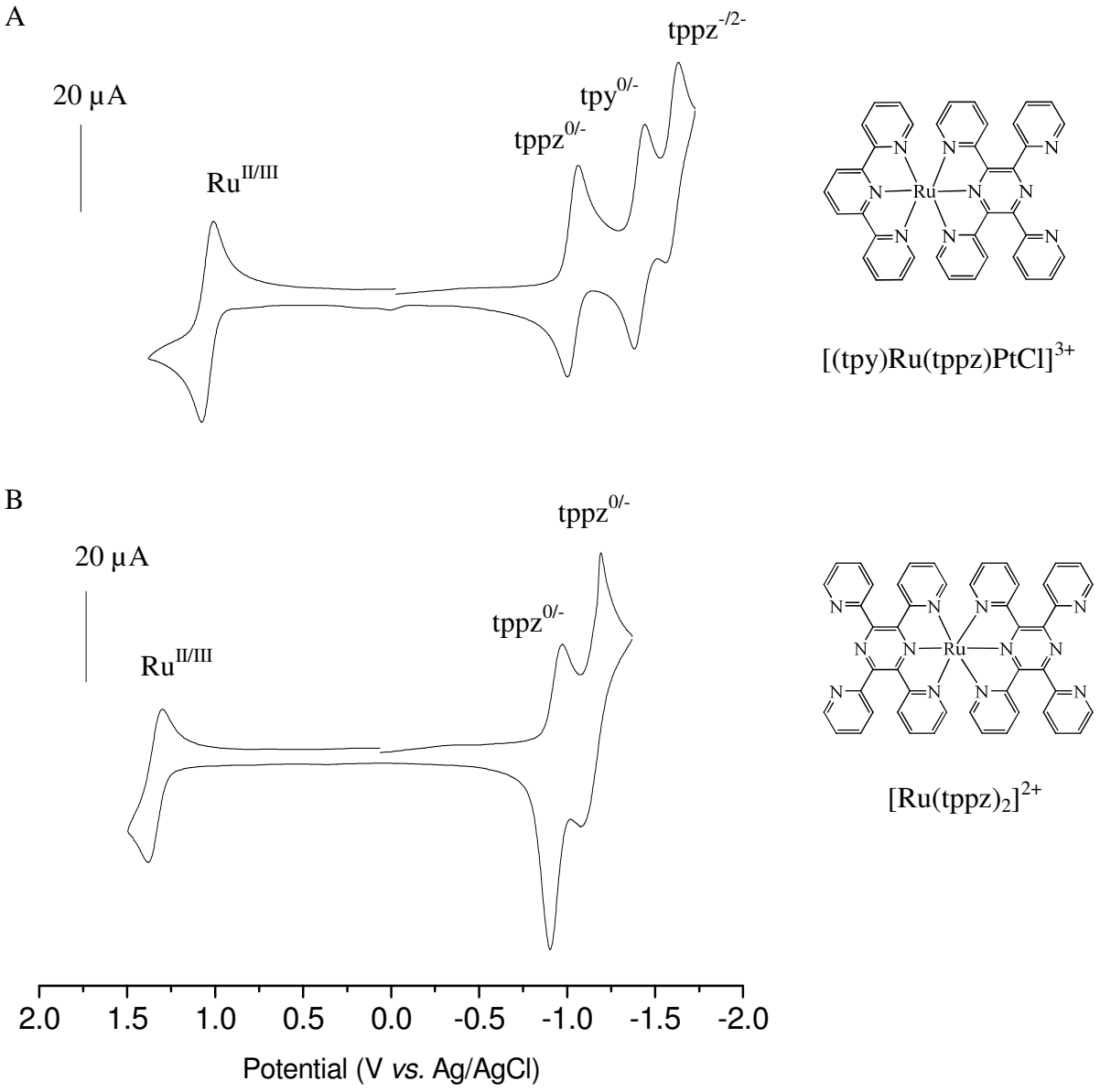

Figure 4.49. Cyclic voltammetry of the monometallic complexes, $[(tpy)Ru(tppz)](PF_6)_2$ (A) and $[Ru(tppz)_2](PF_6)_2$, (B) in CH_3CN with 0.1 M Bu_4NPF_6, scan rate = 100 mV/s. Potentials reported vs. Ag/AgCl (0.21 V vs. NHE), tpy = 2,2':6',2''-terpyridine, tppz = 2,3,5,6-tetrakis(2-pyridyl)pyrazine

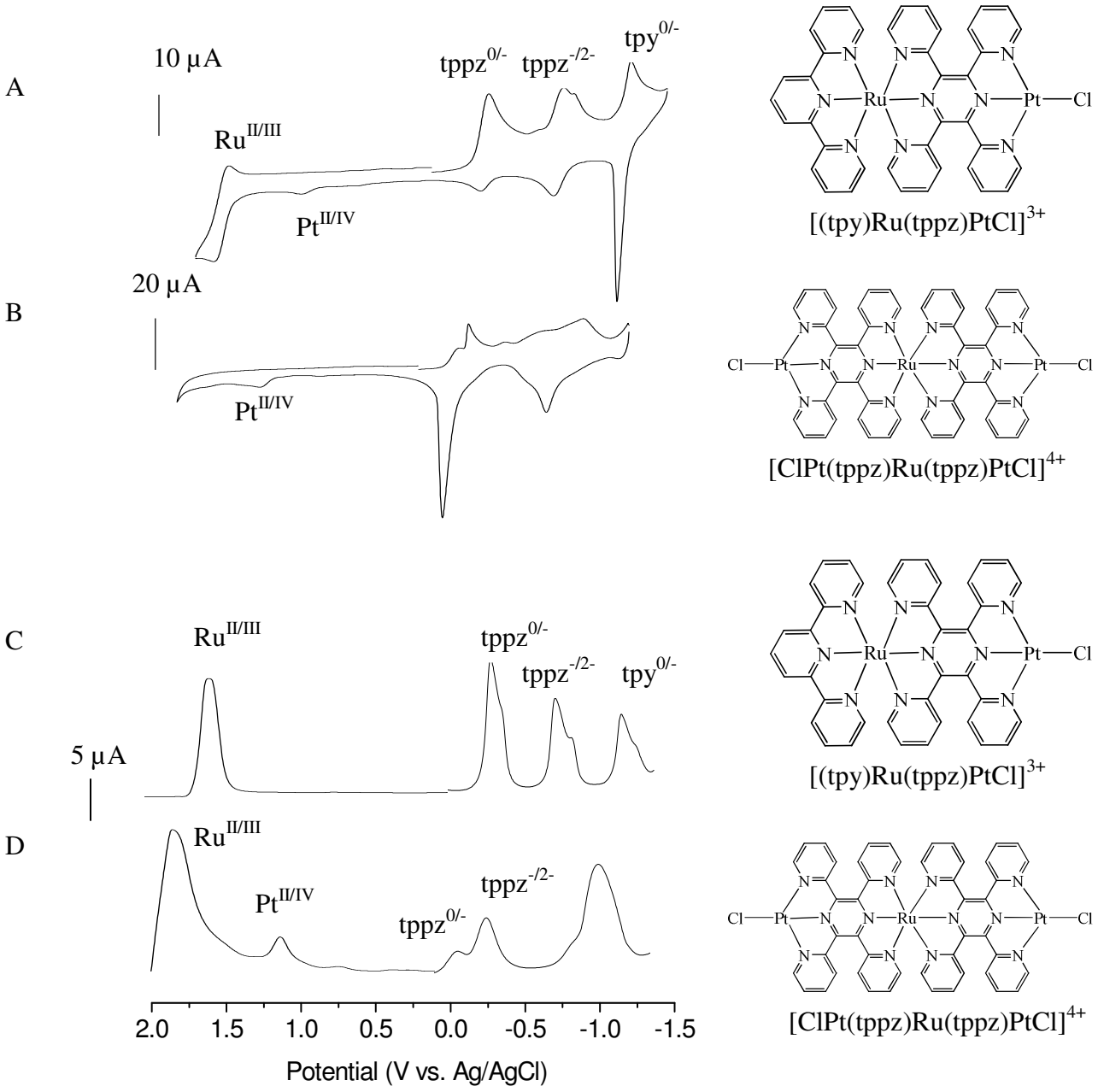

Figure 4.50. Cyclic voltammetry (A and B, scan rate = 100 mV/s) and square wave voltammetry (C and D, Step potential E = 4 mV, S.W. Amplitude = 25 mV, Frequency = 15 Hz) of bimetallic complex, $[(tpy)Ru(tppz)PtCl](PF_6)_3$ (A, C), and trimetallic complex, $[ClPt(tppz)Ru(tppz)PtCl](PF_6)_4$ (B, D) in CH_3CN with 0.1 M Bu_4NPF_6, Potentials reported vs. Ag/AgCl (0.21 V vs. NHE), tpy = 2,2':6',2''-terpyridine, tppz = 2,3,5,6-tetrakis(2-pyridyl)pyrazine

4.2.1 Electrochemical Properties of Monometallic Precursors

The cyclic voltammograms of $[(tpy)Ru(tppz)](PF_6)_2$ was shown in **Figure 4.49 (A)**. One reversible oxidation ($i_p^c/i_p^a \approx 1$) and three reversible reduction ($i_p^c/i_p^a \approx 1$) were observed for $[(tpy)Ru(tppz)](PF_6)_2$. The oxidation at 1.40 V was assigned as $Ru^{II/III}$ metal based process, indicative of the Ru metal center as the site of the localization of HOMO. The first reduction at -0.95 V was assigned as $tppz^{0/-}$ based reductions, reflective of the ligand as the localization of the LUMO. The second reduction peak at -1.39 V corresponds to $tpy^{0/-}$ electron transfer. The third reduction at -1.61 V was assigned as a second tppz based reduction, $tppz^{-/2-}$ on the basis of the reductions observed in the tpy, and tppz free ligands and $[Ru(tpy)_2](PF_6)_2$.[29]

The cyclic voltammograms of $[Ru(tppz)_2](PF_6)_2$ was shown in **Figure 4.49 (B)**. One reversible oxidation ($i_p^c/i_p^a \approx 1$) and two reversible redox ($i_p^c/i_p^a \approx 1$) processes were observed. The oxidation at 1.54 V was assigned as $Ru^{II/III}$ metal based process. The two successive reductions at -0.85 V and -1.06 V were ascribed to the first reduction for each tppz. For comparison, the $Ru^{II/III}$ couple of the monometallic synthon, $[Ru(tppz)_2](PF_6)_2$, is shifted to more positive potential by 120 mV relative to $[(tpy)Ru(tppz)](PF_6)_2$. The more positive first reduction potential observed for $[Ru(tppz)_2](PF_6)_2$ compared to $[(tpy)Ru(tppz)](PF_6)_2$ is due to the lower lying π^* orbitals of the tppz than tpy, supporting the ligand based reduction assignments on this type of metal complexes. Significant adsorption and desorption peaks are observed upon ligand reduction and reoxidation.

The assignments of the cyclic voltammograms of $[(tpy)Ru(tppz)](PF_6)_2$ and $[Ru(tppz)_2](PF_6)_2$ as well as the reported data here are consistent with previous reports of Brewer,[27] Thummel[29] and Abruna[40,27, 29, 40].

4.2.2 Electrochemical Properties of Ru^{II},Pt^{II} Mixed-metal Complexes

The cyclic voltammograms of $[(tpy)Ru(tppz)PtCl](PF_6)_3$ and $[ClPt(tppz)Ru(tppz)PtCl](PF_6)_4$ (**Figure 4.50 A, B**) were carried out at the same conditions as the monometallic complexes. Comparing to the monometallic complex, the cyclic voltammograms of Ru^{II},Pt^{II} mixed-metal complexes, particularly the trimetallic

complex, are distorted and the peaks are ill-resolved. Significant adsorption and desorption processes are also seen for these couples.

In the CV of $[(tpy)Ru(tppz)PtCl](PF_6)_3$, the $i_p^c/i_p^a \neq 1$ for all reductive processes is indicative of the quasi-reversible processes. Such quasi-reversible electrochemical properties is consistent with the molecular association of $[(tpy)Ru(tppz)PtCl](PF_6)_3$ in solution.

The ESI-MS data suggests $[(tpy)Ru(tppz)PtCl]^{3+}$ is associated in solution, giving assembly of dimers, trimers, etc. For the dimer, this process can be expressed as equilibrium balanced by the intermolecular attraction and coulombic repulsion (electrostatic interaction):

$$[Ru,Pt]^{3+} + [Ru,Pt]^{3+} \longleftrightarrow [Ru,Pt]^{3+}[Ru,Pt]^{3+}$$

In an applied electrical field (potential), take the reduction process as an example, the electroactive molecules ($[Ru,Pt]^{3+}$) which are electrostatically distributed along the electrode will be reduced by gaining electrons:

$$[Ru,Pt]^{3+} + e^- \longrightarrow [Ru,Pt]^{2+}$$

This process is then reversed by switching the potential scan resulting in oxidation of the electrochemically reduced species.

$$[Ru,Pt]^{2+} \longrightarrow [Ru,Pt]^{3+} + e^-$$

In the reduced form, $[Ru,Pt]^{2+}$ complex has a lower charge (+2 vs. +3) and should be more prone to associate due to the decreased electrostatic repulsion.

The reduction and oxidation potential of the complexes should be sensitive to its degree of association, and these processes occur at different potentials in the monomers, dimmers, etc. The $Pt^{II/III/IV}$ couple should be particularly sensitive to Pt…Pt associations

in solution. This process should give rise to quasi-reversible and ill-reduced electrochemistry.

A more distorted CV (**Figure 4.50 B)** was observed for the trimetallic complex, $[ClPt(tppz)Ru(tppz)PtCl](PF_6)_4$ than bimetallic complex, $[(tpy)Ru(tppz)PtCl](PF_6)_3$. This may result from the different intermolecular association between $[(tpy)Ru(tppz)PtCl](PF_6)_3$ and $[ClPt(tppz)Ru(tppz)PtCl](PF_6)_4$. The $[ClPt(tppz)Ru(tppz)PtCl](PF_6)_4$ should undergo chain-like molecular assembly as demonstrated in the crystal structure. This complex has Pt at each end of the molecule. Additionally, the $[Ru(tppz)_2]^{2+}$ synthon displays more significant adsorption following reduction which would further complicate the electrochemistry, **Figure 4.49 (B)**.

A more sensitive voltammetric method, square wave voltammetry (SWV), is used to provide better signal/noise ratio for $[(tpy)Ru(tppz)PtCl](PF_6)_3$ (**Figure 4.50 C**) and $[ClPt(tppz)Ru(tppz)PtCl](PF_6)_4$ (**Figure 4.50 D)**. The SWV also display significant adsorption behavior but allow better signal/noise. Interestingly, comparing the SWV of $[(tpy)Ru(tppz)PtCl](PF_6)_3$ and $[ClPt(tppz)Ru(tppz)PtCl](PF_6)_4$, a peak at ca 1.24 V was observed for $[ClPt(tppz)Ru(tppz)PtCl](PF_6)_4$, ascribing to the irreversible oxidation of $Pt^{II/IV}$. This may be due to the "open-ended" aggregation of $[ClPt(tppz)Ru(tppz)PtCl](PF_6)_4$ will make Pt sites not involved in Pt···Pt bonding, resulting in the observed oxidation. This value is comparable to the oxidation potential of $Pt^{II/IV}$ in [(tpy)PtCl]+ at 1.15 V vs. Ag/AgCl in DMF (**Appendix, Figure A.13**). In contrast, the Pt-Cl in $[(tpy)Ru(tppz)PtCl](PF_6)_3$ will be involved in Pt···Pt bonding when just two monomers assemble, weakening the signal from the any unassembled $Pt^{II/IV}$ oxidation.

4.2.3 Comparison of Electrochemical Properties of $Ru^{II}Pt^{II}$ Complexes with their Monometallic Precursors

The electrochemistry of $[(tpy)Ru(tppz)PtCl](PF_6)_3$ and $[ClPt(tppz)Ru(tppz)PtCl](PF_6)_4$ consist of $Ru^{II/III}$ based oxidations and ligand based reductions, **Table 4.12**. CV and SWV of these complexes display complicated electrochemistry, which is reflective the composition of the electroactive subunits and

intermolecular association in solution. The electrochemical properties provide insight into the relative orbital energies of HOMO and LUMO.

The electrochemical properties of $[(tpy)Ru(tppz)PtCl](PF_6)_3$ and $[ClPt(tppz)Ru(tppz)PtCl](PF_6)_4$ as well as their monometallic synthons are compared. The Ru center coordinated to two tppz ligands in $[ClPt(tppz)Ru(tppz)PtCl](PF_6)_4$ is more difficult to oxidize (1.83 V vs. Ag/AgCl) relative to $[(tpy)Ru(tppz)PtCl](PF_6)_3$ (1.63 V vs. Ag/AgCl), consistent with the better π accepting ability of the tppz ligand relative to tpy. Platinum coordination to the monometallic synthons $[(tpy)Ru(tppz)](PF_6)_2$ and $[Ru(tppz)_2](PF_6)_2$ also impacts the $Ru^{II/III}$ oxidation as evidenced by the $Ru^{II/III}$ couple of $[ClPt(tppz)Ru(tppz)PtCl](PF_6)_4$ occurring at the most positive potential, indicating the Ru-based HOMO. The peak observed at 1.24 V vs. Ag/AgCl for $[ClPt(tppz)Ru(tppz)PtCl](PF_6)_4$ was assigned to the irreversible $Pt^{II/IV}$. The $Pt^{II/IV}$ oxidation occurred at a more positive potential in the trimetallic complex, $[ClPt(tppz)Ru(tppz)PtCl](PF_6)_4$ relative to the bimetallic complex, $[(tpy)Ru(tppz)PtCl](PF_6)_3$ (1.12 V vs. Ag/AgCl), consistent with the more positive charge of the trimetallic systems.

The reductive electrochemistry of $[(tpy)Ru(tppz)PtCl](PF_6)_3$ and $[ClPt(tppz)Ru(tppz)PtCl](PF_6)_4$ display tppz based reductions that occur at significantly more positive potentials compared to their monometallic synthons, $[(tpy)Ru(tppz)](PF_6)_2$ and $[Ru(tppz)_2](PF_6)_2$, respectively, **Table 4.12**. This positive shift implies that the coordination of Pt^{II} to the remote site of tppz affords significant stabilization of the tppz(π^*) acceptor orbitals in $[(tpy)Ru(tppz)PtCl](PF_6)_3$ and $[ClPt(tppz)Ru(tppz)PtCl](PF_6)_4$. For example, the $tppz^{0/-}$ couple shifts from -0.95 and -0.85 V vs. Ag/AgCl in $[(tpy)Ru(tppz)](PF_6)_2$ and $[Ru(tppz)_2](PF_6)_2$, respectively, to -0.16 and -0.03 V in $[(tpy)Ru(tppz)PtCl](PF_6)_3$ and $[ClPt(tppz)Ru(tppz)PtCl](PF_6)_4$ respectively. Stabilization of the tppz(π^*) orbital upon Pt coordination is significantly larger than with Ru coordination where the $tppz^{0/}$ process occurs at -0.30 V vs. Ag/AgCl for $[(tpy)Ru(tppz)Ru(tppz)](PF_6)_4$.[20] This is consistent with the electrochemistry of $[(bpy)_2Ru(dpp)PtCl_2]^{2+}$ vs $[(bpy)_2Ru(dpp)Ru(bpy)_2]^{4+}$,[121] which shows the ligand based first reduction at -0.49 V and -0.66 V after and before the Pt coordination. These tppz bridged systems have very low ligand based reduction potentials.

The electrochemical properties of $[(tpy)Ru(tppz)PtCl](PF_6)_3$ and $[ClPt(tppz)Ru(tppz)PtCl](PF_6)_4$ establish a Ru(dπ) HOMO (highest occupied molecular orbital) and tppz (π*) LUMO (lowest unoccupied molecular orbital) in these structural motifs. The electrochemistry predicts a lowest lying Ru(dπ)→tppz(π*) ^{3}MLCT excited state with a lower energy MLCT for $[(tpy)Ru(tppz)PtCl](PF_6)_3$ than $[ClPt(tppz)Ru(tppz)PtCl](PF_6)_4$.

4.3 Electronic Absorption and Emission Spectroscopy

Ruthenium polypyridyl complexes exhibit intense transitions in the UV region arising from the ligand based $n \rightarrow \pi^*$ and $\pi \rightarrow \pi^*$ transitions. The visible regions of the electronic absorption spectra display a large red shift upon complexation of Pt. The visible region is dominated by MLCT transitions from each metal to each acceptor ligand. The emission of polyazine complexes arises from the lowest lying ^{3}MLCT. A summary of the light absorbing and photophysical properties are given in **Table 4.13**.

Table 4.13. Summary of the spectroscopic data of $[(tpy)Ru(tppz)PtCl](PF_6)_3$ and $[ClPt(tppz)Ru(tppz)PtCl](PF_6)_4$ with their precursors, where tpy = 2,2':6',2''-terpyridine, tppz = 2,3,5,6-tetrakis(2-pyridyl)pyrazine.

Complex	λ_{max}^{abs} (nm)[a]	ε at λ_{max}^{abs} ($\times 10^{-4}$ $M^{-1}cm^{-1}$)	λ_{max}^{em} (nm)[b]	τ (ns)[b]
$[(tpy)Ru(tppz)](PF_6)_2$	472	1.6	667	67
$[Ru(tppz)_2](PF_6)_2$	478	2.3	646	81
$[(tpy)Ru(tppz)PtCl](PF_6)_2$	530	2.8	810	N/A[c]
$[ClPt(tppz)Ru(tppz)PtCl](PF_6)_4$	538	3.0	754	80

[a] Reported for the lowest energy ^{1}MLCT;

[b] Measured in deoxygenated CH_3CN;

[c] Weak emission for which an accurate lifetime can not be measured.

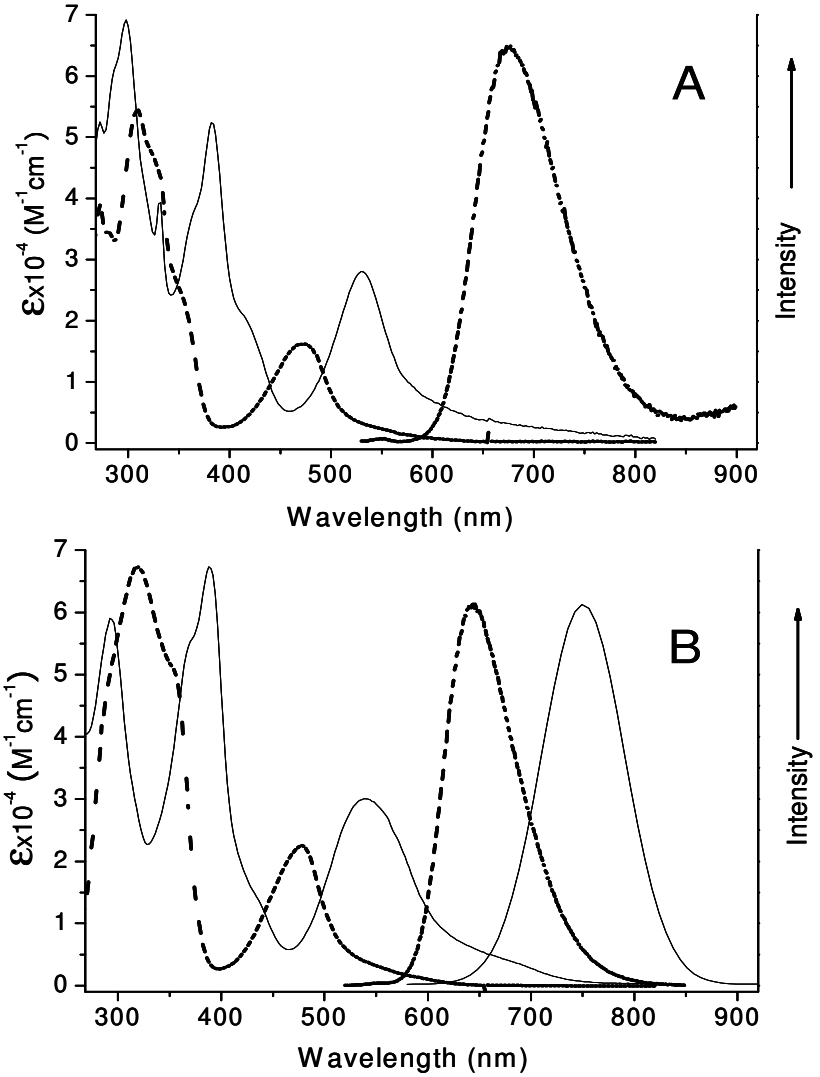

Figure 4.51. Electronic absorption and emission spectra for the mixed-metal supramolecular complexes and monometallic synthons (A) $[(tpy)Ru(tppz)](PF_6)_2$ (-----)and $[(tpy)Ru(tppz)PtCl](PF_6)_3$ (—) and (B) $[Ru(tppz)_2](PF_6)_2$ (-----) and $[ClPt(tppz)Ru(tppz)PtCl](PF_6)_4$ (—) measured in CH_3CN at RT (tpy = 2,2′,6′,2″-terpyridine and tppz = 2,3,5,6-tetrakis(2-pyridyl)pyrazine).

4.3.1 Electronic Absorption Spectroscopy

Light absorbing properties of the title complexes were investigated by electronic absorption spectroscopy. The electronic absorption spectra of the bimetallic and trimetallic complexes with their monometallic synthons are summarized in **Table 4.13** and the spectra shown in **Figure 4.51**.

The monometallic synthons display $\pi \rightarrow \pi^*$ transitions in the UV with MLCT transitions in the visible to both acceptor ligands with the Ru→tppz CT band being lowest in energy.[221] This $[Ru(tppz)_2](PF_6)_2$ MLCT band (λ_{max}^{abs} = 478) slightly shifts to lower energy compared to $[(tpy)Ru(tppz)](PF_6)_2$ (λ_{max}^{abs} = 472). This red shift is a result of the stabilization of the tppz π^* acceptor orbital, consistent with their electrochemical properties.

The complexes $[(tpy)Ru(tppz)PtCl](PF_6)_3$ and $[ClPt(tppz)Ru(tppz)PtCl](PF_6)_4$ are efficient light absorbers displaying intraligand (IL) $\pi \rightarrow \pi^*$ transitions in the UV and MLCT transitions in the visible, with the lowest energy transition being Ru(dπ)→tppz(π^*) MLCT in nature. Consistent with the stabilization of tppz(π^*) orbital upon Pt coordination, the Ru(dπ)→tppz(π^*) MLCT transitions are red shifted in $[(tpy)Ru(tppz)PtCl](PF_6)_3$ (λ_{max}^{abs} = 530 nm) and $[ClPt(tppz)Ru(tppz)PtCl](PF_6)_4$ (λ_{max}^{abs} = 538 nm) relative to their monometallic synthons. This stabilization of the tppz(π^*) orbital is consistent with the positive shift of the $tppz^{0/-}$ couple, as observed in the electrochemistry of $[(tpy)Ru(tppz)PtCl](PF_6)_3$ and $[ClPt(tppz)Ru(tppz)PtCl](PF_6)_4$, relative to their monometallic synthons. The spectroscopic properties of $[(tpy)Ru(tppz)PtCl](PF_6)_3$ and $[ClPt(tppz)Ru(tppz)PtCl](PF_6)_4$ suggests that upon light absorption, charge transfer is promoted towards the coordinated Pt center to the tppz BL.

4.3.2 Luminescent Properties of $[(tpy)Ru(tppz)PtCl](PF_6)_3$ and $[ClPt(tppz)Ru(tppz)PtCl](PF_6)_4$

Ruthenium polyazine complexes often possess lowest lying ^{3}MLCT states that are emissive. The prototypical bis-tridentate complex $[Ru(tpy)_2]^{2+}$, is not emissive, attributed to the presence of low-lying ligand field (^{3}LF) states that are thermally accessible at room temperature leading to rapid deactivation of the Ru(dπ)→tpy(π*) ^{3}MLCT state. Ruthenium complexes of the tridentate BL tppz have been shown to be emissive due to stabilization of the Ru(dπ)→tppz(π*) ^{3}MLCT state, which limits thermal population of the ^{3}LF state. The RT emission spectra recorded in deoxygenated CH_3CN solutions of the monometallic complexes $[(tpy)Ru(tppz)](PF_6)_2$ and $[Ru(tppz)_2](PF_6)_2$ and the trimetallic complex, $[ClPt(tppz)Ru(tppz)PtCl](PF_6)_4$, are shown in **Figure 4.51**. The complexes $[(tpy)Ru(tppz)](PF_6)_2$ and $[Ru(tppz)_2](PF_6)_2$ emit at 668 and 646 nm, respectively.

The trimetallic complex $[ClPt(tppz)Ru(tppz)PtCl](PF_6)_4$ displays a Ru(dπ)→tppz(π*) ^{3}MLCT emission centered at 754 nm with an excited state lifetime (τ) of 80 ns and Φ^{em} of 5.4 x 10^{-4}. The photophysical properties of $[ClPt(tppz)Ru(tppz)PtCl](PF_6)$ are comparable with $[(tpy)Ru(tppz)Ru(tppz)](PF_6)_4$; λ_{max}^{em} = 830 nm, τ = 100 ns; and Φ^{em} = 4.0 x 10^{-4}.[30] The Ru(dπ)→tppz(π*) ^{3}MLCT emission of $[ClPt(tppz)Ru(tppz)PtCl](PF_6)_4$ complex is significantly red-shifted relative to $[Ru(tppz)_2](PF_6)_2$, consistent with the stabilized tppz(π*) orbital upon Pt^{II} coordination. The intense emission of $[ClPt(tppz)Ru(tppz)PtCl](PF_6)_4$ affords a probe into its excited state reactivity and the 80 ns lifetime, significant time for excited state reactions.

4.3.3 Concentration Dependent Study of the Luminescent Property of [(tpy)Ru(tppz)PtCl](PF$_6$)$_3$

The difference in excited state properties of [(tpy)Ru(tppz)PtCl](PF$_6$)$_3$ and [ClPt(tppz)Ru(tppz)PtCl](PF$_6$)$_4$ complexes is an interesting result imparted by the difference in their structures. Platinum terpyridine complexes are known to undergo intermolecular Pt$^{\cdots}$Pt interactions that lead to quenching of the otherwise emissive ^{3}MLCT excited states. Such an interaction in our system is supported by the ESI-MS data. From the single crystal structure, the Pt$^{\cdots}$Pt interactions were observed in the solid state for [(tpy)Ru(tppz)PtCl](PF$_6$)$_3$. The Pt$^{\cdots}$Pt interactions in [(tpy)Ru(tppz)PtCl](PF$_6$)$_3$ to quench the ^{3}MLCT excited state requires the assembly of only two molecules, such quenching effect is concentration dependent. Measured under typical conditions, [(tpy)Ru(tppz)PtCl](PF$_6$)$_3$ does not display a detectable emission. When a CH_3CN solution of [(tpy)Ru(tppz)PtCl](PF$_6$)$_3$ is diluted to below 2.5 x 10^{-5} M, an extremely weak emission is observed at 810 nm (**Figure 4.52**). The emission intensity increases with decreasing metal complex concentration in marked contrast to most chromophores. This implies association via Pt$^{\cdots}$Pt interactions quenchs the emission of the bimetallic and the equilibrium of assembly lies largely towards assembled dimers, trimers, etc.

There is one emitting state in the monomer of bimetallic complex. The bimetallic complexes are prone to undergo intermolecular association in solution. Take the dimer of bimetallic complex as an example (**Figure 3.45, C**), both emitting states in the dimer is quenched via a direct attachment of the tppz to a Pt engaged Pt$^{\cdots}$Pt assembly. By contrast, the trimetallic complex is emissive even at higher concentrations. There are two emitting states in the monomer of the trimetallic complex. When the trimetallic molecules undergo intermolecular associations, take the dimer of trimetallic complex as an example (**Figure 3.46, C**), the two external emitting states should not be quenched even though the two internal emitting states are quenched. The emission of trimetallic complex might arise from the two external emitting states in the dimers. Even with large aggregation, the trimetallic complex has at each end unassembled Ru-tppz-Pt units. These ^{3}MLCT states can't all be quenched on the two tppz ligands in [ClPt(tppz)Ru(tppz)PtCl](PF$_6$)$_4$ even with assembly.

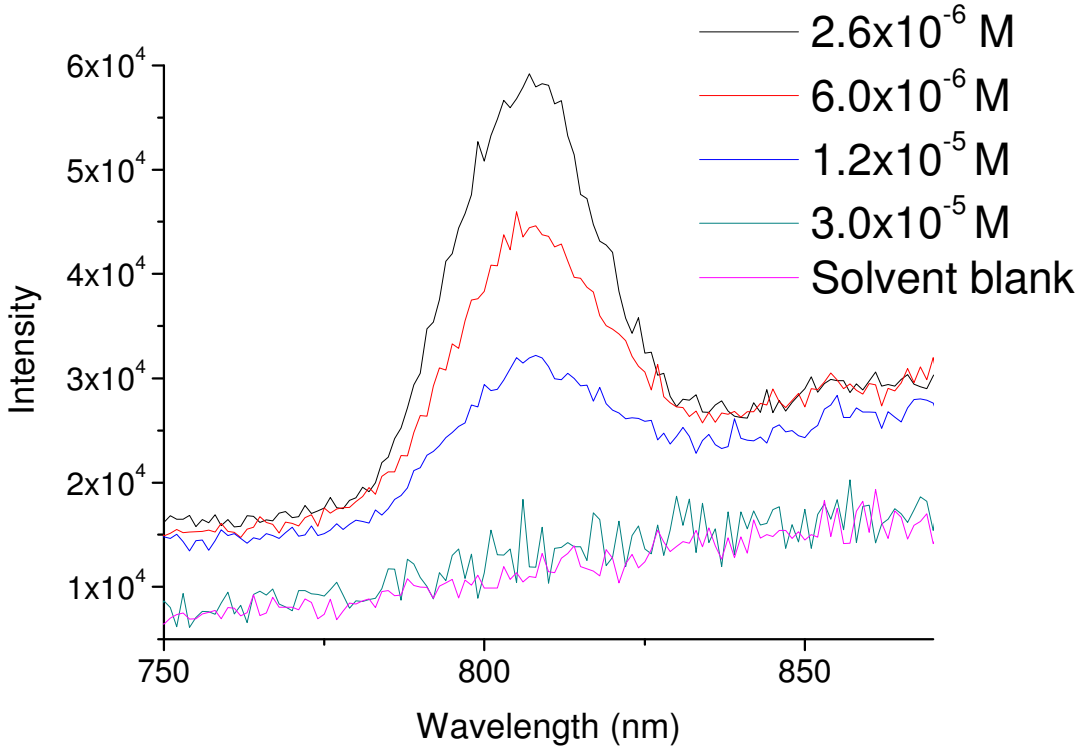

Figure 4.52. The concentration dependent emission spectra of $[(tpy)Ru(tppz)PtCl](PF_6)_3$

4.3.4 Solid State Emission Property of $[ClPt(tppz)Ru(tppz)PtCl](PF_6)_4$

Solid state emission was probed and $[ClPt(tppz)Ru(tppz)PtCl](PF_6)_4$ maintains the characteristic ^{3}MLCT emission at λ_{max}^{em} = 764 nm, while $[(tpy)Ru(tppz)PtCl](PF_6)_3$ does not display a detectable emission in the solid state, **Figure 4.53.**

Confocal laser induced emission scanning microscopy was applied to compare the luminescence difference between the bimetallic and trimetallic complexes (The experiments were conducted with the assistance from Dr. Kristi R. DeCourcy at Virginia Tech). No signal was observed for bimetallic powder in the confocal image, **Figure 4.53 (A)**. In contrast, the trimetallic powder displays intense emission, **Figure 4.53 (B)**.

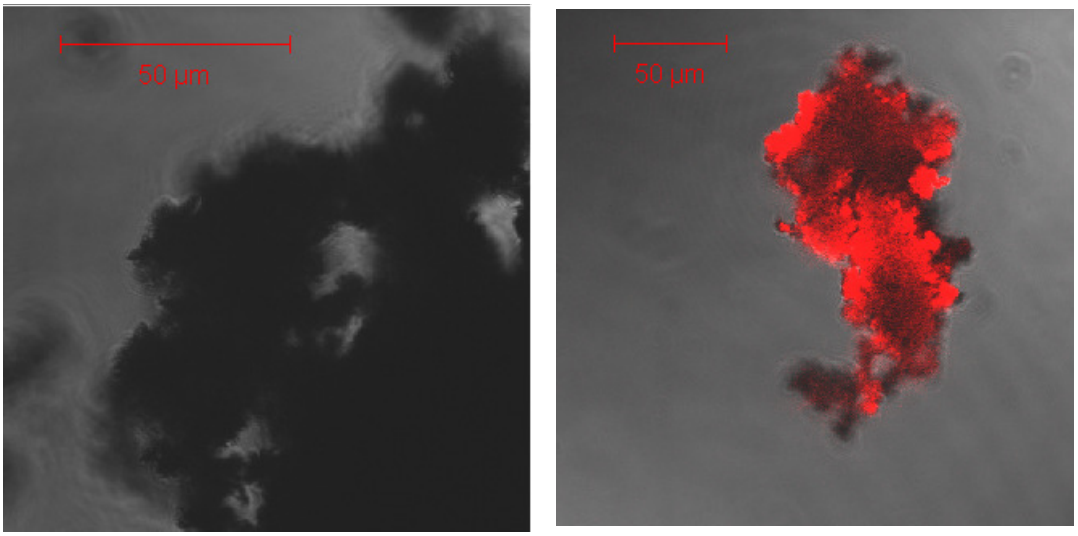

A B

Figure 4.53. Confocal laser scanning microscopy analysis of bimetallic powder $[(tpy)Ru(tppz)PtCl](PF_6)_3$ (A), trimetallic powder of $[ClPt(tppz)Ru(tppz)PtCl](PF_6)_4$ (B). The samples were excited with the 543 nm laser line (helium-neon) and emission detected by using a long pass filter (>633 nm).

Chapter 5. Applications: Metal Complex-DNA Interactions

The design of mixed metal supramolecular complexes of the type described above involves the coupling of a ruthenium polyazine light absorber to platinum bioactive sites. The supramolecular assemblies provide a TL-LA-BL-BAS (TL = terminal ligand, LA = light absorber, BL = bridging ligand, BAS = bioactive site) architecture in the bimetallic complex, $[(tpy)Ru(tppz)PtCl](PF_6)_3$, and BAS-BL-LA-BL-BAS architecture in the trimetallic complex, $[ClPt(tppz)Ru(tppz)PtCl](PF_6)_4$. These complexes are unique in their coupling of Ru bis(tridentate) LA units to a Pt^{II} center.[125]

The Ru^{II},Pt^{II} bimetallic complexes are efficient light absorbers. The tppz BL provides a low lying π* acceptor orbital affording a stabilized ^{3}MLCT state. Both title complexes possess low energy absorptions corresponding to the Ru(dπ)→tppz(π*) MLCT transition at 530 nm and 538 nm for $[(tpy)Ru(tppz)PtCl](PF_6)_3$ ($\varepsilon = 2.8\times10^4$ $M^{-1}cm^{-1}$) and $[ClPt(tppz)Ru(tppz)PtCl](PF_6)_4$ ($\varepsilon = 3.0\times10^4$ $M^{-1}cm^{-1}$), respectively, as shown in **Figure 4.51.**

5.1 Thermal Binding Study

The BAS Pt^{II} site in the $[(tpy)Ru(tppz)PtCl](PF_6)_3$ and $[ClPt(tppz)Ru(tppz)PtCl](PF_6)_4$ complexes possesses a labile chloride ligand similar to cisplatin. This labile site should allow for the covalent binding of these complexes to the nitrogen bases of DNA. The ability of the complexes to bind double stranded DNA was therefore examined by agarose gel electrophoresis. The DNA binding assays shown in **Figure 5.54** and **Figure 5.55** were conducted by Mr. A. J. Prussin, II.[125] This method provides a useful means for assessing covalent binding to DNA and comparing the binding properties of different metal complexes. The principle of this method is that molecules migrate in the gel as a function of their mass, charge, and shape, with supercoiled DNA migrating faster than open circular molecules of the same mass and charge. For these studies, the complexes were incubated for 2 hours with pUC18 plasmid DNA in phosphate buffer. Small aliquots of the solutions (10 μL containing 0.1 μg of

DNA) were mixed with 2 μL glycerol based gel loading buffer and loaded into the wells of a gel made with 0.8 % w/w agarose, 0.55 % w/w boric acid, and 1.08 % w/w Trisbase.

The DNA binding abilities of the $[(tpy)Ru(tppz)PtCl](PF_6)_3$ and $[ClPt(tppz)Ru(tppz)PtCl](PF_6)_4$ complexes were first probed as a function of the DNA base pair (BP) to metal complex (MC) ratio. DNA binding assays for these complexes and cisplatin are shown in **Figure 5.54**. In this study the metal complexes were incubated with circular pUC18 plasmid DNA at various BP:MC ratios at room temperature (RT) prior to analysis by agarose gel electrophoresis. In each case, lane λ is a molecular weight standard (23, 9.4, 6.6, 4.4, 2.3 and 2.0 kb). Lane C is the pUC18 DNA controls, showing the major supercoiled (Form I) and minor nicked (Form II) forms of the circular plasmid. Lanes 1-8 are the pUC18 DNA incubated with BP:MC ratios as 1:1, 2:1, 3:1, 5:1, 10:1, 20:1, 30:1, and 50:1, respectively.

Both title complexes bind to DNA as illustrated by the retardation of migration of the pUC18 plasmid through the agarose gel. This effect was found to be greater for both title complexes than for cisplatin (**Figure 5.54 A, B, and C**). This more pronounced effect has also been observed for the related bpy and tpy systems and could result from the higher cationic charge and molecular mass of our supramolecular complexes compared to cisplatin, from enhanced DNA binding or from larger changes in DNA structure upon MC binding.[121, 256] The migration of DNA in the presence of the trimetallic complex, $[ClPt(tppz)Ru(tppz)PtCl](PF_6)_4$, at a 10:1 BP:MC ratio was comparable to its migration in the precence of bimetallic complex, $[(tpy)Ru(tppz)PtCl](PF_6)_3$, at a 5:1 BP:MC ratio as shown in **Figure 5.54** B, C. This is consistent with the number of BAS in these metal complexes, implying that both Pt^{II} sites can bind to DNA in the trimetallic complex. Although the type of adduct that is formed (interstrand, intrastrand or monofunctional) cannot be determined from these experiments, these results confirm the covalent binding mode of these metal complexes with DNA and their promise as a new class of anticancer drugs having DNA as a target.

The impact of temperature on the covalent binding of $[(tpy)Ru(tppz)PtCl](PF_6)_3$ and $[ClPt(tppz)Ru(tppz)PtCl](PF_6)_4$ to circular plasmid DNA was also examined. Circular DNA contains a constant number of superhelical turns. A compound that unwinds DNA reduces the number of superhelical turns and therefore slows its migration through the gel.

This supercoiling of DNA has been shown to be disrupted by binding of the metal complexes such as cisplatin.[257-259] Cisplatin induces DNA unwinding process followed by crosslinking to reduce the size of the cisplatin-DNA adduct.[260] Lippard and coworkers have quantitatively determined the degree of DNA unwinding produced in specific adducts of cisplatin.[261]

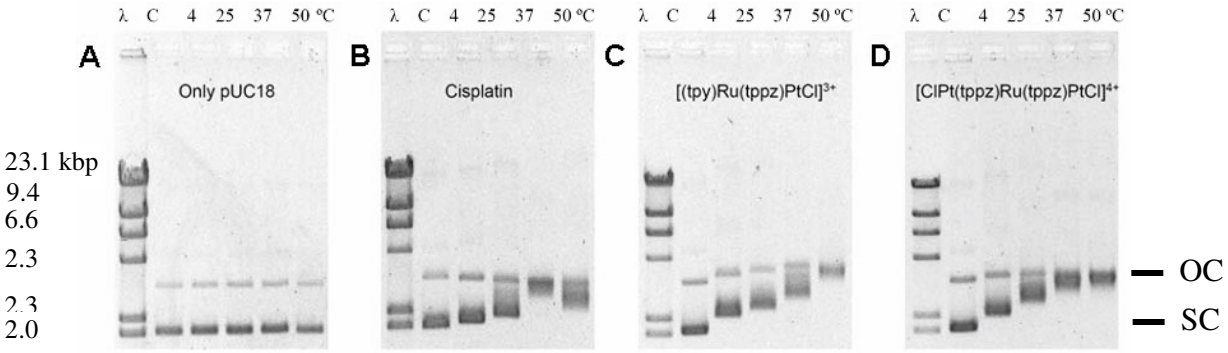

Figure 5.54. Binding study of cisplatin (A), $[(tpy)Ru(tppz)PtCl](PF_6)_3$ (B), and $[ClPt(tppz)Ru(tppz)PtCl](PF_6)_4$ (C) using circular plasmid pUC18 DNA with different BP:MC ratios at RT. Lanes 1, 2, 3, 5, 10, 20, 30 and 50 are the metal complex-DNA with the BP:MC ratios as 1:1, 2:1, 3:1, 5:1, 10:1, 20:1, 30:1, and 50:1 respectively. tpy = 2,2′:6′,2″-terpyridine and tppz = 2,3,5,6-tetrakis(2-pyridyl)pyrazine).

In this study, BP:MC ratios of 5:1 and 10:1 were used for $[(tpy)Ru(tppz)PtCl](PF_6)_3$ and $[ClPt(tppz)Ru(tppz)PtCl](PF_6)_4$, respectively, to maintain the same stoichiometry of Pt^{II} BAS to DNA BPs. The results of this study are shown in **Figure 5.55**. In all four panels, lane λ corresponds to the molecular weight marker. Lane C is the pUC18 DNA control. Lanes 4, 25, 37, and 50 are the MC-DNA mixture incubated at 4, 25, 37, and 50ºC, respectively for 2 hours. As a control, circular plasmid pUC18 DNA was incubated at different temperatures in the absence of metal complex, showing that this treatment by itself had no effect on the conformation of the plasmid (**Figure 5.55 A**). In contrast, incubation with cisplatin (**Figure 5.55 B**) resulted in retardation of DNA migration through the gel due to the unwinding of the supercoiled DNA, an effect that was

substantially enhanced with increasing incubation temperature (**Figure 5.55 A**, lanes 4, 25 and 37). The plasmid exhibited the slowest migration in the sample incubated at 37ºC,

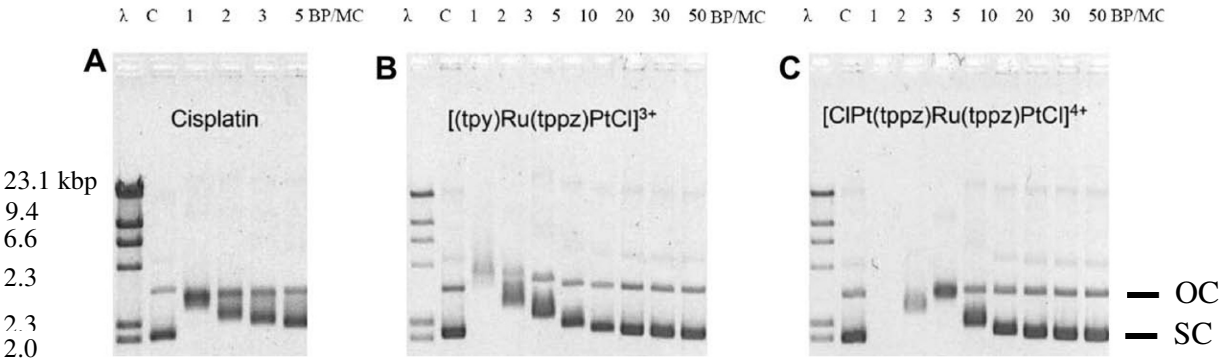

Figure 5.55. The impact of temperature on DNA binding to pUC18 DNA by metal complexes (A), cisplatin with 5:1 BP:MC (B), $[(tpy)Ru(tppz)PtCl](PF_6)_3$ with 5:1 BP:MC (C), and $[ClPt(tppz)Ru(tppz)PtCl](PF_6)_4$ with 10:1 BP:MC (D) at 4ºC, 25ºC, 37ºC and 50ºC. (tpy = 2,2′:6′,2″-terpyridine and tppz = 2,3,5,6-tetrakis(2-pyridyl)pyrazine).

suggesting that cisplatin had fully unwound the DNA in this case. At 50ºC (**Figure 5.55 A**, lane 50), cisplatin appeared to have introduced negative supercoils into the DNA, causing the plasmid to migrate more rapidly through the gel. Similar patterns have been reported in kinetic studies of cisplatin-DNA binding.[258, 260] The title complexes, $[(tpy)Ru(tppz)PtCl](PF_6)_3$ and $[ClPt(tppz)Ru(tppz)PtCl](PF_6)_4$, also reduced the migration of DNA in the gel as a function of temperature. This suggests that covalent binding of the MC to DNA is enhanced with increased incubation temperature, resulting in unwinding of the supercoiled DNA. However the title complexes did not lead to DNA compaction or rewinding at 50ºC as observed for cisplatin (lane 50 in **Figure 5.55 B, C, and D**). This may reflect a difference in the type of binding of our metal complexes compared to cisplatin, which is not surprising given the single labile Pt-Cl bond on the BAS compared to two Pt-Cl labile bonds in cisplatin. Single labile Pt-Cl bonds in our complexes only allow for the formation of monofunctional DNA adducts compared to the bifunctional DNA adducts formed by cisplatin. In the trimetallic complex of

[ClPt(tppz)Ru(tppz)PtCl]$(PF_6)_4$, there are also two Pt-Cl BAS at 180º vs. the 90º in cisplatin. This might allow the trimetallic interact to form more inter-strand crosslinks of DNA vs. the primarily intrastrand crosslinking presented by cisplatin. In addition, the bimetallic and trimetallic complexes have higher positive charges than cisplatin. The higher cationic charge and molecular weight of these mixed-metal complexes could result in a higher degree of DNA binding or a larger impact on DNA structure relative to cisplatin.

In summary, studies were performed on the interaction with DNA of Ru^{II},Pt^{II} mixed-metal supramolecular complexes of the form LA-BL-BAS and BAS-LA-BL-BAS. The complexes, [(tpy)Ru(tppz)PtCl]$(PF_6)_3$ and [ClPt(tppz)Ru(tppz)PtCl]$(PF_6)_4$, represent the first Ru^{II},Pt^{II} polyazine systems bridged by tppz BL shown to bind DNA. These complexes are efficient light absorbers with intense transitions throughout the UV and visible with the lowest transition being MLCT in nature to the tppz acceptor orbital. The title complexes exhibit enhanced modification of DNA structure as compared to a well known anticancer drug, cisplatin at much higher BP:MC ratios, displaying their promise as a new class of anticancer agents. DNA binding was also shown to be temperature dependent. The metal complexes, [(tpy)Ru(tppz)PtCl]$(PF_6)_3$ and [ClPt(tppz)Ru(tppz)PtCl]$(PF_6)_4$, displayed apparent enhanced unwinding of DNA with increase in temperature. The temperature dependent DNA interaction of the designed complexes was found to be different from that of cisplatin, presumably due to the presence of only a single labile chloride, higher molecular weight and positive charge in the title complexes compared to cisplatin. Work is currently in progress to further explore the mechanism of DNA binding of these and related systems.

5.2 Light Activated DNA Interactions

The emissive trimetallic complex [ClPt(tppz)Ru(tppz)PtCl]Cl_4 was studied further to assay light activated interactions of the complex with DNA. An emission titration and light activated agarose gel electrophoresis study were performed to investigate the photoinitiated interactions of this complex with DNA. In the emission titration studies, the emission properties of the trimetallic complex [ClPt(tppz)Ru(tppz)PtCl]Cl_4 at a constant concentration c = 1.3×10^{-5} M in an aqueous 10 mM sodium phosphate buffer (pH = 7) were monitored upon exposure to disodium-guanosine-5′-monophosphate (Na_2GMP), supercoiled pUC18 DNA and calf thymus DNA with the ratios of BP:MC = 5, 10, 20 and 40. In the gel electrophoresis study, a gel shift assay was planned to probe the photoreactivity of [ClPt(tppz)Ru(tppz)PtCl]Cl_4 with DNA using circular pUC18 with a 20:1 BP:MC ratio in an aqueous 10 mM sodium phosphate buffer (pH =7). The solutions were photolyzed with a 5W LED at 455 nm for one hour, and then assayed using gel electrophoresis and electronic absorption spectroscopy

5.2.1 Emission Titration

An emission titration experiment was conducted with the trimetallic complex dissolved in 10 mM sodium phosphate buffer (pH = 7) with addition of the dexoynucleotide disodium-guanosine-5′-monophosphate (Na_2GMP). A solution of 1.3×10^{-5} M [ClPt(tppz)Ru(tppz)PtCl]Cl_4 in 10 mM phosphate buffer (pH = 7) was assayed by emission spectroscopy. The emission was monitored as a function of added Na_2GMP. When the trimetallic complex was exposed to increasing amount of Na_2GMP, reduction of emission was observed, **Figure 5.56**. The chloride salt of trimetallic complex [ClPt(tppz)Ru(tppz)PtCl]Cl_4 showed luminescence in the aqueous solution (λ_{max}^{em} = 748 nm in H_2O). This emission is similar to that observed for the PF_6 salt of trimetallic complex in the organic solvent CH_3CN (λ_{max}^{em} = 764 nm). Upon introduction of Na_2GMP to an aqueous solution of the $[ClPt(tppz)Ru(tppz)PtCl]^{4+}$, the luminescence was quenched. The GMP could bond to the Pt site of the complex leading to an expected shift in the emission maxima. For this complex, emission quenching is seen. The guanine (G) ($E_{oxd/GMP}$ = 0.80 V vs. Ag/AgCl in aqueous solution)[262] is highly susceptible to oxidative

due to its lowest oxidation (oxd) potential among the four bases (G, C, A and T). Adding Na_2GMP to the $[ClPt(tppz)Ru(tppz)PtCl]Cl_4$ solution may result in excited state electron transfer or energy transfer quenching of the Ru chromophore. This would lead to quenching of the Ru ^{3}MLCT emission. The ^{3}MLCT excited states of Ru chromophores are often good oxidizing agents. The excited state reduction potential of the trimetallic complex can be estimated by the $E_{0\text{-}0}$ of the excited state (ES) and the ground state (GS) reduction (red) potential of the trimetallic complex. This analysis provides:

$$MC + h\upsilon \rightarrow MC^*$$

$$E_{red}^{ES} = E_{red}^{GS} + E_{0\text{-}0} = 0.28 \text{ V vs. Ag/AgCl}$$

This provides the driving force for the reactions ($E_{red}^{ES} < E_{oxd/GMP}$):

$$MC^* + G \rightarrow MC^- + G^+ (E_{redox})$$

$$E_{redox} = E_{oxd/GMP} - E_{red/trimetallic\ complex}^{ES} = 0.52 \text{ V}$$

Since the change in Gibbs free energy (ΔG) can be computed from E_{redox}. The sign of the change in free energy ($\Delta G = -nEF < 0$) associated with this process indicates the reaction will procede spontaneously.

Similar emission titration experiments were performed on $[ClPt(tppz)Ru(tppz)PtCl]Cl_4$ with addition of calf thymus or pUC18 DNA at BP:MC ratios of 5, 10, 20, and 40. After addition of even the lowest amount of DNA, no emission was detected in either case. The polyanionic properties of calf thymus or pUC18 DNA should faciliate the metal complex and DNA association leading to enhanced quenching of the luminescence of $[ClPt(tppz)Ru(tppz)PtCl]Cl_4$.

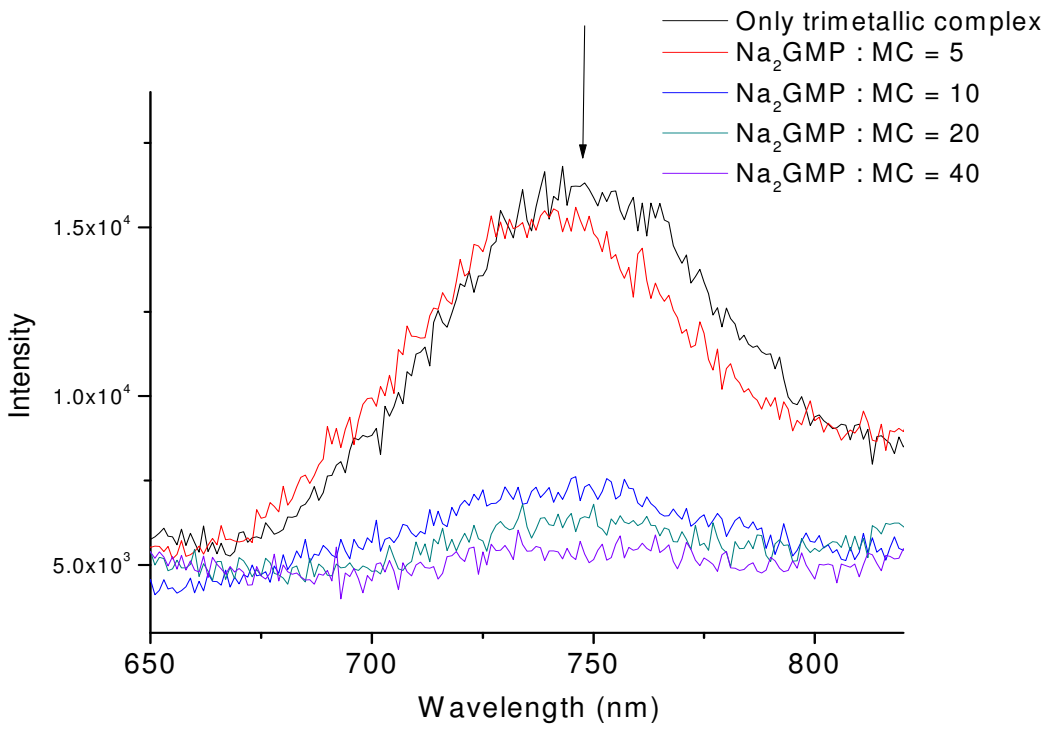

Figure 5.56. Emission titration data for of 1.3×10^{-5} M $[ClPt(tppz)Ru(tppz)PtCl]Cl_4$ in 10 mM phosphate buffer (pH = 7) upon addition of guanosine 5'-monophosphoric acid disodium salt (Na_2GMP) with the 5, 10, 20 and 40 Na_2GMP:MC ratios. The solution was deoxygenated by bubbling with Ar for 15 minutes before conducting the emission measurements.

5.2.2 Photoreactivity of $[ClPt(tppz)Ru(tppz)PtCl]Cl_4$ with DNA

The complex $[ClPt(tppz)Ru(tppz)PtCl]Cl_4$ was dissolved in 10 mM phosphate buffer (pH = 7) and combined mixed with pUC18 DNA in a 20:1 BP:MC ratio. The effect of irradiation at 455 nm using a 5 W LED light source were then examined using a gel electrophoresis assay. Interestingly, a reddish precipitate was observed after irradiation of the trimetallic complex/pUC18 (BP:MC = 20) sample for one hour. The morphology of the condensate of DNA with the trimetallic complex is illustrated in **Figure 5.57**. This structure is characteristic of condensed DNA morphology. DNA condensation behaviors

has been observed for ruthenium (II) polypyridyl complexes although to date no demonstration of light activated DNA condensation is reported.[263] The electronic absorbance spectra (**Figure 5.58**) of the photolyzed solution before and after photolysis indicate that neither the cationic trimetallic complex nor the anionic DNA are present in solution after photolysis. This solution has essentially no light absorbing species present. When loaded the supernatant to an agarose gel, no DNA was observed for the gel electrophoresis assay of pUC18 after photolysis, **Figure 5.59**. In this figure, Lane λ represents Lambda DNA HindIII digest molecular weight marker, Lane C represents pUC18 DNA without the metal complex, which shows that the pUC18 DNA exists

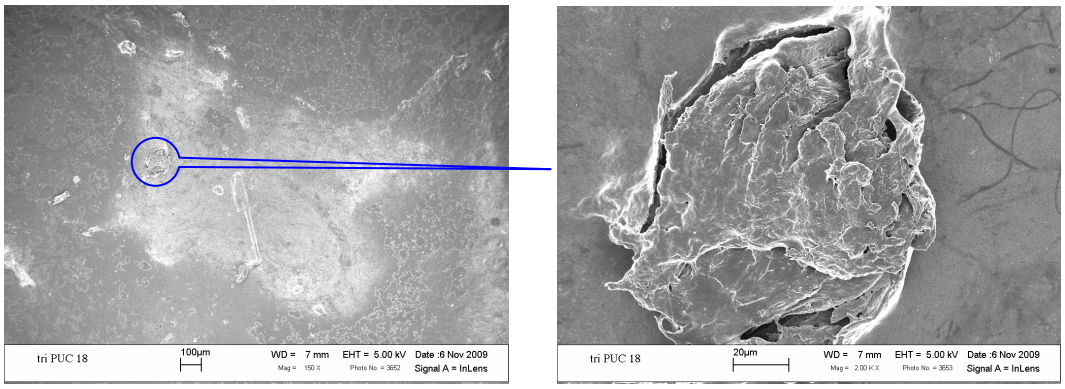

Figure 5.57. The morphology of the condensed pUC18 DNA with the trimetallic complex at a 20:1 BP:MC ratio irradiated at 455 nm for 1 hr using a 5 W LED light source.

primarily in the supercoiled form. Lane 1 represents the supercoiled pUC18 DNA with the trimetallic complex added (BP:MC = 20) without photolysis, which shows the trimetallic complex binds to DNA providing a slight slowing of migration of the pUC18 DNA through the gel. Lane 2 represents the sample photolyzed with 455 nm LED for one hour, which contains no dectable DNA, suggesting that no DNA is left in the solution. It is well known that cationic metals with high charge density such as Mg^{2+} can condense DNA,[264] providing a compact less soluble form. The observed photochemistry of the trimetallic complex with DNA is consistent with light activated DNA condensation. This is not typically seen for Ru^{II},Pt^{II} polyazine complexes. To the best of our knowledge, this

observation is the first case of light activated DNA condensation by a metal complex. The nature of the trimetallic complex provides the possibility for multiple binding modes with DNA as we indicated in **Section 5.1**. In the presence of light, the excited metal complex may lose chloride to give rise to enhanced DNA crosslinking. This light induced binding to DNA by two sites on one molecule can lead to crosslinking and compaction of DNA. Such DNA condensation provides possible areas to inhibit DNA unwinding and double strand separation needed for cell replication. This exciting new method to use visible light to efficiently condense DNA should provide an oxygen independent means to prohibit DNA replication in cancerous cells, may offer a new approach into development of light activated cancer treatment. The application of these systems in photodynamic therapy is underway. Further study is required to elucidate the detail of the DNA-MC interaction mechanism. This unusual result is the subject of ongoing investigation.

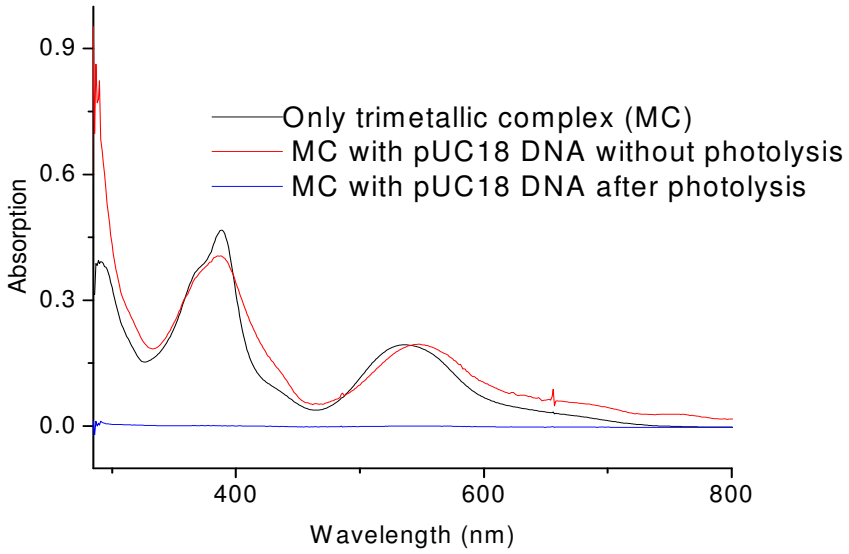

Figure 5.58. Electronic absorption spectra of $[ClPt(tppz)Ru(tppz)PtCl]Cl_4$ in the absence (—) and presence of pUC18 (—) and following photolysis (—) in 10 mM phosphate buffer (pH = 7). Sample was photolyzed with 455 nm light from a 5W LED for one hour.

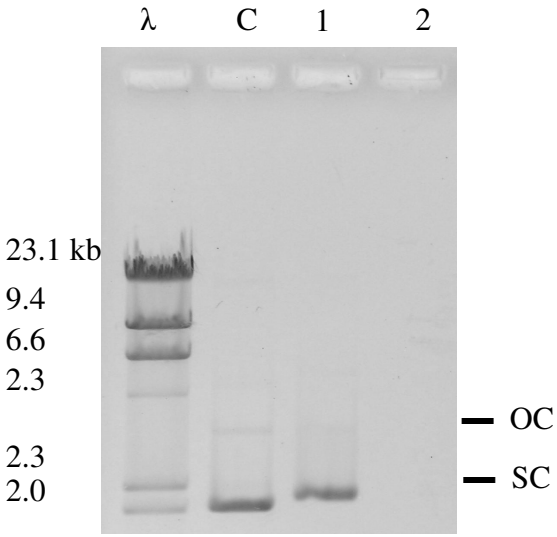

Figure 5.59. Agarose gel electrophoresis studies on the MC-DNA interactions of the complex $[ClPt(tppz)Ru(tppz)PtCl]Cl_4$ with BP:MC = 20. Lane λ is the Lambda DNA hindIII digest molecular weight marker with bands at 23.1, 9.4, 6.6, 4.4, 2.3 and 2.0 k base pairs, Lane C is pUC18 DNA control without added metal complex, Lane 1 is the metal complex with pUC18 DNA at a 20:1 BP:MC ratio without photolysis, and Lane 2 is the metal complex with pUC18 DNA at a 20:1 BP:MC ratio after 1 hr photolysis at 455 nm using a 5 W LED light source. SC = supercoiled pUC18 DNA, OC = open circular pUC18 DNA.

Chapter 6. Conclusions and Future Work

6.1 Highlights of the Contributions

The design, synthesis, identification, characterization and DNA binding properties of Ru^{II},Pt^{II} mixed-metal supramolecules, $[(tpy)Ru(tppz)PtCl](PF_6)_3$ and $[ClPt(tppz)Ru(tppz)PtCl](PF_6)_4$ (tpy = 2,2':6',2''-terpyridine and tppz = 2,3,5,6-tetrakis(2-pyridyl)pyrazine), were reported in this dissertation focusing on stereochemistry, electrochemistry, photochemistry and biochemistry. A variety of analytical techniques including mass spectrometry, NMR spectroscopy, X-ray crystallography, scanning electron microscopy, cyclic voltammetry, electronic absorption spectroscopy, emission spectroscopy, confocal laser induced spectroscopy, and DNA gel electrophoresis have been used for characterization of these Ru^{II},Pt^{II} mixed-metal supramolecules. Here are the main accomplishments in this dissertation:

1. Two mixed-metal tppz bridged complexes have been prepared and studied in detail that couple a Ru light absorber to a reactive Pt metal center.

2. The composition and geometry of mixed-metal complexes $[(tpy)Ru(tppz)PtCl](PF_6)_3$ and $[ClPt(tppz)Ru(tppz)PtCl](PF_6)_4$ was confirmed in solid state by X-ray crystallography and in solution by NMR techniques.

3. The chirality of these tridentate complexes bridged by tppz in solution was demonstrated for the first time since the discovery of the tppz ligand at 1959. The stereoisomers were characterized by analyses of the single crystal structures and NMR spectroscopy.

4. Electrochemically, a very low first tppz-based reduction was observed in each of the complexes: $[(tpy)Ru(tppz)PtCl](PF_6)_3$ and $[ClPt(tppz)Ru(tppz)PtCl](PF_6)_4$, predicting a low-lying ^{3}MLCT. This low-

lying ^{3}MLCT is essential to initiate a photochemical reaction with low energy light.

5. An emissive tridentate complex, [ClPt(tppz)Ru(tppz)PtCl](PF$_6$)$_4$ (λ_{max}^{em} = 754 nm and τ = 80 ns) was reported. In contrast, a barely detectable emission was observed for its analog, [(tpy)Ru(tppz)PtCl](PF$_6$)$_3$. A design consideration that should be generally applicable.

6. One of the most interesting discoveries was the light-activated DNA condensation by the trimetallic complex, [ClPt(tppz)Ru(tppz)PtCl](PF$_6$)$_4$. This new reactivity provides a totally unprecedented mode of action for photodynamic therapy.

6.2 Conclusions in Detail

This work involved the design and synthesis of the mixed-metal complexes, [(tpy)Ru(tppz)PtCl](PF$_6$)$_3$ and [ClPt(tppz)Ru(tppz)PtCl](PF$_6$)$_4$, that couple the Pt reactive center to the ruthenium-based chromophore via a tppz bridging ligand. These supramolecular assemblies provide a TL-LA-BL-RM (TL = terminal ligand, LA = light absorber, BL = bridging ligand, RM = reactive metal center) architecture in the bimetallic complex, [(tpy)Ru(tppz)PtCl](PF$_6$)$_3$, and RM-BL-LA-BL-RM architecture in the trimetallic complex, [ClPt(tppz)Ru(tppz)PtCl](PF$_6$)$_4$. These complexes are of interest in that they provide LA and RM in a framework that exhibits rich redox, spectroscopic, and photophysical properties. Sytems with coupled LA and RM units hold promise for a variety of applications including solar energy conversion and antitumor agent development.

The bimetallic and trimetallic complexes, [(tpy)Ru(tppz)PtCl](PF$_6$)$_3$ and [ClPt(tppz)Ru(tppz)PtCl](PF$_6$)$_4$, were prepared using a building block method. After the synthesis of the monometallic precursors, [(tpy)Ru(tppz)](PF$_6$)$_2$ and [Ru(tppz)$_2$](PF$_6$)$_2$, the next step was to incorporate the Pt^{II}-Cl moiety to form the bimetallic and trimetallic complexes. This was done under careful reaction control by dissolving [(DMSO)$_2$PtCl$_2$]

in CH_3CN and adding the monometallic precursor dropwise. This stepwise approach provides the systematic assembly of the supramolecular architectures with controllable properties and high purity. The platinum metal center was incorporated last as a reactive metal is substitutionally labile, making typical adsorption chromatography undesirable following Pt incorporation.

The identity of the title complexes was confirmed by FAB-MS and ESI-MS. As expected, similar FAB-MS fragmentation patterns were observed for both $[(tpy)Ru(tppz)PtCl](PF_6)_3$ and $[ClPt(tppz)Ru(tppz)PtCl](PF_6)_4$, with experimental isotopic distribution patterns matching the theoretical values. The FAB mass spectral analysis showed $[M\text{-}PF_6]^+$ peaks at m/z = 1243 for the bimetallic complex and $[M\text{-}PF_6+H^+]^+$ at m/z = 1773 for the trimetallic complex, respectively. The fragmentation patterns observed were consistent with the composition of the complexes. Surprisingly, different ESI-MS patterns were observed for $[(tpy)Ru(tppz)PtCl](PF_6)_3$ and $[ClPt(tppz)Ru(tppz)PtCl](PF_6)_4$. ESI-MS confirmed formation of assemblies in solution showing a dimer, trimer and tetramer of the bimetallic complex, $[(tpy)Ru(tppz)PtCl](PF_6)_3$ with appropriate isotopic patterns. The different states of charge (z) were confirmed by the isotopic peak separation with 1, 0.5 and 0.33 m/z units for z = 1+, 2+ and 3+ charge, respectively. Peaks at m/z = 2632, 1937 and 1706 were assigned to the singly charged dimer $[2M\text{-}PF_6]^+$, doubly charged trimer $[3M\text{-}2PF_6]^{2+}$ and triply charged tetramer $[4M\text{-}3PF_6]^{3+}$ of $[(tpy)Ru(tppz)PtCl](PF_6)_3$, respectively. This ESI-MS data provides evidence of the assembly of the complexes, likely through Pt···Pt interactions in solution. Typically in the literature, Pt···Pt interactions were established by analysis of the structures of the complexes in the solid state. To the best of our knowledge, this is the first time that trimers and tetramers of Pt complexes have been characterized in solution by mass spectrometry. In contrast, the assembly of the trimetallic complex of $[ClPt(tppz)Ru(tppz)PtCl](PF_6)_4$ was not detectable by ESI-MS method, which may be reflective of the large size and charge on this system.

The characterization of the bimetallic and trimetallic complexes, $[(tpy)Ru(tppz)PtCl](PF_6)_3$ and $[ClPt(tppz)Ru(tppz)PtCl](PF_6)_4$, was conducted by a

combination of NMR techniques. The assignments of the ^{1}H-NMR spectra provided for some unexpected complexity. In view of the many factors that influence the δ of ^{1}H resonances for polypyridyl ruthenium supramolecules, consideration of a number of factors and careful analysis is required to assign their ^{1}H chemical shifts. ^{1}H chemical shift is impacted by electron withdrawing effects from the metal coordination, ring current effects are particularly impacted for the H^6 protons which locate over the aromatic rings. The resonances at δ 8.65 and 8.26 ppm correspond to the H^6 for the free ligands of tpy and tppz, respectively. Both upfield and downfield shifts were observed in the ^{1}H resonance of the complexes compared to the free ligands. Upfield shifts of H^6 in the tpy units resulting from the ring current effects were observed in the complexes, $[Ru(tpy)_2]^{2+}$, $[(tpy)Ru(tppz)]^{2+}$ and $[(tpy)Ru(tppz)PtCl]^{3+}$, displaying δ at 7.34, 7.59 and 7.66 ppm, respectively. By contrast, downfield shifts of the H^6C of tppz units with the similar chemical environments as tpy units in the above complexes were observed in $[Ru(tppz)_2]^{2+}$ and $[(tpy)Ru(tppz)]^{2+}$, displaying δ at 8.76 and 8.73 ppm, respectively. Interestingly, upfield shifts of the H^6C of the tppz unit were observed again in $[(tpy)Ru(tppz)PtCl](PF_6)_3$ and $[ClPt(tppz)Ru(tppz)PtCl](PF_6)_4$ after incorporating the Pt metals, displaying δ at 7.48 and 7.85 ppm, respectively. ^{195}Pt-NMR resonances at δ_{Pt} = -2579 ppm (vs. δ_{Pt} = 1613 ppm for K_2PtCl_4 in D_2O) in CD_3CN at RT were observed for the trimetallic complex, $[ClPt(tppz)Ru(tppz)PtCl](PF_6)_4$, and δ_{Pt} = -2500 ppm for the bimetallic complex, $[(tpy)Ru(tppz)PtCl](PF_6)_3$. This downfield shift is consistent with electron withdrawing effects due to the two Pt electron deficient Pt centers being bound in the trimetallic complex vs. only one Pt in the bimetallic complex. A combination of 1D ^{1}H-NMR, ^{195}Pt-NMR, 2D ^{1}H-^{1}H COSY, NOESY and ^{195}Pt-^{1}H HMQC provides firm assignments of this series of complexes.

The ligand tppz, once bound to two metals, presents a chiral system. NMR spectra provide insight into the structures of these complexes in solution. The bimetallic complex $[(tpy)Ru(tppz)PtCl](PF_6)_3$ has only one chiral μ-tppz unit and thus has two enantiomers occuring with equal probability, left handed (M) and right-handed (P). On the other hand, there are two chiral centers in the trimetallic complex, $[ClPt(tppz)Ru(tppz)PtCl](PF_6)_4$. Therefore, three stereoisomers, left-handed (M-M), right-handed (P-P) and a combination

of both (M-P) are possible in $[ClPt(tppz)Ru(tppz)PtCl](PF_6)_4$. These stereoisomers can interconvert at RT as suggested by the fluxional behavior seen on the time scale of NMR. Variable temperature dynamic NMR analysis of $[ClPt(tppz)Ru(tppz)PtCl](PF_6)_4$ supports this conclusion, a phenomenon yet to be observed for tppz bridged complexes in solution, broadening of the resonances at δ 7.85 and 7.50 ppm of protons H^6C and H^5C at RT in CH_3CN coalescence as expected for two sets of stereoisomers. As expected, sharp resonances with the characteristic splitting pattern for H^6C and H^5C were observed upon increasing the temperature to 60ºC, reflective of fast exchanges among the isomers at this temperature. Two individual resonances for H^6C and H^5C were observed upon decreasing the temperature to -20ºC with 2:1 peak ratios, showing the slow exchange of the three isomers at -20ºC. The nonequivalent integration (2:1) indicates a difference in the energies of the the enantiomers (M-M and P-P) and the mesomer (M-P or P-M). The trimetallic complex represents the first identified chiral molecule of tppz in solution characterized by NMR since the discovery of the tppz ligand at 1959.

The pair of enantiomers left-handed (M-M) and right-handed (P-P) were also confirmed by the X-ray crystallography in solid state. X-ray crystallographic analysis of these systems in the solid state represents the first crystallographically characterized mixed-metal complexes bridged by tppz ligand. The bis(tridentate) structures as well as the stereoisomers of $[(tpy)Ru(tppz)PtCl](PF_6)_3$ and $[ClPt(tppz)Ru(tppz)PtCl](PF_6)_4$ are observed in the solid state by the analysis of their crystal structures. This analysis revealed that $[(tpy)Ru(tppz)PtCl](PF_6)_3$ and $[ClPt(tppz)Ru(tppz)PtCl](PF_6)_4$ were crystallized in the centrosymmetric space groups of C_2/c and $P2_1/c$, containing equal amounts of enantiomers in well-defined patterns as the racemic compound crystalline. A strong Pt···Pt interaction with a short interatomic distance of 3.3218(5) Å was observed in $[(tpy)Ru(tppz)PtCl](PF_6)_3$, with stabilization by C-H···Cl hydrogen bonds. Analysis of the crystal packing of $[ClPt(tppz)Ru(tppz)PtCl](PF_6)_4$ reveals that the molecules are arranged without this close Pt···Pt intermolecular interaction. The cooperative effect of multiple C-H···Cl hydrogen bonding from both sides of the trimetallic complex stabilizes the network aggregates in the crystal. The short C-H···Cl hydrogen bond directs self-assembly along a continuous one-dimensional chain, enhanced by π···π interactions from

the peripheral pyridyl rings. The average interplanar separation through π···π interactions in the plane is 3.2 Å, with the Pt ···Pt distance at 4.699 Å. The chloro group provides electrostatic stabilization because Pt-Cl groups point to π-electron rich aromatic rings. The presence of C-H···Cl hydrogen bondings, C-H···π interactions, π···π interactions, and Pt···Pt interactions play an important role in the assembly of such Ru^{II},Pt^{II} tridentate systems.

SEM was conducted to show the hierarchical assembly of open-ended trimetallic molecules into long range 3D flower-like materials. The exquisite and uniform arrangements of the molecules can be manipulated via a slow solvent evaporation process. With progressively increasing the concentration, 1D nanowire and macroscopic bundles were produced at the very beginning of evaporation. These open nanowires were then further assembled into 2D lamellar structures. Finally, the layers were extended to three dimensions to form the 3D flowerlike networks, with the Pt sites decorating the surface of these materials.

A comparative study of the electrochemical properties of the title complexes and related tridentate systems was performed. The complexes, $[(tpy)Ru(tppz)PtCl](PF_6)_3$ and $[ClPt(tppz)Ru(tppz)PtCl](PF_6)_4$, display $Ru^{II/III}$ oxidation at 1.63 and 1.83 V vs. Ag/AgCl, respectively. These complexes display very low potential $tppz^{0/-}$ at -0.16 vs. Ag/AgCl for $[(tpy)Ru(tppz)PtCl](PF_6)_3$, at -0.03 vs. Ag/AgCl for $[ClPt(tppz)Ru(tppz)PtCl](PF_6)_4$, relative to their monometallic synthons, $[(tpy)Ru(tppz)](PF_6)_2$ (-0.95 and -1.39 V vs. Ag/AgCl) and $[Ru(tppz)_2](PF_6)_2$ (-0.85 and -1.06 V vs. Ag/AgCl). This is consistent with the bridging coordination of the tppz ligand by incorporating Pt metals. The first ligand-based reduction in the tridentate Ru^{II},Pt^{II} mixed-metal complexes, $[(tpy)Ru(tppz)PtCl](PF_6)_3$ (-0.17 V vs. Ag/AgCl) and $[ClPt(tppz)Ru(tppz)PtCl](PF_6)_4$ (-0.03 V vs. Ag/AgCl), occurred at a more positive potential compared to those in the bidentate Ru^{II},Pt^{II} mixed-metallic complexes, $[(bpy)_2Ru(dpp)PtCl_2](PF_6)_2$ (-0.49 V vs. Ag/AgCl) and $[(bpy)_2Ru(dpq)PtCl_2](PF_6)_2$ (-0.28 V vs. Ag/AgCl), implying that the tppz(π*) LUMO in the tridentate systems are lower energy than in the bidentate systems.

The lower lying LUMO of the tridentate complexes predicts a lower lying ^{3}MLCT excited state.

The photophysical properties of the bimetallic and trimetallic complexes were investigated in solution and the solid state. The mixed-metal complexes display very low energy tppz(π^*) acceptor orbitals, reflective of the first ligand based reduction potential. The complexes are efficient light absorbers with intense transitions throughout the UV and visible regions with the lowest transition being MLCT in nature to the tppz acceptor orbital. The mixed-metal Ru^{II},Pt^{II} complexes exhibited intense MLCT at lower energy [(tpy)Ru(tppz)PtCl](PF$_6$)$_3$, λ_{max}^{abs} = 530 nm, $\varepsilon = 2.8 \times 10^{-4}$ $M^{-1}cm^{-1}$; [ClPt(tppz)Ru(tppz)PtCl](PF$_6$)$_4$, λ_{max}^{abs} = 538 nm, $\varepsilon = 3.0 \times 10^{-4}$ $M^{-1}cm^{-1}$ compared to the monometallic precursors: [(tpy)Ru(tppz)](PF$_6$)$_3$, λ_{max}^{abs} = 472 nm, $\varepsilon = 1.6 \times 10^{-4}$ $M^{-1}cm^{-1}$; [Ru(tppz)$_2$](PF$_6$)$_3$, λ_{max}^{abs} = 478 nm, $\varepsilon = 2.3 \times 10^{-4}$ $M^{-1}cm^{-1}$. In marked contrast to most bis-tridentate Ru^{II} complexes such as $[Ru(tpy)_2]^{2+}$, the tppz bridged complex [ClPt(tppz)Ru(tppz)PtCl](PF$_6$)$_4$, displays an intense visible emission at λ_{max}^{em} = 754 nm with quantum yield of $\Phi^{em} = 5.4 \times 10^{-4}$ and lifetime of τ = 80 ns at RT in CH_3CN from the Ru→μ-tppz ^{3}MLCT emissive state. The trimetallic complex, [ClPt(tppz)Ru(tppz)PtCl](PF$_6$)$_4$, maintains the strong emission property in the solid state with λ_{max}^{em} = 764 nm, visualized by the confocal laser induced emission scanning microscopy. The closely related complex [(tpy)Ru(tppz)PtCl](PF$_6$)$_3$, displays only an extremely weak emission in dilute CH_3CN solution and no detectable emission in the solid state. This is likely a characteristic of the Ru^{II},Pt^{II} bimetallic in which even dimer formation through Pt···Pt interaction can simultaneously quench all ^{3}MLCT excited states. The presence of the two Ru-tppz-Pt sites in each molecule in the trimetallic complex prohibits the Pt···Pt interaction from simultaneously quenching both Ru→tppz CT excited states, a design consideration that should be generally applicable.

Interactions of the title complexes with DNA were investigated. Both title complexes were shown to covalently bind to DNA via the Pt^{II}-Cl site. The effect of incubating these metal complexes with DNA on the subsequent migration of DNA through an agarose gel was found to be more dramatic than that observed for the well known anticancer drug,

cis-$[Pt(NH_3)_2Cl_2]$ (cisplatin). This effect was enhanced with increased incubation temperature. Unwinding of supercoiled plasmid DNA upon binding of the metal complex was found to be more pronounced for the trimetallic complex, $[ClPt(tppz)Ru(tppz)PtCl](PF_6)_4$, than for the bimetallic complex, $[(tpy)Ru(tppz)PtCl](PF_6)_3$, consistent with reactivity of both Pt bioactive sites.

One of the most exciting observations was that the trimetallic complex $[ClPt(tppz)Ru(tppz)PtCl]Cl_4$ can induce the condensation of DNA in presence of visible light. The photolysis of solution of 20:1 base pairs:metal complex with visible light λ = 455 nm provides for rapid condensation of the DNA leaving the solution free of metal complex and DNA. SEM imaging shows the DNA forms large, ca. 80 μm condensed particles. The bimetallic does not display this interesting photoreactivity, indicating the two Pt^{II}-Cl sites are important for DNA photocondensation. Condensed DNA is not able to be replicated. Given these remarkable preliminary results of the light-activated DNA condensation, this exciting method holds the promise in the applicaiton of this material in photodynamic therapy. Condensed DNA is not able to be replicated.

The work highlighted in this dissertation provided considerable insight into the properties of light absorber-reactive metal assemblies. Detailed analysis of the bimetallic vs. trimetallic systems uncovered many similarties and striking differences. The trimetallic system shows dynamic ^{1}H-NMR, displays a long-lived emissive ^{3}MLCT excited state and photocondense DNA in marked contrast to the bimetallic system. This study indicates careful analysis of closely related systems, is important to fully explore the properties of multicomponent polyazine bridged systems.

6.3 Future Work

This project discovered many interesting properties and reactivity patterns, which open up this new structural motif for future exploration. Future work can be governed by the results of the studies in this dissertation:

The remote chloride ligands on the Pt site give the mixed-metal complexes an easily substituted site on this reactive metal. Of particular interest would be a molecular design to eliminate Pt···Pt interactions by the substitution of Cl with a bulky group L (L = Ph_3N or Ph_3P). Modification on the tpy ligand with R_1, R_2 and R_3 (R_1, R_2 and R_3 = 4,4′,4″-tri-tert-butyl) in the bimetallic complex, $[(tpy)Ru(tppz)PtCl](PF_6)_3$ could also prevent Pt···Pt assembly, allowing a means to test the hypothesis that such assembly is important in our current bimetallic complex. Related systems should be explored to improve the luminescent properties and to derive structure activity relationships, **Figure 6.60**.

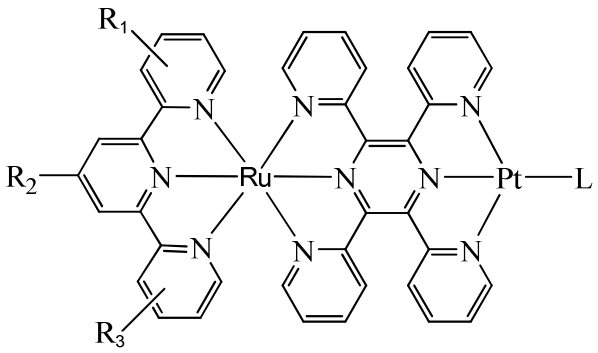

Figure 6.60. Proposed modifications on the bimetallic complex of $[(tpy)Ru(tppz)PtCl](PF_6)_3$, where R_1, R_2 and R_3 = 4,4′,4″-tri-tert-butyl and L = Ph_3N or Ph_3P

Replacing the Ru with other metal centers has the potential to change the redox and spectroscopic properties of these complexes. The use of Os, Rh, Ir and even the first row

transition metals in place of the Ru center would change the energy of the HOMO, leading to perturbation of the electrochemical, photophysical, photochemical and magnetic properties. For example, the use of Os for Ru metal conter might lead to intense ^{3}MLCT absorption in a therapeutic window as a result of the higher energy dπ orbitals on Os.

The supramolecular assemblies, $[(tpy)Ru(tppz)PtCl](PF_6)_3$ and $[ClPt(tppz)Ru(tppz)PtCl](PF_6)_4$, would be extended by incorporating more $(tppz)Ru^{II}$ units to form longer one-dimensional molecular wires, **Figure 6.61**. Attachment of one more Ru^{II} through the BL tppz to the system would provide a further stabilized ^{3}MLCT state with additional metal-metal communication. In addition, a charge separated state could be experimentally characterized for a system such as $[(tpy)Ru(tppz)Ru'(tppz')PtCl]^{5+}$, where HOMOs locate on Ru′, and LUMOs locate on tppz′. Electronic coupling could be simulated modeled by computational study.

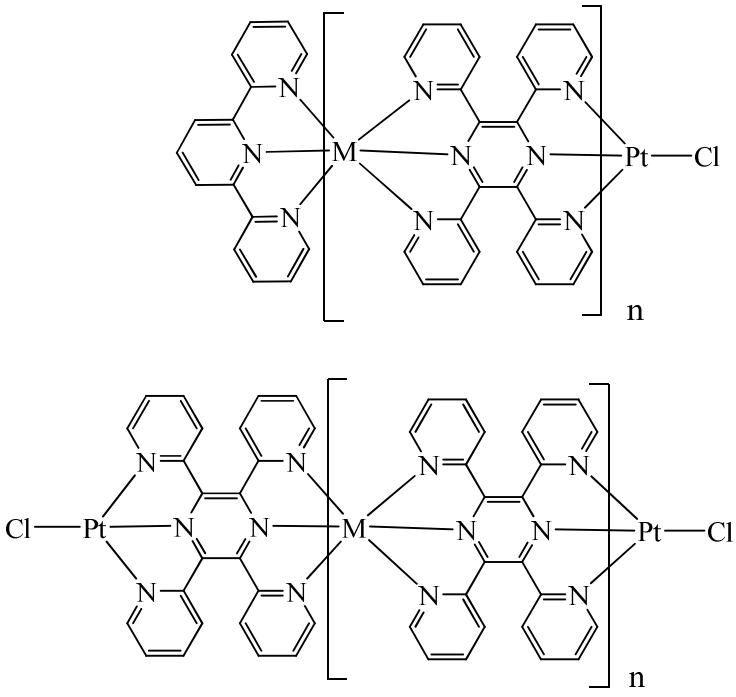

M = Ru, Os, Ir

Figure 6.61. Proposed molecular wires

Although gel electrophoresis studies have contributed significantly to understanding the DNA binding properties of bimetallic and trimetallic complexes, it cannot provide insight into binding specificity or information on the kinetics of binding. The chemical shift of ^{195}Pt is sensitive to the environment and has a wide chemical shift window (10000 ppm). ^{195}Pt-NMR spectroscopy has long been used to study the *in vivo* DNA binding activity of antitumor agents such as cisplatin and carboplatin. Further research on the ^{195}Pt resonance should be conducted to study the kinetics of the DNA-binding process.

Additional studies should be performed to exploit the possible applications of the title complexes in photodynamic therapy. Due to their intense absorption in the visible region, the title complexes should be further investigated as a candidate for DNA photocleavage or photobinding. Other factors such as photolysis time and O_2 dependence should also be investigated. The chirality of these systems may provide stereospecific interactions with chiral biomolecules such as DNA.

The current study on [ClPt(tppz)Ru(tppz)PtCl](PF$_6$)$_4$ has provided a solid platform to further investigate its photocatalytic property. Although tridentate complexes of Ru^{II} and Pt^{II} have been explored for water splitting, the mechanism behind H_2-evolving or O_2-evolving activities is still a matter of debate.[59, 265-267] The simple NMR profile of the trimetallic complex as well as its analogs provide a means for monitoring the functions of the metal complex in a photocatalytic process. In addition, ^{195}Pt-NMR can be used to monitor the reaction pathway and the reaction mechanism over time.

Putting things in prespective, it is always challenging for chemists to develop multifunctional systems via self-assembling (mimicking the natural process) with a well-defined structure and a specific reactivity or catalysis. The identification and confirmation of the structure and properties of the assemblies [ClPt(tppz)Ru(tppz)PtCl](PF$_6$)$_4$ and [(tpy)Ru(tppz)PtCl](PF$_6$)$_3$ in this dissertation provided considerable insight into the study of the multifunctional metallosupramolecules. Careful analyses of complexes of this type are needed to fully understand structure function relationships. This is highlighted by the remarkable structure similiartiy of the

bimetallic and trimetallic complexes reported herein as well as their striking contrast properties which may not have been undercovered without the herein reported careful comparative study.

Reference

1. Balzani, V.; Juris, A.; Venturi, M.; Campagna, S.; Serroni, S., Luminescent and redox-active polynuclear transition metal complexes. *Chem. Rev.* **1996,** 96, (2), 759-833.
2. Kirchhoff, J. R.; McMillin, D. R.; Marnot, P. A.; Sauvage, J. P., Photochemistry and photophysics of bis(terpyridyl) complexes of Ru(II) in fluid solution-evidence for the formation of an Eta-2-diphenylterpyridine complex. *J. Am. Chem. Soc.* **1985,** 107, (5), 1138-1141.
3. Young, R. C.; Nagle, J. K.; Meyer, T. J.; Whitten, D. G., Electron-transfer quenching of non-emitting excited-states of $Ru(tpp)(py)_2$ and $[Ru(Trpy)_2]^{2+}$. *J. Am. Chem. Soc.* **1978,** 100, (15), 4773-4778.
4. Janes, R.; Moore, E., *[Book] Metal-ligand bonding*. Open University Press: 2004.
5. Atkins, P.; De Paula, J., *[book] Physical chemistry.* W. H. Freeman & Co,: New York. **2006**.
6. Bagotsky, V., *[Book] Fundamentals of electrochemistry.* Wiley-Interscience, Hoboken, NJ**. 2006**.
7. Silberberg, M., *[Book] Chemistry: The molecular nature of matter and change.* Glencoe/McGrawHill. fifthe edition.
8. Taube, H., Electron transfer between metal complexes: retrospective. *Science* **1984,** 226, (4678), 1028-1036.
9. Ito, T.; Hamaguchi, T.; Nagino, H.; Yamaguchi, T.; Washington, J.; Kubiak, C. P., Effects of Rapid Intramolecular Electron Transfer on Vibrational Spectra. *Science* **1997,** 277, (5326), 660-663.
10. Ito, T.; Hamaguchi, T.; Nagino, H.; Yamaguchi, T.; Kido, H.; Zavarine, I. S.; Richmond, T.; Washington, J.; Kubiak, C. P., Electron Transfer on the Infrared Vibrational Time Scale in the Mixed Valence State of 1,4-Pyrazine- and 4,4‘-Bipyridine-Bridged Ruthenium Cluster Complexes. *J. Am. Chem. Soc.* **1999,** 121, (19), 4625-4632.
11. Das, A. K.; Sarkar, B.; Fiedler, J.; Zalis, S.; Hartenbach, I.; Strobel, S.; Lahiri, G. K.; Kaim, W., A five-center redox system: molecular coupling of two noninnocent imino-o-benzoquinonato-ruthenium functions through a π-ccceptor bridge. *J. Am. Chem. Soc.* **2009,** 131, (25), 8895-8902.
12. Ito, T.; Imai, N.; Yamaguchi, T.; Hamaguchi, T.; Londergan, C.; Kubiak, C., Observation and dynamics of "Charge-transfer isomers". *Angew. Chem. Int. Ed.* **2004,** 43, (11), 1376-1381.
13. Robin, M.; Day, P., Mixed valence chemistry-a survey and classification. *Adv. Inorg. Chem. Radiochem.* **1967,** 10, 247-275.
14. Burstall, F. H., *J. Chem. Soc.* **1936**, 173-175.
15. Juris, A.; Balzani, V.; Barigelletti, F.; Campagna, S.; Belser, P.; Vonzelewsky, A., Ru(II) Polypyridine Complexes - Photophysics, Photochemistry, Electrochemistry, and Chemi-Luminescence. *Coord. Chem. Rev.* **1988,** 84, 85-277.
16. Kalyanasundaram, K., Photophysics, photochemistry and solar-energy conversion with tris(bipyridyl)ruthenium(II) and its analogs. *Coord. Chem. Rev.* **1982,** 46, (Oct), 159-244.
17. Nicewicz, D. A.; MacMillan, D. W. C., Merging Photoredox Catalysis with Organocatalysis: The Direct Asymmetric Alkylation of Aldehydes. *Science* **2008,** 322, (5898), 77-80.
18. Campagna, S.; Serroni, S.; Bodige, S.; MacDonnell, F. M., Absorption Spectra, Photophysical Properties, and Redox Behavior of Stereochemically Pure Dendritic Ruthenium(II) Tetramers and Related Dinuclear and Mononuclear Complexes. *Inorg. Chem.* **1999,** 38, (4), 692-701.
19. Winkler, J.; Netzel, T.; Creutz, C.; Sutin, N., Direct observation of metal-to-ligand charge-transfer (MLCT) excited states of pentaammineruthenium (II) complexes. *J. Am. Chem. Soc.* **1987,** 109, (8), 2381-2392.
20. Berger, R.; McMillin, D., Localized states in reduced and excited-state ruthenium (II) terpyridyls. *Inorg. Chem.* **1988,** 27, (23), 4245-4249.
21. Fang, Y. Q.; Taylor, N. J.; Laverdiere, F.; Hanan, G. S.; Loiseau, F.; Nastasi, F.; Campagna, S.; Nierengarten, H.; Leize-Wagner, E.; Van Dorsselaer, A., Ruthenium(II) complexes with improved photophysical properties based on planar 4'-(2-pyrimidinyl)-2,2 ': 6',2 "-terpyridine ligands. *Inorg. Chem.* **2007,** 46, (7), 2854-2863.
22. Abrahamsson, M.; Jager, M.; Osterman, T.; Eriksson, L.; Persson, P.; Becker, H. C.; Johansson, O.; Hammarstrom, L., A 3.0 υs Room Temperature Excited State Lifetime of a Bistridentate Ru^{II}-Polypyridine Complex for Rod-like Molecular Arrays. *J. Am. Chem. Soc.* **2006,** 128, (39), 12616-12617.

23. Abrahamsson, M.; Wolpher, H.; Johansson, O.; Larsson, J.; Kritikos, M.; Eriksson, L.; Norrby, P. O.; Bergquist, J.; Sun, L.; Akermark, B.; Hammarstrom, L., A New Strategy for the Improvement of Photophysical Properties in Ruthenium(II) Polypyridyl Complexes. Synthesis and Photophysical and Electrochemical Characterization of Six Mononuclear Ruthenium(II) Bisterpyridine-Type Complexes. *Inorg. Chem.* **2005,** 44, (9), 3215-3225.
24. Medlycott, E. A.; Hanan, G. S., Designing tridentate ligands for ruthenium(ii) complexes with prolonged room temperature luminescence lifetimes. *Chem. Soc. Rev.* **2005,** 34, (2), 133-142.
25. Medlycott, E. A.; Hanan, G. S., Synthesis and properties of mono- and oligo-nuclear Ru(II) complexes of tridentate ligands: The quest for long-lived excited states at room temperature. *Coord. Chem. Rev.* **2006,** 250, (13-14), 1763-1782.
26. Maestri, M.; Armaroli, N.; Balzani, V.; Constable, E.; Thompson, A., Complexes of the ruthenium (II)-2,2':6',2"-terpyridine family: effect of electron-accepting and-donating substituents on the photophysical and electrochemical properties. *Inorg. Chem.* **1995,** 34, (10), 2759-2767.
27. Arana, C. R.; Abruna, H. D., Monomeric and Oligomeric Complexes of Ruthenium and Osmium with Tetra-2-Pyridyl-1,4-Pyrazine (tppz). *Inorg. Chem.* **1993,** 32, (2), 194-203.
28. Petersen, J. D., *Supramolecular Photochemistry* **1987,** NATO ASI Series, (214), 135.
29. Thummel, R. P.; Chirayil, S., Ruthenium(II) Complexes of Tetra-2-Pyridyl-1,4-Diazine. *Inorg. Chim. Acta.* **1988,** 154, (1), 77-81.
30. Vogler, L. M.; Brewer, K. J., Building Block Approach to the Construction of Long-Lived Osmium(II) and Ruthenium(II) Multimetallic Complexes Incorporating the Tridentate Bridging Ligand 2,3,5,6-Tetrakis(2-pyridyl)pyrazine. *Inorg. Chem.* **1996,** 35, (4), 818-824.
31. Ruminski, R. R.; Letner, C., Synthesis and characterization of rhodium (III) complexes bound to the novel bridging ligand 2, 3, 5, 6-tetra (2-pyridyl) pyrazine(tppz). *Inorg. Chim. Acta.* **1989,** 162, (2), 175-177.
32. Reginaldo C. Rocha, Francisca N. R., Hershel Jude, Andrew P. Shreve, Javier J. Concepcion, Thomas J. Meyer,, Observation of Three Intervalence-Transfer Bands for a Class II-III Mixed-Valence Complex of Ruthenium. *Angew. Chem. Int. Ed.* **2008,** 47, (3), 503-506.
33. Sauvage, J. P.; Collin, J. P.; Chambron, J. C.; Guillerez, S.; Coudret, C.; Balzani, V.; Barigelletti, F.; Decola, L.; Flamigni, L., Ruthenium(II) and osmium(II) bis(terpyridine) complexes in covalently-linked multicomponent systems-synthesis, electrochemical-behavior, absorption-spectra, and photochemical and photophysical properties. *Chem. Rev.* **1994,** 94, (4), 993-1019.
34. Barigelletti, F.; Flamigni, L.; Balzani, V.; Collin, J. P.; Sauvage, J. P.; Sour, A.; Constable, E. C.; Thompson, A. M. W. C., Luminescence properties of rigid rod-like binuclear ruthenium(II)-osmium(II) terpyridine complexes-electronic interaction through phenyl bridges. *J. Chem. Soc. Chem. Commun.* **1993**, (11), 942-944.
35. Constable, E. C.; Thompson, A. M. W. C., Multinucleating 2,2'-6',2"-terpyridine ligands as building-blocks for the assembly of coordination polymers and oligomers. *J. Chem. Soc. Dalton Trans.* **1992**, (24), 3467-3475.
36. Collin, J.; Lainé, P.; Launay, J.; Sauvage, J.; Sour, A., Long-range coupling in a mixed-valence diruthenium complexes containing bis-terpyridine ligands of various lengths as bridges. *J. Chem. Soc. Chem. Commun.* **1993,** 1993, (5), 434-435.
37. Ghumaan, S.; Sarkar, B.; Chanda, N.; Sieger, M.; Fiedler, J.; Kaim, W.; Lahiri, G. K., 2,2'-Dipyridylketone (dpk) as Ancillary Acceptor and Reporter Ligand in Complexes $[(dpk)(Cl)Ru(tppz)Ru(Cl)(dpk)]^{n+}$ where tppz = 2,3,5,6-Tetrakis(2-pyridyl)pyrazine. *Inorg. Chem.* **2006,** 45, (19).
38. Ghumaan, S.; Sarkar, B.; Chanda, N.; Sieger, M.; Fiedler, J.; Kaim, W.; Lahiri, G. K., 2,2 '-Dipyridylketone (dpk) as ancillary acceptor and reporter ligand in complexes $[(dpk)(Cl)Ru(u-tppz)Ru(Cl)(dpk)]^{(n+)}$ where tppz=2,3,5,6-tetrakis(2-pyridyl)pyrazine. *Inorg. Chem.* **2006,** 45, (19), 7955-7961.
39. Vogler, L. M.; Franco, C.; Jones, S. W.; Brewer, K. J., Ruthenium Chromophores Containing Terpyridine and a Series of Polyazine Bridging Ligands. *Inorg. Chim. Acta.* **1994,** 221, (1-2), 55-59.
40. Vogler, L. M.; Jones, S. W.; Jensen, G. E.; Brewer, R. G.; Brewer, K. J., Comparing the spectroscopic and electrochemical properties of ruthenium and osmium complexes of the tridentate polyazine ligands 2,2':6',2"-terpyridine and 2,3,5,6-tetrakis(2-pyridyl)pyrazine. *Inorg. Chim. Acta.* **1996,** 250, (1-2), 155-162.

41. Lee, J. D.; Vrana, L. M.; Bullock, E. R.; Brewer, K. J., A tridentate-bridged ruthenium-rhodium complex as a stereochemically defined light-absorber-electron-acceptor dyad. *Inorg. Chem.* **1998,** 37, (14), 3575-3580.
42. Winkler, J. R.; Netzel, T. L.; Creutz, C.; Sutin, N., Direct Observation of Metal-to-Ligand Charge-Transfer (MLCT) Excited-States of Pentaammineruthenium(II) Complexes. *J. Am. Chem. Soc.* **1987,** 109, (8), 2381-2392.
43. Vogler, L. M.; Scott, B.; Brewer, K. J., Investigation of the photochemical, electrochemical, and spectroelectrochemical properties of an iridium(III)/ruthenium(II) mixed-metal complex bridged by 2,3,5,6-tetrakis(2-pyridyl)pyrazine. *Inorg. Chem.* **1993,** 32, (6), 898-903.
44. Flores-Torres, S.; Hutchison, G. R.; Soltzberg, L. J.; Abruna, H. D., Ruthenium molecular wires with conjugated bridging ligands: Onset of band formation in linear inorganic conjugated oligomers. *J. Am. Chem. Soc.* **2006,** 128, (5), 1513-1522.
45. Fantacci, S.; DeAngelis, F.; Wang, J.; Bernhard, S.; Selloni, A., A Combined Computational and Experimental Study of Polynuclear Ru-TPPZ Complexes: Insight into the Electronic and Optical Properties of Coordination Polymers. *J. Am. Chem. Soc.* **2004,** 126, (31), 9715-9723.
46. Flores-Torres, S.; Hutchison, G. R.; Soltzberg, L. J.; Abruna, H. D., Ruthenium Molecular Wires with Conjugated Bridging Ligands: Onset of Band Formation in Linear Inorganic Conjugated Oligomers-Sup. *J. Am. Chem. Soc.* **2006,** 128, (5), 1513-1522.
47. Kishi, S.; Kato, M., Thermal and photo control of the linkage isomerism of bis(thiocyanato)(2,2 '-bipyridine)platinum(II). *Inorg. Chem.* **2003,** 42, (26), 8728-8734.
48. Denmark., S. E.; Diegel., J. S., *[Book] Topics in stereochemistry.* 2006 by John Wiley & Sons, Inc. **2006,** 25.
49. Amouri, H.; Gruselle, M., *[Book] Chirality in Transition Metal Chemistry-Molecules, supramolecular assemblies and materials*. Wiley: 2008.
50. Biagini, M.; Ferrari, M.; Lanfranchi, M.; Marchio, L.; Pellinghelli, M., Chirality in mononuclear square planar complexes. *J. Chem. Soc.Dalton. Trans.* **1999,** 1999, (10), 1575-1580.
51. Wadas, T. J.; Wang, Q. M.; Kim, Y. J.; Flaschenreim, C.; Blanton, T. N.; Eisenberg, R., Vapochromism and its structural basis in a luminescent Pt(II) terpyridine-nicotinamide complex. *J. Am. Chem. Soc.* **2004,** 126, (51), 16841-16849.
52. Yam, V. W. W.; Chan, K. H. Y.; Wong, K. M. C.; Zhu, N. Y., Luminescent platinum(II) terpyridyl complexes: Effect of counter ions on solvent-induced aggregation and color changes. *Chem. Eur. J.* **2005,** 11, (15), 4535-4543.
53. Yam, V. W. W.; Wong, K. M. C.; Zhu, N. Y., Solvent-induced aggregation through metal...metal/pi...pi interactions: Large solvatochromism of luminescent organoplatinum(II) terpyridyl complexes. *J. Am. Chem. Soc.* **2002,** 124, (23), 6506-6507.
54. Du, P.; Schneider, J.; Brennessel, W. W.; Eisenberg, R., Synthesis and structural characterization of a new vapochromic Pt(II) Complex based on the 1-terpyridyl-2,3,4,5,6-pentaphenylbenzene (TPPPB) ligand. *Inorg. Chem.* **2008,** 47, (1), 69-77.
55. Daws, C.; Exstrom, C.; Sowa Jr, J.; Mann, K., "Vapochromic" compounds as environmental Sensors. 2. synthesis and near-infrared and infrared dpectroscopy studies of [Pt (arylisocyanide)$_4$][Pt(CN)$_4$] upon exposure to volatile organic compound vapors. *Chem. Mater.* **1997,** 9, (1), 363-368.
56. Exstrom, C. L.; Sowa, J. R., Jr.; Daws, C. A.; Janzen, D.; Mann, K. R.; Moore, G. A.; Stewart, F. F., Inclusion of organic vapors by crystalline, solvatochromic [Pt(aryl isonitrile)$_4$][Pd(CN)$_4$] compounds. "vapochromic" environmental sensors. *Chem. mater.* **2002,** 7, (1), 15-17.
57. Wong, K. M. C.; Tang, W. S.; Lu, X. X.; Zhu, N. Y.; Yam, V. W. W., Functionalized platinum(II) terpyridyl alkynyl complexes as colorimetric and luminescence pH sensors. *Inorg. Chem.* **2005,** 44, (5), 1492-1498.
58. Periana, R. A.; Taube, D. J.; Gamble, S.; Taube, H.; Satoh, T.; Fujii, H., Platinum catalysts for the high-yield oxidation of methane to a methanol derivative. *Science* **1998,** 280, (5363), 560-564.
59. Du, P.; Schneider, J.; Jarosz, P.; Eisenberg, R., Photocatalytic generation of hydrogen from water using a platinum(II) terpyridyl acetylide chromophore. *J. Am. Chem. Soc.* **2006,** 128, (24), 7726.
60. Cortes, M.; Carney, J.; Oppenheimer, J.; Downey, K.; Cummings, S., Photoinduced electron transfer and energy transfer reactions of hydroxo-(2,2:6,2 -terpyridine) platinum (II). *Inorg. CHim. Acta.* **2002,** 333, (1), 148-151.

61. Wang, H. J. A.; Nathans, J.; Van Del Marel, G.; Van Boom, J. H.; Rich, A., Molecular structure of a double helical DNA fragment intercalator complex between deoxy CpG and a terpyridine platinum compound. *Nature* **1978,** 276, 471-474.
62. Van der Schilden, K.; Garcia, F.; Kooijman, H.; Spek, A. L.; Haasnoot, J. G.; Reedijk, J., A highly flexible dinuclear ruthenium(II)-platinum(II) complex: Crystal structure and binding to 9-ethylguanine. *Angew. Chem. Int. Ed.* **2004,** 43, (42), 5668-5670.
63. Lippard, S. J.; Bond, P. J.; Wu, K. C.; Bauer, W. R., Stereochemical requirements for intercalation of platinum complexes into double-stranded DNA. *Science* **1976,** 194, (4266), 726-728.
64. Jennette, K.; Gill, J.; Sadownick, J.; Lippard, S., Metallointercalation reagents. Synthesis, characterization, and structural properties of thiolato (2, 2', 2"-terpyridine) platinum (II) complexes. *J. Am. Chem. Soc.* **1976,** 98, (20), 6159-6168.
65. Dewan, J. C.; Lippard, S. J.; Bauer, W. R., Synthesis and structure of a bis[terpyridineplatinum(II)] complex and its evaluation as a metallointercalator. *J. Am. Chem. Soc.* **1980,** 102, (2), 858-860.
66. Ratilla, E. M. A.; Scott, B. K.; Moxness, M. S.; Kostic, N. M., Terminal and new bridging coordination of methylguanidine, arginine, and canavanine to Platinum(II) - the 1st crystallographic study of bonding between a transition-metal and a guanidine ligand. *Inorg. Chem.* **1990,** 29, (5), 918-926.
67. Ratilla, E. M. A.; Brothers, H. M.; Kostic, N. M., A transition-metal chromophore as a new, sensitive spectroscopic tag for proteins - selective covalent labeling of histidine-residues in cytochromes-C with chloro(2,2'-6',2"-terpyridine)platinum(II) chloride. *J. Am. Chem. Soc.* **1987,** 109, (15), 4592-4599.
68. Ratilla, E. M. A.; Kostic, N. M., Guanidyl groups - new metal-binding ligands in biomolecules - reactions of chloro(2,2'.6',2"-Terpyridine)platinum(II) with arginine in 2 cytochromes C and with other guanidyl ligands. *J. Am. Chem. Soc.* **1988,** 110, (13), 4427-4428.
69. Eryazici, I.; Moorefield, C. N.; Newkome, G. R., Square-Planar Pd(II), Pt(II), and Au(III) Terpyridine Complexes: Their Syntheses, Physical Properties, Supramolecular Constructs, and Biomedical Activities. *Chem. Rev.* **2008,** 108, (6), 1834-1895.
70. Lu, W.; Mi, B. X.; Chan, M. C. W.; Hui, Z.; Che, C. M.; Zhu, N. Y.; Lee, S. T., Light-emitting tridentate cyclometalated platinum(II) complexes containing sigma-alkynyl auxiliaries: Tuning of photo- and electrophosphorescence. *J. Am. Chem. Soc* **2004,** 126, (15), 4958-4971.
71. Kazuhiro Uemura, K. F., Hiroyuki Nishikawa, Saiko Arai, Kazuko Matsumoto, Hiroki Oshio,, Paramagnetic platinum-rhodium octamers bridged by halogen ions to afford a quasi-1D system. *Angew. Chem. Int. Ed.* **2005,** 44, (34), 5459-5464.
72. Kui, S. C. F.; Sham, I. H. T.; Cheung, C. C. C.; Ma, C.-W.; Yan, B.; Zhu, N.; Che, C.-M.; Fu, W.-F., Platinum(II) complexes with pi-conjugated, naphthyl-substituted, cyclometalated ligands (RC^N^N): Structures and photo- and electroluminescence. *Chem. Eur. J.* **2007,** 13, (2), 417-435.
73. Yersin, H.; Blasse, G., *[Book] Electronic and vibronic spectra of transition metal complexes*. Springer-Verlag: 1994.
74. Aldridge, T. K.; Stacy, E. M.; McMillin, D. R., Studies of the room-temperature absorption and emission-spectra of $[Pt(trpy)X]^+$ systems. *Inorg. Chem.* **1994,** 33, (4), 722-727.
75. Tears, D. K. C.; McMillin, D. R., Exciplex quenching of photoexcited platinum(II) terpyridines: influence of the orbital parentage. *Coord. Chem. Rev.* **2001,** 211, 195-205.
76. Wilson, M. H.; Ledwaba, L. P.; Field, J. S.; McMillin, D. R., Push-pull effects and emission from ternary complexes of platinum(II), substituted terpyridines, and the strong-field cyanide ion. *Dalton. Trans.* **2005**, (16), 2754-2759.
77. McMillin, D. R.; Moore, J. J., Luminescence that lasts from Pt(trpy)Cl+ derivatives (trpy=2,2 ';6 ',2 "-terpyridine). *Coord. Chem. Rev.* **2002,** 229, (1-2), 113-121.
78. Lai, S. W.; Lam, H. W.; Lu, W.; Cheung, K. K.; Che, C. M., Observation of Low-Energy Metal-Metal-to-Ligand Charge Transfer Absorption and Emission: Electronic Spectroscopy of Cyclometalated Platinum(II) Complexes with Isocyanide Ligands. *Organometallics* **2002,** 21, (1), 226-234.
79. Yam, V. W. W.; Chan, K. H. Y.; Wong, K. M. C.; Chu, B. W. K., Luminescent dinuclear platinum(II) terpyridine complexes with a flexible bridge and "sticky ends". *Angew. Chem. Int. Ed.* **2006,** 45, (37), 6169-6173.
80. Hu, Y. Z.; Wilson, M. H.; Zong, R. F.; Bonnefous, C.; McMillin, D. R.; Thummel, R. P., A luminescent Pt(II) complex with a terpyridine-like ligand involving a six-membered chelate ring. *Dalton Transations* **2005**, (2), 354-358.
81. Ma, B.; Djurovich, P. I.; Thompson, M. E., Excimer and electron transfer quenching studies of a cyclometalated platinum complex. *Coord. Chem. Rev.* **2005,** 249, (13-14), 1501-1510.

82. Pettijohn, C. N.; Jochnowitz, E. B.; Chuong, B.; Nagle, J. K.; Vogler, A., Luminescent excimers and exciplexes of PtII compounds. *Coord. Chem. Rev.* **1998,** 171, 85-92.
83. Lu, W.; Chan, M. C. W.; Zhu, N. Y.; Che, C. M.; Li, C. N.; Hui, Z., Structural and spectroscopic studies on Pt center dot center dot center dot Pt and pi-pi interactions in luminescent multinuclear cyclometalated platinum(II) homologues tethered by oligophosphine auxiliaries. *J. Am. Chem. Soc* **2004,** 126, (24), 7639-7651.
84. Wong, K. M. C.; Tang, W. S.; Chu, B. W. K.; Zhu, N. Y.; Yam, V. W. W., Synthesis, photophysical properties, and biomolecular labeling studies of luminescent platinum(II)-terpyridyl alkynyl complexes. *Organometallics* **2004,** 23, (14), 3459-3465.
85. Yutaka, T.; Mori, I.; Kurihara, M.; Mizutani, J.; Tamai, N.; Kawai, T.; Irie, M.; Nishihara, H., Photoluminescence switching of azobenzene-conjugated Pt(II) terpyridine complexes by trans-cis photoisomerization-sup. *Inorg. Chem.* **2002,** 41, (26), 7143-7150.
86. Jude, H.; Krause Bauer, J. A.; Connick, W. B., An outer-sphere two-electron platinum reagent. *J. Am. Chem. Soc.* **2003,** 125, (12), 3446-3447.
87. Buchner, R.; Field, J. S.; Haines, R. J.; Cunningham, C. T.; McMillin, D. R., Luminescence properties of salts of the $[Pt(trpy)Cl]^+$ and $[Pt(trpy)(MeCN)]^{2+}$ chromophores: Crystal structure of $[Pt(trpy)(MeCN)](SbF_6)_2$. *Inorg. Chem.* **1997,** 36, (18), 3952-3956.
88. Yam, V. W. W.; Tang, R. P. L.; Wong, K. M. C.; Ko, C. C.; Cheung, K. K., Synthesis and ion-binding studies of a platinum(II) terpyridine complex with crown ether pendant. X-ray crystal structure of $[Pt(trpy)(S\text{-benzo-15-crown-5})](PF_6)$. *Inorg. Chem.* **2001,** 40, (3), 571-+.
89. Lai, S. W.; Chan, M. C. W.; Cheung, K. K.; Che, C. M., Spectroscopic properties of luminescent platinum(II) vomplexes vontaining 4,4',4' '-Tri-tert-butyl-2,2':6',2' '-terpyridine ($^tBu_3tpy$). Crystal structures of $[Pt(^tBu_3tpy)Cl]ClO_4$ and $[Pt(^tBu_3tpy)\{CH_2C(O)Me\}]ClO_4$. *Inorg. Chem.* **1999,** 38, (19), 4262-4267.
90. Bailey, J.; Hill, M.; Marsh, R.; Miskowski, V.; Schaefer, W.; Gray, H., Electronic spectroscopy of chloro (terpyridine) platinum (II). *Inorg. Chem.* **1995,** 34, (18), 4591-4599.
91. Shikhova, E.; Danilov, E.; Kinayyigit, S.; Pomestchenko, I.; Tregubov, A.; Camerel, F.; Retailleau, P.; Ziessel, R.; Castellano, F., Excited-state absorption properties of platinum (II) terpyridyl acetylides. *Inorg. Chem.* **2007,** 46, (8), 3038-3048.
92. Chen, W. H.; Reinheimer, E. W.; Dunbar, K. R.; Omary, M. A., Coarse and fine tuning of the electronic energies of triimineplatinum(II) square-planar complexes. *Inorg. Chem.* **2006,** 45, 2770.
93. Hayoun, R.; Zhong, D. K.; Rheingold, A. L.; Doerrer, L. H., Gold(III) and platinum(II) polypyridyl double salts and a general metathesis route to metallophilic interactions. *Inorg. Chem.* **2006,** 45, (16), 6120.
94. Sakuda, E.; Funahashi, A.; Kitamura, N., Synthesis and spectroscopic properties of platinum (II) terpyridine complexes having an arylborane charge transfer unit. *Inorg. Chem* **2006,** 45, (26), 10670-10677.
95. Chakraborty, S.; Wadas, T. J.; Hester, H.; Flaschenreim, C.; Schmehl, R.; Eisenberg, R., Synthesis, structure, characterization, and photophysical studies of a new platinum terpyridyl-based triad with covalently linked donor and acceptor groups. *Inorg. Chem.* **2005,** 44, (18), 6284-6293.
96. Todd, J. A.; Turner, P.; Ziolkowski, E. J.; Rendina, L. M., (2,2 ': 6 ',2 "-Terpyridine)platinum(II) complexes (thioalkyl)dicarba-closo-dodecaborane(12) containing ligands. *Inorg. Chem.* **2005,** 44, (18), 6401-6408.
97. Yutaka, T.; Mori, I.; Kurihara, M.; Mizutani, J.; Tamai, N.; Kawai, T.; Irie, M.; Nishihara, H., Photoluminescence switching of azobenzene-conjugated Pt(II) terpyridine complexes by trans-cis photoisomerization. *Inorg. Chem.* **2002,** 41, (26), 7143-7150.
98. Lu, W.; Xiang, H.; Zhu, N.; Che, C., The $^3\pi\pi^*$ Emission of $Cy_3PAu(CC)_nAuPCy_3$ (n= 3, 4): Effect of Chain Length upon Acetylenic $^3\pi\pi^*$ Emission. *Organometallics* **2002,** 21, (11), 2343-2346.
99. Lu, W.; Chan, M. C. W.; Cheung, K. K.; Che, C. M., pi-pi interactions in organometallic systems. Crystal structures and spectroscopic properties of luminescent mono-, bi-, and trinuclear trans-cyclometalated platinum(II) complexes derived from 2,6-diphenylpyridine. *Organometallics* **2001,** 20, (12), 2477-2486.
100. Yam, V. W. W.; Wong, K. M. C.; Zhu, N. Y., Luminescent platinum(II) terpyridyl-capped carbon-rich molecular rods - an extension from molecular- to nanometer-scale dimensions. *Angew. Chem. Int. Ed.* **2003,** 42, (12), 1400-1403.

101. Kui, S. C. F.; Chui, S. S. Y.; Che, C. M.; Zhu, N., Structures, photoluminescence, and reversible vapoluminescence properties of neutral platinum(II) complexes containing extended π-conjugated cyclometalated ligands. *J. Am. Chem. Soc.* **2006,** 128, (25), 8279.
102. Lu, W.; Zhu, N.; Che, C.-M., Tethered trinuclear cyclometalated platinum(II) complexes: from crystal engineering to tunable emission energy. *Chem. Commun.* **2002**, (8), 900-901.
103. Goshe, A. J.; Steele, I. M.; Ceccarelli, C.; Rheingold, A. L.; Bosnich, B., Supramolecular Recognition. Terpyridyl Palladium and Platinum Molecular Clefts and Their Association with Planar Platinum Complexes-Sup. *J. Am. Chem. Soc.* **2003,** 125, (8), 444-451.
104. Yam, V. W. W.; Hui, C. K.; Yu, S. Y.; Zhu, N. Y., Syntheses, luminescence behavior, and assembly reaction of tetraalkynylplatinate(II) complexes: Crystal structures of $[Pt(^tBu_3trpy)(CCC_5H_4N)Pt(^tBu_3trpy)](PF_6)_3$ and $[Pt_2Ag_4(CCCCC_6H_4CH_3\text{-}4)_8(THF)_4]$. *Inorg. Chem.* **2004,** 43, (2), 812-821.
105. Okamura, R.; Wada, T.; Aikawa, K.; Nagata, T.; Tanaka, K., A platinum-ruthenium dinuclear complex bridged by bis(terpyridyl)xanthene. *Inorg. Chem.* **2004,** 43, (22), 7210-7217.
106. Campagna, S.; Di Pietro, C.; Loiseau, F.; Maubert, B.; McClenaghan, N.; Passalacqua, R.; Puntoriero, F.; Ricevuto, V.; Serroni, S., Recent advances in luminescent polymetallic dendrimers containing the 2,3-bis(2 '-pyridyl)pyrazine bridging ligand. *Coord. Chem. Rev.* **2002,** 229, (1-2), 67-74.
107. Fuchs, Y.; Lofters, S.; Dieter, T.; Shi, W.; Morgan, R.; Strekas, T. C.; Gafney, H. D.; Baker, A. D., Spectroscopic and Electrochemical Properties of Dimeric Ruthenium(II) Diimine Complexes and Determination of Their Excited-State Redox Properties. *J. Am. Chem. Soc* **1987,** 109, (9), 2691-2697.
108. Braunstein, C. H.; Baker, A. D.; Strekas, T. C.; Gafney, H. D., Spectroscopic and Electrochemical Properties of the Dimer Tetrakis(2,2'-Bipyridine)(Mu-2,3-Bis(2-Pyridyl)Pyrazine)Diruthenium(II) and Its Monomeric Analog. *Inorg. Chem.* **1984,** 23, (7), 857-864.
109. Puntoriero, F.; Serroni, S.; Galletta, M.; Juris, A.; Licciardello, A.; Chiorboli, C.; Carnpagna, S.; Scandola, F., A new heptanuclear dendritic ruthenium(II) complex featuring photoinduced energy transfer across high-energy subunits. *Chemphyschem.* **2005,** 6, (1), 129-138.
110. Sahai, R.; Rillema, D. P., A ruthenium (II)/platinum (II) binuclear complex bridged by 2, 2'-bipyrimidine. *Inorg. Chim. Acta.* **1986,** 118, (2), 35-37.
111. Sahai, R.; Baucom, D.; Rillema, D., Strongly luminescing ruthenium (II)/ruthenium (II) and ruthenium (II)/platinum (II) binuclear complexes. *Inorg. Chem.* **1986,** 25, (21), 3843-3845.
112. Yam, V. W.-W.; Lee, V. W.-M.; Cheung, K.-K., Synthesis, photophysics and electrochemistry of a novel luminescent organometallic ruthenium(II)/platinum(II) binuclear complex and its ruthenium(II)/dichloro-platinum(II) and palladium(II) counterparts. X-Ray crystal structure of [Ru(bpy)2(μ-2,3-dpp)PtCl2]2+[2,3-dpp = 2,3-bis(2-pyridyl)pyrazine]. *J. Chem. Soc., Chem. Commun.* **1994**, 2075-2076.
113. Yam, V.; Lee, V.; Cheung, K., Synthesis, photophysics, electrochemistry, and reactivity of ruthenium (II) polypyridine complexes with organoplatinum (II) moieties. crystal structure of $[Ru(bpy)_2(u\text{-}2, 3\text{-}dpp)PdCl_2]^{2+}$. *Organometallics* **1997,** 16, (13), 2833-2841.
114. Ruminski, R.; Nelson, J.; Culver, W., Synthesis and characterization of Pt (II) and Pt (II)/Ru (II) complexes with the bidentate bridging ligand dipyrido (2, 3-a:3,2-h) phenazine (dpop). *Inorg. Chim. Acta.* **2005,** 358, (1), 93-101.
115. Sahai, R.; RILLEMA, D., A novel hetero-oligomer containing one ruthenium (II), and three platinum (II) metal centres bridged by 2, 3-bis (2-pyridyl) quinoxaline. *J. Chem. Soc. Chem. Commun.* **1986**, (14), 1133-1134.
116. Armaroli, N.; Flamigni, L.; Barthram, A.; Gessi, A.; Barigelletti, F.; Ward, M., Spectroscopic, luminescence and electrochemical studies on a pair of isomeric complexes $[(bipy)_2Ru(AB)PtCl_2][PF_6]_2$ and $[Cl_2Pt(AB)Ru(bipy)_2][PF_6]_2$, where AB is the bis-bipyridyl bridging ligand 2,2': 3', 2": 6', 2"-quaterpyridine. *New J. Chem.* **1998,** 22, (8), 913.
117. Milkevitch, M.; Brauns, E.; Brewer, K. J., Spectroscopic and electrochemical properties of a series of mixed-metal d(6),d(8) bimetallic complexes of the form $[(bpy)_2M(BL)PtCl_2]^{2+}$ (bpy=2,2'-bipyridine; BL=dpq (2,3-bis(2-pyridyl)quinoxaline) or dpb (2,3-bis(2-pyridyl)benzoquinoxaline); M=Os-II or Ru-II). *Inorg. Chem.* **1996,** 35, (6), 1737-39.
118. Okamura, R.; Wada, T.; Aikawa, K.; Nagata, T.; Tanaka, K., A platinum-ruthenium dinuclear complex rridged by bis(terpyridyl)xanthene. *Inorg. Chem.* **2004,** 43, (22), 7210-7217.
119. Ventura, B.; Barbieri, A.; Barigelletti, F.; Batcha Seneclauze, J.; Retailleau, P.; Ziessel, R., Trichromophoric Systems from Square-Planar Pt-Ethynylbipyridine and Octahedral Ru- and Os-

Bipyridine Centers: Syntheses, Structures, Electrochemical Behavior, and Bipartition of Energy Transfer. *Inorg. Chem.* **2008,** 47, (15), 7048-7058.
120. Ozawa, H.; Haga, M.; Sakai, K., A Photo-Hydrogen-Evolving Molecular Device Driving Visible-Light-Induced EDTA-Reduction of Water into Molecular Hydrogen. *J. Am. Chem. Soc.* **2006,** 128, (15), 4926-4927.
121. Williams, R. L.; Toft, H. N.; Winkel, B.; Brewer, K. J., Synthesis, characterization, and DNA binding properties of a series of Ru, Pt mixed-metal complexes. *Inorg. Chem.* **2003,** 42, (14), 4394-4400.
122. Fang, Z.; Swavey, S.; Holder, A.; Winkel, B.; Brewer, K. J., DNA binding of mixed-metal supramolecular Ru, Pt complexes. *Inorg. Chem. Commun.* **2002,** 5, (12), 1078-1081.
123. Miao, R.; Mongelli, M. T.; Zigler, D. F.; Winkel, B. S. J.; Brewer, K. J., A multifunctional tetrametallic Ru-Pt supramolecular complex exhibiting both DNA binding and photocleavage. *Inorg. Chem.* **2006,** 45, (26), 10413-10415.
124. Jain, A.; Winkel, B. S. J.; Brewer, K. J., In vivo inhibition of E-coli growth by a Ru(II)/Pt(II) supramolecule [(tpy)RuCl(dpp)$PtCl_2$](PF_6). *J. Inorg. Biochem.* **2007,** 101, (10), 1525-1528.
125. Prussin II, A. J.; Zhao, S.; Jain, A.; Winkel, B. S. J.; Brewer, K. J., DNA interaction studies of tridentate bridged Ru(II)-Pt(II) mixed-metal supramolecules. *J Inorg. Biochem.* **2009,** 103, (3), 427-431.
126. Sakai, K.; Ozawa, H.; Yamada, H.; Tsubomura, T.; Hara, M.; Higuchi, A.; Haga, M., A tris (2, 2 -bipyridine) ruthenium (II) derivative tethered to a cis-$PtCl_2$(amine)$_2$ moiety: syntheses, spectroscopic properties, and visible-light-induced scission of DNA. *Dalton. Trans.* **2006,** 2006, (27), 3300-3305.
127. Qu, Y.; Farrell, N., Synthesis and chemical properties of a heterodinuclear (Pt, Ru) DNA-DNA and DNA-protein crosslinking agent. *Inorg. Chem.* **1995,** 34, (13), 3573-3576.
128. Van Houten, B.; Illenye, S.; Qu, Y.; Farrell, N., Homodinuclear (Pt, Pt) and heterodinuclear (Ru, Pt) metal compounds as DNA-protein cross-linking agents: potential suicide DNA lesions. *Biochemistry* **1993,** 32, (44), 11794-11801.
129. Milkevitch, M.; Shirley, B. W.; Brewer, K. J., Mixed-metal polymetallic platinum complexes designed to interact with DNA. *Inorg. Chim. Acta.* **1997,** 264, (1-2), 249-256.
130. Herman, A.; Tanski, J.; Tibbetts, M.; Anderson, C., Synthesis, characterization, and in vitro evaluation of a potentially selective anticancer, mixed-metal [ruthenium (III) platinum (II)] trinuclear complex. *Inorg. Chem.* **2008,** 47, (1), 274-280.
131. Baruah, H.; Day, C. S.; Wright, M. W.; Bierbach, U., Metal−Intercalator-Mediated Self-Association and One-Dimensional Aggregation in the Structure of the Excised Major DNA Adduct of a Platinum−Acridine Agent. *J. Am. Chem. Soc.* **2004,** 126, (14), 4492-4493.
132. Barry, C. G.; Baruah, H.; Bierbach, U., Unprecedented monofunctional metalation of adenine nucleobase in guanine- and thymine-containing dinucleotide sequences by a cytotoxic platinum-acridine hybrid agent. *J. Am. Chem. Soc.* **2003,** 125, (32), 9629-9637.
133. Milkevitch, M.; Storrie, H.; Brauns, E.; Brewer, K. J.; Shirley, B. W., A new class of supramolecular, mixed-metal DNA-binding agents: The interaction of Ru-II,Pt-II and Os-II,Pt-II bimetallic complexes with DNA. *Inorg. Chem.* **1997,** 36, (20), 4534-4538.
134. Miao, R.; Mongelli, M. T.; Zigler, D. F.; Winkel, B. S. J.; Brewer, K. J., A multifunctional tetrametallic Ru-Pt supramolecular complex exhibiting both DNA binding and photocleavage-sup. *Inorg. Chem.* **2006,** 45, (26), 10413-10415.
135. (a) Milkevitch, M., Mixed-metal ruthenium-platinum polyazine supramolecules: synthesis, characterization and exploration of DNA binding. [electronic resource]:Virginia Tech, 2000.
136. Barron, L. D., True and false chirality and absolute asymmetric synthesis. *J. Am. Chem. Soc* **1986,** 108, (18), 5539-5542.
137. Barron., L. D., Chirality and life. *Space. Sci. Rev.* **2008,** 135, 187-201.
138. Avalos, M.; Babiano, R.; Cintas, P.; Jimenez, J. L.; Palacios, J. C.; Barron, L. D., Absolute Asymmetric Synthesis under Physical Fields: Facts and Fictions. *Chem. Rev.* **1998,** 98, (7), 2391-2404.
139. Hazen, R. M.; Sholl, D. S., Chiral selection on inorganic crystalline surfaces. *Nature Materials* **2003,** 2, (6), 367-374.
140. Fasel, R.; Parschau, M.; Ernst, K. H., Amplification of chirality in two-dimensional enantiomorphous lattices. *Nature* **2006,** 439, (7075), 449-452.
141. Pincock, R. E.; Perkins, R. R.; Ma, A. S.; Wilson, K. R., Probability Distribution of Enantiomorphous Forms in Spontaneous Generation of Optically Active Substances. *Science* **1971,** 174, (4013), 1018-1020.

142. Bailey, J.; Chrysostomou, A.; Hough, J.; Gledhill, T.; McCall, A.; Clark, S.; Menard, F.; Tamura, M., Circular polarization in star-formation regions: implications for biomolecular homochirality. *Science* **1998,** 281, (5377), 672.
143. Podlech, J., New insight into the source of biomolecular homochirality: an extraterrestrial origin for molecules of life? *Angew. Chem. Int. Ed.* **1999,** 38, (4).
144. Rikken, G. L. J. A.; Raupach, E., Enantioselective magnetochiral photochemistry. *Nature* **2000,** 405, (6789), 932-935.
145. Barron, L. D., Chemistry: Chirality, magnetism and light. *Nature* **2000,** 405, (6789), 895-896.
146. Barron, L. D., Magnetic molecules: Chirality and magnetism shake hands. *Nat. Mater.* **2008,** 7, (9), 691-692.
147. Salam, A., The role of chirality in the origin of life. *Journal of Molecular Evolution* **1991,** 33, (2), 105-113.
148. Martin Quack, How Important is Parity Violation for Molecular and Biomolecular Chirality? *Angew. Chem. Int. Ed.* **2002,** 41, (24), 4618-4630.
149. Ben L. Feringa, R. A. v. D., Absolute Asymmetric Synthesis: The Origin, Control, and Amplification of Chirality. *Angew. Chem. Int. Ed.* **1999,** 38, (23), 3418-3438.
150. García., L. P.; Amabilino., D. B., Spontaneous resolution under supramolecular control. *Chem. Soc. Rev.* **2002,** 31, (6), 342-356.
151. Jacques, J.; Collet, A.; Wilen, S., *[Book] Enantiomers, racemates, and resolutions*. Wiley New York: 1981.
152. Anslyn., E. V.; Dougherty., D. A., *[Book] Sterrochemistry.* Modern Physical Organic Chemistry. **2006**, 297-344.
153. Sauvage, J.-P., *[Book] Transition metals in supramolecular chemistry.* Wiley **1999**.
154. Chen, Y.; Yekta, S.; Yudin, A. K., Modified BINOL Ligands in Asymmetric Catalysis. *Chem. Rev.* **2003,** 103, (8), 3155-3212.
155. Parker, D., NMR determination of enantiomeric purity. *Chem. Rev.* **1991,** 91, (7), 1441-1457.
156. Bifulco, G.; Dambruoso, P.; Gomez-Paloma, L.; Riccio, R., Determination of Relative Configuration in Organic Compounds by NMR Spectroscopy and Computational Methods. *Chem. Rev.* **2007,** 107, (9), 3744-3779.
157. Seco, J. M.; Quinoa, E.; Riguera, R., The Assignment of Absolute Configuration by NMR. *Chem. Rev.* **2004,** 104, (1), 17-118.
158. Jameson, C. J.; Murad, S., On using the NMR chemical shift to assess polar-nonpolar cross-intermolecular interactions. *Chem. Phys. Lett.* **2003,** 380, (5-6), 556-562.
159. Robert, M.; Francis, X.; David, J., *[Book] Spectrometric identification of organic compounds.* John Wiley & Sons, New York **1998**.
160. Cini, R.; Donati, A.; Giannettoni, R., Synthesis and structural characterization of chloro(2,2 ';6 ',2 "-terpyridine)platinum trichloro(dimethylsulfoxide)platinate(II). Density functional analysis of model molecules. *Inorg. Chim. Acta.* **2001,** 315, (1), 73-80.
161. Constable, E. C.; Lewis, J., NMR-Studies on Ruthenium(II) Alpha,Alpha'-Diimine Complexes - Further Evidence for Unique Reactivity at H-3,3' of Coordinated 2,2'-Bipyridines. *Inorg. Chim. Acta.* **1983,** 70, (2), 251-253.
162. Rillema, D.; Jones, D., Structure of tris (2,2-bipyridyl) ruthenium (II) hexafluorophosphate,$[Ru(bipy)_3][PF_6]_2$; X-ray crystallographic determination. *J. Chem. Soc., Chem. Commun.* **1979,** 1979, (19), 849-851.
163. Eggleston, D.; Goldsby, K.; Hodgson, D.; Meyer, T., Structural variations induced by changes in oxidation state and their role in electron transfer. Crystal and molecular structures of cis-$[Ru(bpy)_2Cl_2]$. 3.5 H_2O and cis-$[Ru(bpy)_2Cl_2]Cl.2H_2O$. *Inorg. Chem.* **1985,** 24, (26), 4573-4580.
164. Toma, S. H.; Uemi, M.; Nikolaou, S.; Tomazela, D. M.; Eberlin, M. N.; Toma, H. E., {trans,-1,4-bis[(4-pyridyl)ethenyl]benzene}(2,2 '-bipyridine)ruthenium(II) complexes and their supramolecular assemblies with beta-cyclodextrin. *Inorg. Chem.* **2004,** 43, (11), 3521-3527.
165. Leising, R. A.; Kubow, S. A.; Takeuchi, K. J., Synthesis and Characterization of (Nitro)Ruthenium Complexes That Utilize Identical Trans-Positioned Tertiary Phosphine-Ligands. *Inorg. Chem.* **1990,** 29, (22), 4569-4574.
166. Heijden, M.; Van Vliet, P.; Haasnoot, J.; Reedijk, J., Synthesis and characterization of cis-(2, 2'-bipyridine)(2, 2'-biquinoline) dichlororuthenium (II) and its co-ordination chemistry with imidazole derivatives. *J. Chem. Soc. Dalton trans.* **1993**, (24), 3675-3679.

167. Nikolaou, S.; Uemi, M.; Toma, H. E., Total assignment of ^{1}H and ^{13}C NMR spectra of a bridged triruthenium cluster-polypyridine dimer based on 2D (COSY, HMQC, and HMBC) techniques. *Spectroscopy Letters* **2001,** 34, (3), 267-277.
168. Gelling, A.; Orrell, K. G.; Osborne, A. G.; Sik, V., The energetics and mechanism of fluxionality of 2,2':6',2"-terpyridine derivatives when acting as bidentate ligands in transition-metal complexes. A detailed dynamic NMR study. *J. Chem. Soc. Dalton Trans.* **1998**, (6), 937-945.
169. Gelling, A.; Olsen, M. D.; Orrell, K. G.; Osborne, A. G.; Sik, V., Synthesis and dynamic NMR studies of fluxionality in rhenium(I), platinum(II) and platinum(IV) complexes of 'back-to-back' 2,2':6 ',2"-terpyridine ligands. *J. Chem. Soc. Dalton Trans.* **1998**, (20), 3479-3488.
170. Laurent Barloy; Shailesh Ramdeehul; Claire Carlotti; Francis Taulelle; Jean Fischer, Allylpalladium(II) Complexes Bearing Potentially Tridentate Ligands: Synthesis, Solution Dynamics, and Crystal Structures. *Eur. J. Inorg. Chem.* **2000,** (12), 2523-2532.
171. Abel, E.; Orrell, K.; Osborne, A.; Pain, H.; Hursthouse, M.; Malik, K., 2,2:6,2 -Terpyridine (terpy) acting as a fluxional bidentate ligand. Part 4. cis-[$M(C_6F_5)_2$ (terpy)](M = Pd or Pt): nuclear magnetic resonance studies of their solution dynamics and crystal structure of cis-[$Pd(C_6F_5)_2$(terpy)]. *J. Chem. Soc. Dalton Trans.* **1994,** 1994, (23), 3441-3449.
172. Goodwin., H. A.; Lions., F., Tridentate Chelate Compounds. II. *J. Am. Chem. Soc.* **1959,** 81, 6415.
173. Bock, H.; Vaupel, T.; Nather, C.; Ruppert, K.; Havlas, Z., Structures of Charge-Perturbed and Sterically Overcrowded Molecules .13. Diprotonated Tetra(2-Pyridyl)Pyrazine and Its Chemical Mimesis Due to Different Hydrogen Bridges. *Angew. Chem. Int. Ed.* **1992,** 31, (3), 299-301.
174. Greaves, B.; Stoecklievans, H., A Tetragonal Form of Tetra(2-Pyridyl)Pyrazine (Tppz). *Acta. Crystal. C* **1992,** 48, 2269-2271.
175. Maekawa, M.; Minematsu, T.; Konaka, H.; Sugimoto, K.; Kuroda-Sowa, T.; Suenaga, Y.; Munakata, M., Syntheses and structural characterizations of novel mono- and dinuclear iridium hydrido complexes with polydentate nitrogen donor ligands. *Inorg. Chim. Acta.* **2004,** 357, (12), 3456-3472.
176. Padgett, C. W.; Pennington, W. T.; Hanks, T. W., Conformations and binding modes of 2,3,5,6-Tetra(2'-pyridyl)pyrazine. *Crystal Growth & Design* **2005,** 5, (2), 737-744.
177. Campos-Fernandez, C. S.; Smucker, B. W.; Clerac, R.; Dunbar, K. R., Reactivity studies of 2,3,5,6-tetra(2-pyridyl)pyrazine (tppz) with first-row transition metal ions. *Israel Journal of Chemistry* **2001,** 41, (3), 207-218.
178. Chanda, N.; Laye, R. H.; Chakraborty, S.; Paul, R. L.; Jeffrey, J. C.; Ward, M. D.; Lahiri, G. K., Dinuclear ruthenium(II) complexes [{(L)ClRuII}(2)(mu-tppz)](2+) (L = an arylazopyridine ligand) incorporating tetrakis(2-pyridyl) pyrazine (tppz) bridging ligand: synthesis, structure and spectroelectrochemical properties. *J. Chem. Soc. Dalton Trans.* **2002**, (18), 3496-3504.
179. Graf, M.; Stoeckli-Evans, H.; Escuer, A.; Vicente, R., Significant antiferromagnetic exchange in copper(II) and nickel(II) dinuclear complexes of the substituted pyrazine ligand 2,3,5,6-tetra(2-pyridyl)pyrazine (TPPZ): magnetic properties, synthesis and crystal structure. *Inorg. Chim. Acta.* **1997,** 257, (1), 89-97.
180. Hartshorn, C. M.; Daire, N.; Tondreau, V.; Loeb, B.; Meyer, T. J.; White, P. S., Synthesis and Characterization of Dinuclear Ruthenium Complexes with Tetra-2-pyridylpyrazine as a Bridge. *Inorg. Chem.* **1999,** 38, (13), 3200-3206.
181. Burkholder, E.; Zubieta, J., Solid state coordination chemistry: construction of 2D networks and 3D frameworks from phosphomolybdate clusters and binuclear Cu(II) complexes. The syntheses and structures of [{Cu_2(tpypyz)(H_2O)2}(Mo_5O_{15})($HOPO_3$)$_2$] nH_2O [n = 2, 3; tpypyz = tetra(2-pyridyl)pyrazine]. *Chem. Commun.* **2001**, (20), 2056-2057.
182. Graf, M.; Greaves, B.; Stoeckli-Evans, H., Crystal and molecular structures of Cu(II) and Zn(II) complexes of 2,3,5,6-tetra(2-pyridyl)pyrazine (TPPZ): an old ligand revisited. *Inorg. Chim. Acta.* **1993,** 204, (2), 239-246.
183. Hagrman, D.; Hagrman, P.; Zubieta, J., Polyoxomolybdate clusters and copper-organonitrogen complexes as building blocks for the construction of composite solids. *Inorg. Chim. Acta.* **2000,** 300-302, 212-224.
184. Yap, G. P. A.; Hadadzadeh, H.; Crutchley, R. J., cis,cis-μ-2,3,5,6-Tetra-2-pyridylpyrazineN1,N2,N6:N3,N4,N5-bis[dichloro(dimethylsulfoxide-S)ruthenium(II)] dihydrate acetone disolvate. *Acta Crystallographica: E*, 2006, 62, m2002-m2004.
185. Teles, W. M.; Speziali, N. L.; Filgueiras, C. A. L., Synthesis of a polymetallic Pt, Sn complex containing square planar and trigonal bipyramidal platinum centres: Crystal and molecular structure of

bis{chlorotriethylphosphinoplatinum(II)}[mu]-2,3,5,6-tetrakis([alpha]-pyridyl)pyrazinetetrakis(trichlorostannyl)triethylphosphinoplatinate(II). *Polyhedron* **2000,** 19, (7), 739-742.
186. Chen, X. Y.; Femia, F. J.; Babich, J. W.; Zubieta, J., Synthesis, characterization and crystal structures of mono-, di- and trinuclear rhenium(I) tricarbonyl complexes with 2,3,5,6-tetra(2-pyridyl)pyrazine. *Inorg. Chim. Acta.* **2001,** 315, (1), 66-72.
187. Metcalfe, C.; Spey, S.; Adams, H.; Thomas, J. A., Extended terpyridyl and triazine complexes of d(6)-metal centres. *J. Chem. Soc. Dalton* **2002**, (24), 4732-4739.
188. Graf, M.; Stoeckli-Evans, H., Tetraprotonated Tetra (2-pyridyl) pyrazine: Pyrazine-2, 3, 5, 6-tetra (2-pyridinium) Tetrachloride Dihydrate. *Acta Crystallogr., Sect. E: Cryst. Struct. Commun.* **1996,** 52, (12), 3073-3075.
189. Sakai, K.; Kurashima, M., [μ-2,3,5,6-tetrakis(2-pyridyl)pyrazine]bis-[chloroplatinum(II)] bis[trichloro(dimethyl sulfoxide)platinate(II)]. *Acta Crystallogr. Sect. E: Struct. Rep. Online* **2003,** 59, M411-M413.
190. Yuasa, J.; Fukuzumi, S., An OFF-OFF-ON Fluorescence Sensor for Metal Ions in Stepwise Complex Formation of 2,3,5,6-Tetrakis(2-pyridyl)pyrazine with Metal Ions. *J. Am. Chem. Soc.* **2006,** 128, (51), 17154.
191. Yuasa, J.; Fukuzumi, S., OFF-OFF-ON switching of fluorescence and electron transfer depending on stepwise complex formation of a host ligand with guest metal ions. *J. Am. Chem. Soc.* **2008,** 130, (2), 566-575.
192. Carlson, C. N.; Kuehl, C. J.; DaRe, R. E.; Veauthier, J. M.; Schelter, E. J.; Milligan, A. E.; Scott, B. L.; Bauer, E. D.; Thompson, J. D.; Morris, D. E.; John, K. D., Ytterbocene Charge-Transfer Molecular Wire Complexes. *J. Am. Chem. Soc* **2006,** 128, (22), 7230-7241.
193. Flores-Torres, S.; Hutchison, G. R.; Soltzberg, L. J.; Abruna, H. D., Ruthenium Molecular Wires with Conjugated Bridging Ligands: Onset of Band Formation in Linear Inorganic Conjugated Oligomers. *J. Am. Chem. Soc.* **2006,** 128, (5), 1513-1522.
194. Horiuchi, S.; Kumai, R.; Tokunaga, Y.; Tokura, Y., Proton Dynamics and Room-Temperature Ferroelectricity in Anilate Salts with a Proton Sponge. *J. Am. Chem. Soc.* **2008,** 130, (40), 13382-13391.
195. Brown, M.; Cook, B.; Sloan, T., Stereochemical notation in coordination chemistry. Mononuclear complexes. *Inorg. Chem.* **1975,** 14, (6), 1273-1278.
196. Brown, M.; Cook, B.; Sloan, T., Stereochemical notation in coordination chemistry: mononuclear complexes of coordination numbers seven, eight, and nine. *Inorg. Chem.* **1978,** 17, (6), 1563-1568.
197. Connelly, N. G.; Damhus, T.; Harshorn, R. M.; Hutton, A. T., *[Book] Nomenclature of inorganic chemistry: IUPAC recommendations.* **2005**.
198. R. S. Cahn; Christopher Ingold; V. Prelog, Specification of Molecular Chirality. *Angew. Chem. Int. Ed.* **1966,** 5, (4), 385-415.
199. Crego-Calama., M.; Reinhoudt., D. N., *[Book] Topics in current chemistry-supramolecular chirality*. Springer-Verlag Berlin Heidelberg: 2006 Vol. 265.
200. Seeber, G.; Tiedemann, B. E. F.; Raymond, K. N., *[Book]* S*upramolecular chirality in coordination chemistry.* **2006,** 265, 147-183.
201. Murphy, C. J.; Arkin, M. R.; Jenkins, Y.; Ghatlia, N. D.; Bossmann, S. H.; Turro, N. J.; Barton, J. K., Long-Range Photoinduced Electron-Transfer through a DNA Helix. *Science* **1993,** 262, (5136), 1025-1029.
202. Boisdenghien, A.; Moucheron, C.; Kirsch-DeMesmaeker, A., $[Ru(phen)_2(PHEHAT)]^{2+}$ and $[Ru(phen)_2(HATPHE)]^{2+}$: Two Ruthenium(II) Complexes with the Same Ligands but Different Photophysics and Spectroelectrochemistry. *Inorg. Chem.* **2005,** 44, (21), 7678-7685.
203. Rosenberg, B.; Van Camp, L.; Krigas, T., Inhibition of cell division in Escherichia coli by electrolysis products from a platinum electrode. *Nature* **1965,** 205, (4972), 698-699.
204. Rosenberg, B.; Vancamp, L.; TROSKO, J.; MANSOUR, V., Platinum compounds: a new class of potent antitumour agents. *Nature* **1969,** 222, 385-387.
205. Takahara, P. M.; Rosenzweig, A. C.; Frederick, C. A.; Lippard, S. J., Crystal structure of double-stranded DNA containing the major adduct of the anticancer drug cisplatin. *Nature* **1995,** 377, (6550), 649-652.
206. Sherman, S. E.; Lippard, S. J., Structural Aspects of Platinum Anticancer Drug-Interactions with DNA. *Chem. Rev.* **1987,** 87, (5), 1153-1181.

207. Takahara, P.; Frederick, C.; Lippard, S., Crystal-Structure of the Anticancer Drug Cisplatin Bound to Duplex DNA. *J. Am. Chem. Soc* **1997,** 119, (20), 4795-4795.
208. Schollhorn, H.; Raudaschlsieber, G.; Muller, G.; Thewalt, U.; Lippert, B., DNA-intrastrand guanine, guanine cross-linking by cisplatin - comparison of 3 model compounds with head-head orientation of the nucleobases. *J. Am. Chem. Soc.* **1985,** 107, (21), 5932-5937.
209. Schroder, G.; Sabat, M.; Baxter, I.; Kozelka, J.; Lippert, B., cis-[Pt(NH_3)$_2$(9-MeA-N7)(9-EtGH-N7)](PF_6)5H_2O (9-MeA = 9-Methyladenine; 9-EtGH = 9-Ethylguanine): A Right-Handed Helicoidal Model Compound for the Intrastrand A, G Cross-Link in Duplex DNA. *Inorg. Chem.* **1997,** 36, (3), 490-493.
210. Wong, E.; Giandomenico, C. M., Current status of platinum-based antitumor drugs (review). *Chem. Rev.* **1999,** 99, 2451-66.
211. Baruah, H.; Barry, C. G.; Bierbach, U., Platinum-intercalator conjugates: From DNA-targeted cisplatin derivatives to adenine binding complexes as potential modulators of gene regulation. *Cur.r Top. Med. Chem.* **2004,** 4, (15), 1537-1549.
212. Reedijk, J., The Mechanism of Action of Platinum Antitumor Drugs. *Pure and Appl. Chem.* **1987,** 59, (2), 181-192.
213. Boerner, L. J. K.; Zaleski, J. M., Metal complex-DNA interactions: from transcription inhibition to photoactivated cleavage. *Curr. Opin. Chem. Biol.* **2005,** 9, (2), 135-144.
214. Wong, Y.-S.; Lippard, S. J., X-Ray Crystal Structure of a 2:2 Chloroterpyridineplatinum(11)-Adenosine-5'-monophosphate Intercalation Complex. *J.Chem.Soc. Chem. Commun.* **1977**, 824.
215. Wang, A. H.; Nathans, J.; Marel, G. v. d.; Boom, J. H. v.; Rich, A., Molecular structure of a double helical DNA fragment intercalator complex between deoxy CpG and a terpyridine platinum compound. . *Nature* **1978,** 276, (5687), 471-474.
216. Karlijn van der Schilden, F. G., Huub Kooijman Anthony L. Spek Jaap G. Haasnoot Jan Reedijk, A Highly Flexible Dinuclear Ruthenium(II)-Platinum(II) Complex: Crystal Structure and Binding to 9-Ethylguanine. *Angew. Chem. Int. Ed.* **2004,** 43, (42), 5668-5670.
217. Rice, J. H.; Williamson, A. N.; Schramm, R. F.; Wayland, B. B., Palladium(II) and platinum(II) alkyl sulfoxide complexes. Examples of sulfur-bonded, mixed sulfur- and oxygen-bonded, and totally oxygen-bonded complexes. *Inorg. Chem.* **1972,** 11, (6), 1280-4.
218. Sullivan., B. P.; Salmon., D. J.; Meyer., a. T. J., Mixed phosphine 2,2'-bipyridine complexes of ruthenium. *Inorg. Chem.* **1978,** 17, (12), 3334.
219. Sullivan, B. P.; Calvert, J. M.; Meyer, T. J., Cis-Trans Isomerism in (Trpy)(Pph3)Rucl2 - Comparisons between the Chemical and Physical-Properties of a Cis-Trans Isomeric Pair. *Inorg. Chem.* **1980,** 19, (5), 1404-1407.
220. Thummel, R. P.; Jahng, Y., Polyaza Cavity-Shaped Molecules .9. Ruthenium(II) Complexes of Annelated Derivatives of 2,2'-6,2''-Terpyridine and Related Systems - Synthesis, Properties, and Structure. *Inorg. Chem.* **1986,** 25, (15), 2527-2534.
221. Zhao, S.; Arachchige, S. M.; Slebodnick, C.; Brewer, K. J., Synthesis and Study of the Spectroscopic and Redox Properties of Ru^{II},Pt^{II} Mixed-Metal Complexes Bridged by 2,3,5,6-Tetrakis(2-pyridyl)pyrazine. *Inorg. Chem.* **2008,** 47, (14), 6144-6152.
222. Moucheron, C.; Kirsch-De Mesmaeker, A.; Dupont-Gervais, A.; Leize, E.; Van Dorsselaer, A., Synthesis and Characterization by Electrospray Mass Spectrometry of a Novel Dendritic Heptanuclear Complex of Ruthenium(II). *J. Am. Chem. Soc.* **1996,** 118, (50), 12834-12835.
223. Reza Zadmard; Arno Kraft; Thomas Schrader; Uwe Linne, Relative Binding Affinities of Molecular Capsules Investigated by ESI-Mass Spectrometry. *Chemistry - A European Journal* **2004,** 10, (17), 4233-4239.
224. Christoph A. Schalley; Thomas Muller; Petra Linnartz; Matthias Witt; Mathias Schafer; Arne Lutzen, Mass Spectrometric Characterization and Gas-Phase Chemistry of Self-Assembling Supramolecular Squares and Triangles. *Chemistry - A European Journal* **2002,** 8, (15), 3538-3551.
225. Wang, P.; Newkome, G. R.; Wesdemiotis, C., Mass spectrometry analysis of organometallic assemblies: Bis-terpyridine-Ru(II) connectivity. *Int. J. Mass Spectrum* **2006,** 255, 86-92.
226. Daniel, J.; Friess, S.; Rajagopalan, S.; Wendt, S.; Zenobi, R., Quantitative determination of noncovalent binding interactions using soft ionization mass spectrometry. *Int. J. of Mass Spectrum.* **2002,** 216, (1), 1-27.

227. Vis, H.; Heinemann, U.; Dobson, C. M.; Robinson, C. V., Detection of a Monomeric Intermediate Associated with Dimerization of Protein Hu by Mass Spectrometry. *J. Am. Chem. Soc.* **1998,** 120, (25), 6427-6428.
228. Schmuck, C.; Rehm, T.; Grohn, F.; Klein, K.; Reinhold, F., Ion pair driven self-assembly of a flexible bis-zwitterion in polar solution: Formation of discrete nanometer-sized cyclic dimers. *J. Am. Chem. Soc.* **2006,** 128, (5), 1430-1431.
229. CrysAlisPro v1.171, O. D. W., Poland, **2007**.
230. Sheldrick, G. M. S. N., ver. 6.12; Bruker Analytical X-ray Systems,; Inc.: Madison, W., 2001., **2001**.
231. Spek, A. L., Single-crystal structure validation with the program PLATON. *J. Appl. Cryst.* **2003,** 36, 7-13.
232. Miao, R.; Mongelli, M. T.; Zigler, D. F.; Winkel, B. S. J.; Brewer, K. J., A multifunctional tetrametallic Ru-Pt supramolecular complex exhibiting both DNA binding and photocleavage. *Inorg. Chem.* **2006,** 45, (26), 10413-10415.
233. Caspar, J. V.; Kober, E. M.; Sullivan, B. P.; Meyer, T. J., Application of the Energy Gap Law to the Decay of Charge-transfer Excited States. *J. Am. Chem. Soc.* **1982,** 104, 630.
234. Kober, E.; Sullivan, B.; Dressick, W.; Caspar, J.; Meyer, T., Highly luminescent polypyridyl complexes of osmium (II). *J. Am. Chem. Soc.* **1980,** 102, (24), 7383-7385.
235. Sergeyev, V.; Novoskoltseva, O.; Pyshkina, O.; Zinchenko, A.; Rogacheva, V.; Zezin, A.; Yoshikawa, K.; Kabanov, V., Secondary structure of DNA is recognized by slightly cross-linked cationic hydrogel. *J. Am. Chem. Soc.* **2002,** 124, (38), 11324-11333.
236. Asara, J.; Uzelmeier, C.; Dunbar, K.; Allison, J., Analysis of Transition-Metal Compounds Containing Tetrathiafulvalene Phosphine Ligands by Fast Atom Bombardment Mass Spectrometry: Limitations and the Development of Matrix Additives for the Desorption of Multiply Charged Complexes. *Inorg. Chem.* **1998,** 37, (8), 1833-1840.
237. Liang, X.; Suwanrumpha, S.; Freas, R., Fast atom bombardment tandem mass spectrometry of (polypyridyl) ruthenium (II) complexes. *Inorg. Chem.* **1991,** 30, (4), 652-658.
238. Laine, P.; Bedioui, F.; Ochsenbein, P.; Marvaud, V.; Bonin, M.; Amouyal, E., A New Class of Functionalized Terpyridyl Ligands as Building Blocks for Photosensitized Supramolecular Architectures. Synthesis, Structural, and Electronic Characterizations. *J. Am. Chem. Soc* **2002,** 124, (7), 1364-1377.
239. Polson, M. I. J.; Medlycott, E. A.; Hanan, G. S.; Mikelsons, L.; Taylor, N. L.; Watanabe, M.; Tanaka, Y.; Loiseau, F.; Passalacqua, R.; Campagna, S., Ruthenium complexes of easily accessible tridentate ligands based on the 2-aryl-4,6-bis(2-pyridyl)-s-triazine motif: Absorption spectra, luminescence properties, and redox behavior. *Chem-Eur J* **2004,** 10, (15), 3640-3648.
240. Aihara, J., Magnetotropism of biphenylene and related hydrocarbons. A circuit current analysis. *J. Am. Chem. Soc.* **1985,** 107, (2), 298-302.
241. Aihara, J.-i., Circuit Resonance Energy: A Key Quantity That Links Energetic and Magnetic Criteria of Aromaticity. *J. Am. Chem. Soc.* **2006,** 128, (9), 2873-2879.
242. Schubert., U. S.; Hofmeier., H.; George, R. N., *[Book] Modern terpyridine chemistry.* Wiley-VCH Verlag GmbH & Co. KGaA, Weiheim**, 2006**.
243. Constable, E. C.; Seddon, K. R., A Deuterium-Exchange Reaction of the "Tris-(2,2'-Bipyridine)Ruthenium(II) Cation - Evidence for the Acidity of the 3,3'-Protons. *J. Chem. Soc., Chem. Commun.* **1982**, (1), 34-36.
244. Becker, M.; Port, R. E.; Zabel, H. J.; Zeller, W. J.; Bachert, P., Monitoring local disposition kinetics of carboplatin in vivo after subcutaneous injection in rats by means of Pt-195 NMR. *Journal of Magnetic Resonance* **1998,** 133, (1), 115-122.
245. Gabano, E.; Marengo, E.; Bobba, M.; Robotti, E.; Cassino, C.; Botta, M.; Osella, D., Pt-195 NMR spectroscopy: A chemometric approach. *Coord. Chem. Rev.* **2006,** 250, (15-16), 2158-2174.
246. Priqueler, J. R. L.; Butler, I. S.; Rochon, F. D., An overview of Pt-195 nuclear magnetic resonance spectroscopy. *Applied Spectroscopy Reviews* **2006,** 41, (3), 185-226.
247. Appleton, T.; Hall, J.; Ralph, S., 15 N and 195 Pt NMR spectra of platinum ammine complexes: trans- and cis-influence series based on 195 Pt- 15 N coupling constants and 15 N chemical shifts. *Inorg. Chem.* **1985,** 24, (26), 4685-4693.
248. Jain, A.; Wang, J.; Mashack, E. R.; Winkel, B. S. J.; Brewer, K. J., Multifunctional DNA Interactions of Ru–Pt Mixed Metal Supramolecular Complexes with Substituted Terpyridine Ligands. *Inorg. Chem.* **2009,** ASAP.

249. Bain, A. D., Chemical exchange in NMR. *Progress in Nuclear Magnetic Resonance Spectroscopy* **2003,** 43, (3-4), 63-103.
250. McMurtrie, J.; Dance, I., Engineering the metal-terpy grid with complexes containing 4 '-hydroxy terpyridine. *Crystengcomm.* **2005,** 7, 230-236.
251. Gagne, R.; Koval, C.; Lisensky, G., Ferrocene as an internal standard for electrochemical measurements. *Inorg. Chem.* **1980,** 19, (9), 2854-2855.
252. Ruminski, R.; Kiplinger, J.; Cockroft, T.; Chase, C., Triammineruthenium (II) complexes bound with the novel bridging ligand 2,3,5,6-tetrakis (2-pyridyl) pyrazine (tppz). *Inorg. Chem.* **1989,** 28, (2), 370-373.
253. Sauvage, J. P.; Collin, J. P.; Chambron, J. C.; Guillerez, S.; Coudret, C.; Balzani, V.; Barigelletti, F.; De Cola, L.; Flamigni, L., Ruthenium(II) and Osmium(II) Bis(terpyridine) Complexes in Covalently-Linked Multicomponent Systems: Synthesis, Electrochemical Behavior, Absorption Spectra, and Photochemical and Photophysical Properties. *Chem. Rev.* **1994,** 94, (4), 993-1019.
254. Young, R. C.; Nagle, J. K.; Meyer, T. J.; Whitten, D. G., Electron transfer quenching of nonemitting excited states of $[Ru(TPP)(py)_2]$ and $Ru(trpy)_2]^{2+}$. *J. Am. Chem. Soc.* **1978,** 100, (15), 4773-4778.
255. Winkler, J. R.; Netzel, T. L.; Creutz, C.; Sutin, N., Direct observation of metal-to-ligand charge-transfer (MLCT) excited states of pentaammineruthenium(II) complexes. *J. Am. Chem. Soc.* **1987,** 109, (8), 2381-2392.
256. Milkevitch, M.; Shirley, B. W.; Brewer, K. J., Mixed-metal polymetallic complexes designed to interact with DNA. *Inorg. Chimi. Acta.* **1997,** 264, 249-256.
257. Lippard, S. J., Platinum Complexes - Probes of Polynucleotide Structure and Anti-Tumor Drugs. *Accounts Chem. Res.* **1978,** 11, (5), 211-217.
258. Cohen, G. L.; Bauer, W. R.; Barton, J. K.; Lippard, S. J., Binding of Cis-Dichlorodiammineplatinum(II) and Trans-Dichlorodiammineplatinum(Ii) to DNA - Evidence for Unwinding and Shortening of the Double Helix. *Science* **1979,** 203, (4384), 1014-1016.
259. Malina, J.; Hofr, C.; Maresca, L.; Natile, G.; Brabec, V., *Biophysical Journal* **2000,** 78, 2008-2021.
260. Mong, S.; Haung, C. H.; Preatyko, A. W.; Crooke, S. T., *Cancer Research* **1980,** 40, 3313-3317.
261. Bellon, S. F.; Coleman, J. H.; Lippard, S. J., *Biochemistry* **1991,** 30, 8026-8035.
262. Abdullin, T.; Nikitina, I.; Bondar', O., Adsorption and oxidation of purine bases and their derivatives on electrodes modified with carbon nanotubes. *Russian Journal of Electrochemistry* **2008,** 44, (12), 1345-1349.
263. Sun, B.; Guan, J.-X.; Xu, L.; Yu, B.-L.; Jiang, L.; Kou, J.-F.; Wang, L.; Ding, X.-D.; Chao, H.; Ji, L.-N., DNA Condensation Induced by Ruthenium(II) Polypyridyl Complexes [Ru(bpy)2(PIPSH)]2+ and [Ru(bpy)2(PIPNH)]2+. *Inorg. Chem.* **2009,** 48, (11), 4637-4639.
264. Chiu, T.; Dickerson, R., 1 Å crystal structures of B-DNA reveal sequence-specific binding and groove-specific bending of DNA by magnesium and calcium. *J. Mol. Biol.* **2000,** 301, (4), 915-945.
265. Okazaki, R.; Masaoka, S.; Sakai, K., Photo-hydrogen-evolving activity of chloro (terpyridine) platinum (II): a single-component molecular photocatalyst. *Dal. Tans.* **2009**, 6127-33.
266. Eisenberg, R., Chemistry: rethinking water splitting. *Science* **2009,** 324, (5923), 44-45.
267. Du, P.; Schneider, J.; Li, F.; Zhao, W.; Patel, U.; Castellano, F. N.; Eisenberg, R., Bi- and terpyridyl platinum(II) chloro complexes: molecular catalysts for the photogeneration of hydrogen from water or simply precursors for colloidal platinum? *J. Am. Chem. Soc.* **2008,** 130, (15), 5056-5058.

Appendix

Figure A.1. (I) FAB mass spectrum of $[(tpy)Ru(tppz)PtCl](PF_6)_3$, (II) Isotopic distribution of $[(tpy)Ru(tppz)PtCl](PF_6)_3$ obtained when one PF_6^- is lost (Formula: $[C_{39}H_{27}ClN_9PtRuP_2F_{12}]^+$) as acquired by M-Scan, Inc. (III) Calculated isotopic distribution of $[(tpy)Ru(tppz)PtCl](PF_6)_3$ from ChemBio Draw Ultra 11.0 161

Figure A.2. (I) FAB mass spectrum of $[ClPt(tppz)Ru(tppz)PtCl](PF_6)_4$, (II) Isotopic distribution of $[ClPt(tppz)Ru(tppz)PtCl](PF_6)_4$ obtained when one PF_6^- is lost ($[M-PF_6]^+$, Formula: $[C_{48}H_{32}Cl_2N_{12}Pt_2RuP_3F_{18}]^+$) as acquired by M-Scan, Inc. (III) Calculated isotopic distribution of $[ClPt(tppz)Ru(tppz)PtCl](PF_6)_4$ from ChemBio Draw Ultra 11.0..... 162

Figure A.3. (I) ESI mass spectrum of $[(tpy)Ru(tppz)PtCl](PF_6)_3$ showing the isotopic distribution pattern of the dimer $[2M-PF_6]^+$, $[C_{78}H_{54}Cl_2N_{18}Pt_2Ru_2P_5F_{30}]^+$, (II) Calculated isotopic distribution of the dimer from ChemBio Draw Ultra 11.0..... 163

Figure A.4. (I) ESI mass spectrum of $[(tpy)Ru(tppz)PtCl](PF_6)_3$ showing the isotopic distribution pattern of the trimer, $[3M-2PF_6]^{2+}$, $[C_{117}H_{81}Cl_3N_{27}Pt_3Ru_3P_7F_{42}]^{2+}$, (II) Calculated isotopic distribution of the dimer from ChemBio Draw Ultra 11.0..... 164

Figure A.5. (I) ESI mass spectrum of $[(tpy)Ru(tppz)PtCl](PF_6)_3$ showing isotopic distribution pattern of the tetramer, $[4M-3PF_6]^{3+}$, $[C_{156}H_{108}Cl_4N_{36}Pt_4Ru_4P_9F_{54}]^{3+}$, (II) Calculated isotopic distribution of the dimer by ChemBio Draw Ultra 11.0 165

Figure A.6. Comparison of the ESI mass spectra of $[(tpy)Ru(tppz)PtCl](PF_6)_3$ in different solvents 166

Figure A.7. Concentration dependent intensity of the monomer ion fragmentation $[M-PF_6]^+$ (peak at 1243) for $[(tpy)Ru(tppz)PtCl](PF_6)_3$ at different concentrations in CH_3CN. 167

Figure A.8. 400 MHz ^1H-^1H COSY of $[Ru(tppz)_2](PF_6)_4$ in CD_3CN at 298 K 168

Figure A.9. 400 MHz ^1H-^1H COSY of $[(tpy)Ru(tppz)](PF_6)_2$ in CD_3CN at 298 K..... 169

Figure A.10. 400 MHz ^1H-^1H COSY of $[(tpy)Ru(tppz)PtCl](PF_6)_3$ in CD_3CN at 298 K 170

Figure A.11. 400 MHz ^1H-^1H COSY of $[ClPt(tppz)Ru(tppz)PtCl](PF_6)_4$ in CD_3CN at 298 K..... 171

Figure A.12. Cyclic voltammetry of the monometallic complexes, $[Ru(tpy)_2](PF_6)_2$ (I), $[(tpy)Ru(tppz)](PF_6)_2$ (II), $[Ru(tppz)_2](PF_6)_2$ (III), and the bimetallic complex $[(tpy)Ru(tppz)PtCl](PF_6)_3$ (IV) in CH_3CN with a scan rate of 100 mV/s 172

Figure A.13. Cyclic voltammetry of the monometallic complexes, $[(tpy)PtCl](PF_6)$ in 0.1 M Bu_4NPF_6 in DMF with a scan rate of 100 mV/s..... 173

Figure A.14. Cyclic voltammetry of the monometallic complexes, $[(tpy)Ru(tppz)Ru(tpy)](PF_6)_4$ in 0.1 M Bu_4NPF_6 in CH_3CN with a scan rate of 100 mV/s. 174

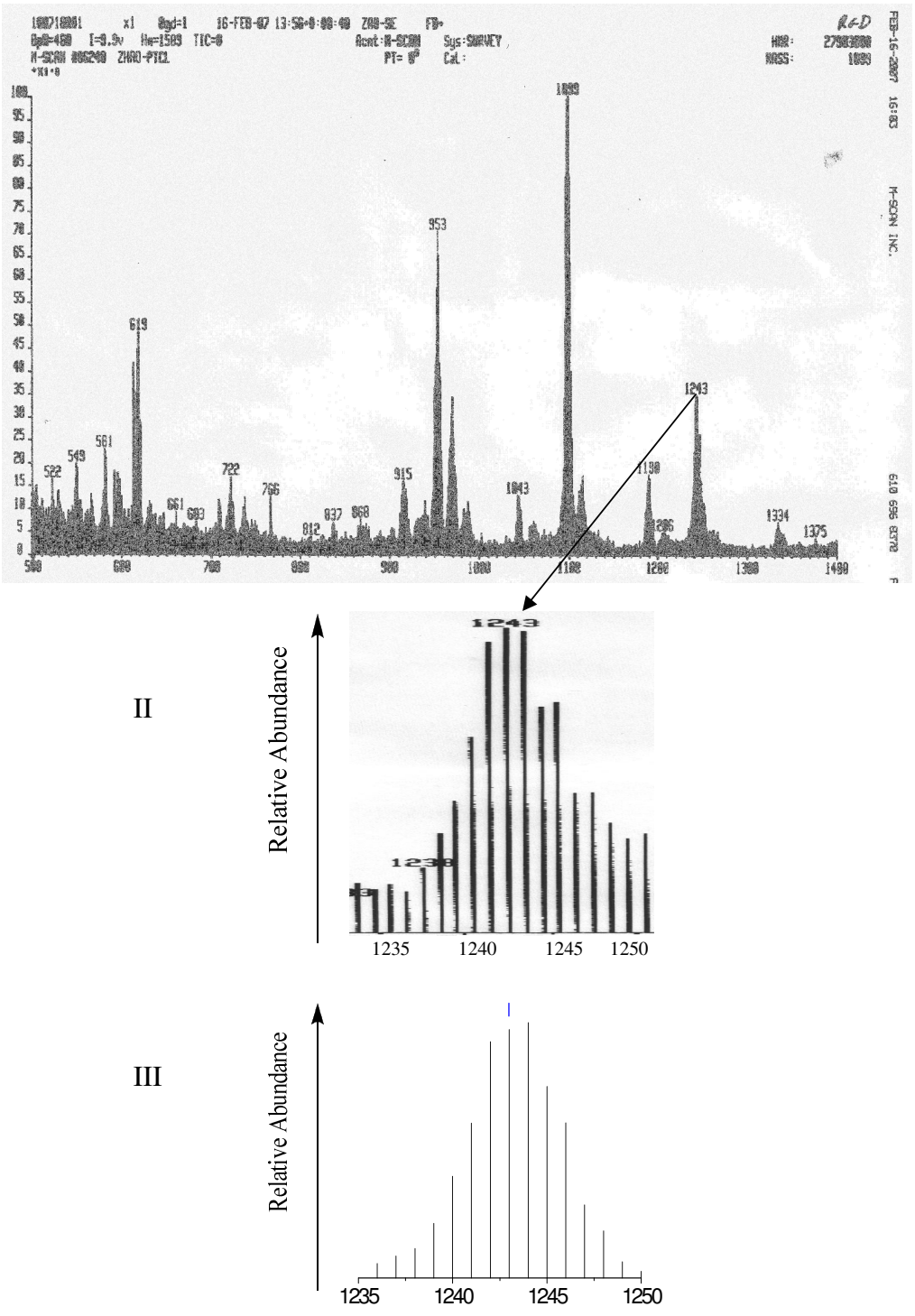

Figure A.1. (I) FAB mass spectrum of $[(tpy)Ru(tppz)PtCl](PF_6)_3$, (II) Isotopic distribution of $[(tpy)Ru(tppz)PtCl](PF_6)_3$ obtained when one PF_6^- is lost (Formula: $[C_{39}H_{27}ClN_9PtRuP_2F_{12}]^+$) as acquired by M-Scan, Inc. (III) Calculated isotopic distribution of $[(tpy)Ru(tppz)PtCl](PF_6)_3$ from ChemBio Draw Ultra 11.0

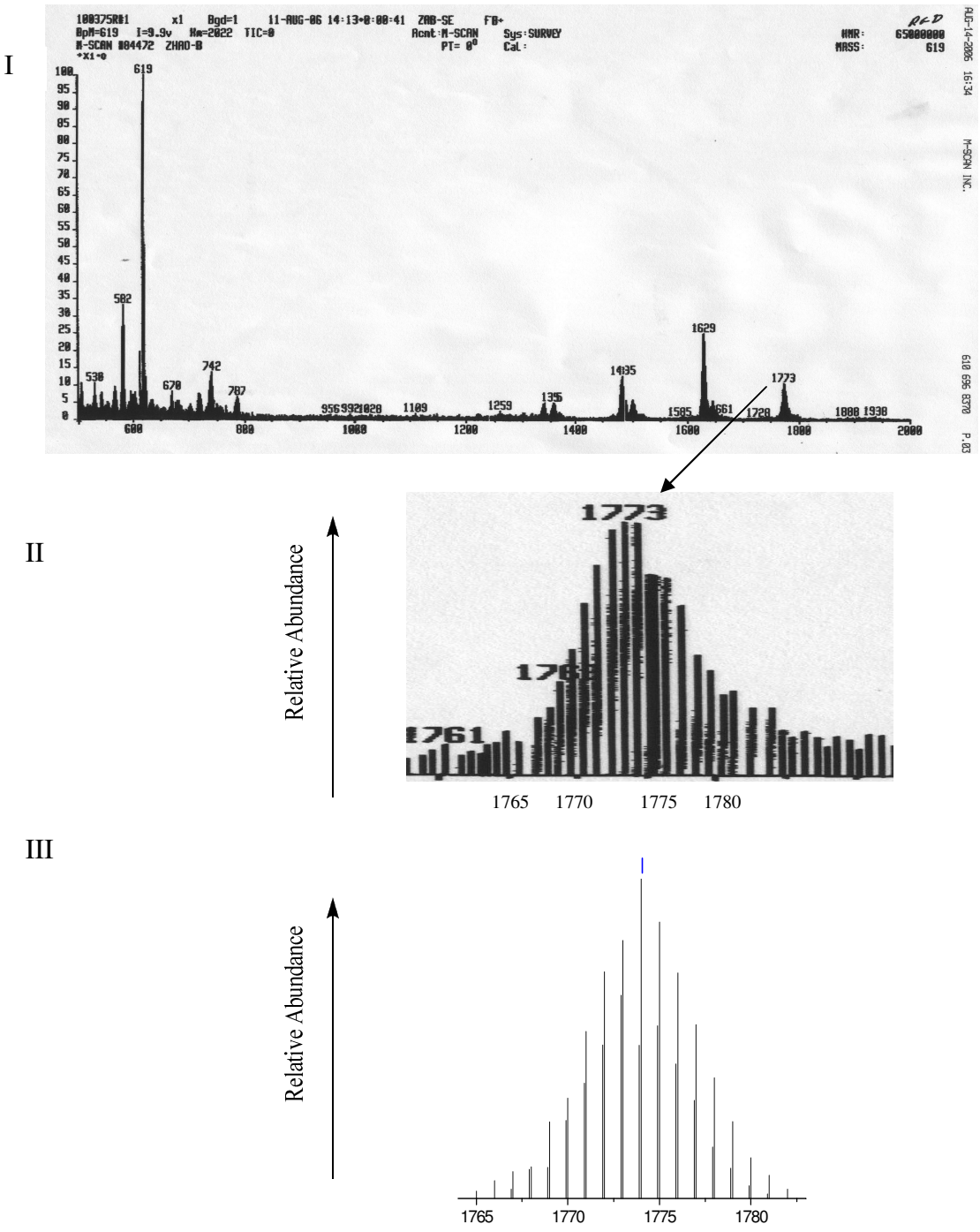

Figure A.2. (I) FAB mass spectrum of $[ClPt(tppz)Ru(tppz)PtCl](PF_6)_4$, (II) Isotopic distribution of $[ClPt(tppz)Ru(tppz)PtCl](PF_6)_4$ obtained when one PF_6^- is lost ($[M\text{-}PF_6]^+$, Formula: $[C_{48}H_{32}Cl_2N_{12}Pt_2RuP_3F_{18}]^+$) as acquired by M-Scan, Inc. (III) Calculated isotopic distribution of $[ClPt(tppz)Ru(tppz)PtCl](PF_6)_4$ from ChemBio Draw Ultra 11.0

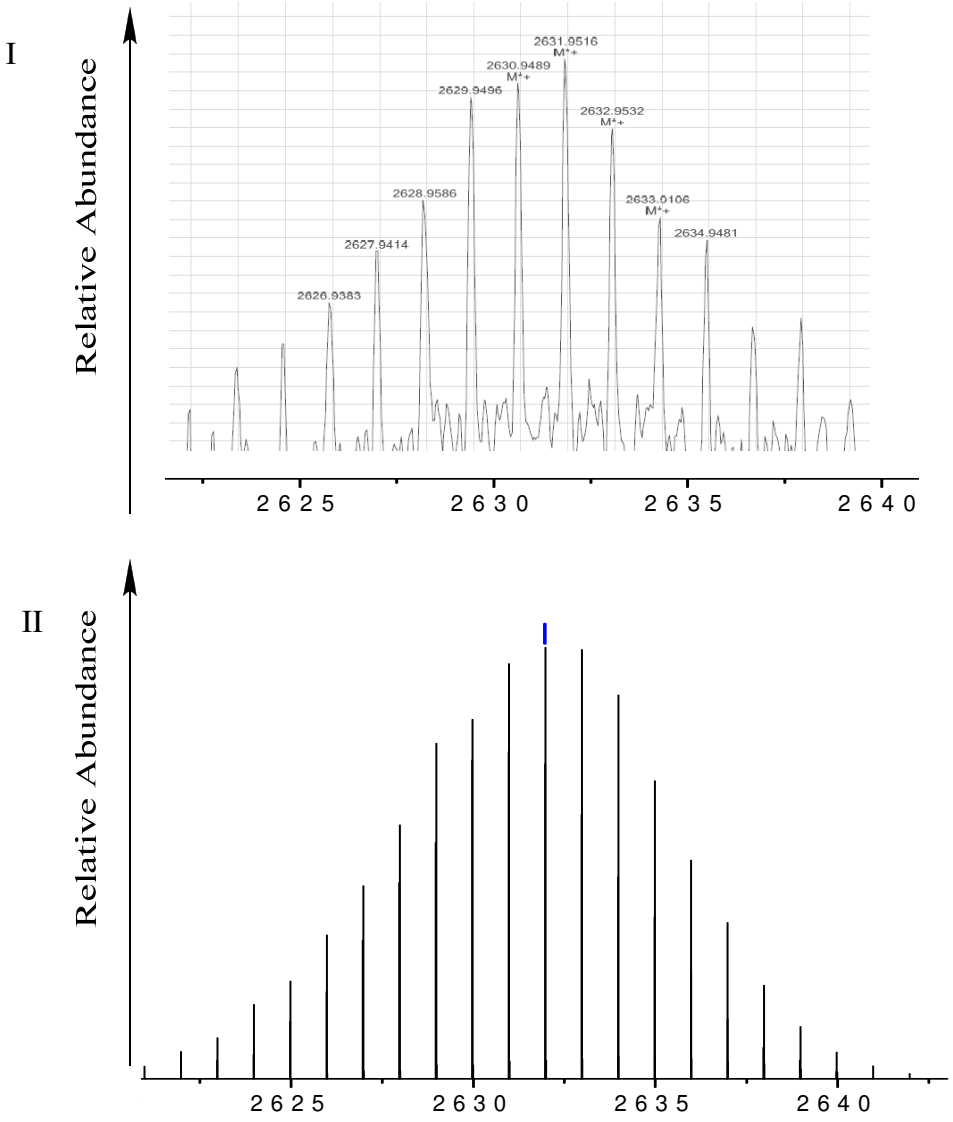

Figure A.3. (I) ESI mass spectrum of $[(tpy)Ru(tppz)PtCl](PF_6)_3$ showing the isotopic distribution pattern of the dimer $[2M\text{-}PF_6]^+$, $[C_{78}H_{54}Cl_2N_{18}Pt_2Ru_2P_5F_{30}]^+$, (II) Calculated isotopic distribution of the dimer from ChemBio Draw Ultra 11.0

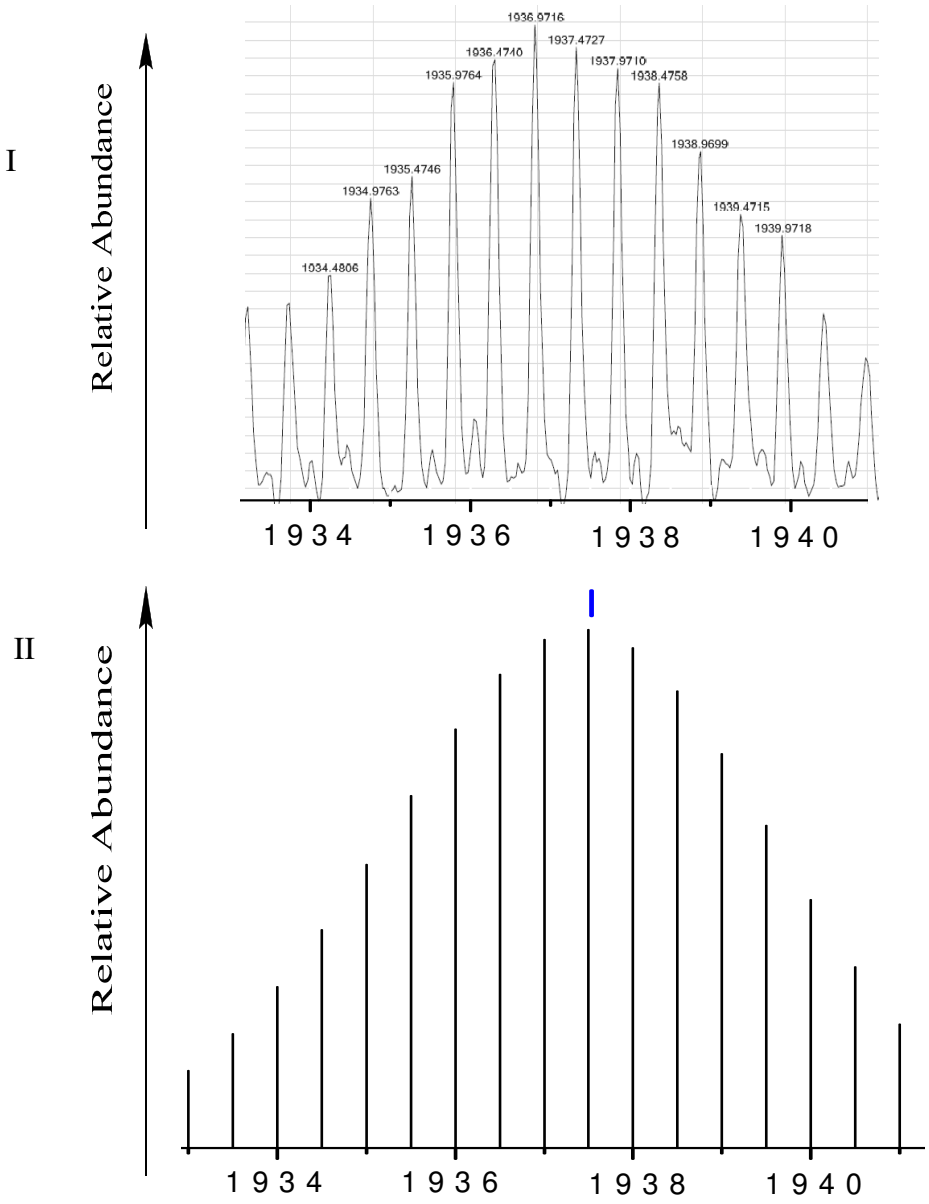

Figure A.4. (I) ESI mass spectrum of $[(tpy)Ru(tppz)PtCl](PF_6)_3$ showing the isotopic distribution pattern of the trimer, $[3M\text{-}2PF_6]^{2+}$, $[C_{117}H_{81}Cl_3N_{27}Pt_3Ru_3P_7F_{42}]^{2+}$, (II) Calculated isotopic distribution of the dimer from ChemBio Draw Ultra 11.0

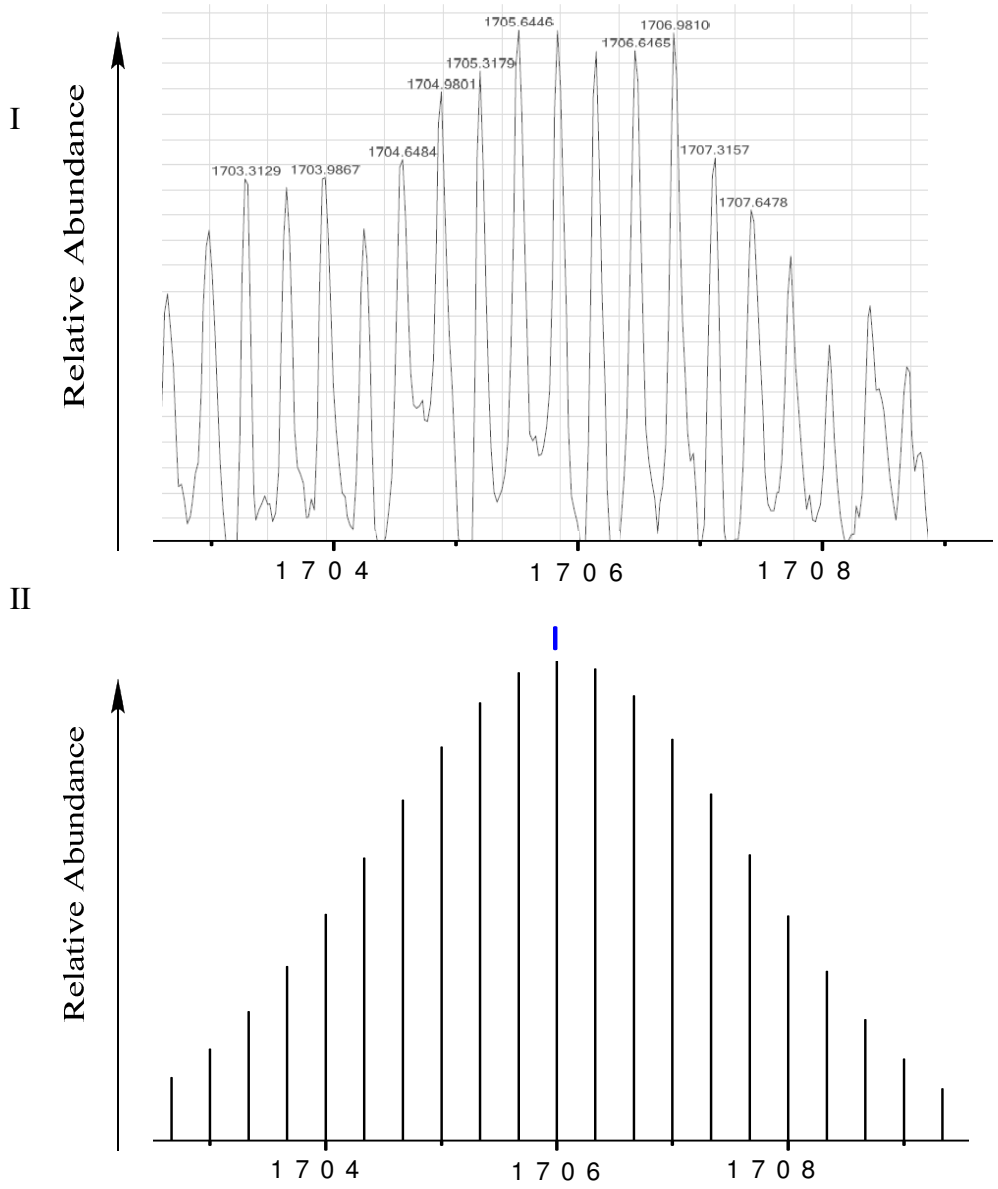

Figure A.5. (I) ESI mass spectrum of $[(tpy)Ru(tppz)PtCl](PF_6)_3$ showing isotopic distribution pattern of the tetramer, $[4M\text{-}3PF_6]^{3+}$, $[C_{156}H_{108}Cl_4N_{36}Pt_4Ru_4P_9F_{54}]^{3+}$, (II) Calculated isotopic distribution of the dimer by ChemBio Draw Ultra 11.0

In CH_3CN

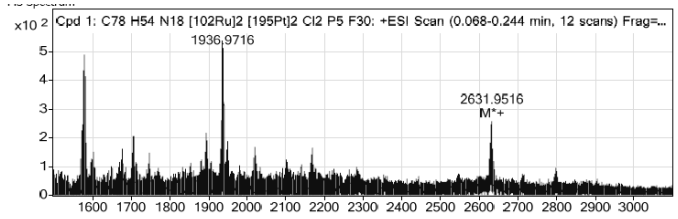

In DMSO

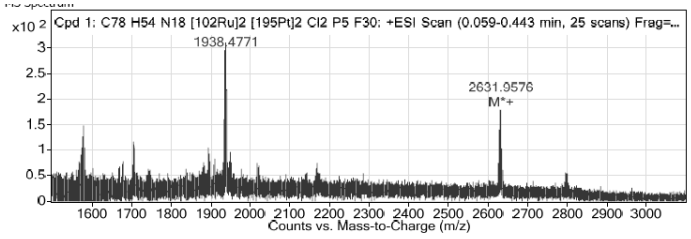

In DMF

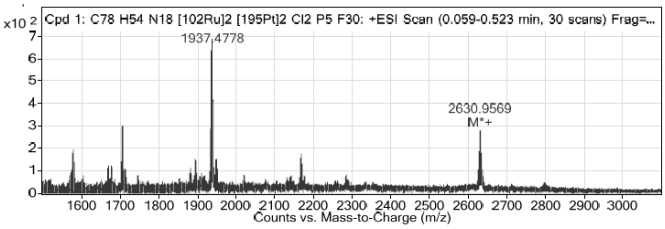

In acetone

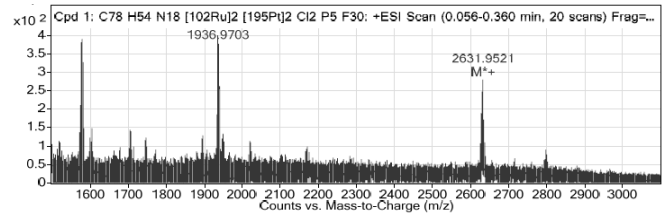

Figure A.6. Comparison of the ESI mass spectra of $[(tpy)Ru(tppz)PtCl](PF_6)_3$ in different solvents

2×10^{-3} M

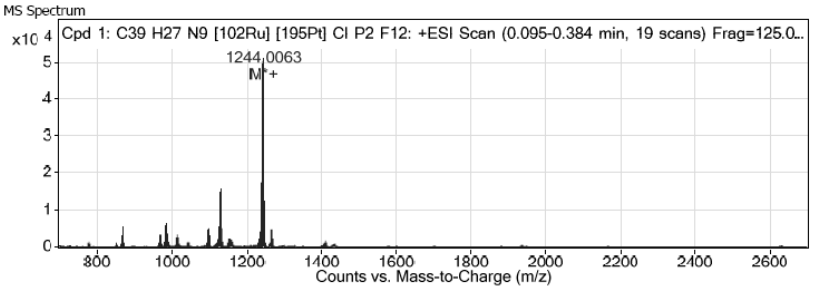

4×10^{-4} M

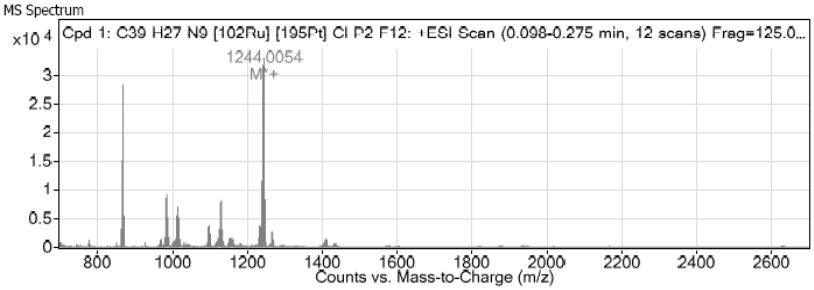

4×10^{-5} M

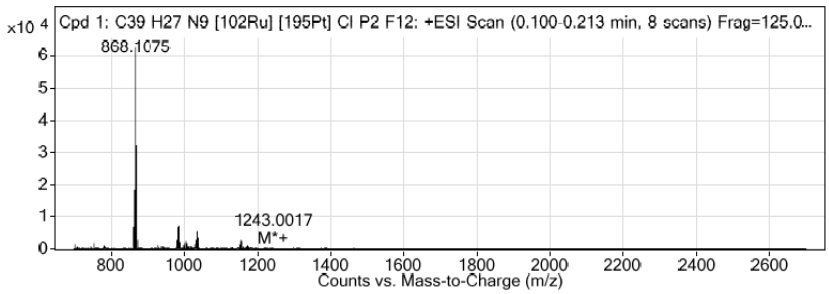

Figure A.7. Concentration dependent intensity of the monomer ion fragmentation $[M\text{-}PF_6]^+$ (peak at 1243) for $[(tpy)Ru(tppz)PtCl](PF_6)_3$ at different concentrations in CH_3CN.

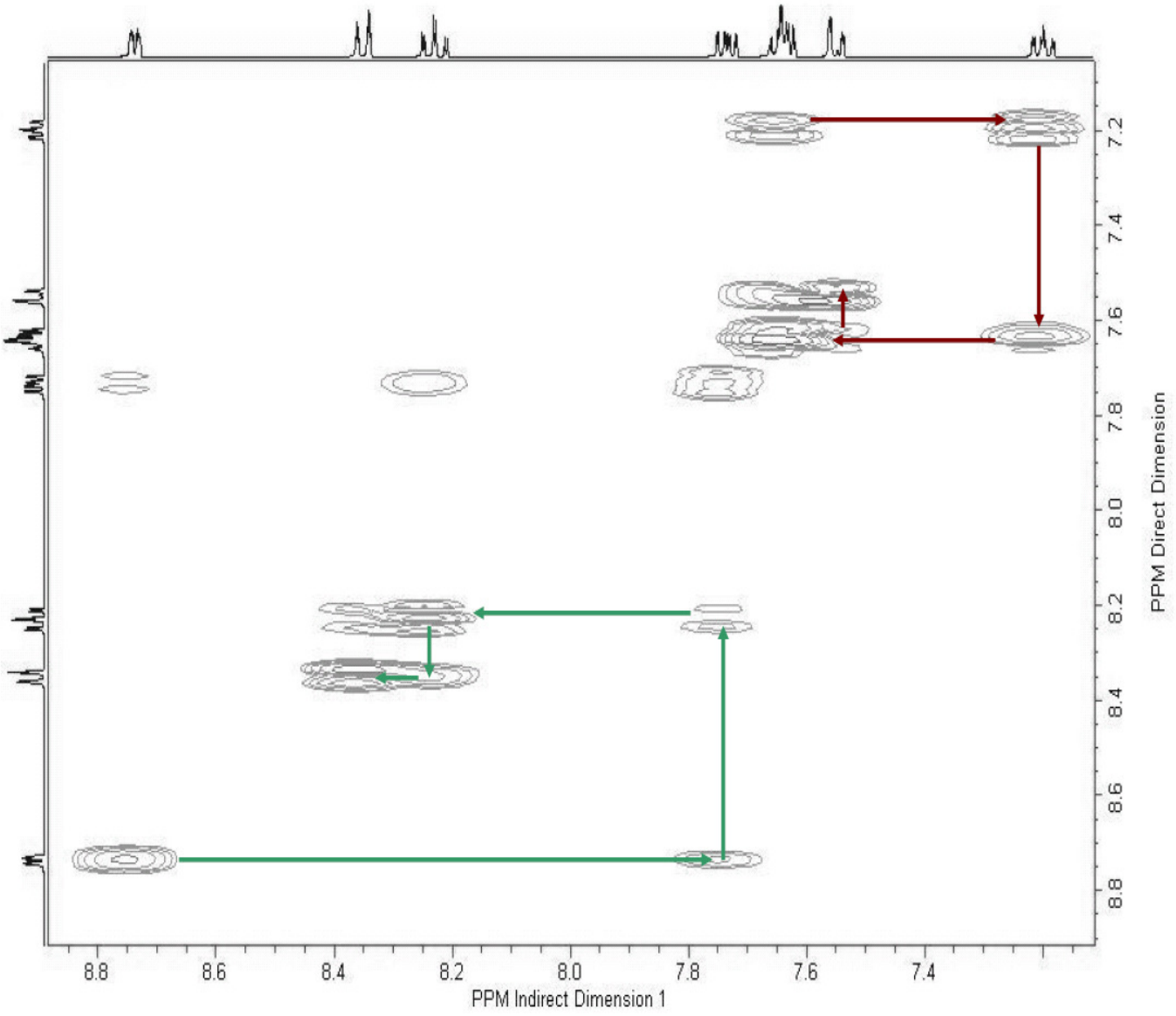

Figure A.8. 400 MHz ^{1}H-^{1}H COSY of $[Ru(tppz)_2](PF_6)_4$ in CD_3CN at 298 K

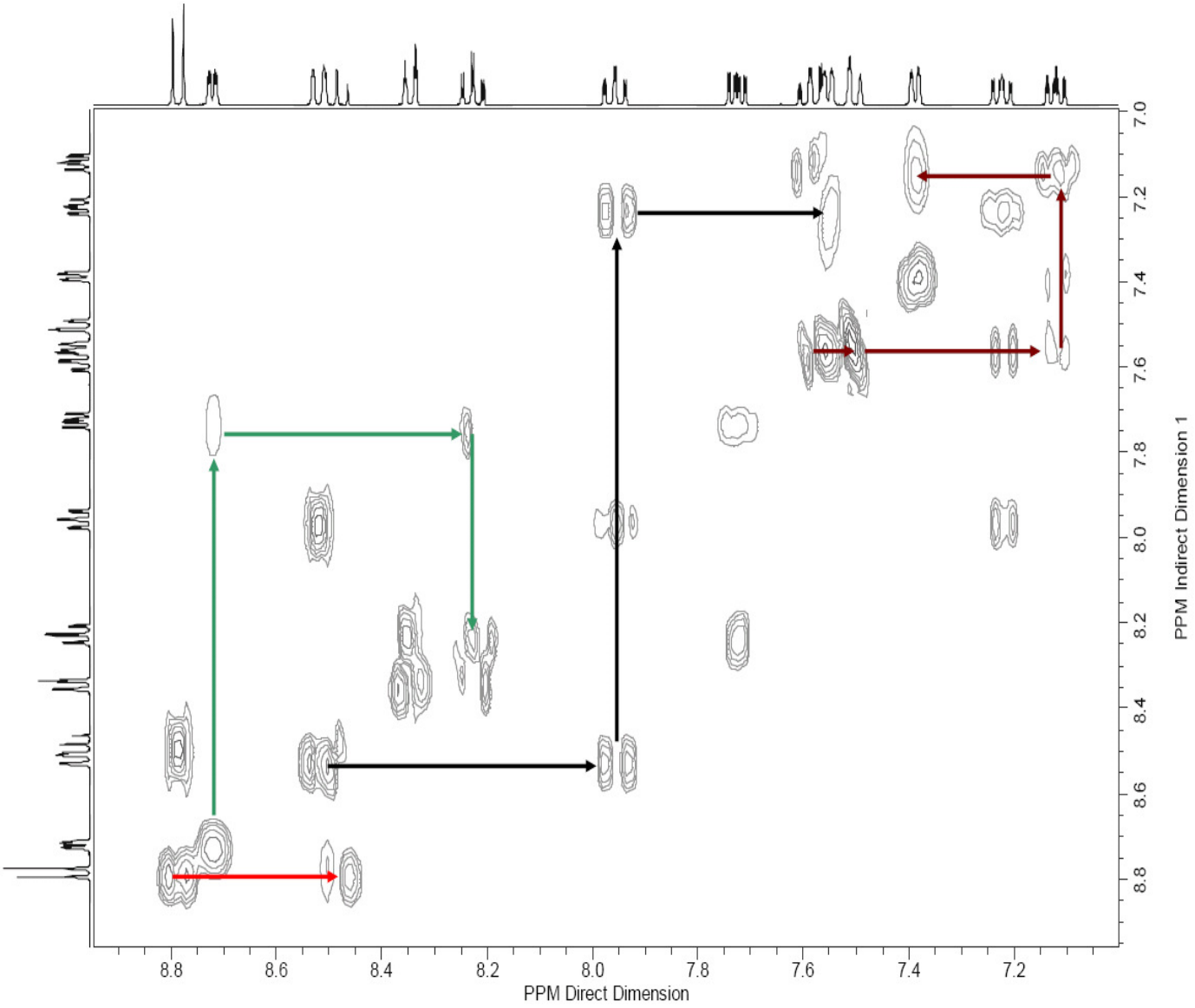

Figure A.9. 400 MHz ^{1}H-^{1}H COSY of $[(tpy)Ru(tppz)](PF_6)_2$ in CD_3CN at 298 K

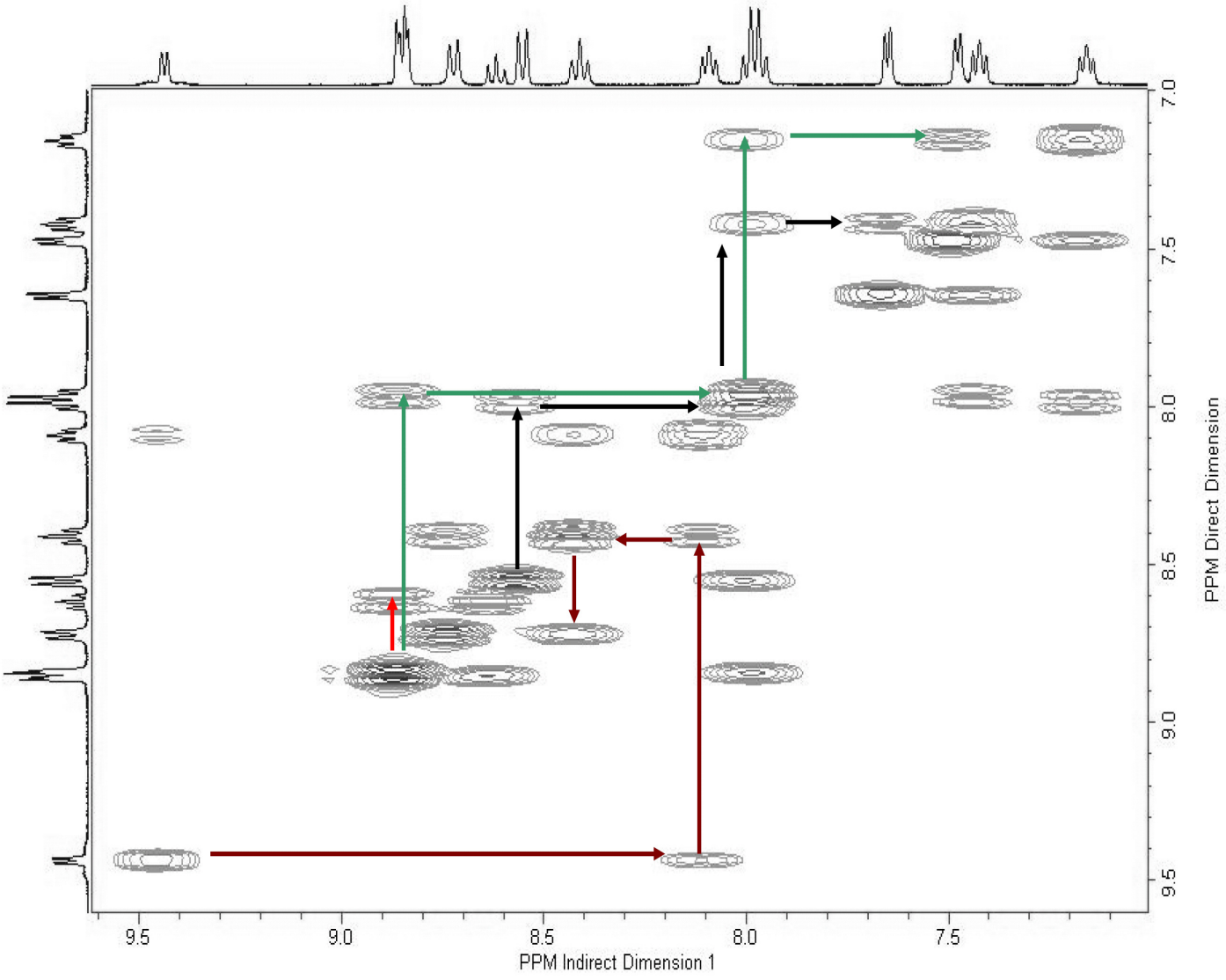

Figure A.10. 400 MHz ^{1}H-^{1}H COSY of [(tpy)Ru(tppz)PtCl](PF$_6$)$_3$ in CD$_3$CN at 298 K

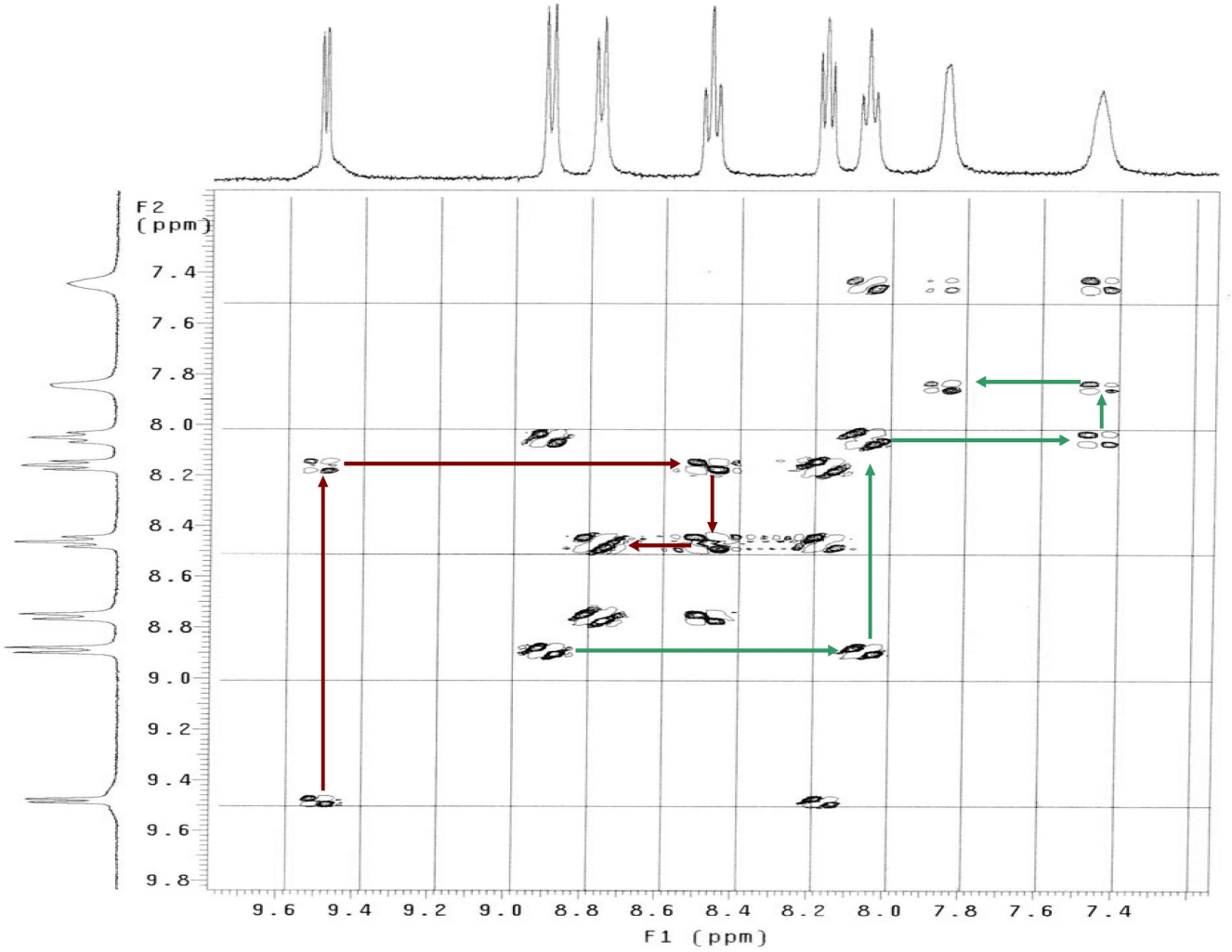

Figure A.11. 400 MHz ^{1}H-^{1}H COSY of [ClPt(tppz)Ru(tppz)PtCl](PF$_6$)$_4$ in CD_3CN at 298 K

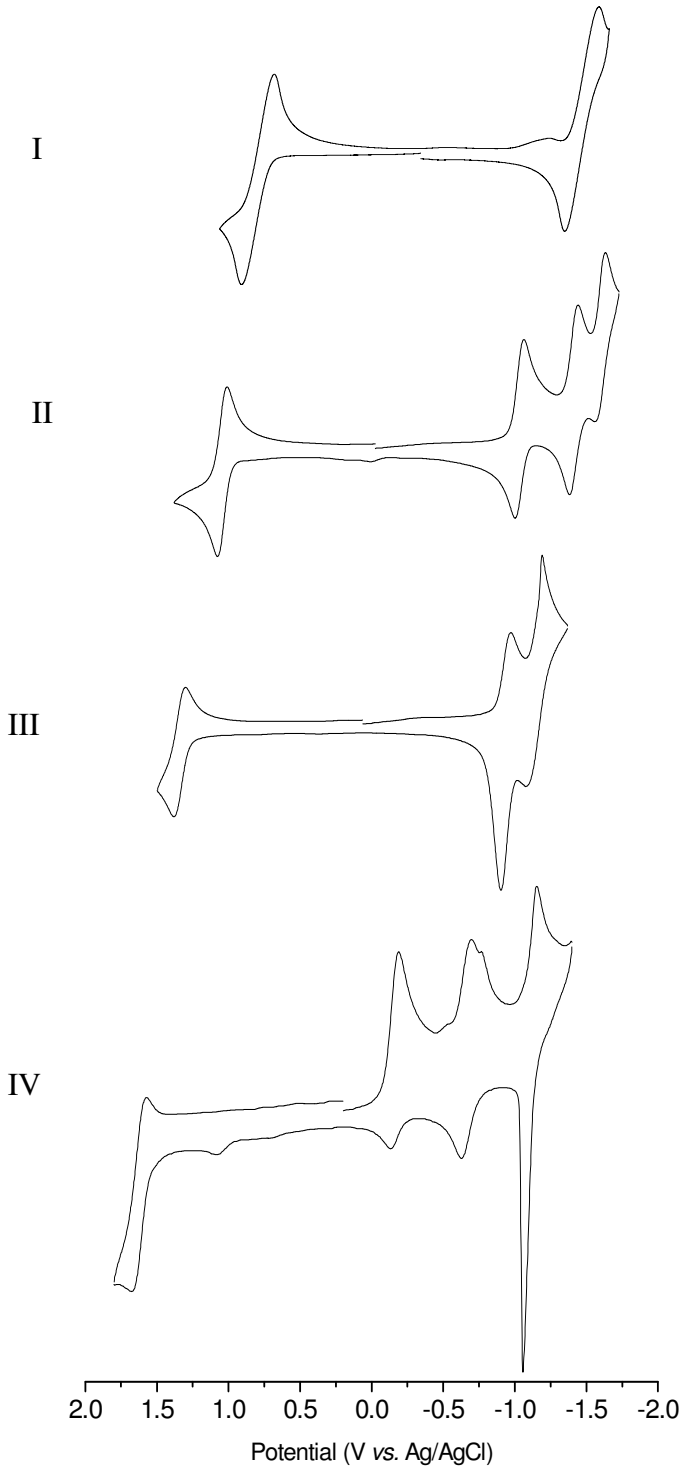

Figure A.12. Cyclic voltammetry of the monometallic complexes, $[Ru(tpy)_2](PF_6)_2$ (I), $[(tpy)Ru(tppz)](PF_6)_2$ (II), $[Ru(tppz)_2](PF_6)_2$ (III), and the bimetallic complex $[(tpy)Ru(tppz)PtCl](PF_6)_3$ (IV) in CH_3CN with a scan rate of 100 mV/s

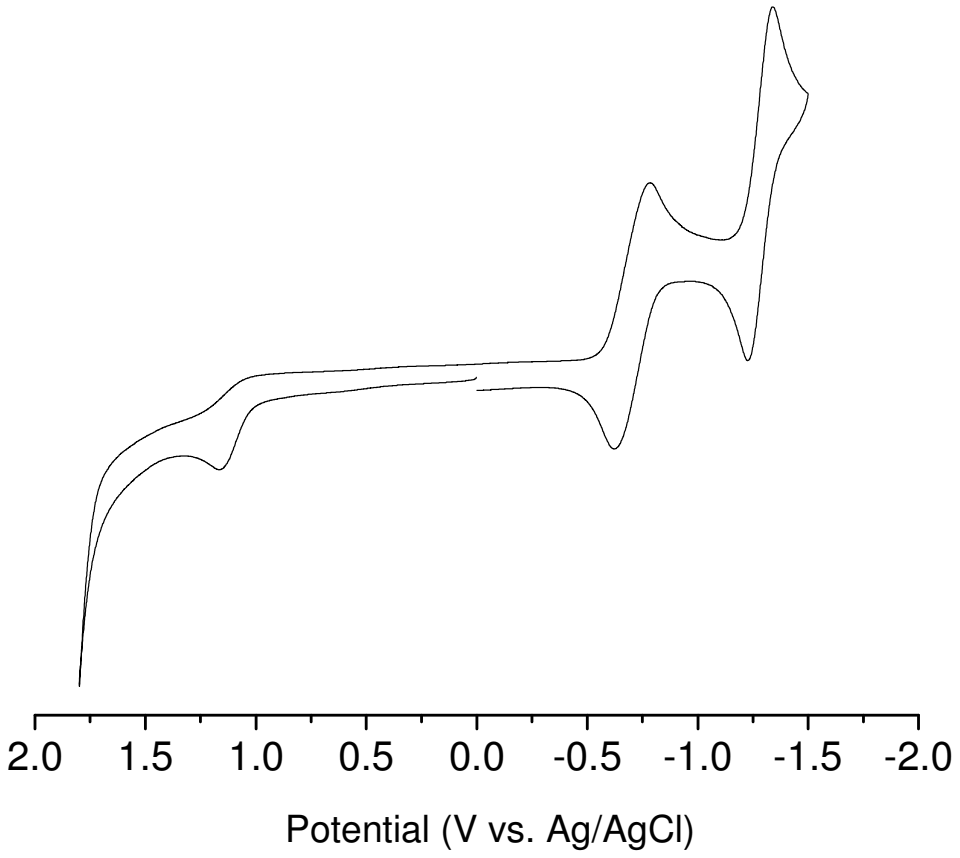

Figure A.13. Cyclic voltammetry of the monometallic complexes, [(tpy)PtCl](PF_6) in 0.1 M Bu_4NPF_6 in DMF with a scan rate of 100 mV/s.

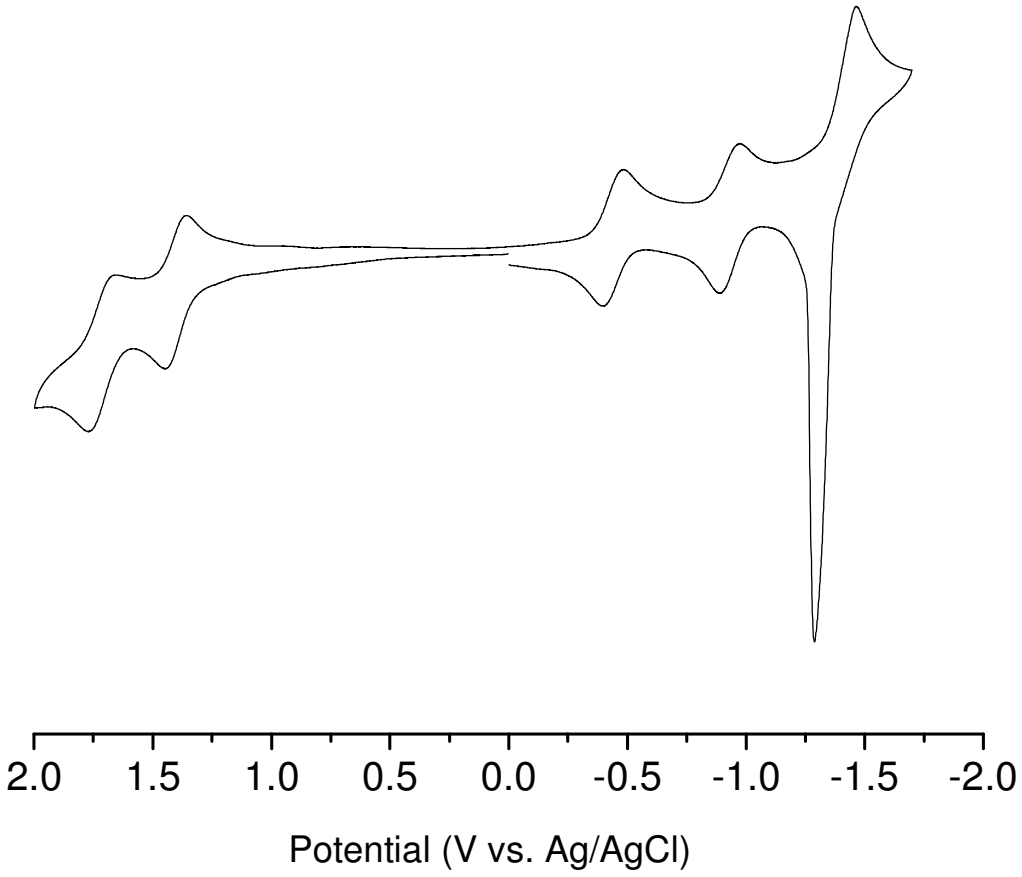

Figure A.14. Cyclic voltammetry of the monometallic complexes, $[(tpy)Ru(tppz)Ru(tpy)](PF_6)_4$ in 0.1 M Bu_4NPF_6 in CH_3CN with a scan rate of 100 mV/s.